CHARACTERIZATION AND INTERPRETATION OF VOLCANIC ACTIVITY AT REDOUBT, BEZYMIANNY AND KARYMSKY VOLCANOES THROUGH DIRECT AND REMOTE MEASUREMENTS OF VOLCANIC EMISSIONS

By

Taryn M. López

RECOMMENDED:

Jonathan Dehn

Rainer Newberry

William Simpson

Cynthia Werner

Catherine Cahill, Advisory Committee Chair

William Simpson
Chair, Department of Chemistry and Biochemistry

APPROVED:

Paul Layer
Dean, College of Natural Science and Mathematics

John Eichelberger, Dean of the Graduate School

1-18-13
Date

CHARACTERIZATION AND INTERPRETATION OF VOLCANIC ACTIVITY AT REDOUBT, BEZYMIANNY AND KARYMSKY VOLCANOES THROUGH DIRECT AND REMOTE MEASUREMENTS OF VOLCANIC EMISSIONS

A

DISSERTATION

Presented to the Faculty
of the University of Alaska Fairbanks

in Partial Fulfillment of the Requirements
for the Degree of

DOCTOR OF PHILOSOPHY

By

Taryn M. López, B.S., M.S.

Fairbanks, Alaska

May 2013

ABSTRACT

Surface measurements of volcanic emissions can provide critical insight into surface activity and subsurface processes at active volcanoes including the influx or ascent of magma, changes in conduit permeability, and relative eruption size. In this dissertation I employ direct and remote measurements of volcanic emissions to characterize activity and elucidate subsurface processes at three active volcanoes.

The 2009 eruption of Redoubt Volcano, Alaska, produced elevated SO_2 emissions that were detected by the Ozone Monitoring Instrument (OMI) satellite sensor for over three months. This provided a rare opportunity to characterize Redoubt's daily SO_2 emissions and to validate the OMI measurements. Order of magnitude variations in daily SO_2 mass were observed, with over half of the cumulative SO_2 emissions released during the explosive phase of the eruption. Correlations among OMI daily SO_2 mass, tephra mass and acoustic energies during the explosive phase suggest that OMI data may be used to infer eruption size and explosivity.

From 2007 through 2010 direct and remote measurements of volcanic gas composition and flux were measured at Bezymianny Volcano, Kamchatka, Russia. During this period Bezymianny underwent five explosive eruptions. Estimates of passive and eruptive SO_2 emissions suggest that the majority of SO_2 is released passively. Order of magnitude variations in total volatile flux observed throughout the study period were attributed to changes in the depth of gas exsolution and separation from the melt at the time of sample collection. These findings suggest that exsolved gas composition may be used to detect magma ascent prior to eruption at Bezymianny Volcano.

Karymsky Volcano, Kamchatka, Russia, is a dynamic volcano which exhibited four end-member activity types during field campaigns in 2011 and 2012, including: discrete ash explosions, pulsatory degassing, gas jetting, and explosive eruption. These activity types were characterized quantitatively and uniquely distinguished using a multiparameter

dataset based on infrasound, thermal imagery, and volcanic emissions. These observations suggest a decoupling between exsolved volatiles and magma at depth. I propose that variations in magma degassing depth influence the flux and proportions of decompression- and crystallization-induced degassing, as well as conduit permeability, can explain the variations in volcanic activity.

TABLE OF CONTENTS

Page

Signature Page i
Title Page ii
ABSTRACT iii
Table of Contents v
List of Figures x
List of Tables xii
Acknowledgements xiii
CHAPTER 1: Introduction 1
1.1 Volcanic Emissions 1
1.2 Volcanic Degassing 2
1.2.1 Introduction to Volcanic Degassing 2
1.2.2 Volatile Exsolution 2
1.2.3 Volatile-Melt Separation 4
1.2.4 Shallow Secondary Processes Affecting Gas Composition 5
1.3 Volcanic Ash 7
1.4 Volcanic Emissions Measurement Techniques 7
1.4.1 Direct Fumarole Samples 8
1.4.2 Remote Sensing of Volcanic Emissions 9
1.4.2.1 Satellite-based Ultraviolet Remote Sensing 10
1.4.2.2 Ground-based Ultraviolet Remote Sensing 11
1.4.2.3 Ground-based Infrared Remote Sensing (NicAIR) 13
1.4.2.4 Ground-based Infrared Remote Sensing (FLIR) 15
1.4.3 Infrasound 16
1.5 Dissertation Overview 17
1.5.1 Dissertation Aims 17
1.5.2 Dissertation Organization 18
References Cited 26

CHAPTER 2: Evaluation of Redoubt Volcano's Sulfur Dioxide Emissions by the Ozone Monitoring Instrument 33
ABSTRACT 33
2.1 Introduction 34
2.2 Overview of the 2009 Redoubt Eruption 36
2.3 Methods 37
2.3.1 UV Remote Sensing of SO_2 37
2.3.2 Airborne Measurements Using a Correlation Spectrometer 38
2.3.3 Overview of the Ozone Monitoring Instrument 39
2.3.4 Column Density Comparison Methods 40
2.3.5 OMI Measurements of SO_2 Mass 43
2.3.6 Plume Speed and Daily SO_2 Emission Rate Calculation Methods 44
2.4 Observations and Results 46
2.4.1 Summary of Observations 46
2.4.2 Column Density Comparison Results 46
2.4.3 Daily SO_2 Masses and Emission Rates 48
2.4.4 Emission Rate Calculation Method Comparison 48
2.4.5 Emission Rate Detection Limit 49
2.4.6 Cumulative SO_2 Masses and Emission Rates for the Sample Period 49
2.5 Discussion 50
2.5.1 Challenges and Advantages of Using OMI SO_2 Data 50
2.5.2 Uncertainties in Airborne SO_2 Measurements 51
2.5.3 Evaluation of Column Density Analysis 51
2.5.4 Evaluation of Daily SO_2 Mass 54
2.5.5 Evaluation of OMI-Derived Emission Rates 55
2.5.6 Discussion of Cumulative SO_2 Masses 57
2.5.7 Correlations between Eruptive Activity and OMI-Derived SO_2 Measurements 58
2.5.8 Apparent Periodicity in OMI Measured SO_2 Masses 61
2.5.9 Evaluation of OMI as a Volcano Monitoring Tool 62

2.6 Conclusions....62
2.7 Acknowledgements....64
References Cited....85
CHAPTER 3: Constraints on Magma Processes, Subsurface Conditions, and Total Volatile Flux at Bezymianny Volcano in 2007-2010 from Direct and Remote Volcanic Gas Measurements....92
ABSTRACT....92
3.1 Geologic Setting and Recent Eruptive Activity....93
3.2 Methodology....95
3.2.1 Direct Fumarole Sampling....95
3.2.2 FLYSPEC SO_2 Flux....95
3.2.3 OMI Explosive SO_2 Mass....98
3.3 Results....98
3.3.1 Timeline of Volcanic Activity and Sample Collection....98
3.3.2 Fumarole Composition....99
3.3.3 Passive SO_2 Flux....100
3.3.4 Explosive SO_2 Mass....101
3.4 Discussion....103
3.4.1 Comparison of Eruptive and Passive Degassing....103
3.4.2 Total Volatile Flux....104
3.4.3 Subsurface Processes Affecting Gas Composition and Flux....105
3.4.3.1 Chemical Signatures of Air Contamination....105
3.4.3.2 Chemical Signatures of Dilution or Scrubbing by Subsurface Water....106
3.4.3.3 Additional Secondary Processes Affecting Surface Emissions....107
3.4.3.4 Volatile Exsolution, Separation from the Melt, and Degassing....108
3.4.4 Comparison with Mutnovsky Volcano's Volatile Emissions....110
3.4.5 Model Constraints on Magma Degassing....111
3.4.5.1 Constraints on Magma Storage Depths....111
3.4.5.2 Constraints on Excess Volatiles....112

3.4.5.3 Constraints on Magma Degassing Depth....115
3.4.6 Proposed Model....116
3.5 Conclusions....117
3.6 Acknowledgements....119
References Cited....135
CHAPTER 4: Characterization of Volcanic Activity at Karymsky Volcano, Kamchatka, Using Observations of Infrasound, Volcanic Emissions and Thermal Imagery....143
ABSTRACT....143
4.1 Introduction....144
4.2 Karymsky Volcano....145
4.3 Methods....146
4.3.1 FLIR Thermal Imaging Camera....147
4.3.2 NicAIR IR Camera for Detection of Ash and SO_2....150
4.3.3 FLYSPEC UV Spectrometer System....153
4.3.4 Infrasound Data and Methods....156
4.4 Results....158
4.4.1 Ash Explosions....158
4.4.2 Pulsatory Degassing....159
4.4.3 Gas Jetting....160
4.4.4 Explosive Eruption....161
4.4.5 Hybrid Activity....162
4.5 Discussion....163
4.5.1 Evaluation of Acoustic and Thermal Radiation Energy....163
4.5.2 Characterization of the Four End Member Activity Types....166
4.5.2.1 Ash Explosions....166
4.5.2.2 Pulsatory Degassing and Gas Jetting....167
4.5.2.3 Explosive Eruption....168
4.5.3 Evaluation of SO_2 Emissions....170
4.5.4 Proposed Models....174

4.5.4.1 Previous Models....174
4.5.4.2 Proposed Model....175
4.5.5 Evaluation of Multiparameter Techniques for Characterizing Activity....180
4.6 Conclusions....182
4.7 Acknowledgements....183
References Cited....201
CHAPTER 5: Conclusions....209
5.1 Using Volcanic Emissions Measurements to Characterize Volcanic Activity....209
5.2 Using Volcanic Emissions Measurements to Infer Subsurface Conditions....211
5.3 Evaluating New Techniques for Remotely Measuring Volcanic Emissions....212
5.4 Comparison of the Target Volcanoes....215
5.5 Final Conclusions....218
References Cited....223

LIST OF FIGURES

Page

Figure 1.1: SO_2 absorption cross-section between 300 and 325 nm.....20
Figure 1.2: Field application of the Lambert-Beer law.....21
Figure 1.3: Photo of the FLYSPEC at Bezymianny Volcano.....22
Figure 1.4: FLYSPEC SO_2 emission rate calculation methods.....23
Figure 1.5: Ash and SO_2 IR camera retrievals.....24
Figure 1.6: Planck's curve.....25
Figure 2.1: Location map.....65
Figure 2.2: OMI detection of SO_2 from Redoubt Volcano.....66
Figure 2.3: Column density comparison between OMI and airborne SO_2 measurements.....67
Figure 2.4: Methods for calculating SO_2 emission rates from OMI data.....69
Figure 2.5: Comparison between corrected airborne and OMI SO_2 CD.....70
Figure 2.6: OMI-derived daily SO_2 mass and emission rates.....71
Figure 2.7: Results of comparison between OMI-derived and airborne SO_2 emission rates.....72
Figure 2.8: Cumulative SO_2 masses emitted from Redoubt Volcano.....73
Figure 2.9: Comparison between SO_2 and tephra masses for Mount Redoubt's explosive events.....74
Figure 2.10: Power Spectral Density analysis of OMI daily SO_2 mass.....75
Figure 3.1: Location map.....120
Figure 3.2: Photo of Bezymianny, Kamen, and Kliuchevskoi Volcanoes.....121
Figure 3.3: Seismicity below Bezymianny and Kliuchevskoi Volcanoes from 2006-2011.....122
Figure 3.4: Timeline of volcanic activity and sample collection at Bezymianny Volcano.....123
Figure 3.5: October 2007 OMI images of explosive SO_2 from Bezymianny Volcano..124
Figure 3.6: May 2010 OMI image of explosive SO_2 from Bezymianny Volcano.....125

Figure 3.7: Ternary diagrams showing Bezymianny fumarole sample composition for 2007, 2009 and 2010 126
Figure 3.8: Possible sources of excess volatiles at Bezymianny Volcano 127
Figure 3.9: Equilibrium degassing behavior as a function of dissolved CO_2 (ppm) and H_2O (wt%) melt concentration 128
Figure 3.10: Proposed degassing model 129
Figure 4.1: Location map 184
Figure 4.2: Photo of the 2011 experimental setup 185
Figure 4.3: IR camera SO_2 retrievals 186
Figure 4.4: FLYSPEC scan region 187
Figure 4.5: Multiparameter observations of the end-member activity types 188
Figure 4.6: Infrasound-based timeline 189
Figure 4.7: Infrasound spectrograms for the four activity types 190
Figure 4.8: Evening photograph of an *explosive eruption* event 191
Figure 4.9: Summary of data associated with *hybrid* activity 192
Figure 4.10: Ash and SO_2 retrievals for four *hybrid* events 193
Figure 4.11: Thermal radiation energy (J) and acoustic energy (J) for each activity type 194
Figure 4.12: Infrasound pressure and SO_2 emission rates surrounding an *explosive eruption* 195
Figure 4.13: Ash mass retrieval for an *explosive eruption* 196
Figure 4.14: Proposed speculative model 197

LIST OF TABLES

Page

Table 2.1: Explosive phase eruption chronology....76
Table 2.2: Daily OMI measured SO_2 masses and derived emission rates *(Method 1)* 78
Table 2.3: Summary of data used in the column density comparison 81
Table 2.4: Daily OMI SO_2 masses and emission rates for explosive events 83
Table 2.A.1: OMI and corrected airborne measurements comparison evaluation 83
Table 2.A.2: Airborne and OMI-derived SO_2 emission rates comparison evaluation....84
Table 3.1: Fumarole concentrations from Bezymianny Volcano 130
Table 3.2: Ratios and total dry-gas concentrations of relevant gas species for Bezymianny fumarole samples 131
Table 3.3: Bezymianny total volatile fluxes, explosive volatile masses, and total annual volatile masses in 2007 and 2009 132
Table 3.4: Mass balance constraints on magma degassing at Bezymianny Volcano 133
Table 4.1: Instruments and methods employed in this study....198
Table 4.2: Multiparameter characteristics of the observed activity....199
Table 4.3: Volatile saturation in the shallow crust 200
Table 5.1: A comparison of instrumental techniques used in this dissertation....220
Table 5.2: Comparison of the target volcanoes 222

ACKNOWLEDGEMENTS

The work presented in this dissertation was accomplished through the help and support of many people. In particular I want to thank my committee, specifically: Cathy Cahill, my advisor, for giving me the opportunity to pursue my own research interests, for believing that I could attain a Ph.D. in Environmental Chemistry, and for her unfailing support along the way; Jon Dehn, for teaching me infrared remote sensing and active volcanism, for bringing me to Stromboli Volcano where I saw my first explosive eruption, for providing me with the field instruments that made my research possible, and for wanting the best for all his students and doing everything he can to make opportunities possible; Cindy Werner, and the rest of the USGS Volcano Emissions Project including Peter Kelly, Mike Doukas and Christoph Kern, who gave me numerous opportunities to be actively involved with USGS Volcano Emissions Project and to assist with the Redoubt Volcano eruption response, and who have taught me a lot about volcanic gases; Bill Simpson, for his patience in teaching me spectroscopy both in and out of the classroom and for his support as both a committee member and department chair; and Rainer Newberry, one of the best teachers I have ever had, for his enthusiasm, patience and support, and who taught me the principles of geochemistry which are the foundations of this work.

I have had numerous non-committee mentors who have played an equally important role in my education. In particular, I would like to thank Pavel Izbekov, who gave me the opportunity to study volcanic gases at some of the most beautiful volcanoes in the world, and for taking the time to teach me an incredible amount about volcanoes and life. I'd also like to thank the rest of PIRE team, including Marina Belousova, Sasha Belousov, Theresa Kayzar, Owen Neill, Ashley Schueller, Wes Thelen, Sergey Ushakov, Sergey Serovetnikov, Slava Pilipenko, and Sergey Senyukov. I couldn't have asked for a better group of people to share my time at remote volcanoes. Your company has enriched my life! I would also like to thank several volcanic gas experts who have taught me

extensively about volcanic gases both in the field and over email correspondence, including: Franco Tassi, Simon Carn, Sergey Ushakov, Deb Bergfeld, Dima Melnikov, Fred Prata, Alessandro Aiuppa, Jake Lowenstern and Bo Galle. Without your help, my Ph.D. in volcanic gases at UAF would not have been possible. I would like to thank Dave Schneider, who has been a fantastic mentor, supporter, and friend and has given me numerous opportunities to be involved with AVO. I would like to thank the rest of the AVO family, including: Steve McNutt, Mike West, David Fee, Chris Nye, Jess Larson, Peter Webley, Rick Wessels, Tina Neal, Kate Bull, Game McGimsey, John Power, John Paskievitch, Cyrus Read, Janet Schaefer, Jeff Freymueller, Michelle Coombs, Tom Murray, Chris Waythomas, Silvio De Angelis, Glenn Thompson, Scott Stihler and the AVO students, especially Sarah Henton, Helena Buurman, Ronni Grapenthin, Owen Neill, Jill Shipman, Annie Worden, Summer Miller, Colin Rowell, and Chris Bruton. I have learned more about volcanoes through my experiences with AVO than I ever could have by reading a book. Thank you for sharing your knowledge, experience and opportunities with me! I'd also like to thank Tom Trainor and Emily Reiter, for their patience in teaching me chemistry, and their confidence that I could succeed as a chemist. I'd like to thank Doug Christiansen, Steve McNutt and Mike West, who gave me the opportunity to be a part of the PLUTONS project, and have all been supportive mentors and friends.

In addition to my academic support network, I'd also like to thank the numerous people who have influenced and supported me in my daily life. For Dea Huff, Dan Carlson, Oliver Damaann, Erin Gleason, Greg Deamer and the rest of my IARC cube-mates. You have significantly enriched my day-to-day life. Thank you for inspiring me, supporting me, and keeping me company on many a late night and long weekend. I feel blessed to have such positive work neighbors. For my fellow GIGSA students, especially Tim Bartholomous, it's been a pleasure working with you and sharing our pursuits. Thank you for all you have taught me and for making grad school fun. For Sarah Henton, Helena Buurman, Ronni Grapenthin, Chloe Peterson, Alida Van Almelo, and Susana Salazar,

you guys have been my rocks. You've shared some of my highest highs and lowest lows. Thank you for your friendship, support, and for always being there for me. For my West Ridge Runners, especially: David Fee, Alida Van Almelo, Ed Debevec, Dave Leonard, Glenn Thompson, Annie Worden, Mike West, Ronni Grapenthin, and Chris Iceman. You guys have been my running partners, friends and therapists. It's been a pleasure to be a part of your team! For Trystan Herriott, my partner for many years, who brought me to Alaska, showed me her remote beauty, and taught me how to survive. I will always be grateful for the love, support, and experiences you shared with me. For my family, especially my parents and my sisters. I am only here today because of the strength, support, love, and opportunities you have given me. Thank you for believing in me and giving me unconditional support in all avenues I've pursued. Last but not least, I would like to thank David Fee, my love, my partner, my mentor, my best friend. You have taught me so much about life and the kind of person I want to be in the short time I've known you. Thank you for believing in me and for all your support and help in helping me achieve my goal of attaining my Ph.D.

This dissertation is dedicated to my grandfather, Richard López, who had a thirst for knowledge and who tried to teach me at a young age to think for myself. I am grateful for your lessons, your love, and your interest in science.

CHAPTER 1: Introduction

1.1 Volcanic Emissions

Volcanic emissions are significant for their role in elucidating subsurface volcanic processes, influencing eruption style, contributing to volcanic eruption hazards, and affecting the local and global environment. Volcanic emissions include gases, which can be emitted passively or explosively, and volcanic ash, which is produced by explosive fragmentation of rock and lava. The surface composition and flux of volcanic gases can be affected by several deep and shallow processes; therefore, changes in gas composition and/or flux over time can be used to estimate relative magma depth according to volatile solubility trends, identify the presence of a shallow water system, and/or infer changes in conduit permeability (Fischer et al., 1996; Giggenbach, 1996). The large volume expansion experienced by volcanic gases during decompression ascent makes magma degassing a strong controlling factor in volcanic eruption style (Wallace and Anderson, 2000; Edmonds, 2008). Specifically, in viscous magmas if volcanic gases are able to exsolve and separate from their source magma and then be released at the surface the eruption may proceed passively; if, however, the expanding volcanic gases remain trapped within their host magma, the resulting eruption will be explosive. Once released at the surface, volcanic emissions can affect the local environment, resulting in crop damage in the vicinity of the volcano and respiratory problems in local populations (Williams-Jones and Rymer, 2000). If a volcano erupts explosively, large quantities of lava and/or rock can be fragmented to form fine silicate ash, which along with abundant volcanic gas produce volcanic clouds. These eruption clouds may undergo gravitational-collapse to form locally-hazardous and destructive pyroclastic flows, and/or get injected to high altitudes within the atmosphere. High altitude eruption clouds are significant because they: (1) enable remote and/or otherwise unmonitored volcanoes' eruptions to be detected and tracked (Prata, 1989; Oppenheimer, 1998; Carn et al., 2009; Prata, 2009), (2) can become a significant aviation hazard for jet aircraft, with both public safety and economic implications (Casadevall, 1994); and (3) provide a significant source of sulfur

dioxide (SO_2) and other gases to the stratosphere, which can affect the global climate (Robock, 2000). While the influence of volcanic emissions is extensive, the focus of this work will be on using the composition, mass, and flux of volcanic emissions, in particular volcanic gases, to characterize volcanic activity and elucidate subsurface processes.

1.2 Volcanic Degassing

1.2.1 Introduction to Volcanic Degassing

The dominant gases emitted at the surface by volcanoes include H_2O, CO_2, and SO_2, which generally make up ~95 mol% of all surface emissions (Symonds et al., 1994), and lesser quantities of HCl, H_2S, CO, HF, H_2, HBr, and other trace species (Symonds et al., 1994; Gerlach, 2004). The composition of these volatiles within a magma is highly dependent on tectonic setting (e.g. subduction zone, spreading center, hot spot, etc.), magma composition, and volatile source (e.g. subducted sediments, dehydrated rocks in the crust, mantle, etc.; (Giggenbach, 1997; Delmelle and Stix, 2000) as well as more localized and/or transient factors such as magma depth, presence of subsurface or surface water, degassing pathways, and conduit permeability. The processes of volcanic degassing, including volatile exsolution, separation from the melt, and degassing at the surface, strongly influence the behavior of active volcanoes. In the following sections I describe each of these processes as well as some of the external factors that influence volcanic degassing. I note that in order to interpret accurately the surface composition of volcanic gases, both shallow (i.e. surface through conduit) and deep (i.e. storage region and below) processes must be considered.

1.2.2 Volatile Exsolution

Volatiles are chemical species that preferentially exist in the gas phase under low (e.g. atmospheric) pressure conditions and are dissolved within magma at depth under high pressure conditions (Wallace, 2005). When a volatile's concentration exceeds its solubility it will exsolve from the melt to form a separate fluid phase under high pressure conditions or a separate gas phase under low pressure conditions. The main processes in

volcanic systems that induce volatile exsolution are: (1) decompression during magma ascent, which in most cases lowers magma solubility, and (2) melt crystallization, which increases the volatile concentration in the melt and induces volatile exsolution (Burnham, 1967; Shinohara, 2008). Volatiles within magma are predominantly incompatible in mineral phases and thus remain preferentially in the melt phase prior to exsolution. Several other species-dependent factors also contribute to volatile solubility within magma, including volatile speciation, the composition and oxygen fugacity of the melt, and the presence of an aqueous phase (Blank and Brooker, 1994; Carroll and Webster, 1994; McMillan, 1994). The magma solubility of H_2O and CO_2, the two most dominant volcanic gases, are fairly well constrained and are both functions of their partial pressures (Blank and Brooker, 1994; McMillan, 1994). Specifically, the solubility of carbon dioxide is directly proportional to its partial pressure; while the solubility of water is proportional to the square root of its partial pressure (Shinohara, 2008). The solubilities of sulfur and halogen species in silicate melts are complex. The speciation and solubility of sulfur is strongly influenced by the oxygen fugacity of the magma and the concentration of iron or alkali metal and alkaline earth elements in the melt (Carroll and Webster, 1994). The solubility and speciation of halogen species such as Cl and F remain poorly constrained, though a number of experiments suggest that the Cl solubility within magma may be strongly dependent on melt composition and may preferentially partition into a separate aqueous phase when possible (Carroll and Webster, 1994).

Solubility trends of magmatic volatiles within an ascending magma show that CO_2 and to a lesser extent SO_2 will exsolve at greater depth than more magma soluble species, such as HCl, HF, and H_2O (e.g. Gerlach, 1986; Giggenbach, 1996; Delmelle and Stix, 2000; Aiuppa et al., 2007; Burton et al., 2007). If the volcano exhibits open-system degassing behavior, where exsolved gases are able to separate from the melt and then ascend through the host magma to degas at the surface, it may be possible to use the ratios of relatively insoluble to soluble gas species obtained from surface measurements to determine the relative pressures of gas exsolution and melt separation (e.g. Burton et al.,

2007; Edmonds and Gerlach, 2007; Aiuppa et al., 2009; Werner et al., 2012), although secondary processes such as hydrothermal scrubbing (Symonds et al., 2001) may complicate interpretations. Solubility trends within magma have been successfully used at several volcanoes to indicate or confirm magma ascent prior to eruption (e.g. Aiuppa et al., 2007; Burton et al., 2007; Werner et al., 2012). Additionally, when used in conjunction with volatile solubility models (e.g. Newman and Lowenstern, 2002; Papale et al., 2006) and melt inclusion volatile concentration, these models can be used to estimate absolute pressures of volatile separation from the melt. This pressure is a proxy for depth and this technique has been used by scientists to estimate the depth of magma degassing and/or the degassing pathways at active volcanoes (Aiuppa et al., 2007; Burton et al., 2007).

1.2.3 Volatile-Melt Separation

Once volatiles have exsolved from their host melt, they can be transported to the surface via two end-member degassing mechanisms: (1) open-system degassing, where volatiles are able to separate from the melt and ascend in advance of the host magma, and (2) closed-system degassing, where exsolved volatiles ascend with their source magma. The ability of exsolved volatiles to separate from the melt is largely controlled by magma viscosity (Sparks, 2003). For low viscosity magmas such as basalts, exsolved volatiles as bubbles can grow through diffusion or coalescence, resulting in a large density contrast between the volatiles and melt. This density contrast allows the volatiles to rise buoyantly through the magma and degas at the surface (Sparks, 2003). The coalescence of bubbles can result in meter-sized volatile slugs that can burst at the surface in the form of Strombolian eruptions (Jaupart and Vergniolle, 1989; Gonnermann and Manga, 2012). Another degassing model has been proposed for basaltic and andesitic magmas in which degassing occurs via magma convection in a conduit, where a larger conduit radius can offset the higher magma viscosity for andesite magma (Kazahaya et al., 1994). In this scenario, low-density, volatile-rich magma ascends in a conduit to shallow depths (<2 km), at which point gases exsolve and degas, which increases the magma density and

causes it to sink down through the conduit (Kazahaya et al., 1994). Higher viscosity silicic magmas do not permit the buoyant ascent of exsolved volatiles; therefore, exsolved volatiles must utilize a different mechanism to escape from the magma or remain trapped. One mechanism that will allow exsolved volatiles to escape from a silicic magma is permeable flow through a magma foam (Eichelberger et al., 1986) or through interconnected bubbles or fractures within brittle magma (Edmonds et al., 2003). If exsolved volatiles remain trapped within an ascending magma, decompression will result in a high gas overpressure that eventually exceeds the confining pressure and fractures the brittle magma during explosive eruption (Gonnermann and Manga, 2012). These degassing mechanisms assume that the volcanic vent (or conduit) is open to the flux of gas and magma to the surface. In the case of volcanoes with shallow, viscous magma, pathways previously open to gas transport can become sealed due to magma crystallization, hydrothermal mineral precipitation, and/or degassing. This "sealing" of the conduit results in an increase in gas overpressure within the upper conduit, and eventually triggers explosive eruption. Prior to this type of eruption, decreases in SO_2 flux have been observed, supporting vent sealing as an eruption mechanism (Stix et al., 1993; Fischer et al., 2002).

1.2.4 Shallow Secondary Processes Affecting Gas Composition

Following exsolution and separation from the melt, volcanic volatiles that are quickly transported to the surface will retain the composition they had at depth, while volatiles that are transported slowly can equilibrate with their surroundings (including melt, wall-rock, hydrothermal fluids) and will reflect a modified composition (Giggenbach, 1996). Interaction between volcanic gases and ground-water or air can modify the original at-depth gas composition. Arc volcanoes typically have high N_2/Ar molar ratios due to contributions of nitrogen originating from subducted slab sediments (Giggenbach, 1996); therefore, air contamination can be identified in volcanic gas samples by low N_2/Ar molar ratios similar to that of air (84.5) or air-saturated water (~45) (Giggenbach, 1997). The highly porous character of many volcanic domes (viscous lava extruded to form a dome-

like structure above the conduit) facilitates interactions between volcanic gases and ambient air, such that air contamination of dome fumarole samples is expected. Atmospheric O_2 can react with reduced volcanic gases to modify their absolute concentrations measured at the surface (Giggenbach, 1987); therefore, interpretations of subsurface redox conditions should be done with care. The deposition of elemental sulfur (Eq. 1) is favored at low temperature, depletes H_2S twice as efficiently as SO_2, and can modify the concentration of sulfur species from depth (Giggenbach, 1987):

(1) $$SO_2 + 2H_2S \leftrightarrow 3S + 2H_2O$$

Oxidation of gas-phase H_2S and SO_2 can modify the initial plume S speciation. Aiuppa et al. (2005) found in a study at Mt. Etna Volcano (Italy) that H_2S is essentially inert in volcanic plumes over second-to-minute time scales. Therefore, for ground-based measurements the effects of this conversion will likely be minimal. Homogeneous and heterogeneous oxidation of SO_2 in volcanic plumes can be significant over hour-to-day time periods. Several studies have been conducted to estimate the loss rate of SO_2 in the atmosphere, which can be used to calculate the initial SO_2 concentration (Oppenheimer et al., 1998). These methods should be applied for satellite observations that may have been acquired up to a day after emission from the volcano. Additionally, considering total S concentration, instead of SO_2 and/or H_2S, can allow trends in gas composition involving S species to be interpreted without concern for air contamination and/or plume oxidation.

Interaction between magmatic gases and subsurface waters, including shallow meteoric water and/or a well-developed hydrothermal system, can also modify the original magmatic gas composition. Specifically, boiling meteoric water can provide an additional source of water vapor and bias the surface emissions toward higher water content (Chiodini and Marini, 1998). Furthermore, upon interaction with subsurface water, the highly water-soluble magmatic gas species such as SO_2 and HCl (for pH > 1) can be removed from the gas phase in a process known as scrubbing (Doukas and Gerlach,

1995; Symonds et al., 2001). The impact of these factors will strongly depend on the volume of water relative to the volume of magmatic gases (e.g. Vaselli et al., 2003; Capaccioni et al., 2007; Werner et al., 2008; Werner et al., 2012), and the temperature and pH of the system at depth (Symonds et al., 2001). The occurrence of scrubbing at depth may be identified through changes in the composition or flux of surface emissions, namely CO_2 and SO_2 (Symonds et al., 2001). The proportions of magmatic versus meteoric water can be distinguished within volcanic gas samples through isotopic analysis of gas condensates (Giggenbach, 1992).

1.3 Volcanic Ash

While the bulk of the research presented here will focus on volcanic gases, I briefly describe here the significance of volcanic ash. Pyroclastic material consisting of bombs (>64 mm), lapilli (~2-64 mm) and ash (<2 mm in diameter), is produced during the explosive fragmentation of magma during volcanic eruption. Fine ash particles in particular can be transported long distances and can provide insight into the source magma and eruption mechanisms associated with the ash emission (Wilson et al., 1978; Sparks et al., 1997). Furthermore, ash cloud heights and volumes can be used to estimate eruption size (Wilson et al., 1978; Newhall and Self, 1982). Finally, ash is known to be hazardous to jet aircraft as it can melt in the jet's turbine engine and cause engine failure, as well as adversely affect other parts of the aircraft (Casadevall, 1994). Therefore, for both public safety and economic reasons it is important for pilots to avoid ash emissions. The absorption of infrared radiation by silicate ash is distinct from that of ice particles or clouds, which means that ash clouds can be detected and tracked using satellite remote sensing techniques that can significantly reduce the ash-aviation hazards described above (Prata, 1989).

1.4 Volcanic Emissions Measurement Techniques

In this dissertation I employ five methods to detect and quantify volcanic emissions. Each technique has advantages and disadvantages with regards to temporal resolution, spatial

resolution, number of species detected, and cost and feasibility of sample collection and analysis. These methods include: (1) direct sampling of fumarole gases using alkaline-filled collection (Giggenbach) bottles (Giggenbach, 1975), (2) satellite remote sensing of plume SO_2 column densities using the Ozone Monitoring Instrument (OMI) satellite sensor (Levelt et al., 2006), (3) ground-based and airborne remote sensing of plume SO_2 column densities using a FLYSPEC ultraviolet (UV) spectrometer system (Horton et al., 2006), (4) ground-based remote sensing of ash and SO_2 using a NicAIR infrared (IR) camera (Prata and Bernardo, 2009), and (5) high temporal resolution imaging of thermal radiation using a FLIR forward looking infrared camera (Spampinato et al., 2011). In addition to these five direct and remote measures of volcanic emissions, I also employ infrasound to measure the pressure released by the emission of volcanic gases and ash, which can be considered an indirect measure of volcanic emissions (Fee and Matoza, 2013).

1.4.1 Direct Fumarole Samples

Fumarolic gases can be sampled directly using alkaline-filled collection bottles in a technique commonly referred to as the Giggenbach method, after the prominent gas geochemist, Werner Giggenbach, who invented this technique (Giggenbach, 1975). In this method a pre-weighed, evacuated 300 mL glass bottle with an inlet port, containing an absorbing solution, is used for sample collection. Volcanic gases are directed into the bottle from the fumarolic vent via a series of thermally-equilibrated, chemically and thermally resistant tubes (e.g. silica, titanium, Pyrex). The bottle's inlet port is opened and gases are allowed to flow into the inverted bottle. During sample collection, the insoluble species fill the bottle's headspace, acid gases are absorbed into the solution, and water condenses in the bottle (Giggenbach, 1975). Once the bottle is full (no more gas bubbles are observed) the bottle is closed and taken back to the laboratory for analysis. In the laboratory, head-space gases are analyzed using gas chromatography, absorbed gases are analyzed using ion chromatography and wet chemistry techniques, and water is quantified by sample mass difference after subtracting the absorbed gas mass.

1.4.2 Remote Sensing of Volcanic Emissions

Volcanic emissions can be detected and quantified remotely based on their ability to absorb and emit electromagnetic radiation, using spectroscopic principles. In this dissertation I employ methods of absorption and emission spectroscopy in the ultraviolet (UV; 250 – 400 nm) and infrared (750 nm – 25 μm) wavelength regions. UV radiation sourced from the sun is either scattered by air molecules or reflected off the Earth's surface, and is used as the radiation source for passive UV remote sensing techniques. Similarly, infrared radiation emitted by all bodies with temperatures above absolute zero provides a source of IR radiation. The abundance of gas and ash emitted by volcanoes can be measured using remote sensing techniques because each chemical species absorbs radiation in a unique manner according to its molecular structure (Engle and Reid, 2006). This characteristic absorption signal can be utilized to identify individual species present in a plume and to determine the abundance of each species over the measured pathlength. Several gaseous species found in volcanic plumes, including SO_2, BrO, ClO, and OClO, have absorption features in the UV region of the electromagnetic spectrum (e.g. Figure 1.1) and can be detected using UV remote sensing if they are present in sufficient quantities (Platt and Stutz, 2008). SO_2 and silicate ash both have absorption features in the IR, and similar methods are used for their detection (Prata, 1989). As SO_2 is an abundant volcanic gas that is virtually absent in the background atmosphere, it is fairly straightforward to detect using remote sensing techniques, and thus will be the principal remotely-sensed gas in this dissertation.

The principles of absorption spectroscopy are described by the Lambert-Beer Law, which states that the absorbance of radiation is proportional to the concentration of the absorbing species N, over a pathlength, L. The product of N and L is known as the column density. Measurements of: (a) incident radiation I_o, or radiation that has not passed through the volcanic plume, and (b) transmitted radiation I, or radiation that has passed through the volcanic plume, are collected in the field. These measurements, along with measurements of the absorption cross-section of the species of interest σ, obtained

from either laboratory measurements or calibration cell measurements, are used to solve the Lambert-Beer Law for the column density of the molecule of interest (Figs. 1.1, 1.2). Units of column density are often given in parts per million meter (ppmm) and for SO_2 1 ppmm is equal to 2.663 x 10^{-6} kg/m^2 (Gerlach, 2003).

1.4.2.1 Satellite-based Ultraviolet Remote Sensing

The Ozone Monitoring Instrument (OMI) is a hyperspectral UV and visible satellite sensor aboard NASA's Aura spacecraft that measures atmospheric abundances of several trace gas species, including SO_2. Aura is a polar orbiting satellite and with a 2600 km swath width and 13 x 24 km pixel size at nadir, OMI is able to acquire full daily global coverage (Levelt et al., 2006). OMI has been collecting continuous atmospheric measurements since it first became operational in September 2004 (Carn et al., 2007). OMI's temporal resolution, consisting of 1 pass per day at equatorial latitudes and up to 3 passes per day at high latitudes, provides the opportunity to obtain a remote snapshot of volcanic SO_2 emissions on any day when they are above OMI's detection limit and not obscured by meteorological clouds. For this dissertation, operational OMI SO_2 data products (OMSO2; downloaded from: http://mirador.gsfc.nasa.gov/cgi-bin/mirador/collectionlist.pl?keyword=omso2) are analyzed using OMIplot software (Carn, 2011). OMSO2 data contain SO_2 measurements derived from the Band Residual Difference (BRD) (Krotkov et al., 2006) and Linear Fit (LF) algorithms (Yang et al., 2007), which retrieve SO_2 CD from measured radiances in up to 10 discrete UV bands between 310 and 360 nm. OMIplot software is used to produce images of SO_2 column density over a user-defined area, to calculate plume SO_2 mass by integrating the SO_2 column density values over the plume area, and to distinguish real SO_2 from noise through the use of SO_2 absorption spectrum peaks and troughs. The operational OMI SO_2 algorithms require an a priori assumption of SO_2 vertical distribution, characterized by the SO_2 layer center of mass altitude (CMA). For each OMI footprint, OMSO2 data products provide four values of total SO_2 column density corresponding to the following a priori CMAs: (1) ~0.9 km for SO_2 in the Planetary Boundary Layer (PBL); (2) ~2.5 km

for SO_2 in the lower troposphere (TRL); (3) ~7.5 km for SO_2 in the mid-troposphere (TRM); and (4) ~17.5 km for SO_2 in the upper troposphere or lower stratosphere (STL) (http://so2.gsfc.nasa.gov/Documentation/OMSO2Readme_V111_0818.htm; (Yang et al., 2007). PBL SO_2 column densities are derived using the BRD algorithm, but SO_2 column densities for the other altitudes are retrieved using the LF algorithm. The user must select the most appropriate SO_2 product for the prevailing geophysical conditions. Since mid-2008, OMI measurements have been affected by a dynamic radiance anomaly, known as the 'row anomaly' (http://www.knmi.nl/omi/research/product/rowanomaly-background.php), which is believed to be the result of partial blockage of the OMI nadir viewing port. Therefore rows impacted by the row anomaly should be excluded from analysis.

1.4.2.2 Ground-based Ultraviolet Remote Sensing

The FLYSPEC is a portable, commercially available, UV spectrometer system consisting of an Ocean Optics USB2000 UV Spectrometer with a spectral range of 187.4 – 347.4 nm and a spectral resolution of 0.5 nm; an integrated GPS for accurate constraints on measurement location and time; two calibration cells containing known quantities of SO_2 for internal calibration; and a stepper-motor and USB hub for automatic instrument operation via its proprietary software, LapFly. All components are contained in a weatherproof box (Horton et al., 2006). The FLYSPEC requires four calibration measurements and the sample spectra, or measurements of light absorbed by the volcanic plume, to be collected in order to calculate the column density of SO_2 in the volcanic plume. The calibration measurements include (a) a reference spectrum collected of clear sky, (b) a spectrum of the high SO_2 calibration cell (~1300 ppmm) on a background of clear sky, (c) a spectrum of the low SO_2 calibration cell (~500 ppmm) on a background of clear sky, and (d) a dark spectrum in which no light is detected by the spectrometer to measure the instrument noise. Once the calibration measurements have been collected, the LapFly software will calculate SO_2 column density using the sample spectra in near-real-time in a modified version of the Beer-Lambert law (Fig. 1.2). The specific

operations employed by the software are as follows: (1) subtraction of the dark spectrum from the sample and reference spectra to remove the effects of instrument noise and obtain the corrected sample and reference spectra, respectively, (2) calculation of absorbance: *-log[(Sample Spectra Corrected)/(Reference Spectra Corrected)] = Absorbance*, and (3) mathematical fit of the absorbance spectrum to the low and high calibration cell spectra to determine the column density in each sample spectrum (Horton et al., 2006).

The FLYSPEC can be operated in two modes to derive SO_2 emission rate (or flux) from the SO_2 column density measurements: (1) stationary scanning mode, and (2) vehicular traverse mode (Williams-Jones et al., 2008). In the stationary scanning mode a series of SO_2 column density measurements are collected from a fixed location by scanning the instruments field-of-view perpendicularly through the plume, beginning in clear sky and ending in clear sky. The scan angles corresponding with plume detection, and the distance from the plume to the instrument are used along with simple geometry to calculate plume width in meters. Plume speed is estimated from wind velocity as determined from spatially calibrated video data (Williams-Jones et al., 2008), Radiosonde measurements (http://weather.uwyo.edu), wind-circle methods (Doukas, 2002), or pilot reports. These measurements are used along with the following equation, modified from Williams-Jones et al. (2008) to calculate SO_2 emission rate (E_{SO2}) in units of metric tons per day (t/d):

$$(2) \qquad E_{SO_2} = vf \int c(w)dw$$

where v is plume speed (m/s), f is an SO_2-specific conversion factor (0.0002302 t s ppm^{-1} m^{-3} d^{-1}) to units of metric tons per day (t/d), c is SO_2 column density (ppmm), and w is the plume width (m).

The vehicular traverse mode involves any mode of transportation in which the FLYSPEC is able to collect zenith-looking radiation measurements while being transported under the plume. These traverses have been done using: fixed-wing aircraft (Doukas and McGee, 2007), helicopter, boat (Rodriguez et al., 2008), car/truck and on foot (Williams-Jones et al., 2008). The vehicular traverse method for emission rate calculation is simpler and has a greater accuracy than the stationary scanning method for two main reasons: (1) the zenith viewing geometry shortens the observed atmospheric pathlength and reduces molecular scattering, and (2) simultaneous SO_2 column density and GPS location measurements provide accurate constraints on the plume width (Williams-Jones et al., 2008). In this method, the FLYSPEC is affixed to the vehicle such that it has a clear view of the sky above. Calibration measurements of reference, dark, high calibration cell, and low calibration cell spectra are collected while under clear (plume free) sky. Then the vehicle traverses under the volcanic plume, beginning and ending each traverse under clear sky. During the vehicular traverse, the FLYSPEC is collecting continuous SO_2 column density and GPS location and time measurements. After sample collection, the SO_2 column density integrated over the plume width (determined from GPS measurements) can be used to derive emission rate using the previously described methods.

1.4.2.3 Ground-based Infrared Remote Sensing (NicAIR)

A NicarNica NicAIR IR multispectral imaging camera originally described in Prata and Bernardo (2009) uses the characteristic absorption features of SO_2 (8.6 μm) and silicate ash (11 to 12 μm) within the infrared region of the electromagnetic spectrum to remotely quantify column densities of SO_2 and ash and to collect time-series imagery of volcanic emissions. The NicAIR uses a commercially available thermal infrared camera core, with a 640 x 512 pixel uncooled microbolometer array detector, with temperature sensitivity in the region of 8-12 μm region. Three narrowband filters (0.5-1.0 μm) centered at 8.6, 10, and 11 μm, and a broadband filter (7-14 μm) are used to detect and quantify fine ash (1-16 μm radii) and SO_2 column densities (g/cm^2). The filters are mounted on a rotatable

"filter wheel", and during operation the camera acquires passive radiation of the image target for ~1 second through each of the four filters. Following each round of filtered image acquisitions a "field calibration" is conducted in which measurement of a temperature controlled black-body shutter is acquired to enable the affects of changing environmental conditions to be constrained. The field calibration measurements are used along with pre- and post-experiment laboratory calibrations, and a radiative transfer model to allow both SO_2 and ash column amounts to be quantified. Time-series SO_2 and ash column density imagery can then be used to calculate plume speeds, using parcel tracking methods, SO_2 emission rates, SO_2 event masses, and ash masses. Plume speeds (m/s) are calculated using a multi-step process. First, individual pixel sizes for the camera geometry and experimental setup are calculated using the known distance to source, camera geometry, and camera detector dimensions following the methods of Prata and Bernardo (2009). Second, multiple (up to 20 per image) horizontal cross-sections of plume SO_2 column density integrated over the plume width (referred to as plume SO_2 cross-sections) are made from the base to the top of the plume within each image (Fig. 1.5, left). Sequential images are then analyzed for spatial trends in SO_2 column density for each cross-section. These values are used along with image acquisition times to estimate plume speeds using plume parcel tracking methods (Williams-Jones et al., 2008). SO_2 emission rates are calculated by multiplying plume SO_2 cross-sections by plume speeds. In some cases, discrete degassing or ash emissions allow SO_2 and/or ash masses to be calculated. These calculations are done by first selecting images that include as much of the emissions from a particular event as possible. Then for each pixel within the image containing SO_2 or ash, the column density (g/m^2) is multiplied by the pixel size (m^2) and then summed together to get a total event SO_2 and/or ash mass. An example ash and SO_2 retrieval from the IR camera can be seen in Figure 1.5. The same methods are used to calculate ash masses, where ash column densities are used in place of SO_2 column densities.

1.4.2.4 Ground-based Infrared Remote Sensing (FLIR)

All objects with temperatures greater than absolute zero emit radiation in the form of thermal power. Thermal power *I*, is a function of temperature *T* according to the Stefan-Boltzmann Law

$$(3.1) \quad I = \sigma\left(T^4\right)$$

where σ is the Stefan-Boltzmann constant (5.6703 x 10^{-8} $Wm^{-2}K^{-4}$). This equation is appropriate for an ideal radiation source that absorbs and re-emits all incident radiation, and is referred to as a black body. Equation 3.1 can be modified to determine the thermal contrast between a hot object *T* (K) and an object at ambient temperature T_0 (K) for non-black body objects according to the following:

$$(3.2) \quad I = \varepsilon\sigma\left(T^4 - T_0^4\right)$$

where ε is emissivity of the hot and ambient temperature objects. Planck's Law relates temperature and radiance as a function of wavelength for a blackbody (Fig. 1.6), and serves as the basis of thermal remote sensing, according to the following:

$$(4) \quad B_\lambda\left(T\right) = \frac{2hc^2}{\lambda^5}\frac{1}{e^{\frac{hc}{\lambda K_B T}} - 1}$$

where B_λ is radiance as a function of wavelength, *T* is the temperature of the black body, *h* is the Planck constant (6.626 x 10^{-34} Js), *c* is the speed of light in a vacuum (2.998 x 10^8 m/s), and K_B is the Boltzmann constant (1.381 x 10^{-23} J/K). Application of these principles allows thermal camera radiance measurements to be used to remotely estimate pixel integrated brightness temperatures. Such measurements have been used extensively by ground-based instruments to successfully characterize behavior of hot eruptive material (Harris et al., 2007). In this study we use a FLIR thermal imaging camera to

acquire high temporal resolution (up to 5 Hz) thermal imagery of volcanic emissions. This thermal camera uses a 320 x 240 pixel focal plane array detector and an uncooled microbolometer with temperature sensitivity over a broadband wavelength region from 7.5-13 microns. Data are analyzed using FLIR ThermaCam Professional software, in which the user-input distance to the source, emissivity, ambient temperature and ambient relative humidity (both measured using a hand-held thermometer/hygrometer in the field) along with the LOWTRAN radiative transfer model to convert measured radiance into temperature according to Planck's Law (Spampinato et al., 2011).

1.4.3 Infrasound

Infrasound is low frequency (<20 Hz) sound waves produced by the acceleration of the atmosphere. Two common processes that can produce infrasound at volcanic vents are: (1) the rapid release and expansion of volcanic gases, and (2) the eruption and/or fragmentation of ash and lava (Fee and Matoza, 2013). In this study infrasound is recorded using 3-6 element arrays of National Center for Physical Acoustics (NCPA) digital microphones (e.g. Fee and Matoza, 2013) with flat response between 0.02 and 250 Hz. Microphones distributed in a centered-triangle array permit source azimuth and trace velocity (propagation velocity across the array) identification, allowing volcanic infrasound to be distinguished from noise and infrasound produced by other sources. Each stand-alone digital microphone consists of a piezo-ceramic acoustic sensor, onboard digitizer, and GPS connected to a battery. To quantify the eruption energetic at a particular volcano and to facilitate comparison of multiple volcanoes, acoustic energy and reduced infrasonic pressure can be calculated for individual eruptive events. The acoustic energy of a volcanic source, E_a, can be determined by integrating the acoustic intensity over time and the region through which it propagates. The acoustic intensity, I, is the average rate of flow of energy through a unit area normal to the direction of propagation, $I=p^2/\rho c$, where p is the excess pressure and ρ the density of the medium. The acoustic energy is then found by:

$$(2) \qquad E_a = \frac{\Omega}{\rho c}\int_0^T \Delta p^2(t)dt$$

Where Ω is the area through which sound passes, ρ is the density of the atmosphere, c is the sound speed, r is the distance to the source, $\Delta p(t)$ is the change in pressure as a function of time, and T the duration of the signal of interest. This is a common technique in volcano acoustics and the assumptions have been well-documented (Johnson and Ripepe, 2011; Fee and Matoza, 2013). Reduced pressure ($p_{ref} = p \times r/r_{red}$) is the infrasound pressure, p, scaled to a common source distance (r_{red} = 1 m here) for comparison between different volcanoes and recording locations. Infrasound array processing is performed using standard methods (e.g. Fee et al., 2011) to determine coherent infrasound signals, trace velocity, and signal coherency.

1.5 Dissertation Overview

1.5.1 Dissertation Aims

The fields of volcanic gas geochemistry and remote sensing of volcanic emissions are relatively young; however scientists and those involved in hazard mitigation are increasingly realizing the importance of these tools for detecting and characterizing volcanic activity. Volcanic gas geochemistry and remote sensing are now regular, accepted, and often invaluable methods used to understand volcanic processes and mitigate volcanic hazards. Additionally, volcanic gas geochemistry can provide useful insight into volcanic processes that can strongly complement geophysical and petrologic observations. Recent technological advancements have enabled higher temporal and spatial resolution remote measurements of volcanic emissions than were previously possible, with the potential to advance significantly our understanding of volcanic degassing processes and improve volcano monitoring. However, while much work has been done to characterize the degassing behavior at some volcanoes, many remote volcanoes remain poorly studied and understood. In this dissertation I aim to increase our understanding of volcanic behavior through measurements of volcanic emissions at three

remote and hazardous arc volcanoes. Specifically, the objectives of this project are as follows: (1) characterize the volcanic activity at Redoubt, Bezymianny, and Karymsky volcanoes using direct and remote volcanic emissions datasets; (2) use remote observations of volcanic emissions, and temporal trends in composition and flux to infer subsurface conditions including: conduit permeability, magma depth, degassing behavior, and/or the presence of a shallow water system; and (3) evaluate the application of several new technologies for the remote monitoring of volcanic emissions. This dissertation will thus add to our knowledge of volcanic eruption processes, as well as enhance monitoring of remote and hazardous volcanoes.

1.5.2 Dissertation Organization

Chapter 2 evaluates near-daily measurements of SO_2 emissions from Redoubt Volcano, Alaska, during its 2009 period of unrest using the Ozone Monitoring Instrument (OMI) satellite sensor. These measurements are used to: (1) evaluate OMI SO_2 column density values for Redoubt's tropospheric plume against near coincident airborne measurements by the Alaska Volcano Observatory, (2) calculate daily SO_2 masses from Redoubt Volcano for the first three months of the eruption, (3) develop simple methods to convert daily OMI-measured SO_2 masses into emission rates to allow satellite data to be directly integrated with airborne SO_2 emissions datasets, (4) calculate cumulative SO_2 emissions from the eruption, and (5) evaluate OMI as a monitoring tool for high-latitude degassing volcanoes. A copy of this chapter is currently published online as: Lopez, T., Carn, S., Werner, C., Fee, D., Kelly, P., Doukas, M., Pfeffer, M., Webley, P., Cahill, C., and Schneider, D., (2012), Evaluation of Redoubt Volcano's sulfur dioxide emissions by the Ozone Monitoring Instrument, *Journal of Volcanology and Geothermal Research.*

Chapter 3 employs direct and remote measurements of volcanic gas composition, SO_2 flux and eruptive SO_2 mass from Bezymianny Volcano, Kamchatka Russia, collected between July 2007 and July 2010 to elucidate volcanic behavior. These data are used along with eruption timing to constrain magma processes, subsurface conditions and total

volatile flux. A significant finding of this research is that according to exsolved gas composition, magma was degassing at relatively shallow depths in the months prior to explosive eruption in 2007 and 2009, which suggests that exsolved gas composition at Bezymianny Volcano may be used to detect magma ascent prior to eruption. A copy of this chapter is currently in press as: Lopez, T., Ushakov, S., Izbekov, P., Tassi, F., Cahill, C., Neill, O., and Werner, C., Constraints on magma processes subsurface conditions and total volatile flux at Bezymianny Volcano in 2007-2010 from direct and remote volcanic gas measurements in the *Journal of Volcanology and Geothermal Research*.

In Chapter 4, a multiparameter dataset consisting of quantitative observations of infrasound, temperature and volcanic emissions are used to characterize diverse activity exhibited by Karymsky Volcano, Kamchatka, Russia during field campaigns in August 2011 and July 2012. Four end-member activity types are identified including: (1) discrete ash explosions, (2) pulsatory degassing, (3) gas jetting, and (4) quiescence followed by explosive eruption. Each activity type has distinct character in the infrasound data, suggesting that Karymsky's activity could be remotely detected and characterized using infrasound as a primary monitoring tool. Based on our observations we propose that the four activity types can be explained by variations in relative depth of degassing magma, which influences the relative proportions and fluxes of decompression and crystallization-induced degassing, and conduit permeability. A version of this chapter is intended for submission to the journal *Geochemistry, Geophysics, Geosystems*.

In Chapter 5, I summarize the ways in which volcanic emissions measurements are used throughout this dissertation to characterize surface activity and infer subsurface processes. I also evaluate the strengths and weaknesses of the measurement techniques employed for the various activity styles observed at the target volcanoes. Finally, I compare the three target volcanoes to identify similarities and differences in their characteristics and eruptive behavior, and recommend instruments and/or methods that would have the greatest utility for monitoring their volcanic emissions.

Figures:

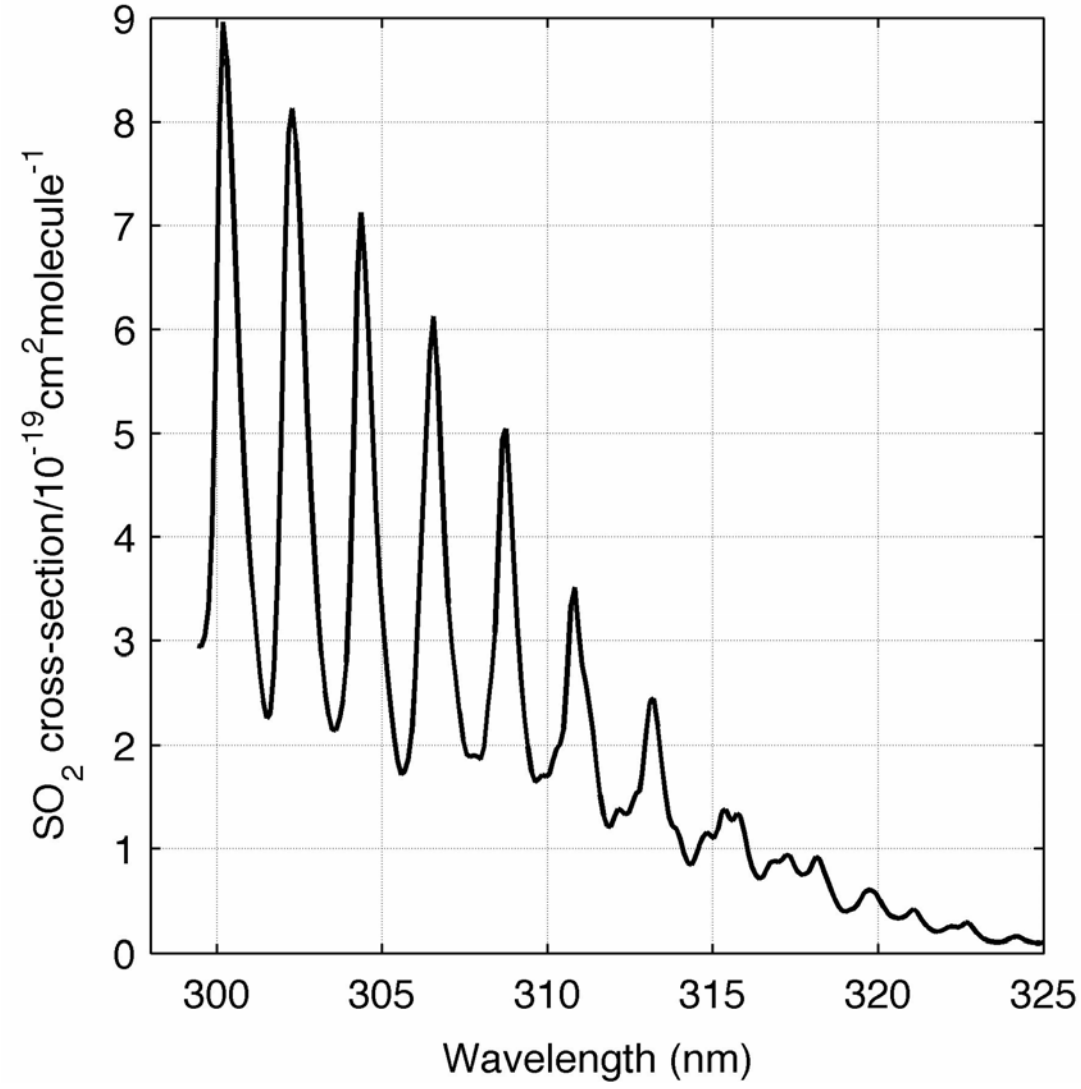

Figure 1.1: SO_2 absorption cross-section between 300 and 325 nm. Data were acquired from Bogumil et al.(2003).

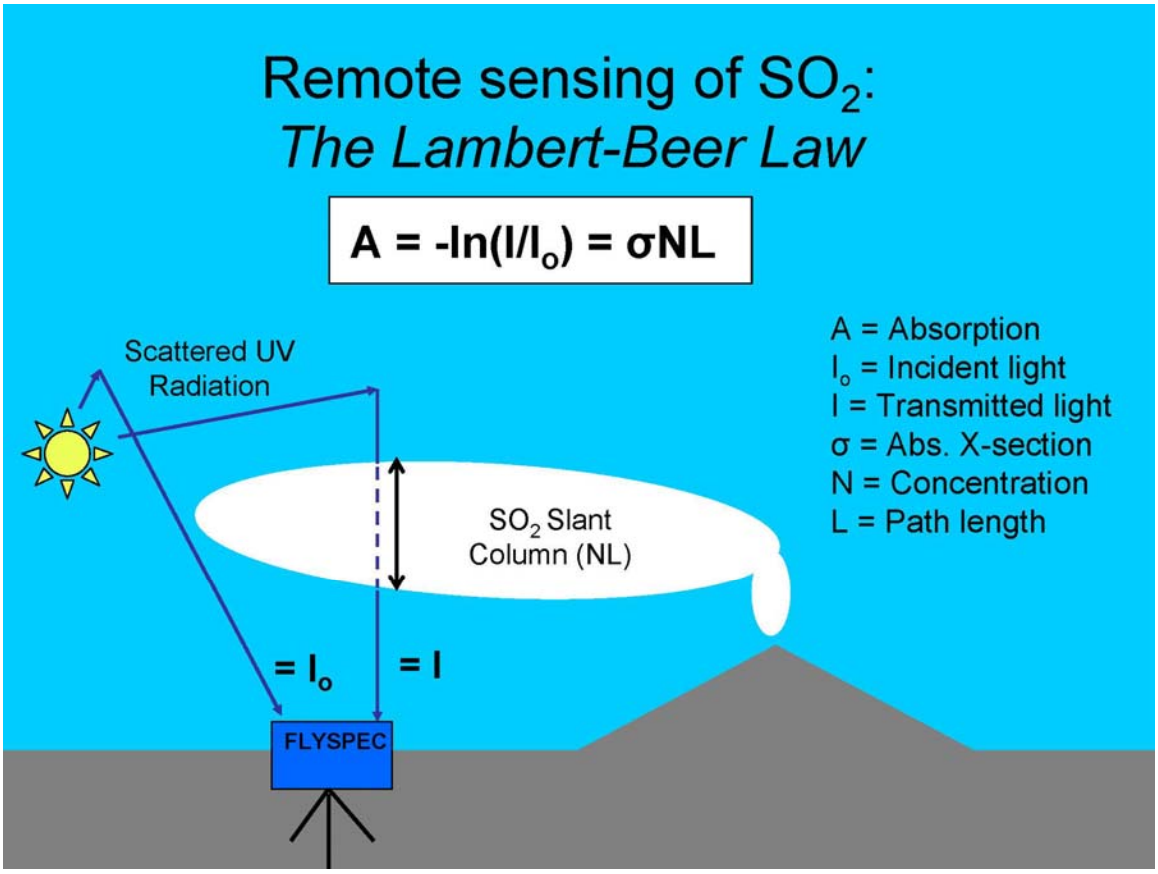

Figure 1.2: Field application of the Lambert-Beer law. Schematic diagram for the remote ground-based detection of SO_2 in a volcanic plume.

Figure 1.3: Photo of the FLYSPEC at Bezymianny Volcano. Measurements of absorbance of UV light by SO_2 in the volcanic plume at Bezymianny volcano are collected via horizontal above-vent scans. Photo taken July 2009.

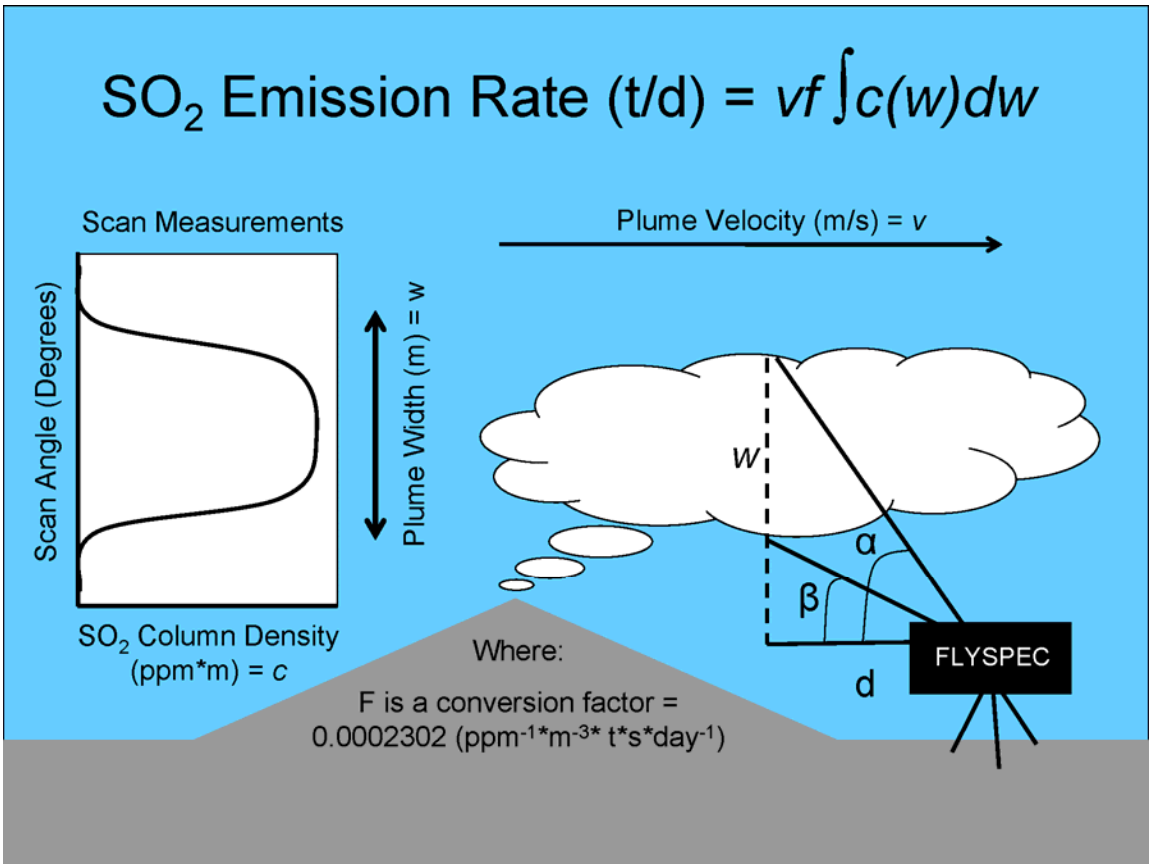

Figure 1.4: FLYSPEC SO_2 emission rate calculation methods. First, a series of SO_2 column density measurements are collected while scanning perpendicular through the plume. The scan angle (α), associated with above background level SO_2 column density values and the distance from the plume are used to calculate plume width in meters. Plume speed is estimated from wind velocity as determined from radiosonde measurements, video data, wind-circle measurements, or pilot reports. The integral of the SO_2 column density measurements (c) over the plume width (w) is calculated, which is then multiplied by the plume speed (v) and a conversion factor (f) of 0.0002302 ($ppm^{-1}m^{-3}tsday^{-1}$) to get an SO_2 emission rate (or flux) in units of metric tons per day (t/d).

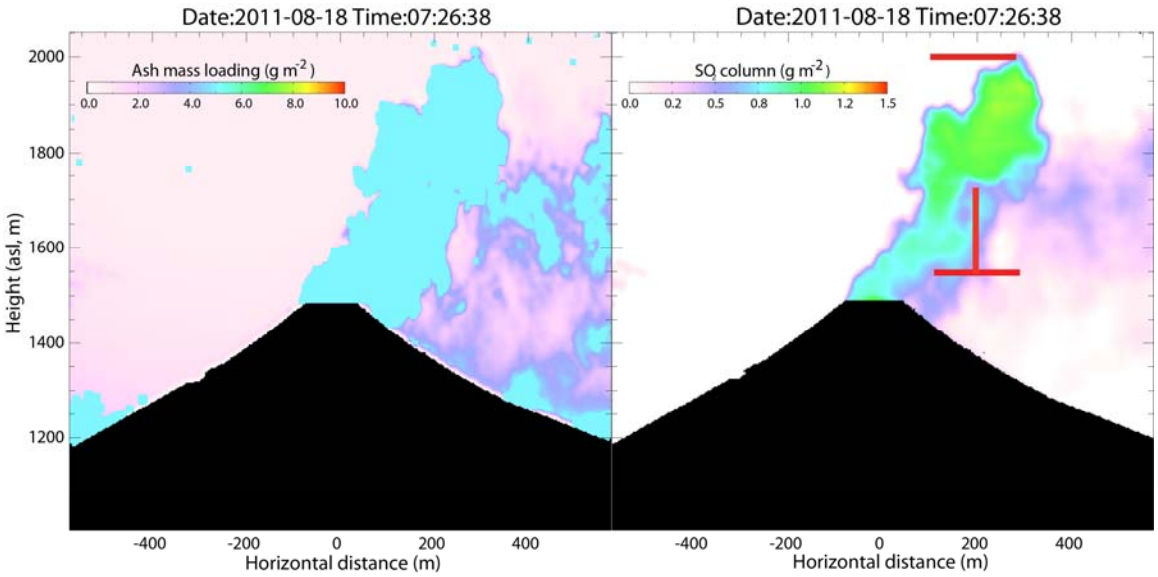

Figure 1.5: Ash and SO_2 IR camera retrievals. Images from Karymsky Volcano, Kamchatka, Russia were acquired on 18 August 2011. Ash column density can be seen in the figure on the left, while SO_2 column density can be seen in the figure on the right. The red lines mark the top and the bottom of the region used for measuring SO_2 cross-sections.

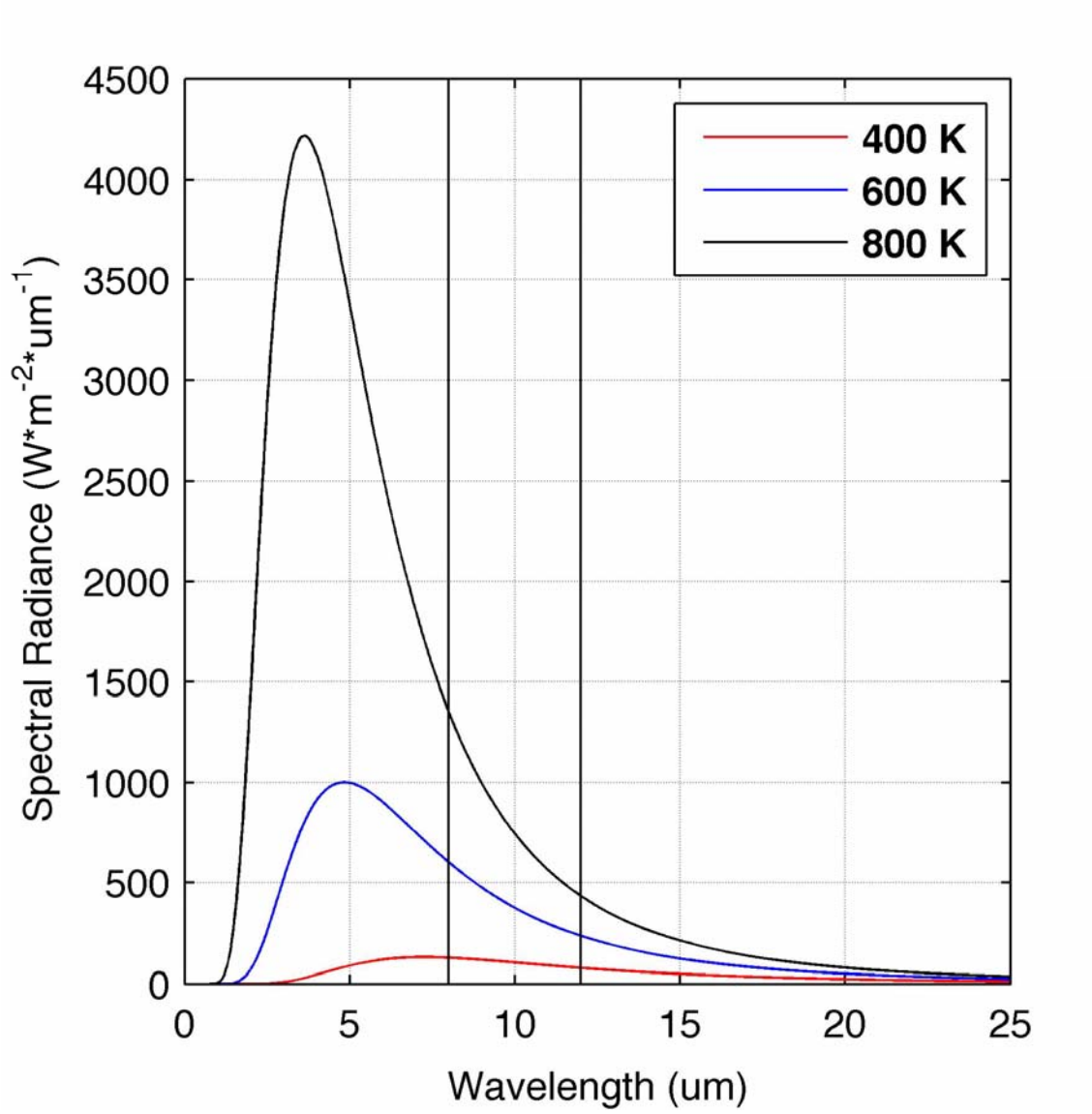

Figure 1.6: Planck's curve. Spectral radiance as a function of wavelength (x-axis, in μm) is shown for 400 K (red), 600 K (blue), and 800 K (black) temperature curves. The 8-12 μm region exploited by the NicAIR and FLIR instruments is marked by vertical black lines.

References Cited:

Aiuppa, A., Inguaggiato, S., McGonigle, A., O'Dwyer, M., Oppenheimer, C., Padgett, M., Rouwet, D. and Valenza, M., 2005. H_2S fluxes from Mt. Etna, Stromboli, and Vulcano (Italy) and implications for the sulfur budget at volcanoes. Geochimica et Cosmochimica Acta, 69(7): 1861-1871.

Aiuppa, A., Moretti, R., Federico, C., Guidice, G., Gurrieri, S., Liuzzo, M., Papale, P., Shinohara, H. and Valenza, M., 2007. Forecasting Etna eruptions by real-time observations of volcanic gas composition. Geology, 35(12): 1115-1118.

Aiuppa, A., Federico, C., Giudice, G., Giuffrida, G., Guida, R., Gurrieri, S., Liuzzo, M., Moretti, R. and Papale, P., 2009. The 2007 eruption of Stromboli volcano: Insights from real-time measurement of the volcanic gas plume CO_2/SO_2 ratio. Journal of Volcanology and Geothermal Research, 182(3-4): 221-230.

Blank, J. and Brooker, R., 1994. Experimental studies of Carbon Dioxide in Silicate Melts: solubility, speciation, and stable carbon isotope behavior. In: M. Carroll and J. Holloway (Editors), Volatiles in Magmas. Reviews in Mineralogy. Mineralogical Society of America, Fredericksburg, pp. 157 - 182.

Bogumil, K., Orphal, J., Homann, T., Voight, S., Spietz, P., Fleischmann, O.C., Vogel, A., Hartmann, M., Kromminga, H., Bovensmann, H., Frerick, J. and Burrows, J.P., 2003. Measurements of molecular absorption spectra with the SCIAMACHY pre-flight model: instrument characterization and reference data for atmospheric remote-sensing in the 230-2380 nm region.

Burnham, C.W., 1967. Hydrothermal fluids at the magmatic stage. In: H.L. Barnes (Editor), Geochemistry of Hydrothermal Ore Deposits. Holt, Rinehart, and Winston, New York, pp. 34-76.

Burton, M., Allard, P., Mure, F. and La Spina, A., 2007. Magmatic gas composition reveals the source depth of slug-driven strombolian explosive activity. Science, 317: 227-230.

Capaccioni, B., Tassi, F., Vaselli, O., Tedesco, D. and Poreda, R., 2007. Submarine gas burst at Panarea Island (southern Italy) on 3 November 2002: A magmatic versus hydrothermal episode. Journal of Geophysical Research-Solid Earth, 112: B05201.

Carn, S., Krueger, A., Krotkov, N., Yang, K. and Levelt, P., 2007. Sulfur dioxide emissions from Peruvian copper smelters detected by the Ozone Monitoring Instrument. Geophysical Research Letters, 34: L09801. doi:10.1029/2006GL029020.

Carn, S., Krueger, A., Krotkov, N., Yang, K. and Evans, K., 2009. Tracking volcanic sulfur dioxide clouds for aviation hazard mitigation. Natural Hazards, 51(2). doi:10.1007/s11069-008-9228-4.

Carn, S., 2011. OMIplot Software. http://vhub.org/resources/682.

Carroll, M. and Webster, J., 1994. Solubilities of Sulfur, Noble Gases, Nitrogen, Chlorine and Fluorine in Magmas. In: M. Carroll and J. Holloway (Editors), Volatiles in Magmas. Reviews in Mineralogy. Mineralogical Society of America, Fredericksburg, pp. 231-279.

Casadevall, T., 1994. The 1989-1990 eruption of Redoubt Volcano, Alaska: Impacts on aircraft operations. Journal of Volcanology and Geothermal Research, 62: 301-316.

Chiodini, G. and Marini, L., 1998. Hydrothermal gas equilibria: The H_2O-H_2-CO_2-CO-CH_4 system. Geochimica et Cosmochimica Acta, 62: 2673-2687.

Delmelle, P. and Stix, J., 2000. Volcanic Gases. In: H. Sigurdsson (Editor), Encyclopedia of Volcanoes. Academic Press, London, pp. 803 - 815.

Doukas, M. and Gerlach, T., 1995. Sulfur dioxide scrubbing during the 1992 eruption of Crater Peak, Spurr Volcano, Alaska. In: T. Keith (Editor), The 1992 Eruption of Crater Peak Vent, Mount Spurr Volcano, Alaska. U.S. Geological Survey Bulletin 2139, Washington, pp. pp. 47-57.

Doukas, M., 2002. A new method for GPS-based wind speed determineations during airborne volcanic plume measurements, U.S. Geological Survey, Open-File Report 02-395.

Doukas, M. and McGee, K., 2007. A compilation of gas emission-rate data from volcanoes of Cook Inlet (Spurr, Crater Peak, Redoubt, Illiamna, and Augustine) and Alaska Peninsula (Douglas, Fourpeaked, Griggs, Mageik, Martin, Peulik, Ukinrek Maars, and Veniaminof), Alaska, from 1995-2006, U.S. Geological Survey, Open-File Report 02-395.

Edmonds, M., Oppenheimer, C., Pyle, D., Herd, R. and Thompson, G., 2003. SO_2 emissions from Soufriere Hills Volcano and their relationship to conduit permeability, hydrothermal interaction and degassing regime. Journal of Volcanology and Geothermal Research, 124: 23-43. doi:10.1016/S0377-0273(03)00041-6.

Edmonds, M. and Gerlach, T., 2007. Vapor segregation and loss in basaltic melts. Geology, 35(8): 751-754. 10.1130/G23464A.1.

Edmonds, M., 2008. New geochemical insights into volcanic degassing. Philosophical Transactions of the Royal Society, A(366): 4559-4579.

Eichelberger, J.C., Carrigan, C.R., Westrich, H.R. and Price, R.H., 1986. Non-explosive silicic volcanism. Nature, 323: 598-602.

Engle, T. and Reid, P., 2006. Physical Chemistry. Jim Smith, San Francisco.

Fee, D., McNutt, S., Lopez, T., Arnoult, K., Szuberla, C. and Olson, J., 2011. Combining local and remote infrasound recordings from the 2009 Redoubt Volcano eruption. Journal of Volcanology and Geothermal Research, Special Issue on the 2009 Redoubt Eruption doi:10.1016/j.volgeores.2011.09.012.

Fee, D. and Matoza, R., 2013. An overview of volcano infrasound: From Hawaiian to plinian, local to global. Journal of Volcanology and Geothermal Research, 249: 123-139. doi:10.1016/j.jvolgeores.2012.09.002.

Fischer, T., Arehart, G., Sturchio, N. and Williams, S., 1996. The relationship between fumarole gas composition and eruptive activity at Galeras Volcano, Colombia. Geology, 24(6): 531 - 534. doi:10.1130/0091-7613(1996)024<0531:TRBFGC>2.3.CO;2.

Fischer, T., Roggensack, K. and Kyle, P., 2002. Open and almost shut case for explosive eruptions: Vent processes determined by SO_2 emission rates at Karymsky volcano, Kamchatka. Geology, 12: 1059-1062.

Gerlach, T., 1986. Exsolution of H_2O, CO_2, and S during eruptive episodes at Kilauea Volcano, Hawaii. Journal of Geophysical Research, 91(B12): 12,177-112,185.

Gerlach, T., 2003. Elevation effects in volcano applications of the COSPEC. In: C. Oppenheimer, D. Pyle and J. Barclay (Editors), Volcanic Degassing. The Geological Society of London, London, pp. 169-175.

Gerlach, T., 2004. Volcanic sources of tropospheric ozone-depleting trace gases. Geochemistry, Geophysics, Geosystems, 5: Q09007.

Giggenbach, W., 1975. A simple method for the collection and analysis of volcanic gas samples. Bulletin of Volcanology, 39: 132-145.

Giggenbach, W., 1987. Redox processes governing the chemistry of fumarolic gas discharges from White Island, New Zealand. Applied Geochemistry, 2: 143-161.

Giggenbach, W., 1992. Isotopic shifts in waters from geothermal and volcanic systems along convergent plate boundaries and their origin. Earth and Planetary Science Letters, 113: 495-510.

Giggenbach, W., 1996. Chemical composition of volcanic gases. In: R. Scarpa and R. Tilling (Editors), Monitoring and Mitigation of Volcano Hazards. Springer, Berlin, pp. 221-256.

Giggenbach, W., 1997. The origin and evolution of fluids in magmatic-hydrothermal systems. In: H.L. Barnes (Editor), Geochemistry of hydrothermal ore deposits. John Wiley and Sons.

Gonnermann, H.M. and Manga, M., 2012. Dynamics of magma ascent in the volcanic conduit. In: S.A. Fagents, T.K.P. Gregg and R.M.C. Lopes (Editors), Modeling Volcanic Processes: The Physics and Mathematics of Volcanism. Cambridge University Press, Cambridge.

Harris, A., Dehn, J. and Calvari, S., 2007. Lava effusion rate definition and measurement: a review. Bulletin of Volcanology, 70: 1-22. doi:10.1007/s00445-007-0120-y.

Horton, K., Williams-Jones, G., Garbeil, H., Elias, T., Sutton, A.J., Mouginis-Mark, P., Porter, J. and Clegg, S., 2006. Real-time measurement of volcanic SO_2 emissions: validation of a new UV correlation spectrometer (FLYSPEC) Bulletin of Volcanology, 68(4): 323-327.

Jaupart, C. and Vergniolle, S., 1989. The generation and collapse of a foam layer at the roof of a basaltic magma chamber. Journal of Fluid Mechanics, 203: 347-380.

Johnson, J.B. and Ripepe, M., 2011. Volcano infrasound: A review. Journal of Volcanology and Geothermal Research, 206(3-4): 61-69. doi:10.1016/j.jvolgeores.2011.06.006.

Kazahaya, K., Shinohara, H. and Saito, G., 1994. Excessive degassing of Izu-Oshima volcano: magma convection in a conduit. Bulletin of Volcanology, 56: 207-216.

Krotkov, N., Carn, S., Krueger, A., Bhartia, P. and Yang, K., 2006. Band residual difference algorithm for retrieval of SO_2 from the Aura Ozone Monitoring Instrument. IEEE Transactions on geoscience and remote sensing, 44(5): 1259-1266. doi:10.1109TGRS.2005.861932.

Levelt, P.F., Hilsenrath, E., Leppelmeier, G.W., van den Oord, G.H.J., Bhartia, P.K., Tamminen, J., de Haan, J.F. and Veefkind, J.P., 2006. Science objectives of the ozone monitoring instrument. Geoscience and Remote Sensing, IEEE Transactions on, 44(5): 1199-1208. doi:10.1109/TGRS.2006.872336.

McMillan, P., 1994. Water solubility and speciation models. In: M. Carroll and J. Holloway (Editors), Volatiles in Magmas. Reviews in Mineralogy. Mineralogical Society of America, Fredericksburg, pp. 131-152.

Newhall, C.G. and Self, S., 1982. The volcanic explosivity index (VEI): An estimate of explosive magnitude for historical volcanism. Journal of Geophysical Research, 87(C2): 1231-1238.

Newman, S. and Lowenstern, J.B., 2002. VolatileCalc: a silicate melt-H_2O-CO_2 solution model written in Visual Basic for excel. Computers & Geosciences, 28(5): 597-604.

Oppenheimer, C., 1998. Volcanological applications of meteorological satellites. International Journal of Remote Sensing, 19(15): 2829-2864.

Oppenheimer, C., Francis, P. and Stix, J., 1998. Depletion rates of sulfur dioxide in tropospheric volcanic plumes. Geophysical Research Letters, 25(14): 2671 - 2674. doi:10.1029/98GL01988.

Papale, P., Moretti, R. and Barbato, D., 2006. The compositional dependence of the saturation surface of $H_2O + CO_2$ fluids in silicate melts. Chemical Geology, 229(1-3): 78-95.

Platt, U. and Stutz, J., 2008. Differential Optical Absorption Spectroscopy Principles and Applications. Springer-Verlag, Berlin - Heidelberg.

Prata, A.J., 1989. Infrared radiative transfer calculations for volcanic ash clouds. Geophysical Research Letters, 16(11): 1293-1296.

Prata, A.J., 2009. Satellite detection of hazardous volcanic clouds and the risk to global air traffice. Natural Hazards, 51: 303-324.

Prata, A.J. and Bernardo, C., 2009. Retrieval of volcanic ash partical size, mass and optical depth from a ground-based thermal infrared camera. Journal of Volcanology and Geothermal Research, 186: 91-107. doi:10.1016/j.volgeores.2009.02.007.

Robock, A., 2000. Volcanic Eruptions and Climate. Reviews of Geophysics, 38(2): 191-219.

Rodriguez, L., Watson, I., Edmonds, M., Ryan, G., Hards, V., Oppenheimer, C. and Bluth, G., 2008. SO_2 loss rates in the plume emitted by Soufriere Hills volcano, Montserrat. Journal of Volcanology and Geothermal Research, 173: 135-147. doi:10.1016/j.jvolgeores.2008.01.003.

Shinohara, H., 2008. Excess degassing from volcanoes and its role on eruptive and intrusive activity. Reviews of Geophysics, 46: RG4005.

Spampinato, L., Calvari, S., Oppenheimer, C. and Boschi, E., 2011. Volcano surveillance using infrared cameras. Earth-Science Reviews, 106: 63-91. doi:10.1016/j.earscirev.2011.01.003.

Sparks, R.S.J., Bursik, M.I., Carey, S.N., Gilbert, J.S., Glaze, L.S., Sigurdsson, H. and Woods, A.W. (Editors), 1997. Volcanic Plumes, Chichester, 574 pp.

Sparks, R.S.J., 2003. Dynamics of magma degassing. In: C. Oppenheimer, D.M. Pyle and J. Barclay (Editors), Volcanic Degassing. Geological Society, London, pp. 5-22.

Stix, J., Zapata, J., Calvache, M., Cortes, G.P., Fischer, T., Gomez, D., Narvaez, L., Ordonez, M., Ortega, A., Torres, R. and Williams, S., 1993. A model of degassing at Galeras Volcano, Colombia, 1988-1993. Geology, 21: 963-967.

Symonds, R., Rose, W., Bluth, G. and Gerlach, T., 1994. Volcanic Gas Studies: Methods, Results, and Applications. In: M. Carroll and J. Holloway (Editors), Volatiles in Magmas. Reviews in Mineralogy. Mineralogical Society of America, Fredericksburg, pp. 1 - 63.

Symonds, R.B., Gerlach, T.M. and Reed, M.H., 2001. Magmatic gas scrubbing: implications for volcano monitoring. Journal of Volcanology and Geothermal Research, 108(1-4): 303-341. doi:10.1016/S0377-0273(00)00292-4.

Vaselli, O., Tassi, F., Montegrossi, G., Duarte, E., Fernandez, E. and Bergamashi, F., 2003. Fumarole migration and fluid chemistry at Poás volcano (Costa Rica) from 1998 to 2001. In: C. Oppenheimer, D. Pyle and J. Barclay (Editors), Volcanic Degassing. Geological Society of London, pp. 247 - 262.

Wallace, P. and Anderson, A., 2000. Volatiles in Magmas. In: H. Sigurdsson (Editor), Encyclopedia of Volcanoes. Academic Press, London, pp. 149-170.

Wallace, P., 2005. Volatiles in subduction zone magmas: concentrations and fluxes based on melt inclusion and volcanic gas data. Journal of Volcanology and Geothermal Research, 140: 217-240.

Werner, C., Hurst, T., Scott, B., Sherburn, S., Christenson, B., Britten, K., Cole-Baker, J. and Mullen, B., 2008. Variability of passive gas emissions, seismicity, and deformation during crater lake growth at White Island Volcano, New Zealand, 2002-2006. Journal of Geophysical Research, 113. 10.1029/2007JB005094.

Werner, C., Evans, W., Kelly, P., McGimsey, G., Pfeffer, M., Doukas, M. and Neal, C., 2012. Deep magmatic degassing versus scrubbing: Elevated CO_2 emissions and C/S in the lead-up to the 2009 eruption of Redoubt Volcano, Alaska. Geochemistry Geophysics Geosystems, 13(3): 1-18. doi:10.1029/2011GC003794.

Williams-Jones, G. and Rymer, H., 2000. Hazards of Volcanic Gases. In: H. Sigurdsson (Editor), Encyclopedia of Volcanoes. Academic Press, London, pp. 997 - 1004.

Williams-Jones, G., Stix, J. and Nadeau, P., 2008. Using the COSPEC in the Field. In: G. Williams-Jones, J. Stix and C. Hickson (Editors), The COSPEC Cookbook: Making SO_2 Measurements at Active Voclanoes. IAVCEI, pp. 63-119.

Wilson, L., Sparks, R.S.J., Huang, T.C. and Watkins, N.D., 1978. The control of volcanic column heights by eruption energetics and dynamics. Journal of Geophysical Research, 83(B4): 1829-1836.

Yang, K., Krotkov, N., Krueger, A., Carn, S., Bhartia, P. and Levelt, P., 2007. Retrieval of large volcanic SO_2 columns from the Aura Ozone Monitoring Instrument: Comparison and limitations. Journal of Geophysical Research, 112: D24S43. doi:10.1029/2007JD008825.

CHAPTER 2: Evaluation of Redoubt Volcano's Sulfur Dioxide Emissions by the Ozone Monitoring Instrument[1]

ABSTRACT

The 2009 eruption of Redoubt Volcano, Alaska, provided a rare opportunity to compare satellite measurements of sulfur dioxide (SO_2) by the Ozone Monitoring Instrument (OMI) with airborne SO_2 measurements by the Alaska Volcano Observatory (AVO). Herein we: (1) compare OMI and airborne SO_2 column density values for Redoubt's tropospheric plume, (2) calculate daily SO_2 masses from Mount Redoubt for the first three months of the eruption, (3) develop simple methods to convert daily measured SO_2 masses into emission rates to allow satellite data to be directly integrated with airborne SO_2 emissions dataset, (4) calculate cumulative SO_2 emissions from the eruption, and (5) evaluate OMI as a monitoring tool for high-latitude degassing volcanoes. A linear correlation (R^2 ~0.75) is observed between OMI and airborne SO_2 column densities. OMI daily SO_2 masses for the sample period ranged from ~60.1 kt on 24 March to below detection limit, with an average daily SO_2 mass of ~6.7 kt. The highest SO_2 emissions were observed during the initial part of the explosive phase and the emissions exhibited an overall decreasing trend with time. OMI SO_2 emission rates were derived using three methods and compared to airborne measurements. This comparison yields a linear correlation (R^2 ~ 0.82) with OMI-derived emission rates consistently lower than airborne measurements. The comparison results suggest that OMI's detection limit for high latitude, springtime conditions varies from ~2,000 to 4,000 t/d. Cumulative SO_2 masses calculated from daily OMI data for the sample period are estimated to range from 542 to 615 kt, with approximately half of this SO_2 produced during the explosive phase of the eruption. These cumulative masses are similar in magnitude to those estimated for the 1989 – 90 Redoubt eruption. Strong correlations between daily OMI SO_2 mass and both tephra mass and acoustic energy during the explosive phase of the eruption suggest that OMI data may be used to infer relative eruption size and explosivity. Further, when used in conjunction with complementary datasets, OMI daily SO_2 masses may be used to help

[1]López, T., Carn, S., Werner, C., Fee, D., Kelly, P., Doukas, M., Pfeffer, M., Webley, P., Cahill, C., and Schneider, D., 2012. Evaluation of Redoubt Volcano's sulfur dioxide emissions by the Ozone Monitoring Instrument, *Journal of Volcanology and Geothermal Research*, Special Issue on the 2009 Redoubt Eruption, doi:10.1016/j.volgeores.2012.03.002.

distinguish explosive from effusive activity and identify changes in lava extrusion rates. The results of this study suggest that OMI is a useful volcano monitoring tool to complement airborne measurements, capture explosive SO_2 emissions, and provide high temporal resolution SO_2 emissions data that can be used with interdisciplinary datasets to illuminate volcanic processes.

2.1 Introduction

Measurements of volcanic sulfur dioxide (SO_2) emissions provide useful information for volcano monitoring and hazard mitigation. Changes in SO_2 emissions frequently precede volcanic eruptions (Daag et al., 1996; McGee et al., 2010) and can indicate processes such as the influx of new magma (Daag et al., 1996), conduit sealing (Fischer et al., 1996; Carn et al., 2008), or scrubbing by hydrothermal waters (Symonds et al., 2001). Thus regular monitoring of volcanic SO_2 emissions may facilitate more accurate eruption forecasting. Recent advancements in detection capabilities of satellite sensors allow lower magnitude SO_2 emissions to be detected than was previously possible from space (Carn et al., 2007; Carn et al., 2008). Hence satellite sensors are now able to detect non-eruptive SO_2 emissions, allowing space-based monitoring of volcanic degassing (Carn et al., 2008). Continual satellite SO_2 measurements have recently been used to identify periods of open-system degassing and conduit sealing at Galeras Volcano, Colombia and Reventador Volcano, Ecuador (Carn et al., 2008); and when used in conjunction with complementary geophysical datasets, helped forecast an impending paroxysmal eruption of Merapi Volcano, Indonesia (Surono et al., 2012). Additionally, volcanic eruption clouds frequently contain ash in addition to SO_2 (and other volatile species), and thus satellite-based detection of SO_2 emissions can in cases be used to track volcanic ash clouds and potentially help mitigate ash-aviation hazards when traditional ash-detection methods are not applicable (Carn et al., 2009; Thomas and Prata, 2011).

The Alaska Volcano Observatory (AVO) is responsible for monitoring over 50 historically active volcanoes (Schaefer et al., 2009) and providing warnings of volcanic

ash clouds present in North Pacific airspace in cooperation with the National Weather Service (NWS) and the Federal Aviation Administration (FAA) (Neal et al., 2010). The traditional method employed by AVO for monitoring volcanic gases is through airborne surveys in which below-plume measurements of SO_2 column density are collected using an ultraviolet (UV) Correlation Spectrometer (COSPEC) (Doukas and McGee, 2007; McGee et al., 2010; Werner et al., 2011). More recently, in situ measurements of CO_2, SO_2, H_2S, and O_3 have been collected by flying contoured traverses within the plume (Doukas and McGee, 2007; McGee et al., 2010; Kelly et al., 2012; Werner et al., 2012b). During periods of quiescence, airborne gas surveys are conducted once or twice per year at more than eight active volcanoes located within ~450 km of Anchorage, Alaska (Fig. 1). During volcanic unrest airborne surveys are conducted more frequently, sometimes as many as two or more per week. Weather restrictions and the cost associated with airborne surveys prevent more frequent measurements at many Alaskan volcanoes, even during unrest. At present, less than half of Alaska's historically active volcanoes are monitored by AVO using onsite instrumentation (including seismometers, GPS stations, web-cameras, etc.). The large number of remote and unmonitored volcanoes, combined with the challenges of obtaining high temporal resolution gas measurements, makes satellite remote sensing of SO_2 emissions a potentially significant monitoring tool. However, in order for satellite SO_2 measurements to be used for volcano monitoring, the data must first be validated and made comparable to standard airborne gas measurements.

The 2009 eruption of Redoubt Volcano, Alaska (60.4852°N, 152.7438°W, 3108 m; Fig. 2.1) provided a rare opportunity to validate satellite measurements of volcanic SO_2 for two reasons: (1) Mount Redoubt produced elevated SO_2 emissions that were detected by the UV Ozone Monitoring Instrument (OMI) on NASA's Aura satellite on a near-daily basis for the three months following the eruption onset, and (2) Mount Redoubt's close proximity to Anchorage (~166 km) enabled AVO scientists to collect airborne measurements of SO_2 on 11 days during this time period that could be compared with the OMI SO_2 data.

In this manuscript we compare SO_2 emissions detected by OMI with contemporaneous airborne gas measurements by: (1) developing a method to enable the OMI and airborne SO_2 column density measurements to be compared accounting for their different spatial resolution (Section 2.3.4), (2) calculating daily OMI measured SO_2 masses from Redoubt (Section 2.3.5), and (3) developing and testing methods to convert daily OMI SO_2 mass into emission rate to allow the OMI data to be directly integrated into existing emissions datasets (Section 2.3.6). We then use the OMI SO_2 data to estimate cumulative SO_2 emissions throughout the 2009 eruption, compare these values to Mount Redoubt's 1989 -1990 eruption, and propose correlations between SO_2 emissions and Redoubt Volcano's 2009 eruptive activity (Sections 2.4.6, 2.5.6 and 2.5.7). Finally, we evaluate OMI as a volcano monitoring tool that can be used to increase volcanic emissions datasets, and improve the monitoring capabilities of AVO and other volcano observatories worldwide (Section 2.5.9).

2.2 Overview of the 2009 Redoubt Eruption

The first observations of unrest leading up to the 2009 eruption of Redoubt Volcano occurred late in July 2008 when AVO geologists conducting fieldwork on Mount Redoubt's edifice smelled H_2S gas (Schaefer et al., 2012), though retrospective analysis found ground deformation signals as early as May 2008 (Grapenthin et al., 2012). Melting of summit ice (Bleick et al., 2012), elevated CO_2 emissions (Werner et al., 2012b) and increased seismicity (Buurman et al., 2012) were all observed throughout the fall and winter of 2008. Further increases in seismicity (Buurman et al., 2012), gas emissions (Werner et al., 2012a), and ice-melt (Bleick et al., 2012) were observed throughout January and February 2009. On 15 March a small phreatic explosion occurred that deposited ash on Mount Redoubt's summit and was associated with elevated gas emissions (Schaefer et al., 2012). On 20 March a seismic swarm began that lasted for 66 hours (Buurman et al., 2012). In the final hours of the swarm, satellite data indicated that extrusion of a lava dome occurred (Bull and Buurman, 2012). At 6:34 (UTC) on 23 March 2009 the first in a series of magmatic explosions that comprised the explosive

phase of Redoubt's eruption (23 March through 4 April 2009) occurred. This phase of the eruption consisted of 19 discrete explosive magmatic eruptions (Bull and Buurman, 2012; Schaefer et al., 2012), many of which produced: ash clouds to stratospheric altitudes (Schneider and Hoblitt, 2012), elevated SO_2 emissions (this study; Werner et al., 2012b), significant infrasound energy (Fee et al., 2011), ash fall (Wallace et al., 2012), pyroclastic flows (Bull and Buurman, 2012; Schaefer et al., 2012), and lahars (Bull and Buurman, 2012; Schaefer et al., 2012). Intermittent dome growth and collapse also occurred throughout this phase (Bull and Buurman, 2012). A detailed chronology of the explosive phase can be found in Table 1. Following the final explosive eruption (Event 19) on 4 April, activity at Redoubt Volcano became effusive in nature, as the final lava dome of the eruption began to grow in the summit crater (Bull and Buurman, 2012). Dome growth was associated with elevated gas emissions that decreased throughout the course of the eruption (Bull and Buurman, 2012; Werner et al., 2012b). Lava effusion continued through 1 July 2009, eventually producing a 5.4×10^7 m^3 dome (dense rock equivalent volume)(Diefenbach et al., 2011). More details of the eruption chronology can be found in Schaefer et al. (2012) and Bull and Buurman (2012).

2.3 Methods

2.3.1 UV Remote Sensing of SO_2

Airborne and satellite-based UV remote sensing can be used to retrieve the abundance of SO_2 within volcanic plumes using scattered UV radiation and principles of absorption spectroscopy (Stoiber et al., 1983). Variations of the Lambert-Beer Law (e.g. Platt and Stutz, 2008) are used to calculate the SO_2 abundance within an atmospheric column, referred to as the SO_2 column density. Satellite derived slant column densities (SCD) are converted to vertical column densities (VCDs) using an air mass factor (AMF; where VCD = SCD/AMF) calculated either geometrically or through a radiative transfer model (Yang et al., 2007). Airborne data acquired with the instrument pointing to zenith represent VCDs. Throughout this manuscript we refer to both measured and derived VCD values as column density (CD).

2.3.2 Airborne Measurements Using a Correlation Spectrometer

Since the 1990's COSPEC (Stoiber et al., 1983) has been the primary tool to measure SO_2 emissions from Alaskan volcanoes (Doukas, 1995; Doukas and Gerlach, 1995; Doukas and McGee, 2007). During the 2009 Redoubt eruption, 11 gas observation flights were conducted within 1.5 hours of OMI overpasses. During each flight measurements of SO_2 CD were collected from a fixed-wing aircraft using an upward-facing Barringer COSPEC V by flying below-plume traverses, perpendicular to plume direction, and downwind from the volcanic source (Doukas and McGee, 2007). Airborne SO_2 CDs were integrated across plume width and multiplied by the wind speed (proxy for plume speed) to derive SO_2 emission rate. Wind speeds were estimated during each gas observation flight according to the wind circle method described by Doukas (2002). Measurements of SO_2 CD were collected at 1 Hz along with simultaneous GPS measurements of time, latitude, longitude, and altitude. Additionally, during most gas observation flights in situ measurements of SO_2 (and other gases) were collected according to the contour method (Gerlach et al., 1997; Doukas and McGee, 2007; Kelly et al., 2012). Because ambient SO_2 concentrations are near zero, these in situ SO_2 measurements along with GPS locations allowed plume width and altitude to be accurately constrained. More details of these methods can be found in Werner et al. (2012) and Kelly et al.(2012).

Airborne measurements are not collected during explosive eruptions due to: (1) the hazards associated with flying near a volcano during an explosive eruption (Werner et al., 2011), (2) the significant attenuation of UV light by volcanic ash, which can prevent SO_2 from being accurately measured (Williams-Jones et al., 2008), and (3) the low temporal resolution of gas flights prohibiting total explosive SO_2 emissions from being fully captured (Werner et al., 2011; Werner et al., 2012b). Therefore our comparison between OMI and airborne measurements is restricted to effusive-phase activity.

2.3.3 Overview of the Ozone Monitoring Instrument

OMI is a hyperspectral UV and visible satellite sensor aboard NASA's Aura spacecraft that measures atmospheric abundances of several trace gas species, including SO_2 (Carn et al., 2007). Aura is a polar orbiting satellite, and with a 2600 km swath width and 13 x 24 km pixel size at nadir, OMI attains full daily global coverage (Levelt et al., 2006). OMI has been collecting continuous atmospheric measurements since it became operational in September 2004 (Carn et al., 2007). OMI's temporal resolution, consisting of 1 pass per day at equatorial latitudes and up to 3 passes per day at high latitudes, provides the opportunity to obtain a remote snapshot of volcanic SO_2 emissions on any day when emissions are above OMI's detection limit and not obscured by meteorological clouds. For this study, operational OMI SO_2 data products (OMSO2; downloaded from: http://mirador.gsfc.nasa.gov/cgi-bin/mirador/collectionlist.pl?keyword=omso2) are analyzed using OMIplot software (Carn, 2011). OMSO2 data contain SO_2 measurements derived from the Band Residual Difference (BRD) (Krotkov et al., 2006) and Linear Fit (LF) algorithms (Yang et al., 2007), which retrieve SO_2 CD from measured radiances in up to 10 discrete UV bands between 310 and 360 nm. OMIplot software is used to produce images of SO_2 CD over a user-defined area, to calculate plume SO_2 mass by integrating the SO_2 CD values over the plume area, and to distinguish real SO_2 from noise through the use of SO_2 absorption spectrum peaks and troughs. The operational OMI SO_2 algorithms require an a priori assumption of SO_2 vertical distribution, characterized by the SO_2 layer center of mass altitude (CMA). For each OMI footprint, OMSO2 data products provide four values of total SO_2 CD corresponding to the following a priori CMAs: (1) ~0.9 km, for SO_2 in the Planetary Boundary Layer (*PBL*); (2) ~2.5 km, for SO_2 in the lower troposphere (*TRL*); (3) ~7.5 km, for SO_2 in the mid-troposphere (*TRM*); and (4) ~17.5 km, for SO_2 in the upper troposphere or lower stratosphere (*STL*) (http://so2.gsfc.nasa.gov/Documentation/OMSO2Readme_V111_0818.htm; (Yang et al., 2007). PBL SO_2 CDs are derived using the BRD algorithm, but SO_2 CDs for the other

altitudes are retrieved using the LF algorithm. The user must select the most appropriate SO_2 product for the prevailing geophysical conditions.

Since mid-2008, OMI measurements have been affected by a dynamic radiance anomaly, known as the 'row anomaly' (http://www.knmi.nl/omi/research/product/rowanomaly-background.php), which is believed to be a result of partial blockage of the OMI nadir viewing port. For the period of measurements considered here, the row anomaly impacted rows 29 through 45 (Fig. 2.2) and these rows were thus excluded from analysis.

Validation of OMI SO_2 CD measurements has been attempted for both anthropogenic emissions in the PBL (Krotkov et al., 2006; Krotkov et al., 2008) and for volcanic SO_2 emissions in the troposphere and stratosphere (Spinei et al., 2010; Carn et al., 2011; Carn and Lopez, 2011). Good qualitative agreement for the low altitude anthropogenic emissions (Krotkov et al., 2008) and strong quantitative agreement between ground-based and OMI measurements for higher altitude (7–17 km) SO_2 CD measured under optimal viewing conditions (Spinei et al., 2010), were found, while the challenges of comparing ground and satellite based measurements of different temporal and spatial resolutions were highlighted by Carn and Lopez (2011). We report here the first detailed comparison between OMI SO_2 data and airborne SO_2 CD measurements for high latitude volcanic SO_2 emissions at lower tropospheric altitudes (~3-6 km). Additionally, we consider a common challenge for satellite measurements of volcanic activity, namely that the volcanic SO_2 emissions are not spatially homogeneous and often cover only a fraction of an OMI pixel. This investigation also includes the first effort to validate OMI-derived SO_2 emission rates to allow satellite measurements to be integrated into typical volcano observatory SO_2 emissions datasets.

2.3.4 Column Density Comparison Methods

Our comparisons between the high spatial resolution airborne measurements of SO_2 CD and the lower spatial resolution OMI measurements use the following criteria: airborne

SO_2 CD measurements must be collected less than 90 minutes before or after an OMI overpass and have sufficient areal extent to allow the fraction of the OMI pixel containing volcanic SO_2 to be clearly defined (referred to as the plume pixel fraction). The airborne SO_2 CD measurements and OMSO2 data in KMZ format are plotted together in *Google Earth Pro*. Plume limits are defined for each airborne traverse when airborne SO_2 CD values are greater than or equal to 1 Dobson Unit (DU; the approximate level of background noise), and are extrapolated to the vent location to define the plume limits. The area of the individual OMI pixels is determined by overlaying OMPIXCOR data products (Kurosu and Celarier, 2010), which show the areal extent of individual pixels including pixel overlap, on top of the OMSO2 KMZ files and aligning the pixel boundaries. *Google Earth Pro* is used to create polygons that outline the perimeter of the plume, the individual pixels, and plume pixel fraction; and then to calculate the fractional area of the plume within each pixel. Airborne SO_2 CD measurements are partitioned into individual OMI pixels, and the average airborne SO_2 CD for each traverse within a plume pixel fraction is calculated (Fig. 2.3). On days when multiple traverses transected a single OMI pixel at different down-wind distances, the average of the spatially different traverses collected most closely in time with the OMI overpass is used. To allow the airborne and OMI SO_2 CD values to be directly compared, we converted the airborne measurements from units of ppm*m to DU, the CD units used by OMI. Gerlach (2003) showed that COSPEC CD values are independent of temperature and pressure such that 1 ppm*m is equal to 2.663×10^{-6} kg/m^2 for a plume at any altitude. We used this along with the conversion from DU to kg/m^2 (1 DU = 2.85×10^{-5} kg/m^2) to derive a conversion factor of 1 ppm*m = 0.0934 DU. Once the average airborne SO_2 CD for each pixel was converted to DU we calculated a corrected airborne SO_2 CD value for the pixel, C_c, (DU):

(1) $$C_c = (C_a \times F_p) + (C_b \times F_b)$$

where C_a is the average airborne SO_2 CD measured within the pixel (DU), F_p is the fraction of the pixel containing plume (>1 DU SO_2), C_b is the average background SO_2

CD value for the pixel, and F_b is the fraction of the pixel containing background (<1 DU SO_2). Because ambient air typically contains 0 DU SO_2, equation (1) simplifies to:

(2) $$C_c = (C_a \times F_p)$$

This equation attempts to correct for the spatial differences between the airborne and OMI datasets, allowing these different measurements to be directly compared (Fig. 2.3).

Accurate plume altitudes from Redoubt Volcano are constrained via airborne methods. The average plume altitude during the effusive phase of the eruption for days with supporting airborne measurements was 3.8 km above sea level (Werner et al., 2012b). The comparison between OMI and corrected airborne CD was conducted for both OMI *TRL* and *PBL* SO_2 retrievals, where the operational *PBL* data products were corrected using a corrected air mass factor based on the total ozone, solar zenith angle, and satellite viewing angle for the specific conditions at Redoubt Volcano according to the method of Krotkov et al. (2008). Both retrievals were used to determine if one exhibited a better agreement with corrected airborne SO_2 CD values, considering that a plume at 3 km altitude above sea level over mountainous terrain may be better retrieved using the plume altitude above terrain level. Average terrain heights (a function of plume direction) below the plume are used to determine the most appropriate CMA on that particular day, such that the *PBL* retrieval was used for plumes <2 km above terrain level and the *TRL* retrieval was used for plumes ≥ 2 km above terrain level. We refer to the most appropriate CMA as the *Selected* altitude. The comparison between OMI *PBL, TRL*, and *Selected* altitude SO_2 CD values and corrected airborne SO_2 CD values was conducted for 16 pixels observed during the study period. This comparison was repeated for a subset of pixels collected under optimal viewing conditions. According to the OMI User's Guide (http://disc.sci.gsfc.nasa.gov/Aura/additional/documentation/README.OMI_DUG.pdf) optimal conditions for OMI PBL SO_2 retrievals include: cloud fractions <0.2, solar zenith

angle <50°, and near nadir satellite viewing angles (<45° from nadir). Considering these factors, a subset of 8 pixels collected under optimal conditions was evaluated, which we refer to as the optimal dataset. The results of the comparison between OMI and corrected airborne SO_2 CD values were evaluated through consideration of the percent difference, where we assume that corrected airborne SO_2 CD values are accurate and represent the true SO_2 CD in Mount Redoubt's plume at the time of the OMI overpass. This assumption is a simplification, as uncertainties in airborne CDs are estimated to be ±10% for cloud-free conditions, and spatial (downwind) and temporal variations in Mount Redoubt's SO_2 emission rates of 10% were observed on the scale of OMI pixels (Werner et al., 2012b). However, we believe this assumption is justified as both the airborne SO_2 CD error and the observed variability in SO_2 emissions are quite low. We consider the advantage of utilizing multiple traverses in our analysis in order to provide more complete spatial coverage of OMI pixels to outweigh the negative effect of introducing minor variability in airborne measured emission rates by considering traverses collected within 90 minutes of an OMI overpass. The *TRL*, *PBL* and *Selected* SO_2 CD values were plotted against the corrected airborne SO_2 CD values to constrain the linear relationship and coefficient of determination (R^2) for each analysis. A linear relationship is expected between OMI and corrected airborne SO_2 CD values, as both methods measure the SO_2 CD of Mount Redoubt's plume, with the primary difference between the measurements being the spatial resolution.

2.3.5 OMI Measurements of SO_2 Mass

Measurements of SO_2 mass detected by OMI in Mount Redoubt's plume were calculated using a multistep process. First, OMI data for a 30° × 40° box with coverage of Redoubt Volcano and the surrounding area (45° to 75° North latitude × 170 to 130° West longitude) referred to as the analysis box (Fig. 2.2) were acquired. This box was selected to provide coverage of mainland Alaska and to include plumes up to ~1 day old for plume speeds of up to 14.5 m/s (the maximum wind speed observed from airborne methods)(Werner et al., 2012b). The image was produced in footprint mode, which

reflects the true shape and orientation of the OMI pixels. If elevated SO_2 emissions from Redoubt Volcano were detected in the OMI image, pixel SO_2 CD values within the apparent plume were verified using OMI ozone algorithm (OMTO3) residuals at four peaks and troughs within the SO_2 absorption spectrum, referred to as SO_2 index values (see Krotkov et al., 2006). If the SO_2 index values were consistent with SO_2 absorption, the plume was assumed to be real and the plume SO_2 mass and area within the analysis box were calculated. The mass of apparent SO_2 representing background conditions within a similar area was also calculated and subtracted from the plume SO_2 mass to correct for background noise. In the case that the entire SO_2 plume could not be contained within a single box (due to separate gas puffs or row anomaly pixels truncating the plume), then several boxes were analyzed and the resultant masses summed. If multiple OMI orbits contained coverage of Mount Redoubt's plume, the procedure was repeated for each orbit. OMI typically provides three overpasses per day with coverage of Redoubt Volcano, though in this case often only one image per day had good coverage of the entire plume. The most representative mass calculated for each day's OMI images, including the best coverage of the plume and/or near-nadir viewing conditions, was selected to be the reported daily SO_2 mass (Table 2.2).

OMI images are "snapshots" of SO_2 emitted and require wind velocities and SO_2 loss rates to be accurately known to constrain the time period of SO_2 emission within the image. We assume that the total SO_2 mass does not change significantly over time scales of 1–3 hours, the time period encompassing OMI's ~3 overpasses of Redoubt Volcano; and that the SO_2 present within the analysis box represents only SO_2 emitted by Redoubt Volcano over the preceding 24 hours.

2.3.6 Plume Speed and Daily SO_2 Emission Rate Calculation Methods

We developed three simple algorithms to convert the OMI measured SO_2 masses (kg) into SO_2 emission rates (tonnes per day [t/d]) to facilitate comparison between the OMI and airborne data and allow direct integration of these datasets. OMI emission rate

calculations require estimates of plume altitude and plume speed. On days when gas observation flights were conducted, plume altitude and speed were determined using the previously described airborne techniques (Section 2.3.2). On other days, local radiosonde data were used along with thermal infrared satellite data to estimate plume top altitudes (Webley et al., 2012), and wind speeds were estimated using the READY system and the HYSPLIT trajectory model with Global Data Assimilation System (GDAS) meteorological data (http://ready.arl.noaa.gov/index.php). Model outputs for the location of Redoubt Volcano, the closest time to the OMI overpass or airborne survey (within 1.5 hours), and the observed plume altitude were used to determine the appropriate wind speed and direction. Fair agreement (R^2 = 0.5) between airborne and modeled wind speeds was observed with an average difference of ±2 m/s (or 20%) and a maximum difference of ±5 m/s (or 110%) suggesting that modeled wind data are an adequate alternative data source when airborne measurements are not possible. Once the plume speed had been estimated, it was used with the following methods to estimate daily SO_2 emission rate (t/d).

In *Method 1,* the SO_2 mass for each image (*M*), is multiplied by the wind speed (*V)*, divided by the length of the plume in the direction of transport (*L*), and converted to t/d (Fig. 4a).

In *Method 2* (Fig. 2.4b), the wind speed (*V*) was used to calculate the distance the plume could have traveled in a period of 24 hours (L_{24}). Next, the SO_2 mass was calculated for the 24 hour plume, providing an emission rate result in units of t/d. This method was only applied when L_{24} was contained within the analysis box, and the plume extended at least as far as L_{24}.

Method 3 uses the same principles as the airborne method to calculate SO_2 emission rates. Specifically, for plumes oriented parallel and/or perpendicular to a pixel boundary, the SO_2 CD within the pixel(s) was multiplied by plume width to calculate a plume SO_2

cross-sectional area in units of DU*m, which was then converted to kg/m (1 DU = 2.85 x 10^{-5} kg/m^2). This value was then multiplied by plume speed (m/s) to yield emission rate in kg/s, which was then converted to t/d.

The OMI-derived emission rates calculated using the three methods were compared to airborne SO_2 emission rates measured on 11 days during the eruption with near-coincident (within 1.5 hours) OMI overpasses. Comparisons were not conducted on days with explosive eruptions as significant pulses of SO_2 were emitted during these explosions that were captured in OMI imagery but were not captured by airborne measurements.

2.4 Observations and Results

2.4.1 Summary of Observations

The study period for comparison of OMI and airborne SO_2 emission measurements was from 23 March 2009 through 12 June 2009 (Table 2.2). While SO_2 emissions from Redoubt Volcano continued past this date, the eruption of Sarychev Peak, Kurile Islands, Russia from 11 to 20 June 2009 (Rybin et al., 2011), produced large SO_2 clouds that traveled across the North Pacific preventing SO_2 from Redoubt Volcano from being accurately distinguished from that of Sarychev Peak. During our study period OMI detected SO_2 from Redoubt Volcano on 67 days, OMI data were not available on three days, and no SO_2 from Redoubt Volcano was detected by OMI on 12 days. Airborne SO_2 measurements were collected on 14 days during the study period (Werner et al., 2012b). Airborne measurements on 11 days were suitable for comparison with OMI derived emission rates and 6 days were suitable for comparison with OMI pixel CD.

2.4.2 Column Density Comparison Results

The data used in the comparison between OMI measured and corrected airborne SO_2 CD values calculated using the *TRL*, *PBL*, and *Selected* plume altitude algorithms can be found in Table 2.3, with the results summarized in Supplementary Material, Table 2.A.1,

and shown in Figure 2.5. In general, for the 3 km ASL plume typically observed at Redoubt Volcano, the operational *TRL* algorithm underestimated SO_2 while the corrected *PBL* algorithm overestimated SO_2 relative to the corrected airborne values (Fig. 2.5). The strongest linear correlation between the OMI and corrected airborne CD values for the 16 pixel analysis was observed for the *PBL* algorithm ($R^2 = 0.75$), followed by the *Selected* algorithm ($R^2 = 0.71$), and a weak correlation was observed for the *TRL* algorithm ($R^2 = 0.38$). The *TRL* algorithm had the smallest average percent difference and smallest standard deviation between OMI and corrected airborne SO_2 CD values for both datasets.

No improvement in linear correlation, average percent difference, or standard deviation was observed from using the optimal dataset, with the exception of a small decrease in average percent difference for the *TRL* algorithm. When the *PBL* and *TRL* algorithms were compared to the *Selected* algorithm, the *Selected* algorithm exhibited a stronger linear correlation than the *TRL* algorithm, and showed minor improvements when compared to the *PBL* algorithm with respect to average percent difference and standard deviation. This suggests that the *Selected* algorithm does not significantly improve results over the standard algorithms with respect to plume altitude above terrain level. Overall the *PBL* algorithm for all pixels had the strongest linear correlation with airborne measurements, while the *TRL* algorithm for all pixels had the smallest average percent difference and standard deviation.

The average airborne SO_2 CD values not corrected for differences in spatial resolution were also compared to the *TRL*, *PBL* and *Selected* altitude algorithm SO_2 CD values. No correlation was found between these measurements ($R^2 < 0.1$ in all cases), suggesting that for sub-pixel plumes, the spatial correction is critical for OMI data to be accurately compared with airborne measurements.

2.4.3 Daily SO_2 Masses and Emission Rates

OMI detected SO_2 emissions from Redoubt Volcano almost daily during both the explosive and effusive phases of the eruption (Fig. 2.6; Table 2.2). On 21 March, two days prior to the explosive phase onset, weak SO_2 emissions (<0.5 kt) from Redoubt Volcano were detected by OMI. The explosive phase daily SO_2 masses (23 March through 4 April) ranged from 60.1 kt (on 24 March) to below detection limit and exhibited a correlation with volcanic activity that is described in detail in Section 2.5.7 (Table 2.4). From 5 April–12 June effusive phase daily SO_2 masses were quite variable and ranged from 24.6 kt (on 12 April) to below detection limit (on multiple days). The daily SO_2 masses from Redoubt Volcano exhibited an overall decreasing trend with time, with average daily OMI SO_2 masses for the explosive phase (n = 13), the effusive phase (n = 69), and the entire study period (n = 82) of 17.3 kt, 4.7 kt, and 6.7 kt, respectively.

Daily OMI-derived *Method 1* SO_2 emission rates ranged from 84,100 t/d (on 24 March) to below detection limit (on multiple days), and followed a similar trend to the daily SO_2 masses (Fig. 2.6). The average *Method 1* emission rates for the explosive phase (n = 13), the effusive phase (n = 69), and the entire study period (n = 82) was 25,800 t/d, 4,200 t/d, and 7,800 t/d, respectively. The resultant emission rates calculated using these three methods were compared to airborne emission rates when available.

2.4.4 Emission Rate Calculation Method Comparison

Airborne SO_2 measurements collected on 11 days had near-coincident OMI images of passive degassing from Redoubt Volcano to allow SO_2 emission rates to be calculated using *Method 1*. Six days had both a near-coincident OMI overpass and a plume at least 24 hours old contained within the OMI analysis box such that emission rates could be calculated using *Method 2*. Four days had SO_2 plumes that traveled parallel or perpendicular to the OMI pixel orientation, such that OMI emission rates could be calculated using *Method 3*. The results of the comparison are shown in Figure 2.7 and summarized in Supplementary Material Table 2.A.2. A strong linear correlation (R^2 =

0.82) between the OMI *Method 1* and airborne emission rates is observed, while weak and no correlations are observed for comparisons with OMI *Methods 2* and *3* (R^2 = 0.34 and 0.01), respectively. In almost all cases, OMI SO_2 emission rates are lower than respective airborne calculations.

2.4.5 Emission Rate Detection Limit

OMI's emission rate detection limit for high latitude springtime conditions was estimated using observations of the maximum SO_2 emission rate determined from airborne measurements that corresponded with non-detection by OMI during the study period. Airborne SO_2 emission rates calculated for 15 and 20 March of 3850 and 940 t/d, respectively, corresponded with non-detection by OMI. In contrast, the remaining days within the sample period when both airborne and OMI emission rates were calculated found that emission rates as low as ~2000 t/d were detected by OMI. This may suggest that OMI's detection limit is >4,000 t/d for early spring conditions and improves with increased UV radiation to <2000 t/d for mid to late spring conditions at Redoubt Volcano and other volcanoes at similar latitudes. It should be noted however, that the airborne measurements on 15 March were collected immediately prior to the phreatic explosion (Bull and Buurman, 2012) and as such these measurements may reflect a short-lived increase in SO_2 that may not be representative of that day's emissions on the spatial scale of an OMI pixel. Additional coincident low-magnitude (<4,000 t/d) airborne and OMI SO_2 emission rate data are required to further constrain OMI's high latitude early springtime detection limit.

2.4.6 Cumulative SO_2 Masses and Emission Rates for the Sample Period

Daily OMI SO_2 masses and derived emission rates from Redoubt Volcano were summed from 19 March through 12 June to calculate the cumulative SO_2 mass emitted (Fig. 2.8). The total cumulative SO_2 mass emitted from Redoubt Volcano during this period as calculated from the daily masses (black diamonds) and *Method 1* emission rates (gray squares) was 542 kt and 615 kt, respectively. According to these values, approximately

one half of the total SO_2 mass released during the study period was emitted during the explosive eruptive phase.

2.5 Discussion

2.5.1 Challenges and Advantages of Using OMI SO_2 Data

Several aspects of OMI's temporal resolution, spatial resolution, and sensitivity to SO_2 were advantageous for this study. OMI's temporal resolution, typically 1 to 3 images per day with (full or partial) coverage of Mount Redoubt's plume, is significantly higher than what is possible through airborne methods. While OMI's spatial resolution is coarser than optimal for Mount Redoubt's average plume size (~6.2 km plume width at an ~11 km downwind distance according to Werner et al., (2012b), it is the highest spatial resolution of current UV satellite sensors. Many infrared sensors (e.g. AIRS, MODIS) have higher temporal and/or spatial resolutions than OMI (Thomas and Watson, 2009), but are less sensitive to SO_2, especially for low altitude plumes (Carn et al., 2005; Prata and Bernardo, 2007; Thomas et al., 2009) such as often observed at Redoubt Volcano. OMI's sensitivity to SO_2 combined with its temporal and spatial resolution allowed detection of Mount Redoubt's plume on approximately 80% of the analyzed days, many of which were ~3 km or less in altitude. Additionally, OMI detected SO_2 throughout the explosive phase when airborne measurements were not possible. This large percentage of detected plumes would not have been possible with other available sensors or through airborne methods alone, making OMI the ideal tool for this study as it provided nearly daily measurements of Mount Redoubt's SO_2 emissions.

There are two main challenges in using OMI data for this study that are unique to OMI and/or UV sensors in general. First OMI's row anomaly often truncated plumes within the OMI image, frequently limiting the number of usable daily images of Mount Redoubt's plume to one. Secondly, as a consequence of Redoubt Volcano's high latitude location and resultant high solar zenith angles in winter months, significant UV attenuation contributed to relatively low signal to noise in early spring images (Bluth et

al., 1993). The main challenges of this study, however, are inherent to the fundamental differences in data collection methods between airborne and satellite measurements. We will discuss these challenges in more detail with respect to CD, mass, and derived emission rates in the following sections.

2.5.2 Uncertainties in Airborne SO_2 Measurements

Throughout this study we compare OMI satellite to airborne COSPEC SO_2 measurements. Airborne measurements by COSPEC have limitations such that they may not represent true daily SO_2 emissions, and thus these uncertainties should be considered in the context of the comparison with OMI measurements. The primary factors that contribute to uncertainty in COSPEC airborne SO_2 emission rate calculations include uncertainty in: (1) calibration cell concentration, (2) plume speed, and (3) retrieved SO_2 CD due to molecular scattering and dilution (Stoiber et al., 1983). While the uncertainty in calibration cell concentration (~5% (Stoiber et al., 1983; Werner et al., 2012b)) and plume speed (~5% (Doukas, 2002)) are fairly minor components, uncertainties in SO_2 CD due to molecular scattering and dilution could be up to a an order of magnitude (Kern et al., 2010). Because airborne measurements were made directly under the plume, scattering and dilution error are minimized (Kern et al., 2010; Werner et al., 2012b). The overall uncertainty in airborne SO_2 CD and calculated emission rates is therefore estimated to be ±10% and ±20%, respectively, for cloud-free conditions (Werner et al., 2012b).

2.5.3 Evaluation of Column Density Analysis

There are several challenges in comparing OMI and airborne CDs that can contribute to deviations from a linear relationship. First, the temporal and spatial differences between OMI and airborne methods along with the variability of Mount Redoubt's emissions make direct comparison between these measurements challenging. OMI acquires an image of Mount Redoubt's plume in less than one minute, while a representative number of airborne plume traverses (5–7) may take over 1 hour to collect. Changes in SO_2

emissions during the period of airborne measurements can contribute to discrepancies between the two datasets. Additionally, because OMI acquires an image of the entire plume, while the airborne measurements only sample a localized cross-section of the plume, it is possible that spatial variability in SO_2 emissions may be more fully captured by OMI. Four to seven airborne SO_2 CD traverses were conducted on the six days evaluated. On five out of six of the days, traverses were collected within 85 minute time periods at distances up to 12 km apart. The average variability in the integrated plume SO_2 area (i.e. SO_2 CD integrated over the plume width) with respect to the mean was ±8%, while the maximum variability was ±23%. This suggests that the down-wind variability in SO_2 emissions on pixel-sized scales will likely be between ±8 and ±23%.

A second concern related to the spatial variability between the OMI and airborne datasets is due to the relatively small plume size compared to the OMI pixel size. Of the 16 pixels analyzed, the highest plume pixel fraction was 0.73, and the average plume pixel fraction was 0.27. The calculation designed to account for the spatial differences between OMI pixels and airborne measurements (Section 2.3.4) depends on OMI SO_2 CD, in addition to accuracy of the traverse plume limit locations, the interpolated plume limits, and area of the pixels and plume fractions. We compare OMI pixel areas from the OMPIXCOR data product (Kurosu and Celarier, 2010) to pixel areas determined in *Google Earth Pro* and find a maximum percent difference between these datasets of 4, with an average percent difference of 1.3. This suggests that our method for determining pixel area is relatively robust. Uncertainties in the plume pixel fraction areas will likely be larger as these values depend on several intermediate calculations.

Third, as shown by the CD comparison analysis, OMI CD values are strongly dependent on the selected plume CMA algorithm, indicating that accurate plume altitude and thickness constraints are critical to accurate OMI CD retrieval. Discrepancies between the actual plume CMA and the assumed CMA used in the *TRL* (2.5 km) and *PBL* (0.9 km) retrievals could contribute to error in retrieved CD.

Finally, spatial variations in and deviations from the assumed atmospheric conditions at Redoubt Volcano, specifically with respect to total ozone column, surface reflectivity, cloud cover, solar zenith angle, presence of ash and/or aerosols, etc. will contribute to uncertainties in OMI CDs. For conditions similar to those observed at Redoubt Volcano (unpolluted atmosphere with CDs less than 100 DU) the estimated uncertainty in CD for the LF and BRD algorithms is ±20% (Yang et al., 2007), and -7 – -23% (Krotkov et al., 2008), respectively. It should be noted that for pixels containing SO_2 plumes above highly reflective snow or clouds, SO_2 CD calculated using the *BRD* retrieval may be overestimated (Krotkov et al., 2008). Figure 2.3 shows visible MODIS imagery of Redoubt's plume and surroundings (acquired within 15 minutes of the OMI overpass) with OMI pixels boundaries outlined in red, such that reflectivity can be evaluated. In particular high surface reflectivity observed on 20 April may be contributing to the anomalously high SO_2 CD values retrieved from the BRD retrieval on that day (Table 2.3).

A comparison between the percent difference between OMI (*TRL*) and airborne SO_2 CD values and other parameters including: total column ozone, satellite viewing angle, solar zenith angle, Aerosol Index, cloud fraction, plume altitude, and plume pixel fraction, was conducted for the 16 analyzed pixels (Table 2.3). No correlation was found between the percent difference and any of these parameters (maximum observed $R^2 = 0.1$), suggesting that no single parameter contributes significantly to the observed discrepancies. The pixel analysis associated with Pixel 2A on 7 June 2009 had the largest observed discrepancy with airborne measurements of ~198% (*TRL* retrieval*)*. This pixel has the following characteristics: (1) a small plume pixel fraction (0.16), (2) a low average airborne CD (2.27 DU), (3) a relatively long time lag between OMI and airborne measurements (69 to 85 minutes), (4) low surface reflectivity, and (5) the plume location was on the edge of the pixel (Fig. 2.3; Table 2.3). These observations suggest that the combined effects of

several non-ideal factors can contribute to large disagreements between OMI and airborne CDs.

The above uncertainties in OMI and corrected airborne SO_2 CDs all contribute in part to the deviations in linearity between these datasets. Our findings suggest that the overall uncertainties in OMI SO_2 CD as determined through comparison with airborne measurements are on average -55% and +79% for the *TRL* and *PBL* retrieval's, respectively (see Supplementary Material, Table 2.A.1 for more details).

2.5.4 Evaluation of Daily SO_2 Mass

We expect the error in the OMI SO_2 mass values to come from three primary sources: (1) error in the SO_2 CD, (2) error in the selected background noise level, and (3) error in assumption that measured SO_2 is <1 day old. Errors in SO_2 CD were discussed previously and are not repeated here.

Variable background noise in the acquired OMI SO_2 images impacted the precision of the calculated daily SO_2 masses. Based on repeat processing of multiple OMI images in which different areas of background noise were subtracted from the measured plume SO_2 mass, we expect an uncertainty in precision for the reported SO_2 masses due to variability in background noise to be ~20%.

Another challenge in calculating daily SO_2 mass and emission rates (*Methods 1 and 2*) from satellite data is to include all the SO_2 emitted in the preceding 24 hours. If we assume a consistent wind direction, wind speed, and a continuous SO_2 source, we can estimate plume age based on the wind speed and the length of the plume as measured by OMI. If we consider the OMI analysis box (45°–75°N, 130°-170°W) and a plume speed of 14.5 m/s (the maximum wind speed observed from Mount Redoubt 2009 airborne measurements (Werner et al., 2012b)), a plume from Redoubt Volcano could reach the eastern extent of the analysis box (~1200 km) in ~1 day. For wind speeds greater than

14.5 m/s, OMI SO_2 mass will be underestimated, whereas for wind speeds less than 14.5 m/s, OMI SO_2 mass will be overestimated. Assuming that the ideal conditions mentioned above persisted throughout the sample period (a simplification), and using the wind speeds and plume lengths used for emission rate *Method 1* calculations, we find that our mass measurements may be overestimated on over half the days, with an average plume age of 1.2 days for the sample period. However, no correlation between SO_2 mass and plume age was observed, suggesting that this source of uncertainty may be minimal. An additional aspect to be considered is the chemical loss of SO_2 within volcanic plumes due to homogenous or heterogeneous reactions, which can also cause OMI to underestimate daily SO_2 emissions (Pfeffer et al., 2006; Bluth and Carn, 2008; Rodriguez et al., 2008). Estimated SO_2 loss rates from the Mount Redoubt 1989-90 eruption were calculated to be $<2.8 \times 10^{-6}$ s^{-1} for tropospheric plumes, suggesting that SO_2 loss at Redoubt Volcano may be negligible over the course of a day (Hobbs et al., 1991; Casadevall et al., 1994; Oppenheimer et al., 1998). However, dispersion of SO_2 by advection and diffusion could also act to lower SO_2 CDs below OMI's detection limit during plume transport.

These various factors can contribute to uncertainties in the daily OMI SO_2 masses, however unlike OMI SO_2 CD and derived emission rates that can be validated using airborne measurements, there are no complementary data available to allow us to estimate the overall uncertainties in the daily SO_2 masses.

2.5.5 Evaluation of OMI-Derived Emission Rates

Each of the emission rate calculation methods has advantages and disadvantages with respect to temporal resolution, processing time required, and measurement uncertainties. *Method 1* is the simplest method and can be applied to all days in which OMI SO_2 masses were calculated. This method produces the highest possible temporal resolution dataset; however it does not consider the age of the plume, so it is possible that *Method 1* may incorporate SO_2 from the previous day's emissions. *Method 2* does considers plume age in the emission rate calculation, but is only applied to days in which the 24 hour old

plume extends to L_{24}, thus limiting the temporal resolution of this dataset. *Method 3* uses the same theory as the airborne emission rate calculation method and should theoretically agree most closely with airborne measurements. Additionally, because this method utilizes the plume SO_2 cross-sectional area near the source, factors such as plume dispersion, dilution, and SO_2 loss are minimized. However, *Method 3* is only applied when the volcanic plume is oriented parallel or perpendicular to an OMI pixel boundary, limiting the opportunities to use this method and resulting in poor temporal resolution. Analysis of *Methods 2* and *3* require more processing time than *Method 1*.

The uncertainties in the OMI-derived emission rates will include the uncertainties associated with SO_2 mass (*Methods 1 & 2*) and CD (*Method 3*) calculations described above (Sections 2.5.4 and 2.5.3, respectively), in addition to the uncertainties in plume speed and length. Of particular note is that the *Method 1* emission rates were calculated using the daily mass associated with the estimated plume top height. For example, a 3 km plume emission rate was estimated using the daily mass from the *TRL* CMA algorithm. The pixel analysis (Section 2.4.2) found that OMI SO_2 CD estimated from the *TRL* algorithm consistently underestimated SO_2 amounts; hence emission rates derived using *TRL* SO_2 data will also be biased low.

Because all three emission rate methods use plume speed in their calculations, the aforementioned plume speed uncertainties (Section 2.3.6) (average of ±2 m/s, max of ±5 m/s) will contribute to the uncertainties in all three emission rate methods. Uncertainties in plume length for *Methods 1* and *2*, are strongly dependent on the wind direction on the day preceding the image acquisition. For ideal conditions, including consistent wind direction, low image noise level, and well defined plume limits, we expect uncertainties in plume length to be ~15%. Often wind direction and speeds are variable, making it challenging to determine the appropriate plume length.

While there are clear sources of positive and negative error in the OMI-derived emission rates, the observations suggest that in most cases these values are lower than airborne measurements. Overall differences between OMI-derived and airborne emission rates are on average -28, -34, and -40%, for *Methods 1*, *2*, and *3*, respectively (see Supplementary Material, Table 2.A.2 for more details). Good agreement between OMI *Method 1* and airborne SO_2 emission rates suggests that the former can be used as a reliable proxy for airborne measurements during passive degassing activity. The strong linear correlation between airborne and OMI *Method 1* data suggests that the equation of fit (Supplementary Material, Table 2.A.2) could potentially be used to correct for OMI underestimation, allowing the OMI data to be better integrated with the airborne emissions dataset. Further testing is required to determine if this correction could be applied to other volcanoes observed by OMI under conditions similar to this study.

2.5.6 Discussion of Cumulative SO_2 Masses

Cumulative SO_2 masses were calculated from daily OMI measured masses and derived emission rates from 19 March through 12 June 2009 and determined to be ~542 and ~615 kt, respectively (Fig. 2.8). Approximately half of the OMI measured cumulative emissions for this study period were emitted during the explosive phase (225 kt from daily masses and 335 kt from daily emission rates), with the rest emitted during the pre-eruptive and effusive phases. The large fraction of cumulative SO_2 mass emitted during the explosive phase is significant because airborne methods are not capable of fully capturing these explosive SO_2 emissions (Section 2.3.2). This highlights OMI's utility as a volcano monitoring tool as it is able to quantify explosive SO_2 emissions and thus provide useful information that cannot be attained through airborne methods alone. It should be noted that the cumulative SO_2 masses estimated by OMI are lower than that estimated from airborne measurements (751.89 kt) for the same time period by approximately 30% and 20% for OMI mass and emission rate methods, respectively (Werner et al., 2012b); however, the cumulative airborne SO_2 mass, calculated by linearly interpolating daily SO_2 mass values, assumes that SO_2 emissions are fairly

consistent over time-scales of days to weeks and thus involves a certain degree of uncertainty.

The explosive and effusive phase cumulative OMI-derived SO_2 masses emitted during Mount Redoubt's 2009 eruption were similar to those estimated for the 1989 – 90 Mount Redoubt eruption using Total Ozone Mapping Spectrometer (TOMS) satellite SO_2 masses and airborne SO_2 emission rates (Casadevall et al., 1994; Schnetzler et al., 1994). Specifically, the cumulative SO_2 mass emitted during the explosive phase in 1989-90 was estimated to be ~175 kt ± 50 kt (Casadevall et al., 1994), which is similar to the SO_2 yield for the 2009 explosive phase reported here. The cumulative SO_2 masses estimated for the dome growth and destruction phase of the 1989-90 eruption (the phase most similar to the 2009 effusive phase) were estimated to range from 572 to 680 kt ±90 kt (Casadevall et al., 1994). These values are approximately double those observed during the 2009 effusive phase; however the time period analyzed was 176 days in 1989-90, as opposed to the 69 days analyzed during the 2009 eruption.

2.5.7 Correlations between Eruptive Activity and OMI-Derived SO_2 Measurements

The relatively high temporal resolution of OMI daily SO_2 mass measurements allows these data to be compared with observations of volcanic activity and other geophysical datasets. In particular, high variability in the OMI SO_2 masses was observed during the explosive phase of Mount Redoubt's 2009 eruption that qualitatively agree with the timing of explosive events described by Bull and Buurman (2012). Additionally a strong correlation between cumulative daily SO_2 mass and relative acoustic energy ($r = 0.996$, according to the Spearman Rank Correlation Test) throughout the explosive phase of the eruption was observed and described in detail by Fee et al.(2011). This suggests that SO_2 mass measured following explosive activity may be used to evaluate relative eruption explosivity (Fee et al., 2010). Finally, a strong linear correlation ($R^2 = 0.97$) is exhibited between OMI SO_2 and tephra masses associated with the explosive events (Fig. 2.9; Wallace, 2012). This suggests that comparable amounts of SO_2 and tephra were emitted

during each day during the explosive phase, such that OMI SO_2 masses from explosive events be used as a proxy for relative eruption size, supporting the findings by Blake (2003). We group the daily SO_2 masses observed during the explosive phase into three categories: high (>10 kt), moderate (1 to 10 kt), and low (<1 kt) (Table 4), and in doing so the following correlations emerge: (1) high OMI SO_2 masses were observed on days corresponding with Events 1-6, 8-15, and 19 (Schaefer et al., 2012); (2) moderate SO_2 masses were observed on days in which no explosive eruptions occurred, but on which lava extrusion was suspected and/or observed by satellite imagery (Bull and Buurman, 2012); and (3) low SO_2 masses were observed on days in which little volcanic activity was observed (though dome growth is expected) (Table 2.4). An exception to (3) occurred on 29 March, when Events 16-18 occurred yet only 0.2 kt of SO_2 was detected.

Using the combined observations of SO_2 emission levels and eruptive activity we propose the following interpretations to describe Mount Redoubt's eruptive activity. First, high SO_2 masses observed were associated with explosive Events 1-5, 7-15, and 19, corresponding with the rapid eruption of a gas-rich magma. The moderate-level SO_2 emissions corresponded temporally with periods of dome growth (as observed from satellite imagery) and the absence of explosive eruptions (Table 2.4; Bull and Buurman, 2012)) . We interpret these moderate-level SO_2 emissions to be due to slow degassing of a shallow or extruding magma. Low SO_2 emissions were observed on three days during the explosive phase, two of which had no explosive events (25 March and 2 April). One possible interpretation of the low SO_2 emissions observed on these dates is limited degassing through a viscous dome, and satellite imagery supports the presence of two domes between Events 6 and 7, and Events 18 and 19, respectively (Bull and Buurman, 2012). An alternate explanation is that due to poor OMI viewing conditions, the SO_2 emissions may have been below OMI's detection limit. The third day with observed low OMI SO_2 emissions occurred on 29 March when explosive Events 16, 17, and 18 occurred at least 19 hours prior to the OMI overpass. We propose that the low SO_2 masses measured following these events may have been due to: (1) the long lag time

between emission and OMI observations enabling the plume to become sufficiently dilute such that OMI only measured low SO_2 masses, and/or (2) these events having smaller eruption mass or lower volatile content and thus less explosive than the other events, such that they produced smaller SO_2 emissions. Low acoustic energies observed from Events 16-18, relative to Events 2-6, as described by Fee et al. (2011) are consistent with (2) as acoustic energies have shown broad correlation with gas emissions (Dalton et al., 2010; Fee et al., 2011).

High variability in daily SO_2 mass emissions during the effusive phase of the eruption from below detection limit to ~24.6 kt (12 April; Fig. 2.6) make relationships between degassing and volcanic activity difficult to constrain during this period. Evidence from satellite imagery, time-lapse photography, and photogrammetry of dome growth was consistent throughout this period (Diefenbach et al., 2011; Bull and Buurman, 2012), and thus degassing of extruding lava can explain the moderate level emissions. We propose that variations in daily OMI measured SO_2 masses throughout this period may be due to a variety of factors including both variations in volcanic and instrument retrieval factors. Specifically, changes in lava composition, vesicularities, and/or extrusion rates could produce changes in SO_2 emission rates. For example, high SO_2 emissions observed by OMI from 4-6 May correlate with increased extrusion rates (Diefenbach et al., 2011), variations in lava composition (Coombs et al., in press), elevated seismicity (Buurman et al., 2012), and an increase in airborne gas emissions (Werner et al., 2012b) all of which support a change in the volcanic system. Other periods of elevated OMI measured SO_2 emissions during the sample period include 8-12 and 18-20 April, which also could be attributed to changing magmatic conditions, however more corroborating evidence is required to develop this hypothesis. Additionally, it is probable that variations in OMI viewing conditions, atmospheric composition, and surface reflectivity may cause apparent variations in SO_2 emission rates (Yang et al., 2007). While clear divisions between levels of SO_2 emissions for different types of volcanic activity were apparent during the explosive phase of the eruption, these same divisions did not apply to the

effusive phase SO_2 emissions. These results suggest that for times corresponding with known explosive eruptions, OMI daily SO_2 masses can be used to infer relative eruption size and explosivity. For other times, OMI daily SO_2 masses may be used to help distinguish explosive from extrusive degassing, and may help resolve variations in lava extrusion rates when used in conjunction with other observational datasets.

2.5.8 Apparent Periodicity in OMI Measured SO_2 Masses

An apparent periodicity is visible within the OMI daily SO_2 masses throughout the sample period (Fig. 2.10). To evaluate the periodicity as a function of time a 12-18 day filter was applied to the SO_2 masses during the study period (Fig. 10, top) using a 2-pole, acausal, butterworth filter (Hayes, 1996). A clear periodic trend can be seen in the filtered data throughout the sample period. To better constrain the dominant period in the data a Power Spectral Density (PSD) estimate was made using Welch's modified periodogram method (Hayes, 1996) (Fig. 2.10, bottom). This method is chosen as it reduces the noise in the power spectra by dividing the data into overlapping segments and then averaging the power spectra. Two dominant periods of approximately four and 15 days within the OMI daily SO_2 mass dataset exist (Fig. 2.10, bottom), though high uncertainties are present due to the limited number of samples (85 days). Several scenarios could explain the periodicities including, but not limited to: (1) changes in OMI viewing geometry; (2) changes in the atmospheric composition and conditions, specifically with respect to ozone and cloud cover (e.g. Prata, 1990); (3) changes within the volcanic system itself such as variations in lava extrusion rate, magma convection and/or ascent, conduit permeability, etc. (Andres et al., 1993; Edmonds et al., 2003; Sutton et al., 2003); and (4) tidal stresses (e.g. Sottili et al., 2007). The PSD methods described above were applied to daily earthquake number at Redoubt Volcano for the sample period and no dominant period was found, supporting a non-volcanic source to the periodicity. OMI has a 16 day or 233 orbit repeat cycle, meaning that OMI's orbital viewing geometry repeats every 16 days or 233 orbits. Certain orbital viewing geometries (e.g. near-nadir overpasses) are more favorable for detection of SO_2 from Redoubt Volcano, which likely contributes to

the apparent 16 day periodicity observed within the OMI daily SO_2 mass dataset. This has implications for monitoring SO_2 emissions with OMI, as changes in measured daily SO_2 masses could be due to either changes in SO_2 production (e.g. volcanic activity or anthropogenic sources), changes in OMI viewing geometries, or both. Future work should be conducted to constrain possible influences by other non-volcanic sources and to evaluate the affect of OMI viewing geometries on measured SO_2 masses.

2.5.9 Evaluation of OMI as a Volcano Monitoring Tool

The results of this study show that OMI was a useful tool for monitoring Mount Redoubt's volcanic SO_2 emissions during the 2009 eruption, and emphasize the utility of OMI as a volcano monitoring technology. Significant advantages in using OMI to monitor SO_2 emissions relative to traditional airborne methods or other satellite sensors include: (1) the ability to detect SO_2 emissions during explosive activity when it may not be safe or feasible to collect airborne measurements; (2) OMI's sensitivity to SO_2, allowing both low altitude (<3 km) and relatively weak (~2,000 t/d SO_2) plumes to be detected, as this type of plume often goes undetected by other satellite sensors; (3) the relatively high temporal resolution of OMI data, one or more per day compared to weekly or biweekly airborne measurements; and (4) the affordability of measurement collection as the data are freely available and only require analyst time for image processing and interpretation. Additionally, we have shown that OMI-derived emission rates agree well with airborne measurements, such that OMI data can be successfully integrated into airborne databases. OMI's ability to detect SO_2 from Redoubt Volcano on a near daily basis make it possible for gas data to be used in conjunction with other high temporal resolution geophysical datasets to help detect changes in volcanic activity and improve AVO's monitoring capabilities, especially for remote Alaskan volcanoes.

2.6 Conclusions

OMI detected SO_2 emissions from Redoubt Volcano on 67 out of 82 days analyzed between 23 March (the onset of the explosive eruption) and 12 June 2009. Comparison

between OMI and corrected airborne SO_2 CD values show that in general for Mount Redoubt's ~3 km plume, the OMI *TRL* altitude algorithm underestimated, while the *PBL* altitude algorithm overestimated SO_2 CD. Good (R^2 = 0.75) and poor (R^2 = 0.38) correlations between OMI and corrected airborne CD values were observed for the *PBL* and *TRL* altitude algorithms, respectively. OMI daily SO_2 masses for the study period ranged from ~60.1 kt on 24 March to below detection limit, with an average daily SO_2 mass emitted during the study period of ~6.7 kt. The highest SO_2 emissions were observed during the initial part of the explosive phase and the emissions exhibited an overall decreasing trend with time, though some periods of higher emissions were observed. OMI SO_2 emission rates were calculated using three methods and compared to airborne measurements. Results of this comparison found good agreement (R^2 = 0.82) between OMI *Method 1* derived and airborne emission rates, with OMI underestimating SO_2 relative to airborne measurements in most cases. The comparison between OMI and airborne calculated emission rates suggests that OMI's detection limit for high latitude, springtime conditions is between 2,000 and 4,000 t/d and may improve with increasing UV radiation, though further comparisons are needed to corroborate this. Cumulative SO_2 masses calculated from OMI daily mass and derived emission rates for the study period are estimated to range from 542 to 615 kt, with approximately half of the cumulative SO_2 having been erupted during the explosive phase of the eruption. These values are similar in magnitude to those estimated for the 1989-90 Mount Redoubt eruption.

The relatively high temporal resolution OMI dataset allowed comparisons with other observational datasets and find strong correlations between OMI daily SO_2 mass and both relative acoustic energy and tephra mass during the explosive phase of the 2009 Mount Redoubt eruption, suggesting that OMI data may be used to infer relative eruption explosivity and size associated with known explosive eruptions. Further, when used in conjunction with other geophysical and geochemical datasets OMI daily SO_2 masses may be used to help distinguish explosive from effusive activity and detect changes in lava effusion rates. The results of this study find that OMI is a useful volcano monitoring tool

to complement airborne measurements, capture explosive SO_2 emissions, identify potentially hazardous volcanic clouds, and provide high temporal resolution SO_2 emissions data that can be used with complementary datasets to elucidate volcanic processes.

2.7 Acknowledgements

The authors are grateful for constructive comments by Chris Waythomas and two anonymous reviewers whose suggestions significantly improved this manuscript. The authors would like to acknowledge pilots Steve Jones and Jerry Morris from Security Aviation as well as AVO scientists Rick Wessels, Game McGimsey and Tina Neal, for their contributions to airborne gas measurement collection. TML would like to thank Kate Bull, Helena Buurman, Ronni Grapenthin, Michelle Coombs, Jon Dehn, Bill Simpson, Rainer Newberry, Owen Neill, Sarah Henton and Trystan Herriott for insightful scientific discussions regarding this work. TML would like to thank Angela Ekstrand for help with figure creation and Helena Buurman for providing daily earthquake data for PSD analysis. SAC acknowledges NASA funding for OMI SO_2 validation (grant NNX09AJ40G). This work has been funded by the Alaska Volcano Observatory, the UAF Geophysical Institute, the Alaska Space Grant Consortium, and the American Recovery and Reinvestment Act (ARRA) grant.

Figures:

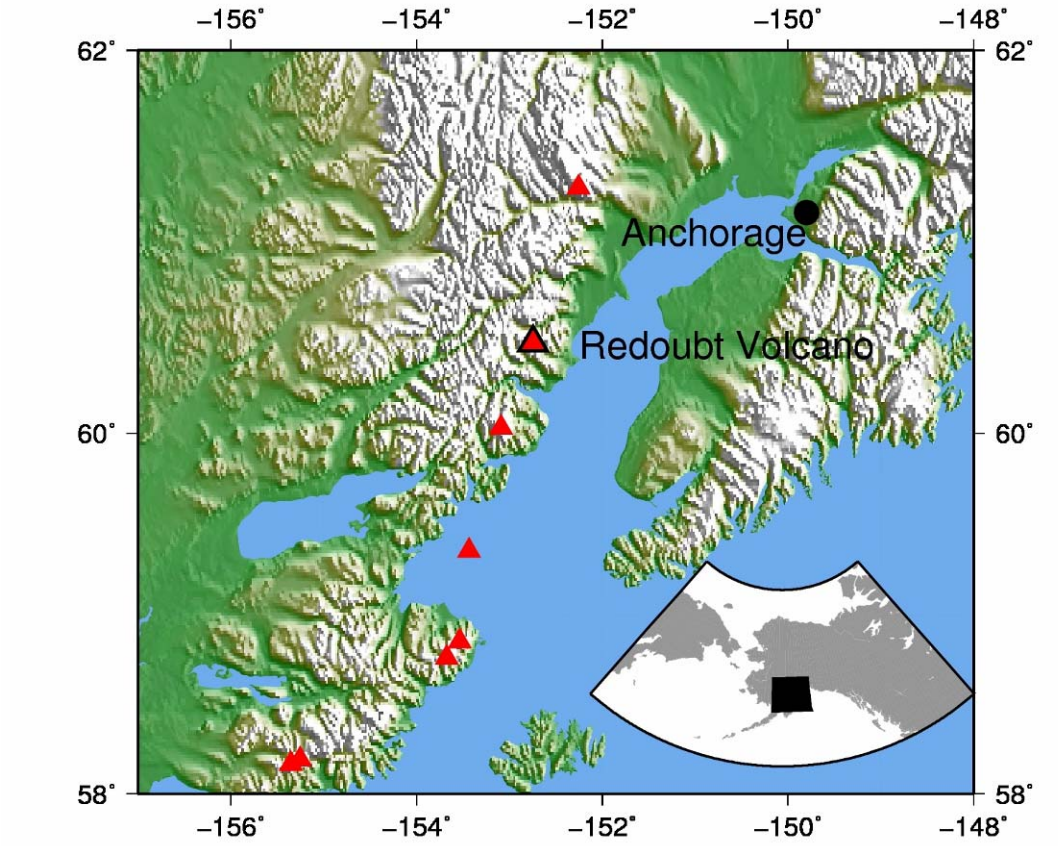

Figure 2.1: Location map. The location of Redoubt Volcano and other volcanoes (black triangles) within the Cook Inlet region, along with Anchorage, the largest population center in Alaska, are shown.

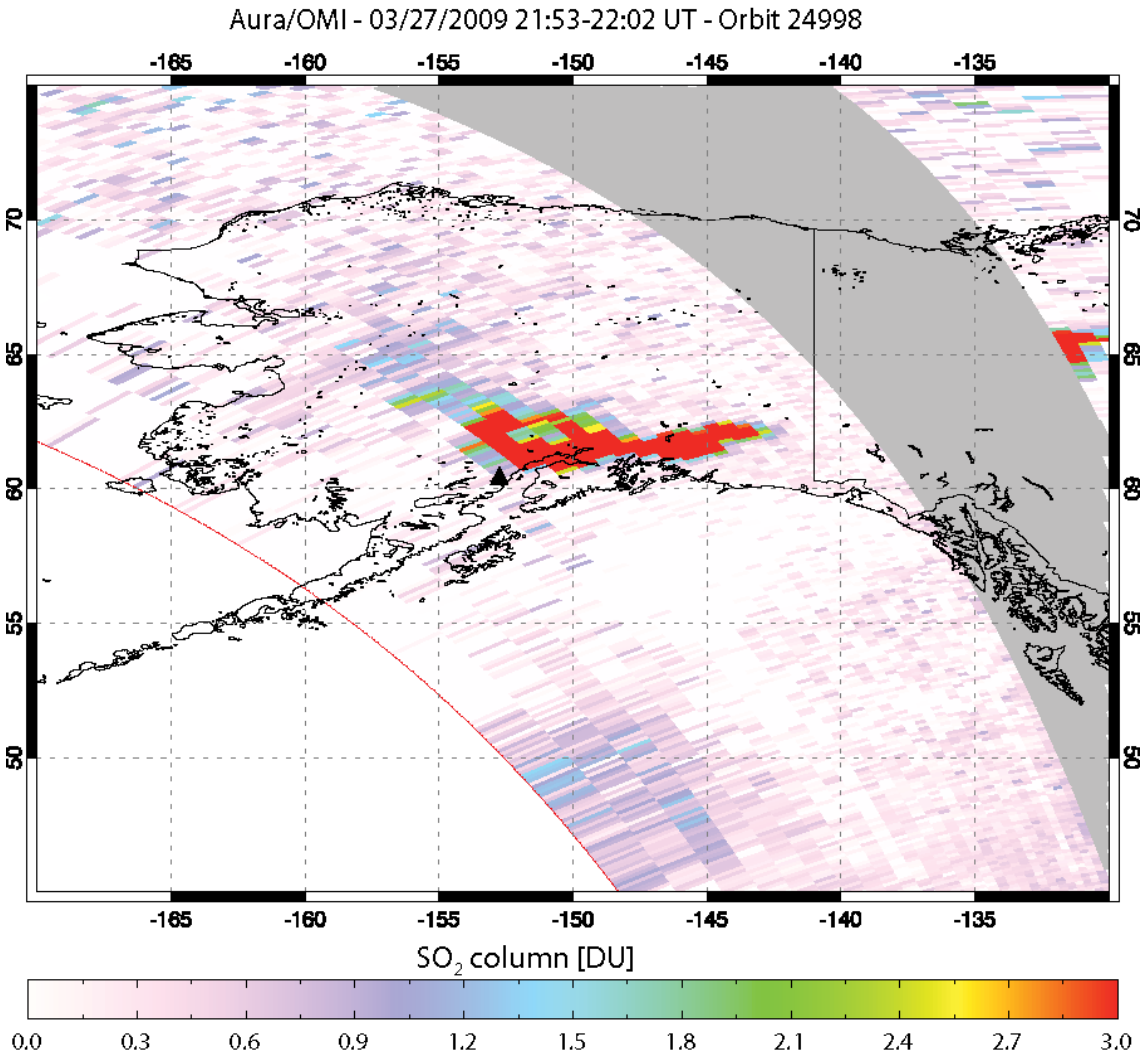

Figure 2.2: OMI detection of SO_2 from Redoubt Volcano. Example OMI image from 27 March 2009 showing OMI SO_2 column density (CMA = 7.5 km) for Mount Redoubt's plume. The area shown is the analysis box. Redoubt Volcano is marked by a black triangle. The swath edge is outlined in red and the row anomaly pixels are shaded gray.

Figure 2.3: Column density comparison between OMI and airborne SO_2 measurements. Comparisons for 16 pixels collected on 20 April (a), 1 May (b), 14 May (c), 26 May (d), 3 June (e), and 7 June (f) are shown. The left side of this figure shows Aqua MODIS visible imagery acquired within 15 minutes of the OMI overpass, with OMI tiled pixel areas outlined in red. Mount Redoubt's plume is visible in MODIS images on 20 April, 14 and 26 May, and 7 June. Surface reflectivity conditions for the analyzed days can be seen. The right side of this figure depicts the OMI measured SO_2 CD for tiled pixel areas with warmer colors representing higher CD values. Accurate pixel areas, including pixel overlap, for the analyzed pixels are outlined in black. Airborne SO_2 CD from the traverses used in the pixel analysis are plotted on top of the OMSO2 data using the same color bar scale, with traverse start and end times labeled. Plume limits, based on airborne CD measurements of SO_2 greater than or equal to 1 DU, are outlined in black. Assigned pixel labels used in the analysis are shown and Redoubt Volcano is marked with a red triangle.

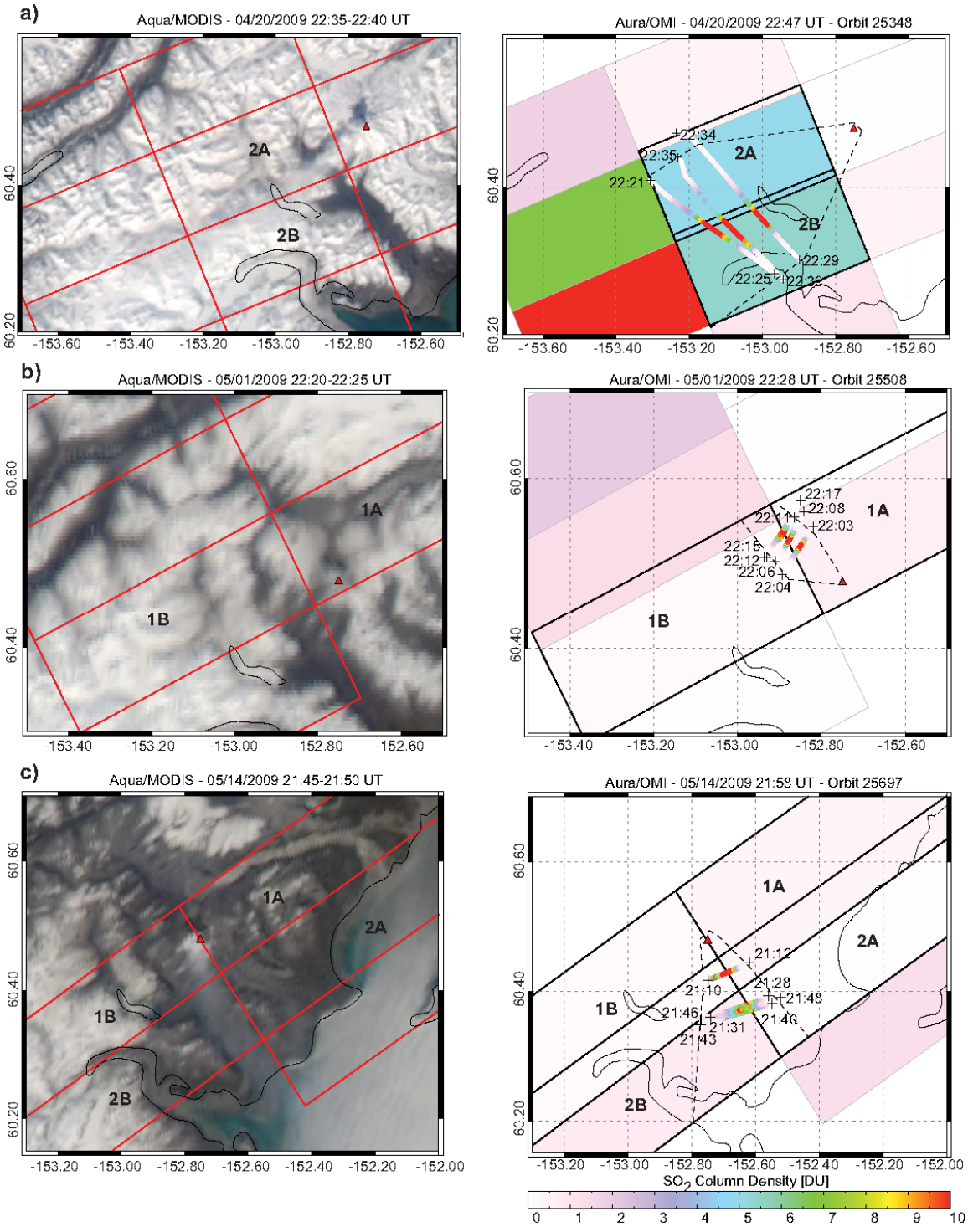
a)
Aqua/MODIS - 04/20/2009 22:35-22:40 UT
2A
2B
60.40
60.20
-153.60 -153.40 -153.20 -153.00 -152.80 -152.60
Aura/OMI - 04/20/2009 22:47 UT - Orbit 25348
22:34
22:35
22:21
2A
2B
22:29
22:25
22:39
b)
Aqua/MODIS - 05/01/2009 22:20-22:25 UT
1A
1B
60.60
60.40
-153.40 -153.20 -153.00 -152.80 -152.60
Aura/OMI - 05/01/2009 22:28 UT - Orbit 25508
22:17
22:08
22:03
22:15
22:12
22:06
22:04
1A
1B
c)
Aqua/MODIS - 05/14/2009 21:45-21:50 UT
1A
2A
1B
2B
60.60
60.40
60.20
-153.20 -153.00 -152.80 -152.60 -152.40 -152.20 -152.00
Aura/OMI - 05/14/2009 21:58 UT - Orbit 25697
1A
2A
21:12
21:28
21:48
21:10
21:46
21:40
21:31
21:43
1B
2B
SO2 Column Density [DU]
0 1 2 3 4 5 6 7 8 9 10

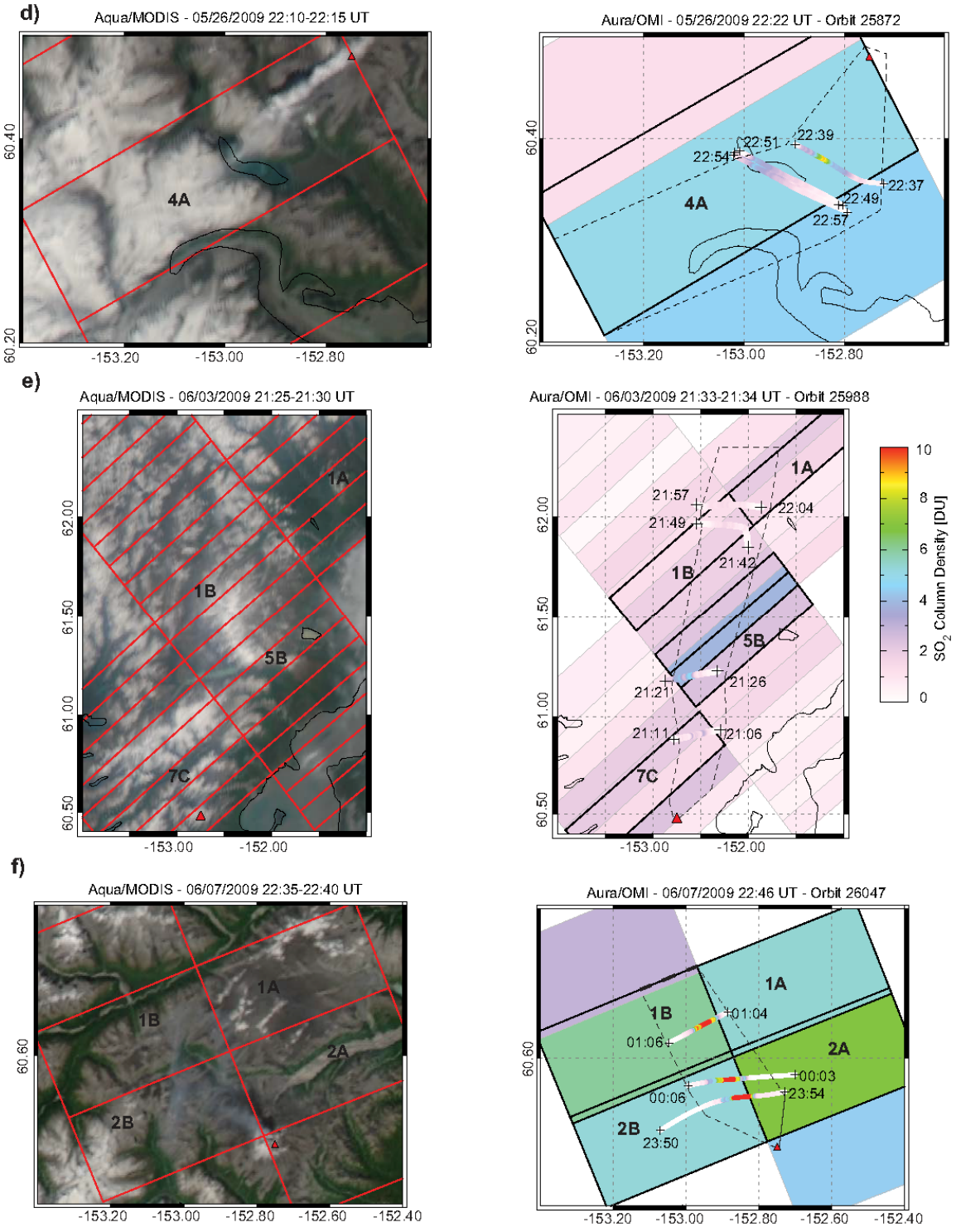

Figure 2.3 continued

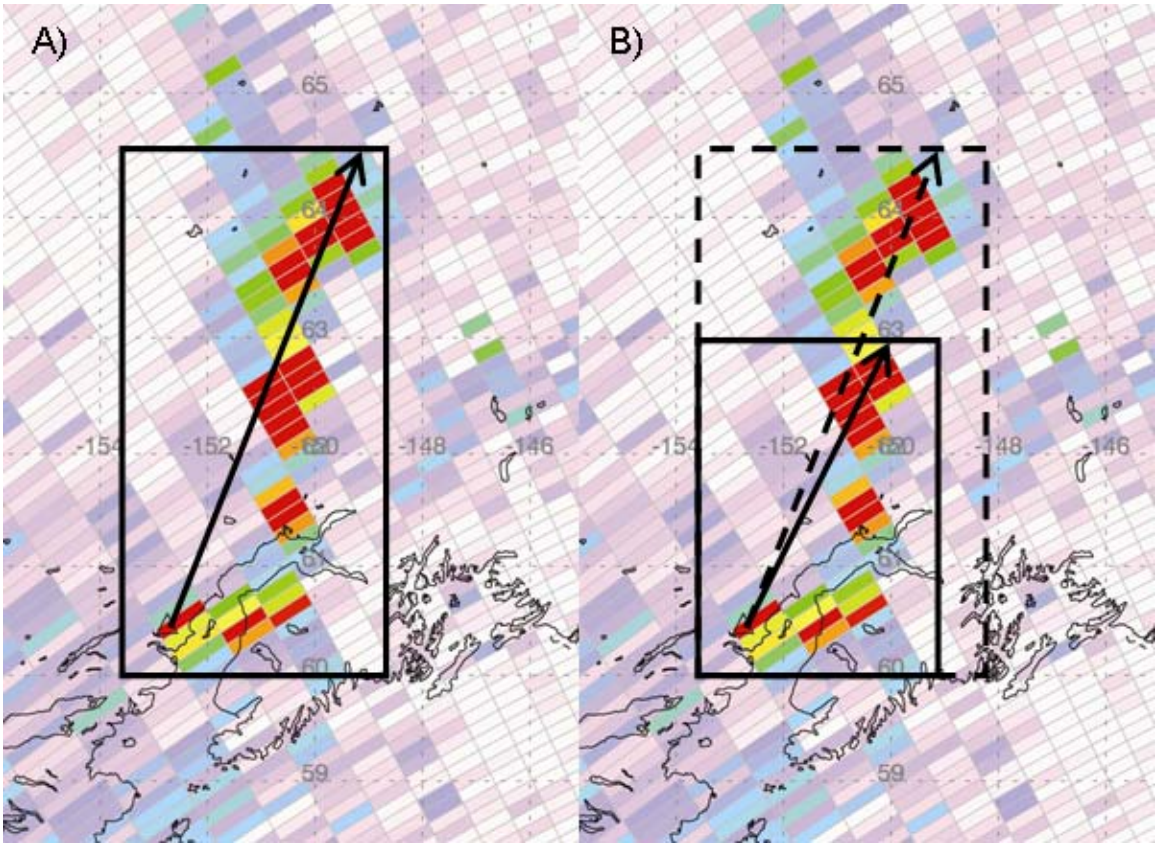

Figure 2.4: Methods for calculating SO_2 emission rates from OMI data. OMI image from 6 June 2009 showing an SO_2 plume from Redoubt Volcano and two methods used to estimate SO_2 emission rate from OMI SO_2 mass. In *Method 1* (a), the mass, *M*, of the visible SO_2 plume is multiplied by the modeled plume speed, *V*, and divided by the plume length, *L* (black arrow), to obtain emission rate. In *Method 2* (b), the modeled plume speed, *V*, is used to calculate the distance the plume could travel in a period of 24 hours, L_{24} (shorter, black arrow). The mass of the plume is calculated to L_{24} to provide a daily SO_2 emission rate.

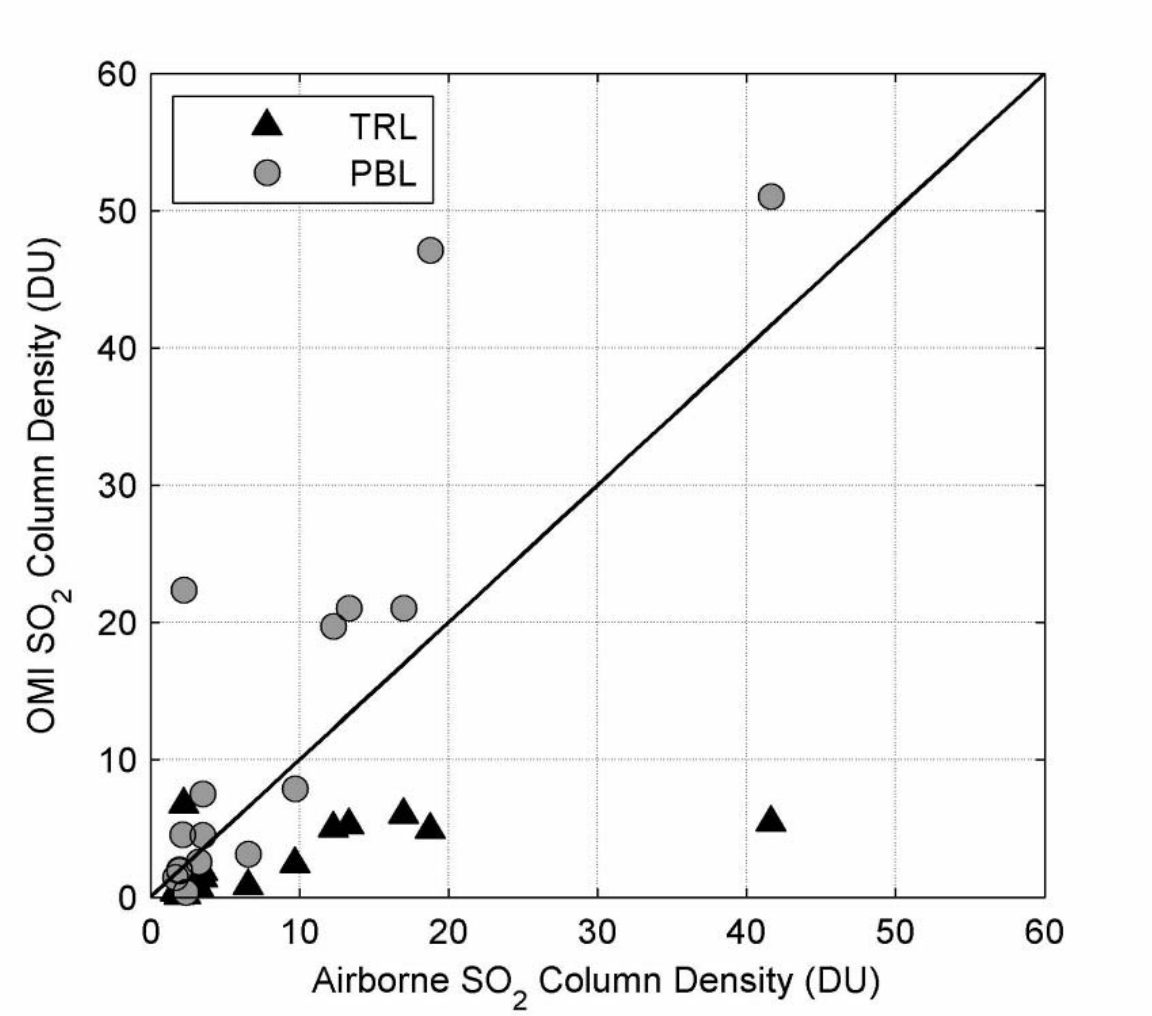

Figure 2.5: Comparison between corrected airborne and OMI SO_2 CD. OMI column density calculated using *TRL* (triangles) and *PBL* (gray circles) retrievals are shown. The black line represents a 1:1 correlation. Uncertainties in airborne SO_2 CD are estimated to be ±10% Werner et al. (2012). Uncertainties in retrieved OMI SO_2 CD for non-polluted conditions are estimated to be -7 – -23% (Krotkov et al., 2008) and ±20% (Yang et al., 2007) for the BRD and LF algorithms, respectively. Average differences between OMI *TRL*, *PBL*, and *Selected* SO_2 CDs and airborne SO_2 CDs are -55%, 79%, and 59%, respectively.

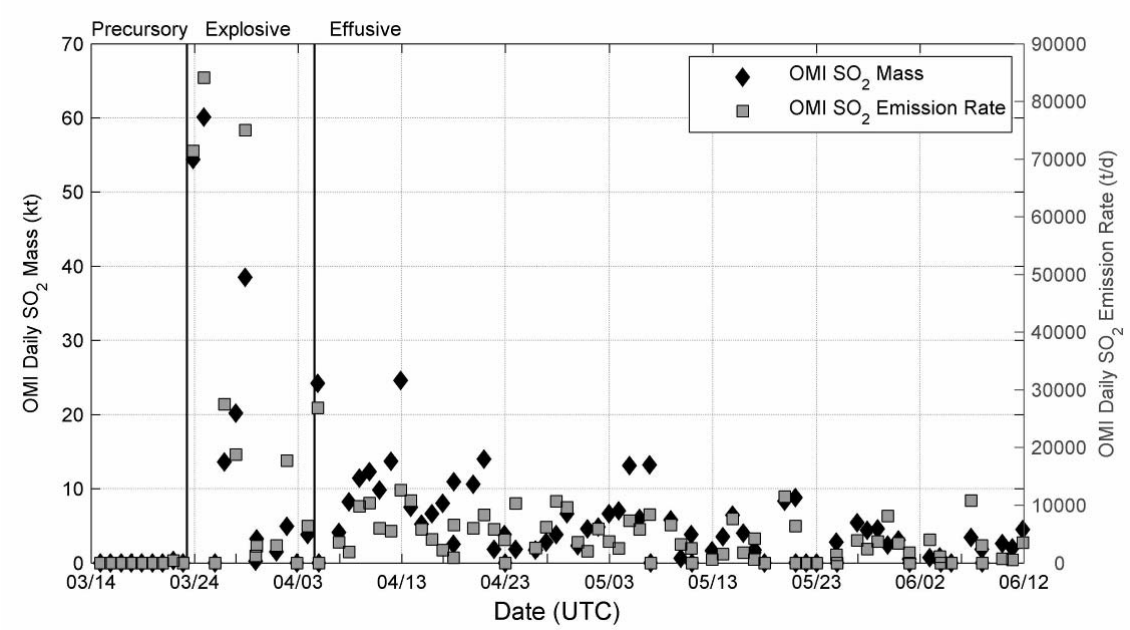

Figure 2.6: OMI-derived daily SO_2 mass and emission rates. OMI daily SO_2 mass (kt) (black diamonds) and OMI *Method 1* calculated SO_2 emission rates (gray squares) from Redoubt Volcano throughout the study period. The black vertical lines represent the temporal breaks between precursory (left), explosive (center), and effusive (right) phases of the eruption.

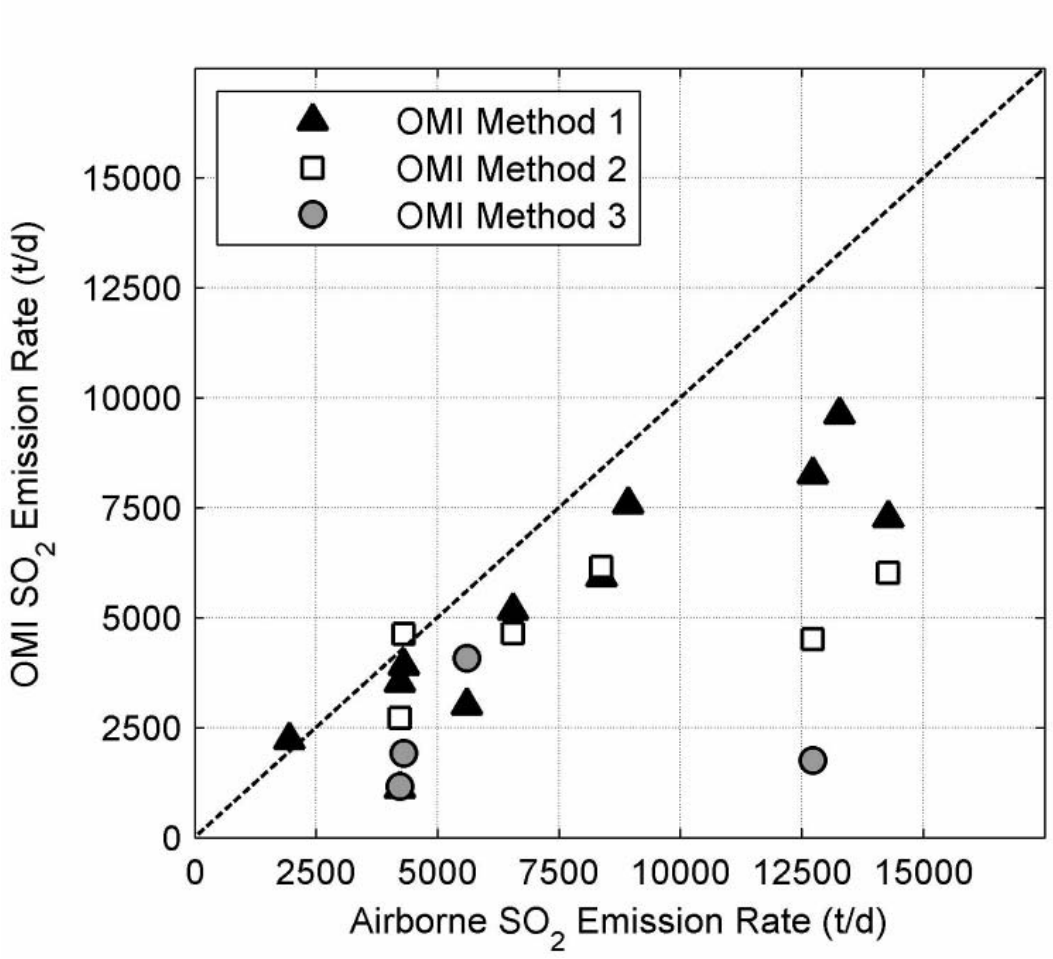

Figure 2.7: Results of comparison between OMI-derived and airborne SO_2 emission rates. The dashed line represents a 1:1 correlation. Average differences between OMI-derived and airborne SO_2 emission rates for OMI *Methods 1*, *2*, and *3* are -28%, -34%, and -40%, respectively. OMI methods underestimate SO_2 emission rates relative to airborne measurements in almost all cases.

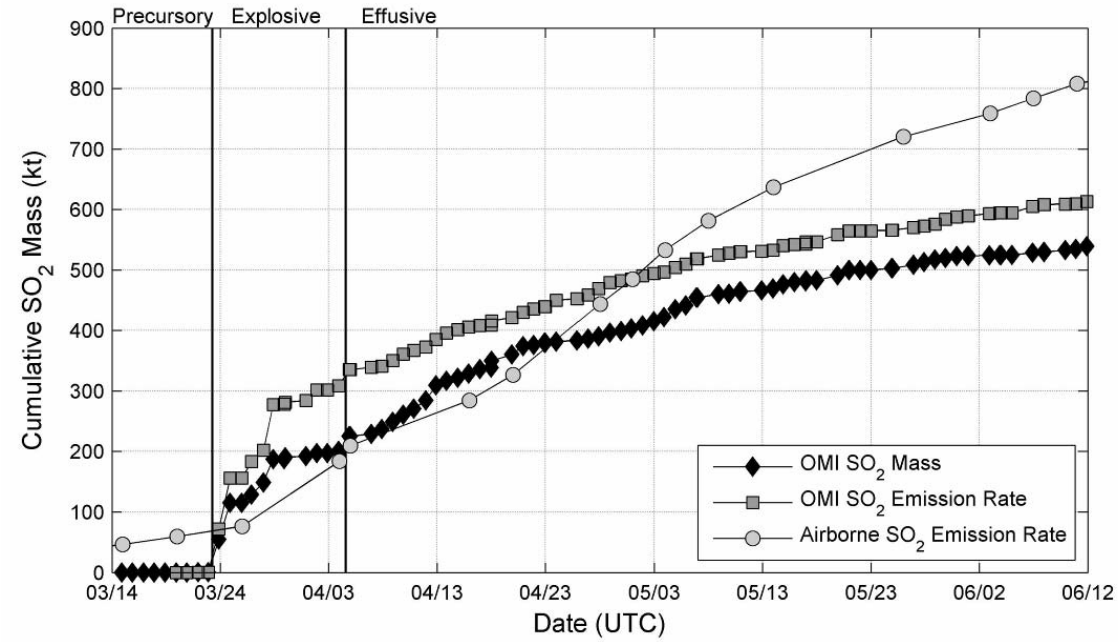

Figure 2.8: Cumulative SO_2 masses emitted from Redoubt Volcano. Cumulative SO_2 masses are estimated from OMI daily mass (black triangles), OMI-derived emission rate (gray squares), and airborne methods (light gray circles). The black vertical lines represent the temporal breaks between precursory (left), explosive (center), and effusive (right) phases of the eruption. Note that airborne measurements from the two months preceding the first OMI detection of Mount Redoubt SO_2, of ~46 kt are included in this figure.

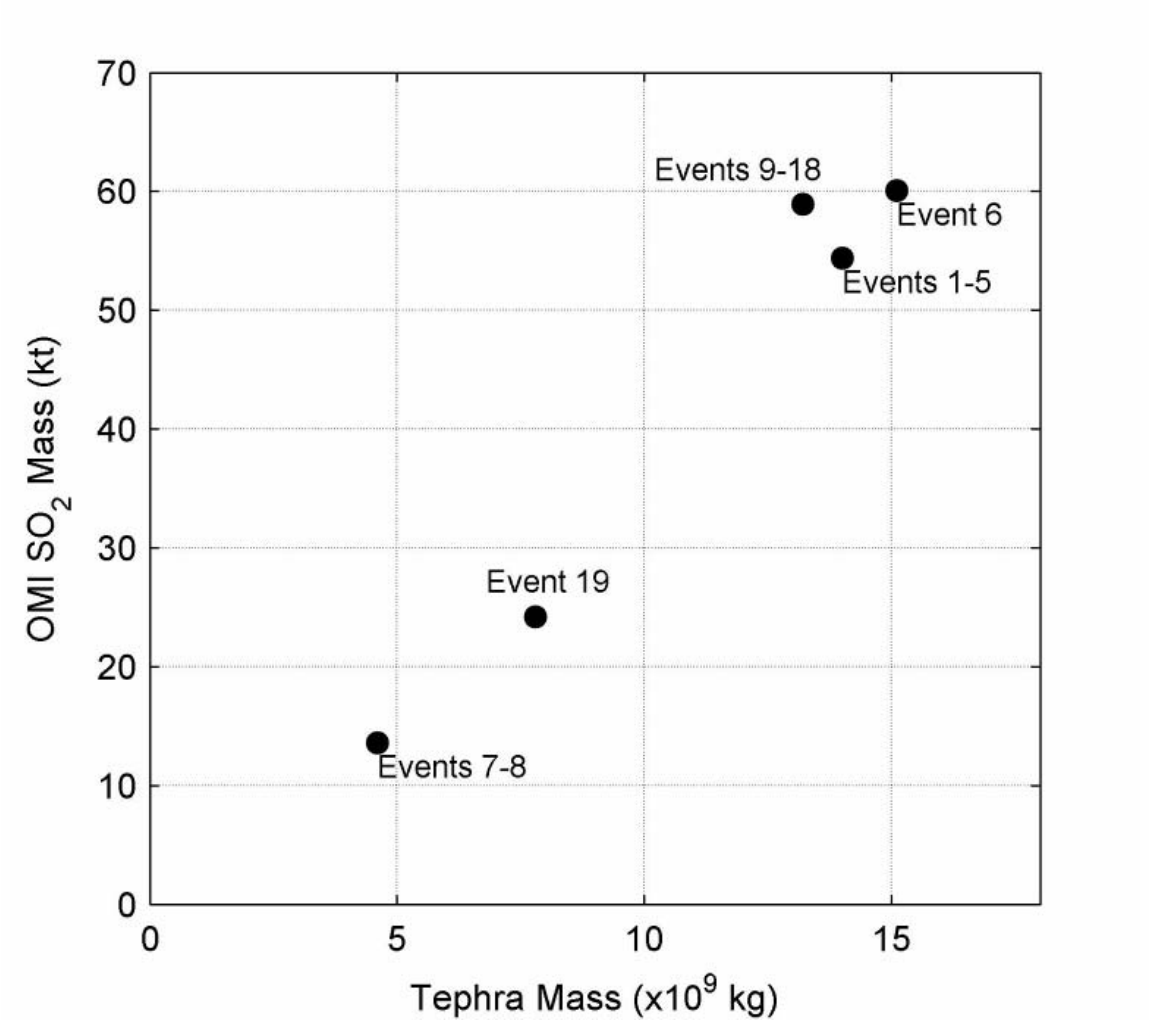

Figure 2.9: Comparison between SO_2 and tephra masses for Mount Redoubt's explosive events. A strong ($R^2 = 0.97$) linear correlation can be seen. Tephra masses from Wallace et al. (2012).

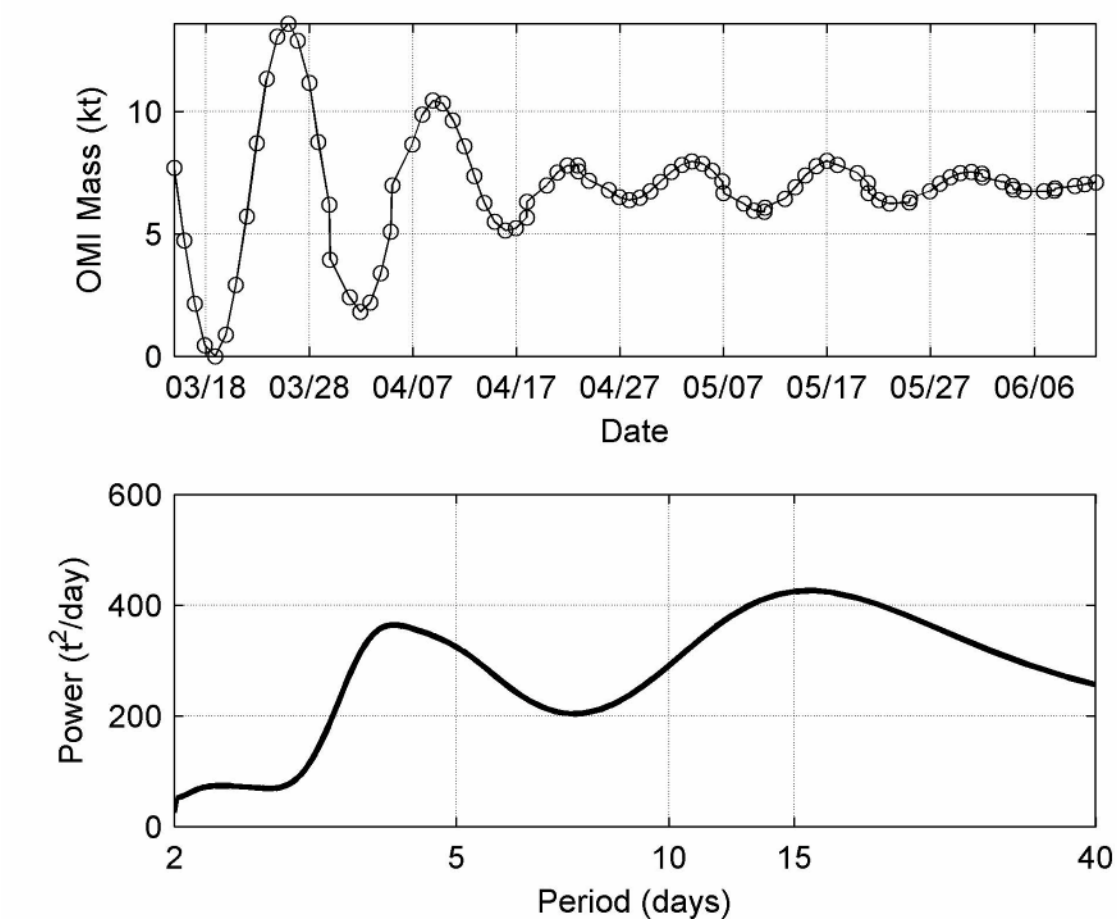

Figure 2.10: Power Spectral Density analysis of OMI daily SO_2 mass. OMI daily measured SO_2 mass data filtered between 12 and 18 days (top) and Power Spectral Density analysis on the 85 day dataset, showing apparent dominant periodicities at ~4 and 16 days (bottom).

Tables:

Table 2.1: Explosive phase eruption chronology.

Date (UTC)	Time (UTC)	Activity	Event No. [1]	Plume Height [5] (km)	Lahar [2]	Pyroclastic Density Current [†,2]	Tephra [2]	Acoustic Group [‡,4]	Gliding Harmonic Tremor [5]
15-Mar-09	21:05	Phreatic explosion [1]	0	4.6					
20-Mar-09	12:00	Onset of 66 hour seismic swarm (end at 6:34 on 23 March) [3]							
23-Mar-09		Satellite observation of lava dome growth prior to Event [1]							
23-Mar-09	6:38	Magmatic Explosion [1]	1	5.5				1	
23-Mar-09	7:02	Magmatic Explosion [1]	2	13.4				2	
23-Mar-09	8:14	Magmatic Explosion [1]	3	14.6	X			2	
23-Mar-09	9:39	Magmatic Explosion [1]	4	13.1	X			2	
23-Mar-09	12:31	Magmatic Explosion [1]	5	18.3	X			2	
24-Mar-09	3:41	Magmatic Explosion [1]	6	18.3	X	X?	X	2	
		Possible lava dome growth between Events 6 and 7 [1]							
26-Mar-09	16:34	Magmatic Explosion [1]	7	8.2	X				
26-Mar-09	17:24	Magmatic Explosion [1]	8	18.9	X	X		2	
27-Mar-09	0:00	Onset of an 8 hour seismic swarm (end at 8:28 on 27 March) [3]							
27-Mar-09	7:47	Magmatic Explosion [1]	9	12.5	X			1	X
27-Mar-09	8:29	Magmatic Explosion [1]	10	14.9	X			3	X
27-Mar-09	16:39	Magmatic Explosion [1]	11	15.6	X	X		3	X
28-Mar-09	1:41	Magmatic Explosion [1]	12	14.6	X		X	3	X
28-Mar-09	3:25	Magmatic Explosion [1]	13	15.2	X	X?	X	3	X
28-Mar-09	7:20	Magmatic Explosion [1]	14	14.6		X?		3	X
28-Mar-09	9:20	Magmatic Explosion [1]	15	14.6	X	X		3	X

Table 2.1: Continued

28-Mar-09	21:40	Magmatic Explosion [1]	16	5.2	X			3
28-Mar-09	23:29	Magmatic Explosion [1]	17	12.5	X			3
29-Mar-09	3:23	Magmatic Explosion [1]	18	14.6	X	X	X	3
		Lava dome growth between events 18 and 19 [2]						
29-Mar-09	7:50	Onset of 1 hour seismic swarm [3]						
2-Apr-09	19:00	Onset of 44 hour seismic swarm (end at 13:58 on 4 April) [3]						
4-Apr-09	13:58	Magmatic Explosion [1]	19	15.2	X	X	X	4
		Lava dome growth following Event 19 [2]						
2-May-09	21:00	Onset of 123 hour seismic swarm (end at 1:00 on 8 May) [3]						

References: [1] Schaefer et al. (2012); [2] Bull and Buurman (2012); [3] Buurman et al. (2012); [4] Fee et al. (2011); [5] Hotovec et al. (2012); [6] Schneider and Hoblitt (2012); and [7] Wallace et al. (2012).

‡ Group 1: >16 min. duration, multiple pulses, low acoustic energies, no ultra long period (ULP) energy.

‡ Group 2: >10 min. duration, sustained infrasound, with no significant variation in amplitude, high acoustic energies, some ULP energy.

‡ Group 3: short duration, high acoustic energies, impulsive onsets, and peak frequencies of ~0.1 Hz.

‡ Group 4: emergent onset, two main pulses with second pulse having high amplitudes and significant ULP energy.

Table 2.2: Daily OMI measured SO_2 masses and derived emission rates (*Method 1*).

Date	Time (UTC)	OMI Orbit	Plume Altitude (km)[1,*]	OMI Altitude Algorithm Used	Wind Velocity (m/s)	OMI SO_2 Mass (kt)	OMI M1 SO_2 Emission Rate (t/d)	Airborne SO_2 Emission Rate (t/d)*	Cumulative SO_2 Mass (kt)	Cumulative SO_2 Emission Rate (kt)
3/14/2009	22:23	24809				0	0		0	0.0
3/15/2009	21:31	24823				0	0		0.0	0.0
3/16/2009	22:14	24838				0	0		0.0	0.0
3/17/2009	21:20	24852				0	0		0.0	0.0
3/18/2009	22:02	24867				0	0		0.0	0.0
3/19/2009	22:45	24882				0	0		0.0	0.0
3/20/2009	21:50	24896				0	0		0.0	0.0
3/21/2009	22:33	24911	NA	TRL	3.7	0.3	400		0.3	0.4
3/22/2009	21:38	24925				0	0		0.3	0.4
3/23/2009	20:40	24940	11	STL	13.07	54.4	71400		54.7	71.8
3/24/2009	21:22	24954	10	STL	19.7	60.1	84100		114.9	155.9
3/25/2009	No detectable plume					0	0		114.9	155.9
3/26/2009	21:10	24983	4	TRL		13.6	27500	3590	128.4	183.4
3/27/2009	23:31	24999	9	STL	8.67	20.2	18800		148.7	202.2
3/28/2009	20:58	25012	8	STL	31.1	38.5	75000		187.2	277.2
3/29/2009	21:41	25027	10	STL	12.55	0.2	1200		187.3	278.4
3/30/2009	0:02	25043	7	STL	5.7	3.2	2900		190.5	281.3
3/31/2009	21:28	25056	6	STL	17.83	1.5	3000		192.0	284.3
4/1/2009	22:11	25071	7	STL	29.23	4.9	17700		196.9	302.0
4/2/2009	No detectable plume					0	0		196.9	302.0
4/3/2009	21:59	25100	7.5	STL	14.13	3.8	6400		200.7	308.4
4/4/2009	21:04	25114	3.8	TRL	9.17	24.2	26900	16650	225.0	335.3
4/5/2009	No data		4.3					11350	225.0	335.3
4/6/2009	22:30	25144	4	TRL	3.35	4.1	3600		229.0	338.9
4/7/2009	21:34	25158	7	STL	2.03	8.2	1900		237.3	340.8
4/8/2009	22:17	25173	7	STL	9.7	11.4	9800		248.6	350.6
4/9/2009	21:22		7	STL	15.4	12.3	10400		261.0	361.0
4/10/2009	20:29	25201	8	STL	9.35	9.8	6000		270.8	367.0
4/11/2009	22:48	25217	11	STL	5.1	13.7	5500		284.5	372.5
4/12/2009	21:53	25213	8	STL	8.27	24.6	12600		309.1	385.1
4/13/2009	20:58	25245	6	STL	28.1	7.5	10800		316.6	395.9
4/14/2009	21:41	25260		STL	12.43	5.2	5800		321.8	401.7
4/15/2009	22:23	25289		STL	7.78	6.6	4100		328.3	405.8
4/16/2009	23:07	25290	4.1*	TRL	2.6*	8.0	2200	1950	336.3	408.0
4/17/2009	23:50	25305	9	STL	2.38	2.5	900		338.8	408.9
4/18/2009	0:33	25320	6	STL	12.85	10.9	6600		349.7	415.5
4/19/2009	21:59	25333	6	STL	9.2	10.6	6000		360.4	421.5

Table 2.2: Continued

4/20/2009	22:42	25348	5.0*	TRL†	5.3*	14.0	8300	12730	374.4	429.8
4/21/2009	21:47	25362		STL	18.9	1.8	5800		376.2	435.6
4/22/2009	22:30	25377		STL	18.23	3.8	4000		380.0	439.6
4/23/2009	Poor data coverage						0		380.0	439.6
4/24/2009	0:00	25407	6	STL	28.1	1.8	10300		381.8	449.9
4/25/2009	21:22	25420		TRL	18	1.7	2600		383.5	452.5
4/26/2009	22:04	25435		TRL	14	2.8	6200		386.3	458.7
4/27/2009	21:10	25449		TRL	24.6	3.8	10700		390.1	469.4
4/28/2009	21:53	25464	3.4*	TRL	10.7*	6.6	9620	13280	396.7	479.0
4/29/2009	22:36	25479		TRL	9.4	2.3	3600		399.1	482.6
4/30/2009	21:40	25493		TRL	6.18	4.6	2000		403.7	484.6
5/1/2009	22:23	25508	3.5*	TRL	14.5*	4.8	5900	8370	408.5	490.5
5/2/2009	23:07	25523		TRL	5.5	6.6	3700		415.0	494.2
5/3/2009	22:11	25551		TRL	2.4	7.0	2500		422.0	496.7
5/4/2009	22:54	25552	3.5*	TRL	7.0*	13.1	7300	14280	435.1	504.0
5/5/2009	21:59	25566		TRL	6.53	6.0	5800		441.1	509.8
5/6/2009	21:04	25580		TRL	8.45	13.2	8400		454.3	518.2
5/7/2009	No data					0			454.3	518.2
5/8/2009	22:29	25610	3.7*	TRL	7.6*	5.8	6600	6560	460.1	524.8
5/9/2009	21:34	25624	3	TRL	17.7	0.6	3200		460.7	528.0
5/10/2009	22:17	25639		TRL	12	3.8	2500		464.4	530.5
5/11/2009	Poor data coverage					0	0		464.4	530.5
5/12/2009	22:05	25668		TRL	5.33	1.6	600		466.0	531.1
5/13/2009	22:48	25683		TRL	5.9	3.5	1500		469.5	532.6
5/14/2009	21:52	25697	3.4*	TRL	7.6*	6.4	7600	8920	475.9	540.2
5/15/2009	22:36	25712		TRL	5.98	4.0	1800		479.9	542.0
5/16/2009	23:19	25727		TRL	5.68	1.4	600		481.3	542.6
5/17/2009	0:02	25742		TRL	7.95	1.7	4200		483.0	546.8
5/18/2009	No detectable plume					0	0		483.0	546.8
5/19/2009	22:11	25770		TRL	14.08	8.3	11500		491.3	558.3
5/20/2009	22:54	25785		TRL	9.73	8.8	6400		500.1	564.7
5/21/2009	No detectable plume					0	0		500.1	564.7
5/22/2009	No detectable plume					0	0		500.1	564.7
5/23/2009	No detectable plume					0	0		500.1	564.7
5/24/2009	22:29	25843		TRL	3.73	2.8	1400		502.9	566.1
5/25/2009	No detectable plume					0	0		502.9	566.1
5/26/2009	22:17	25872	3.5*	TRL	6.3*	5.4	3900	4310	508.3	570.0
5/27/2009	21:22	25886		TRL	3.47	4.4	2400		512.7	572.4
5/28/2009	22:04	25901		TRL	7.6	4.6	3700		517.2	576.1
5/29/2009	21:09	25915		TRL	12.18	2.4	8100		519.6	584.2
5/30/2009	21:52	25930		TRL	8.78	3.1	3400		522.7	587.6
5/31/2009	22:35	25945		TRL	12.6	0.5	1800		523.2	589.4
6/1/2009	No detectable plume					0	0		523.2	589.4
6/2/2009	22:23	25974		TRL	11.95	0.7	4000		523.9	593.4
6/3/2009	21:28	25988	3.4*	TRL	4.0*	0.8	1100	4220	524.7	594.5

Table 2.2: Continued

6/4/2009	No detectable plume				0	0		524.7	594.5	
6/5/2009	No detectable plume					524.7	594.5			
6/6/2009	21:58	26032		TRL	19.13	3.4	10800		528.2	605.3
6/7/2009	22:41	26047	3.8*	TRL	4.9*	1.8	3000	5600	530.0	608.3
6/8/2009	No data					0	0		530.0	608.3
6/9/2009	22:29	26076		TRL	1.23	2.6	700		532.6	609.0
6/10/2009	21:34	26090		TRL	1.67	2.0	500		534.6	609.5
6/11/2009	22:16	26105	3.8*	TRL	3.8*	4.5	3500	4220	539.1	613.0
6/12/2009	23:00	26120		TRL	3.57	2.9	1800		542.0	614.8

[1] Estimated from thermal infrared data and the temperature–altitude method from Webley et al. (2012), unless marked by '*'.
[*]Determined from airborne measurements from Werner et al., (2012b).
[†]According to airborne measurements plume center is at 2.7 km, therefore the TRL algorithm was used in this analysis.

Table 2.3: Summary of data used in the column density comparison.

Date	OMI Orbit	Pixel Label	Pixel Center Latitude	Pixel Center Longitude	TRL SO_2 CD (DU)	Air Mass Factor	Operational PBL SO_2 CD (DU)	Corrected PBL SO_2 CD (DU)	Selected Algorithm	Plume Top (km ASL)	Plume Thickness (km)	Plume Pixel Fraction
4/20/2009	25348	2A	60.4327	-153.0690	4.92	0.30	39.74	47.13	PBL	5.0	3.1	0.71
4/20/2009	25348	2B	60.3191	-152.9760	5.44	0.30	42.80	51.01	PBL	5.0	3.1	0.73
5/1/2009	25508	1A	60.5762	-152.5870	0.66	0.38	2.74	2.59	PBL	3.5	1.7	0.07
5/1/2009	25508	1B	60.4295	-153.1430	0.25	0.37	2.09	2.02	PBL	3.5	1.7	0.06
5/14/2009	25697	1A	60.6374	-152.3050	0.33	0.35	1.40	1.45	TRL	3.4	1.3	0.03
5/14/2009	25697	2A	60.5340	-152.1720	0.10	0.35	1.83	1.90	TRL	3.4	1.3	0.08
5/14/2009	25697	1B	60.2998	-153.2440	0.16	0.34	0.33	0.35	TRL	3.4	1.3	0.03
5/14/2009	25697	2B	60.1970	-153.1100	0.82	0.34	2.97	3.13	TRL	3.4	1.3	0.16
5/26/2009	25872	4A	60.3651	-153.0360	5.02	0.37	20.04	19.73	TRL	4.0	1.9	0.52
6/3/2009	25988	1A	62.2600	-151.5250	1.63	0.34	4.33	4.56	PBL	3.4	1.4	0.30
6/3/2009	25988	1B	61.7780	-152.7010	1.86	0.33	6.91	7.50	PBL	3.4	1.4	0.36
6/3/2009	25988	5B	61.3920	-152.0740	2.41	0.33	7.17	7.89	PBL	3.4	1.4	0.41
6/3/2009	25988	7C	60.6368	-153.0800	1.39	0.32	3.96	4.51	PBL	3.4	1.4	0.27
6/7/2009	26047	2A	60.5909	-152.6110	6.76	0.40	24.78	22.37	PBL	4.9	1.1	0.16
6/7/2009	26047	1B	60.6176	-153.1410	6.00	0.40	23.30	21.03	PBL	4.9	1.1	0.31
6/7/2009	26047	2B	60.5040	-153.0480	5.27	0.40	23.18	21.04	PBL	4.9	1.1	0.21

[a]Optimal pixels contained cloud fractions <0.2, solar zenith angle <50°, and satellite viewing angle <45°.

Table 2.3: Continued

Average Airborne SO_2 CD (DU)	Corrected Airborne SO_2 CD (DU)	Percent Difference Between OMI and Airborne SO_2 CD TRL	Percent Difference Between OMI and Airborne SO_2 CD PBL	Percent Difference Between OMI and Airborne SO_2 CD Selected	Total Column Ozone (DU)	Satellite Viewing Angle (Degrees)	Solar Zenith Angle (Degrees)	Aerosol Index	Cloud Fraction	Minutes Elapsed Between OMI and Airborne Measurements	Optimal Conditions [1]
26.6	18.80	-73.9	150.6	151	494.0	18	49	-1.74	0.00	-44 to -3	Yes
56.9	41.67	-87.0	22.4	22	497.6	18	49	-1.91	0.00	-44 to -3	Yes
46.9	3.23	-79.5	-19.8	-20	338.5	34	45	0.68	0.00	-29 to -6	Yes
34.7	1.95	-87.3	3.5	4	349.3	36	45	1.26	0.00	-29 to -6	Yes
56.3	1.69	-80.4	-13.7	-80.4	355.7	52	42	-0.26	0.00	-51 to -6	No
23.8	1.93	-94.8	-1.6	-94.8	355.8	52	42	-0.26	0.00	-51 to -6	No
78.2	2.38	-93.3	-85.4	-93.3	353.4	55	42	2.70	0.00	-51 to -6	No
41.5	6.55	-87.5	-52.2	-87.5	353.9	55	41	2.72	0.00	-51 to -6	No
23.8	12.26	-59.1	60.8	-59.1	369.9	40	39	1.09	0.19	+20 to +40	Yes
7.3	2.17	-25.0	109.7	110	342.2	57	40	-0.27	0.04	-22 to +78	No
9.9	3.53	-47.4	112.6	113	342.2	60	40	-1.03	0.18	-22 to +78	No
23.4	9.69	-75.1	-18.6	-19	349.7	60	39	-1.09	0.15	-22 to +78	No
13.2	3.50	-60.3	28.9	29	347.9	63	39	-1.30	0.21	-22 to +78	No
14.35	2.27	198.2	887.6	888	344.3	16	38	-1.05	0.00	+69 to +85	Yes
54	16.98	-64.7	23.9	24	342.3	18	38	-1.24	0.00	+69 to +85	Yes
62.75	13.32	-60.4	58.0	58	347.5	18	38	-0.40	0.00	+69 to +85	Yes

Table 2.4: Daily OMI SO_2 masses and emission rates for explosive events.

Events	UTC Date	Time	Daily SO_2 Mass (kt)	Daily M1 SO_2 Emission Rate (t/d)	Hours since last explosion	[1]Qualitative SO_2 Level
1 - 5	3/23/2009	20:40	54.4	71400	8:09	High
6*	3/24/2009	21:22	60.1	84100	17:41	High
	3/25/2009	23:44	0.0	0		Low
7 - 8	3/26/2009	21:10	13.6	27500	3:46	High
9 - 11	3/27/2009	23:31	20.2	18800	6:52	High
12 - 15	3/28/2009	20:58	38.5	75000	11:38	High
16 - 18	3/29/2009	21:41	0.2	1200	18:18	Low
	3/30/2009	00:02	3.2	2900		Moderate
	3/31/2009	21:28	1.5	3000		Moderate
	4/1/2009	22:11	5.0	17700		Moderate
	4/2/2009	21:16	0.0	0		Low
	4/3/2009	21:59	3.8	6400		Moderate
19	4/4/2009	21:04	24.2	26900	7:06	High

[a]Qualitative levels: High≥10 kt; 1<Moderate<10 kt; Low≤1 kt SO_2.

Supplementary Material Table Captions

Table 2.A.1: OMI and corrected airborne measurements comparison evaluation.

Pixel Analysis	Pixel Analysis	Min % Difference	Max % Difference	Average % Difference	Std. Dev. on % Difference	Linear Equation of Fit	R^2
TRL Corrected	16 Pixel	-47	198	-55	70	$y = 0.14x + 1.43$	0.38
PBL	16 Pixel	-2	888	79	214	$y = 1.32x + 1.91$	0.75
Selected	16 Pixel	-2	888	59	116	$y = 1.31x + 0.78$	0.71
TRL Corrected	Optimal	-59	198.2	-39	97	$y = 0.08x + 3.18$	0.19
PBL	Optimal	4	888	148	303	$y = 1.14x + 7.56$	0.70
Selected	Optimal	4	888	132	309	$y = 1.16x + 5.46$	0.64

Table 2.A.2: Airborne and OMI-derived SO_2 emission rates comparison evaluation.

Method	Min % Difference	Max % Difference	Average % Difference	Std. Dev. of % Difference	Linear Equation of Fit †	R^2
Method 1	-10	-74	-28	23	$y = 0.587x + 722$	0.82
Method 2	7	-64	-34	26	$y = 0.1714x + 3336.2$	0.34
Method 3	6	-80	-40	45	$y = -0.0305\ x + 2432$	0.01

†where *y* represents the OMI calculated emission rate (t/d) (*Methods 1, 2* and *3*) and *x* represents the airborne emission rate (t/d) measurements.

References Cited:

Andres, R.J., Rose, W.I., Stoiber, R.E., Williams, S.N., Matias, O. and Morales, R., 1993. A summary of sulfur dioxide emission rate measurements from Guatemalan volcanoes. Bulletin of Volcanology, 55: 379-388. doi:10.1007/BF00301150.

Blake, S., 2003. Correlations between eruption magnitude, SO_2 yield, and surface cooling. In: C. Oppenheimer, D. Pyle and J. Barclay (Editors), Volcanic Degassing. Geological Society, London, pp. 371-380.

Bleick, H., Coombs, M., Bull, K.F. and Wessels, R., 2012. Volcano-ice interactions during the precursory phase of unrest preceding the 2009 eruption of Redoubt Volcano, Alaska. Journal of Volcanology and Geothermal Research, Special Issue on the 2009 Redoubt Eruption. doi:10.1016/j.volgeores.2012.10.008.

Bluth, G. and Carn, S., 2008. Exceptional sulfur degassing from Nyamuragira volcano, 1979-2005. International Journal of Remote Sensing, 29(22): 6667-6685.

Bluth, G.J.S., Schnetzler, C.C., Krueger, A.J. and Walter, L.S., 1993. The contribution of explosive volcanism to global atmospheric sulphur dioxide concentrations. Nature, 366(NA): 327-329. doi:10.1080/01431160802168434.

Bull, K.F. and Buurman, H., 2012. An overview of the 2009 eruption of Redoubt Volcano, Alaska. Journal of Volcanology and Geothermal Research, Special Issue on the 2009 Redoubt Eruption. doi:10.1016/j.volgeores.2012.06.024.

Buurman, H., West, M. and Thompson, G., 2012. Seismicity chronology of the 2009 Redoubt eruption. Journal of Volcanology and Geothermal Research, Special Issue on the 2009 Redoubt Eruption. doi:10.1016/j.volgeores.2012.04.024.

Carn, S., 2011. OMIplot Software. http://vhub.org/resources/682.

Carn, S.A. and Lopez, T.M., 2011. Opportunistic validation of sulfur dioxide in the Sarychev Peak volcanic eruption cloud. Atmos. Meas. Tech., 4: 1705-1712. doi:10.5194/amt-4-1705-2011.

Carn, S.A., Strow, L.L., de Souza-Machado, S., Edmonds, Y. and Hannon, S., 2005. Quantifying tropospheric volcanic emissions with AIRS: The 2002 eruption of Mt. Etna (Italy). Geophys. Res. Lett., 32(2): L02301. doi:10.1029/2004gl021034.

Carn, S., Krueger, A., Krotkov, N., Yang, K. and Levelt, P., 2007. Sulfur dioxide emissions from Peruvian copper smelters detected by the Ozone Monitoring Instrument. Geophysical Research Letters, 34: L09801.

Carn, S.A., Krueger, A.J., Arellano, S., Krotkov, N.A. and Yang, K., 2008. Daily monitoring of Ecuadorian volcanic degassing from space. Journal of Volcanology and Geothermal Research, 176: 141-150. doi:10.1016/j.jvolgeores.2008.01.029.

Carn, S., Krueger, A., Krotkov, N., Yang, K. and Evans, K., 2009. Tracking volcanic sulfur dioxide clouds for aviation hazard mitigation. Natural Hazards, 51(2).

Carn, S.A., Froyd, K.D., Anderson, B.E., Wennberg, P., Crounse, J., Spencer, K., Dibb, J.E., Krotkov, N.A., Browell, E.V., Hair, J.W., Diskin, G., Sachse, G. and Vay, S.A., 2011. In situ measurements of tropospheric volcanic plumes in Ecuador and Colombia during TC^4. Journal of Geophysical Research - Atmosphere, 116.

Casadevall, T., Doukas, M., Neal, C., McGimsey, G. and Gardner, C., 1994. Emision rates of sulfur dioxide and carbon dioxide from Redoubt Volcano, Alaska during the 1989-1990 eruptions. Journal of Volcanology and Geothermal Research, 62: 519-530. doi:10.1016/0377-0273(94)90050-7.

Coombs, M., Sisson, T., Bleick, H., Henton, S., Nye, C., Payne, A., Cameron, C., Larsen, J., Wallace, K. and Bull, K.F., in press. Andesites of the 2009 eruption of Redoubt Volcano, Alaska. Journal of Volcanology and Geothermal Research, Special Issue on the 2009 Redoubt Eruption.

Daag, A., Tubianosa, B., Newhall, C., Tungol, N., Javier, D., Dolan, M., Delos-Reyese, P., Arboleda, R., Martinez, M. and Regalado, T. (Editors), 1996. Monitoring dulfur dioxide emissions at Mount Pinatubo. University of Washington, Seattle.

Dalton, M., Waite, G., Watson, I. and Nadeau, P., 2010. Multiparameter quantification of gas release during weak Strombolian eruptions at Pacaya Volcano, Guatemala. Geophysical Research Letters, 37: L09303. doi:10.0129/2010g1042617.

Diefenbach, A.K., Bull, K.F., Wessels, R.L. and McGimsey, G., 2011. Photogrammetric monitoring of lava dome growth during the 2009 eruption of Redoubt Volcano. Journal of Volcanology and Geothermal Research, Special Issue on the 2009 Redoubt Eruption. doi:10.1016/j.volgeores.2011.12.009.

Doukas, M., 1995. A compilation of sulfur dioxide and carbon dioxide emissions-rate data from Cook Inlet volcanoes (Redoubt, Spurr, Iliamna, and Augustine), Alaska during the period from 1990 - 1994, U.S. Geological Survey.

Doukas, M., 2002. A new method for GPS-based wind speed determineations during airborne volcanic plume measurements, U.S. Geological Survey, Open-File Report 02-395.

Doukas, M. and Gerlach, T., 1995. Sulfur dioxide scrubbing during the 1992 eruption of Crater Peak, Spurr Volcano, Alaska. In: T. Keith (Editor), The 1992 Eruption of Crater Peak Vent, Mount Spurr Volcano, Alaska. U.S. Geological Survey Bulletin 2139, Washington, pp. pp. 47-57.

Doukas, M. and McGee, K., 2007. A compilation of gas emission-rate data from volcanoes of Cook Inlet (Spurr, Crater Peak, Redoubt, Illiamna, and Augustine) and Alaska Peninsula (Douglas, Fourpeaked, Griggs, Mageik, Martin, Peulik, Ukinrek Maars, and Veniaminof), Alaska, from 1995 - 2006. U.S. Geological Survey Open File Report 07-1400.

Edmonds, M., Oppenheimer, C., Pyle, D., Herd, R. and Thompson, G., 2003. SO_2 emissions from Soufriere Hills Volcano and their relationship to conduit permeability, hydrothermal interaction and degassing regime. Journal of Volcanology and Geothermal Research, 124: 23-43.

Fee, D., Garces, M. and Steffke, A., 2010. Infrasound from Tungurahua Volcano 2006 - 2008: Strombolian to Plinian eruptive activity. Journal of Volcanology and Geothermal Research, 193: 67-81. 10.1016/j.jvolgeores.2010.03.006.

Fee, D., McNutt, S., Lopez, T., Arnoult, K., Szuberla, C. and Olson, J., 2011. Combining local and remote infrasound recordings from the 2009 Redoubt Volcano eruption. Journal of Volcanology and Geothermal Research, Special Issue on the 2009 Redoubt Eruption doi:10.1016/j.volgeores.2011.09.012.

Fischer, T., Arehart, G., Sturchio, N. and Williams, S., 1996. The relationship between fumarole gas composition and eruptive activity at Galeras Volcano, Colombia. Geology, 24(6): 531 - 534..

Gerlach, T., 2003. Elevation effects in volcano applications of the COSPEC. In: C. Oppenheimer, D. Pyle and J. Barclay (Editors), Volcanic Degassing. The Geological Society of London, London, pp. 169-175.

Gerlach, T., Delgado, H., McGee, K., Doukas, M., Venegas, J. and Cardenas, L., 1997. Application of the LI-COR CO_2 analyzer to volcanic plumes: A case study, volcan Popocateptetl, Mexico, June 7 and 10, 1995. Journal of Geophysical Research, 102(B4): 8005-8019. doi:10.1029/96JB03887.

Grapenthin, R., Freymueller, J.T. and Kaufman, A.M., 2012. Geodetic observations during the 2009 eruption of Redoubt Volcano, Alaska. Journal of Volcanolgoy and Geothermal Research, Special Issue on the 2009 Redoubt Eruption. doi:10.1016/j.volgeores.2012.04.021.

Hayes, M., 1996. Statistical Digital Signal Processing and Modeling. John Wiley & Sons.

Hobbs, P., Radke, L., Lyons, J., Ferek, R., Coffman, D. and Casadevall, T., 1991. Airborne measurements of particle and gas emissions from the 1990 volcanic eruption of Mount Redoubt. Journal of Geophysical Research, 96(D10): 18,735-718,752.

Kelly, P.J., Kern, C., Lopez, T., Werner, C., Roberts, T.J. and Aiuppa, A., 2012. Rapid chemical evolution of tropspheric volcanic emissions from Redoubt Volcano, Alaska, based on observations of ozone and halogen-containing trace gases. Journal of Volcanology and Geothermal Research, Special Issue on the 2009 Redoubt Eruption. doi:10.1016/j.volgeores.2012.04.023.

Kern, C., Deutschmann, T., Vogel, L., Wohrbach, M., Wagner, T. and Platt, U., 2010. Radiative transfer corrections for accurate spectroscopic measurements of volcanic gas emissions. Bulletin of Volcanology, 72: 233-247. doi:10.1007/s00445-009-0313-7.

Krotkov, N., Carn, S., Krueger, A., Bhartia, P. and Yang, K., 2006. Band residual difference algorithm for retrieval of SO_2 from the Aura Ozone Monitoring Instrument. IEEE Transactions on geoscience and remote sensing, 44(5): 1259-1266. doi:10.1109TGRS.2005.861932.

Krotkov, N., McClure, B., Dickerson, R., Carn, S., Li, C., Bhartia, P., Yang, K., Krueger, A., Li, Z., Levelt, P., Chen, H., Wang, P. and Lu, D., 2008. Validation of SO_2 retreivals from the Ozone Monitoring Instrument over NE China. Journal of Geophysical Research, 113. doi:10.1029/2007JD008818.

Kurosu, T. and Celarier, E., 2010. OMPIXCOR Readme File.

Levelt, P.F., Hilsenrath, E., Leppelmeier, G.W., van den Oord, G.H.J., Bhartia, P.K., Tamminen, J., de Haan, J.F. and Veefkind, J.P., 2006. Science objectives of the ozone monitoring instrument. Geoscience and Remote Sensing, IEEE Transactions on, 44(5): 1199-1208. doi:10.1109/TGRS.2006.872336.

McGee, K., Doukas, M., McGimsey, G., Neal, C. and Wessels, R., 2010. Emission of SO_2, CO_2, and H_2S from Augustine Volcano, 2002–2008. In: J. Power, M. Coombs and J. Freymueller (Editors), The 2006 Eruption of Augustine Volcano, Alaska. U.S. Geological Survey, pp. 609-627.

Neal, C.A., Murray, T.L., Power, J.A., Adleman, J.N., Whitmore, P.M. and Osiensky, J.M., 2010. Hazard information management, interagency coordination, and impacts of the 2005 - 2006 eruption of Augustine volcano. In: J.A. Power, M.L. Coombs and J.T. Freymueller (Editors), The 2006 Eruption of Augustine Volcano, Alaska. U.S. Geological Survey, pp. 645 - 667.

Oppenheimer, C., Francis, P. and Stix, J., 1998. Depletion rates of sulfur dioxide in tropospheric volcanic plumes. Geophysical Research Letters, 25(14): 2671 - 2674. doi:10.1029/98GL01988.

Pfeffer, M., Langmann, B. and Graf, H.-F., 2006. Atmospheric transport and deposition of Indonesian volcanic emissions. Atmospheric Chemistry and Physics, 6: 2525-2537.

Platt, U. and Stutz, J., 2008. Differential Optical Absorption Spectroscopy Principles and Applications. Springer-Verlag, Berlin - Heidelberg.

Prata, A., 1990. Travelling waves in Nimbus-7 SBUV ozone measurements: Observations and theory. Q.J.R. Meteorol. Soc., 116(NA): 1091-1122. doi:10.1002/qj.49711649505.

Prata, A. and Bernardo, C., 2007. Retrieval of volcanic SO_2 column abundance from Atmospheric Infrared Sounder data. Journal of Geophysical Research, 112: D20204.

Rodriguez, L., Watson, I., Edmonds, M., Ryan, G., Hards, V., Oppenheimer, C. and Bluth, G., 2008. SO_2 loss rates in the plume emitted by Soufriere Hills volcano, Montserrat. Journal of Volcanology and Geothermal Research, 173: 135-147. doi:10.1016/j.jvolgeores.2008.01.003.

Rybin, A., Chibisova, M., Webley, P., Steesen, T., Izbekov, P., Neal, C. and Realmuto, V., 2011. Satellite and ground observations of the June 2009 eruption of Sarychev Peak volcano, Matua Island, Central Kuriles. Bull Volcanol. doi:10.1007/s00445-011-0481-0.

Schaefer, J., Cameron, C. and Nye, C., 2009. Historically active volcanoes of Alaska, Miscellaneous Publication. Alaska Division of Geological and Geophysical Surveys.

Schaefer, J., Bull, K.F., Cameron, C., Coombs, M., Diefenbach, A.K., Lopez, T., McNutt, S., Neal, C., Payne, A., Power, J., Schneider, D., Scott, W., Snedigar, S., Thompson, G., Wallace, K., Waythomas, C., Webley, P. and Werner, C., 2012. The 2009 eruption of Redoubt Volcano, Alaska. Alaska Division of Geological and Geophysical Surveys Report of Investigations, 2011-5: 45.

Schneider, D. and Hoblitt, R., 2012. Doppler weather radar observations of the 2009 eruption of Redoubt Volcano, Alaska. Journal of Volcanology and Geothermal Research, Special Issue on the 2009 Rredoubt Eruption. doi:10.1016/j.volgeores.2012.11.004.

Schnetzler, C., Doiron, S., Walter, L. and Krueger, A., 1994. Satellite measurement of sulfur dioxide from the Redoubt eruptions of 1989 - 1990. Journal of Volcanology and Geothermal Research, 62: 353-357. doi:10.1016/0377-0273(94)90041-8.

Sottili, G., Martino, S., Palladino, D.M., Paciello, A. and Bozzano, F., 2007. Effects of tidal stresses on volcanic activity at Mount Etna, Italy. Geophysical Research Letters, 34. doi:10.0129/2006GL028190,2007.

Spinei, E., Carn, S., Krotkov, N., Mount, G., Yang, K. and Krueger, A., 2010. Validation of ozone monitoring instrument SO_2 measurements in the Okmok volcanic cloud over PUllman, WA, July 2008. Journal of Geophysical Research, 115. doi:10.1029/2009JDO13492,2010.

Stoiber, R., Malinconico, L. and Williams, S., 1983. The use of correlation spectrometers at volcanoes. In: H. Tazieff and J. Sabroux (Editors), Forecasting Volcanic Events. El Sevier, Amsterdam - New York, pp. 425-444.

Surono, M., Jousset, P., Pallister, J., Boichu, M., Buongiorno, M., Budisantoso, A., Costa, F., Andreastuti, S., Prata, F., Schneider, D., Clarisse, L., Humaida, H., Sumarti, S., Bignami, C., Griswold, J., Carn, S., Oppenheimer, C. and Lavigne, F., 2012. The 2010 explosive eruption of Java's Merapi volcano - a '100-year' event. Journal of Volcanology and Geothermal Research, 241-242: 121-135.

Sutton, A.J., Elias, T. and Kauahikaua, J., 2003. Lava-Effusion Rates for the Pu'u O'o-Kupaianaha Eruption Derived from SO_2 Emissions and Very Low Frequency Measurements, U.S. Geological Survey, Professional Paper 1676.

Symonds, R.B., Gerlach, T.M. and Reed, M.H., 2001. Magmatic gas scrubbing: implications for volcano monitoring. Journal of Volcanology and Geothermal Research, 108(1-4): 303-341. doi:10.1016/S0377-0273(00)00292-4.

Thomas, H. and Watson, I., 2009. Observations of volcanic emissions from space: current and future perspectives. Nat. Hazards. doi:10.1007/s11069-009-9471-3.

Thomas, H. and Prata, A., 2011. Sulphur dioxide as a volcanic ash proxy during the April-May 2010 eruption of Eyjafjallajokull Volcano, Iceland. Atmospheric Chemistry and Physics, 11: 6871-6880. 10.5194/acp-11-6871-2011.

Thomas, H., Watson, I., Kearney, C., Carn, S. and Murray, S., 2009. A multi-sensor comparison of sulphur dioxide emissions from the 2005 eruption of Sierra Negra volcano, Galapagos Islands. Remote Sensing of the Environment, 113: 1331-1342. doi:10.1016/j.rse.2009.02.019

Wallace, K., Schaefer, J. and Coombs, M., 2012. Character, mass distribution, and origin of tephra-fall deposits from the 2009 eruption of Redoubt Volcano, Alaska. Journal of Volcanology and Geothermal Research, Special Issue on the 2009 Redoubt Eruption. doi:10.1016/j.volgeores.2012.09.015.

Webley, P., Lopez, T., Dean, K., Rinkleff, P., Dehn, J., Cahill, C., Wessels, R., Schneider, D., Ekstrand, A., Bailey, J., Izbekov, P. and Worden, A., 2012. Remote observations of eruptive clouds and surface thermal activity during the 2009 eruption of Redoubt volcano. Journal of Volcanology and Geothermal Research, Special Issue on the 2009 Redoubt Eruption doi:10.1016/j.volgeores.2012.06.023.

Werner, C., Doukas, M. and Kelly, P., 2011. Gas emissions from failed and actual eruptions from Cook Inlet Volcanoes, Alaska, 1989-2006. Bulletin of Volcanology, 73: 155-173. doi:10.0117/s00445-011-0453-4.

Werner, C., Evans, W., Kelly, P., McGimsey, G., Pfeffer, M., Doukas, M. and Neal, C., 2012a. Deep magmatic degassing versus scrubbing: Elevated CO_2 emissions and C/S in the lead-up to the 2009 eruption of Redoubt Volcano, Alaska. Geochemistry Geophysics Geosystems, 13(3): 1-18. doi:10.1029/2011GC003794.

Werner, C., Kelly, P., Doukas, M., Lopez, T., Pfeffer, M., McGimsey, G. and Neal, C., 2012b. Degassing associated with the 2009 eruption of Redout Volcano, Alaska. Journal of Volcanology and Geothermal Research, Special Issue on the 2009 Redoubt Eruption. doi:10.1016/j.jvolgeores.2012.04.012.

Williams-Jones, G., Stix, J. and Nadeau, P., 2008. Using the COSPEC in the Field. In: G. Williams-Jones, J. Stix and C. Hickson (Editors), The COSPEC Cookbook: Making SO_2 Measurements at Active Voclanoes. IAVCEI, pp. 63-119.

Yang, K., Krotkov, N., Krueger, A., Carn, S., Bhartia, P. and Levelt, P., 2007. Retrieval of large volcanic SO_2 columns from the Aura Ozone Monitoring Instrument: Comparison and limitations. Journal of Geophysical Research, 112: D24S43. doi:10.1029/2007JD008825.

CHAPTER 3: Constraints on Magma Processes, Subsurface Conditions, and Total Volatile Flux at Bezymianny Volcano in 2007 – 2010 from Direct and Remote Volcanic Gas Measurements[1]

ABSTRACT

Direct and remote measurements of volcanic gas composition, SO_2 flux, and eruptive SO_2 mass from Bezymianny Volcano were acquired between July 2007 and July 2010. Chemical composition of fumarolic gases, plume SO_2 flux from ground and air-based ultraviolet remote sensing (FLYSPEC), and eruptive SO_2 mass from Ozone Monitoring Instrument (OMI) satellite observations were used along with eruption timing to elucidate magma processes and subsurface conditions, and to constrain total volatile flux. Bezymianny Volcano had five explosive magmatic eruptions between May 2007 and June 2010. The most complete volcanic gas datasets were acquired for the October 2007, December 2009, and May 2010 eruptions. Gas measurements collected prior to the October 2007 eruption have a relatively high ratio of H_2O/CO_2 (81.2), a moderate ratio of CO_2/S (5.47), and a low ratio of S/HCl (0.338), along with moderate SO_2 and CO_2 fluxes of 280 and 980 t/d, respectively, and high H_2O and HCl fluxes of ~45,000 and ~440 t/day, respectively. These results suggest degassing of shallow magma (consistent with observations of lava extrusion) along with potential minor degassing of a deeper magma source. Gas measurements collected prior to the December 2009 eruption are characterized by relatively low H_2O/CO_2 (4.13), moderate CO_2/S (6.84), and high S/HCl (18.7) ratios, along with moderate SO_2 and CO_2 fluxes of ~220 and ~1000 t/d, respectively, and low H_2O and HCl fluxes of ~1700 and ~7 t/d, respectively. These trends are consistent with degassing of a deeper magma source. Fumarole samples collected ~1.5 months following the May 2010 eruption are characterized by high H_2O/CO_2 (63.0), low CO_2/S (0.986), and moderate S/HCl (6.09) ratios. These data are consistent with degassing of a shallow, volatile-rich magma source, likely related to the May eruption. Passive and eruptive SO_2 measurements are used to calculate a total annual SO_2 mass of 109 kt emitted in 2007, with passive emissions comprising ~87–95% of the total. Volatile

[1]López, T., Ushakov, S., Izbekov, P., Tassi, F., Cahill, C., Neill, O., and Werner, C., in press. Constraints on magma processes, subsurface conditions and total volatile flux at Bezymianny Volcano in 2007-2010 from direct and remote volcanic gas measurements, *Journal of Volcanology and Geothermal Research*.

flux for the study period is estimated to range from 1.1 x 10^6 to 18 x 10^6 t/year. Annual CO_2 masses are one to two orders of magnitude larger than can be explained by degassing of dissolved CO_2 within eruptive magma, suggesting that the erupted magma contained a significant quantity of exsolved volatiles sourced either from the eruptive melt or unerupted magma at depth. Variable total volatile fluxes ranging from ~3,000 t/d in 2009 to ~49,000 t/d in 2007 are attributed to variations in the depth of gas exsolution and separation from the melt under open-system degassing conditions. We propose that exsolved volatiles are quickly transported to the surface from ascending magma via permeable flow through a bubble and/or fracture network within the conduit and thus retain their equilibrium composition at the time of segregation from melt. The composition of surface CO_2 and H_2O emissions from 2007 and 2009 are compared with modeled exsolved fluid compositions for a magma body ascending from entrapment depths to estimate depth of fluid exsolution and separation from the melt. We find that at the time of sample collection magma had already begun ascent from the mid-crustal storage region and was located at depths of less than 3.7 km in August 2007, approximately two months prior to the next magmatic eruption, and less than or equal to 4.6 km in July of 2009 approximately five months prior to the next magmatic eruption. These finding suggest that the exsolved gas composition at Bezymianny Volcano may be used to detect magma ascent prior to eruption.

3.1 Geologic Setting and Recent Eruptive Activity

Bezymianny Volcano (55.972°N, 160.595°E, ~2951 m), is one of 12 volcanoes composing the predominantly basaltic Kliuchevskoi Volcanic Group (KVG) (Fedotov and Masurenkov, 1991). It is one of the most active volcanoes in Kamchatka, Russia (Fig. 1) and has erupted on average once or twice per year since 1977 (Bogoyavlenskaya et al., 1991; Braitseva, 1991). Bezymianny Volcano is well known for its 31 March 1956 catastrophic, directed-blast type eruption, which occurred following approximately six months of precursory activity, after ~1000 years of quiescence (Gorshkov, 1959; Braitseva, 1991). Activity since 1956 has been dominated by extrusion of lava domes,

effusion of lava flows, passive degassing, and explosive eruptions associated with the production of lahars, pyroclastic flows, and ash clouds (Bogoyavlenskaya et al., 1991). Eruptive products from Bezymianny Volcano from 1956 through 2010 have ranged from andesite to basaltic-andesite, and have exhibited an overall decrease in SiO_2 content with time from ~60.4 wt.% in 1956 to ~56.8 wt.% in 2010 (Turner et al., in press). Bezymianny Volcano is located on the southern flank of the supposedly extinct Kamen Volcano, and less than 10 km from the highly active Kliuchevskoi Volcano (Figs. 3.1, 3.2), a ~5 km altitude basaltic volcano known for its high rate of magma production (~60 x 10^9 kg/year or ~0.02 km^3/year) (Fedetov et al., 2010). The high magma output of the KVG, located tectonically at the Kamchatka-Aleutian junction, has been proposed to be the result of slab tear of the subducting Pacific Plate to form a "slab window" to mantle asthenosphere (Levin et al., 2002; Davaille and Lees, 2004). Seismic and petrologic models have proposed a shared magma storage region between Bezymianny and Kliuchevskoi Volcanoes at ~25–40 km depth that feeds a separate mid-crustal (~6–20 km depth) storage region (Bogoyavlenskaya et al., 1991; Fedotov et al., 2010; Thelen et al., 2010) where differentiation of Bezymianny magma is thought to occur (Ozerov et al., 1997). More recently, geochemical modeling results suggest that magma is stored in two separate mid-crustal storage regions that are only partially evacuated during eruptions (Turner et al., in press). An additional shallow crustal storage region ~1–1.5 km beneath Bezymianny's crater was proposed for 2007 activity according to seismic data and supported by petrologic data (Thelen et al., 2010; Shcherbakov et al., 2011); though it is not known if this is a long-lived or transient feature. Several recent studies suggest that cyclic magma recharge and/or ascent is occurring at depth beneath Bezymianny Volcano, specifically, (1) pulses of deep (25–35 km) seismicity beneath Bezymianny and Kliuchevskoi Volcanoes (Fig. 3.3), observed in the last ten years with durations of several weeks to several months, have been interpreted to be the result of melt segregation and ascent following eruptive activity (George, 2010); and (2) observations of plagioclase zoning in 2001–2007 eruptive products have been interpreted to indicate frequent recharge of the magma storage region (Shcherbakov et al., 2011).

3.2 Methodology

3.2.1 Direct Fumarole Sampling

Gases were sampled from Bezymianny's dome fumaroles using 300 mL, pre-weighed, evacuated, silica bottles, containing a 4 M KOH and $Cd(CH_3COOH)_2$ solution, in a technique modified from Giggenbach (1975). During sampling, SO_2 dissolves in the caustic solution, while H_2S reacts in solution to form CdS precipitate. Samples were analyzed in the laboratory at the Institute of Volcanology and Seismology, Petropavlovsk-Kamchatsky, Russia. Head-space gases including CH_4, H_2, N_2, O_2, Ar, and CO were analyzed using a gas chromatograph LHM-80 (Kromatograf, Moscow). Liquid and solid phases representing the absorbed gases were analyzed using wet-chemistry and ion chromatography (Gasochrom-3101; Kromatograf, Moscow). First, liquid and solid phases were separated by centrifugation and the liquid phase was split into sample aliquots. The liquid phase representing SO_2 and the solid phase representing H_2S, were oxidized by H_2O_2 to form SO_4^{2-} in solution and were analyzed by ion chromatography. Separate aliquots of the liquid phase were analyzed for CO_2 (as CO_3^{2-}) by acidimetric titration (using 0.1 M HCl), and for HCl (as Cl^-) and HF (as F^-) by ion chromatography. Water was quantified by sample mass difference after subtraction of absorbed gas masses. Analytical uncertainty is <5%.

3.2.2 FLYSPEC SO_2 Flux

Plume SO_2 slant column densities (SCD) were measured using a FLYSPEC ultraviolet (UV) spectrometer system (Horton et al., 2006) in an application of the Lambert-Beer law (Platt and Stutz, 2008). Plume spectra are fit to on-site measurements of low (~500 ppmm) and high (~1300 ppmm) SO_2 calibration cell spectra over the wavelength region of 305–315 nm to quantify absorbance of UV light by plume SO_2. SCD measurements were collected in both traverse mode, where vertical-looking SCD measurements are collected from a helicopter flying below-plume traverses (e.g. Werner et al., 2012), and scanning mode, where measurements are collected from a fixed ground location by scanning through the plume (e.g. Galle et al., 2002; Edmonds et al., 2003a). In both

methods a series of measurements are collected perpendicular to plume direction to acquire an SO_2 SCD plume profile. These measurements are used along with the following equation, modified from Williams-Jones et al. (2008) to calculate SO_2 flux (F_{SO2}) in units of metric tons per day (t/d):

$$(1) \qquad F_{SO_2} = vf \int c(w)dw$$

where v is plume speed (m/s), f is a conversion factor (0.0002302 $t\ s\ ppm^{-1}\ m^{-3}\ d^{-1}$) to units of metric tons per day (t/d), c is SO_2 SCD (ppmm), and w is the plume width (m). Plume speed was calculated using one of two methods. For most scanning measurements simultaneous thermal imagery was collected using a Forward Looking Infrared (FLIR) camera, where known pixel size and distance to plume source were used along with plume parcel tracking methods (Williams-Jones et al., 2008) to calculate plume speed. When thermal imagery data were not available or for measurements collected in traverse mode, wind speed was used as a proxy for plume speed and was modeled for the location of Bezymianny Volcano using the HYSPLIT model (http://ready.arl.noaa.gov/index.php) and GDAS1 (Global Data Assimilation Systems 1) archived data for three hour intervals at elevations ranging from ~2500–3000 m. Modeled wind speeds were interpolated to determine the wind speed for Bezymianny's dome altitude. For helicopter traverse measurements, plume width was determined using integrated GPS position measurements of plume entry and exit with a plume detection threshold of ~10-20 ppmm SO_2 depending on signal/noise at the time of sample collection. For ground-based scanning measurements, plume width was calculated according to basic trigonometry using the scan angles at the position of plume entry and exit and the distance from sample location to plume.

Error estimates for SO_2 flux calculated using a scanning Correlation Spectrometer (COSPEC) in a method similar to the FLYSPEC have been estimated to range from ±13% for optimal conditions to ±42% for poor conditions (Stoiber et al., 1983) with error

in wind speed being the major contributing factor. However, recent research finds that error in SO_2 SCD due to molecular scattering, previously thought to be as low as ±10% (Millan, 1980) could be significantly larger (Mori et al., 2006; Kern et al., 2010). In a sensitivity analysis Kern et al. (2010) highlight the complexities of radiative transfer processes on retrieved SO_2 SCD and determine the error due to individual sampling condition components including distance to plume, vertical versus diagonal geometry, retrieval wavelength region, and plume opacity. For sample conditions typical of our study at Bezymianny Volcano including sample distance ≤ 5km, wavelength region of 305-315 nm, and SO_2 SCD ≤ 400 ppmm, Kern et al. (2010) find error in retrieved SCD due to individual components of ±25% to ± 80% for transparent to translucent plumes, and error up to ±200% for opaque plumes. Lopez et al., (2012) show that modeled wind speeds using the same methods employed here agree with accurate wind circle method wind speeds (Doukas, 2002) to within ±20 to ±110%, while error in wind-speeds (and/or plume rise rates) calculated using the plume-parcel tracking video method are estimated to be ±15 to ±31% (Williams-Jones et al., 2008). We estimate error in plume width for scanning measurements of ±2 to ±5°, equivalent to ±15 to ±24% for a plume at 5 km slant distance. Additionally, changing wind direction (common during the 2009 field campaign), and low signal/noise due to low UV radiation for morning, evening, or cloudy sample conditions would result in higher error in plume width due to poor plume limit definition. Considering the above we calculate total error (square root of sum of squares) due to uncertainties in the independent factors of wind-speed, retrieved SO_2 SCD, and plume width, and find total error of ±33% for optimal conditions, ±88% for moderate conditions, and ±230% for poor conditions. We attempted to exclude measurements collected under poor sample conditions from analysis and therefore assume a total error of ±88%.

3.2.3 OMI Explosive SO_2 Mass

SO_2 masses from explosive eruptions of Bezymianny Volcano, referred to as explosive SO_2 masses, were calculated from satellite measurements by the Ozone Monitoring Instrument (OMI) (Levelt et al., 2006) using operational SO_2 data products (OMSO2 downloaded from: http://mirador.gsfc.nasa.gov/cgi-bin/mirador/collectionlist.pl?keyword=omso2). Masses were calculated using the field of view function within Omiplot software (Carn, 2011) according to the Linear Fit algorithm (Yang et al., 2007). Plume altitudes were estimated by the Kamchatka Volcano Eruption Response Team (KVERT) according to satellite and seismic data. The OMI *a priori* plume center of mass altitude (CMA) product (Krotkov, 2011) that best corresponded with the estimated plume altitude was used to determine eruptive SO_2 mass. Accuracy of OMI SO_2 masses are difficult to determine due to: (1) the inherent sampling differences between satellite (total mass in metric tons) and potential validation measurements (flux in t/d), and (2) the relative paucity of coincident validation measurements. A comparison between airborne COSPEC and nearly coincident OMI measurements at Redoubt Volcano, Alaska, found that OMI SO_2 fluxes were lower than airborne COSPEC measurements in most cases by 28–40% (Lopez et al., 2012), and therefore it is likely that the resulting OMI eruptive SO_2 masses represent conservative minimum estimates.

3.3 Results

3.3.1 Timeline of Volcanic Activity and Sample Collection

Bezymianny Volcano erupted explosively on five occasions between May 2007 and July 2010 (all dates reported as UTC) (Girina, in press): 11 May 2007, 14-15 October 2007, 19 August 2008, 16 December 2009, and 31 May 2010 (Fig. 3.4). Additionally, analysis of seismic data suggests that a small eruption (likely from a very shallow source) occurred on 25 September 2007, and a partial-dome collapse event occurred on 5 November 2007 (Thelen et al., 2010). From 2007 through 2010 four field campaigns were conducted at Bezymianny Volcano in which SO_2 flux and/or fumarole composition

were measured. Both fumarole composition and SO_2 flux were measured during field campaigns in August 2007 and July 2009, SO_2 flux (only) was measured in August 2008, and fumarole composition (only) was measured in 2010. OMI imagery captured explosive SO_2 masses from Bezymianny Volcano associated with the 14–15 October 2007 and 31 May 2010 eruptions. A summary of the eruptive activity and gas sampling timeline is presented in Figure 3.4.

3.3.2 Fumarole Composition

The composition of major and trace gases sampled directly from Bezymianny fumaroles in 2007, 2009, and 2010 in mmol/mol are presented in Table 3.1. Ratios of select volcanic gases and dry-gas concentrations are shown in Table 3.2. Dry-gas concentrations represent volcanic gas concentrations normalized to exclude water, in an effort to minimize secondary effects such as boiling of meteoric water and/or condensation of volcanic H_2O prior to sample collection (Giggenbach and Matsuo, 1991). All samples were collected from the same approximate location on Bezymianny's dome (55.9739°N, 160.5927°E, 2830 m; Fig. 3.1). Comparisons among 2007, 2009 and 2010 fumarole concentrations are discussed below, where qualitative descriptors of high, moderate, and low are used to illustrate the differences in gas composition among the three years.

Two dome fumarole samples were collected on 17 August 2007 with outlet temperatures of 301°C. These samples were characterized by high average H_2O and HCl concentrations (966 and 7.00 mmol/mol respectively), moderate CH_4, H_2, and N_2 concentrations (0.000365, 0.133, and 11.8 mmol/mol, respectively), and low H_2S, SO_2, and CO_2 concentrations (0.0130, 2.35, and 12.4 mmol/mol, respectively). These samples appear to be significantly air contaminated, according to the relatively high concentrations of Ar (0.125 mmol/mol) and O_2 (0.193 mmol/mol).

Two dome fumarole samples were collected on 26 July 2009. These samples had the lowest relative outlet temperatures observed with an average value of 235°C. They are notable for their high average CO_2, SO_2, H_2S, H_2, and N_2 concentrations (186, 28.3, 0.771, 0.360, and 25.4 mmol/mol, respectively) and low H_2O and HCl concentrations (757 and 1.59 mmol/mol, respectively). Oxygen and Ar concentrations (0.357 and 0.300 mmol/mol, respectively) are suggestive of significant air contamination.

Only one dome fumarole sample was collected on 22 July 2010. This sample had the highest observed outlet temperature of 313°C and was characterized by relatively high average H_2O (965 mmol/mol), moderate CO_2, SO_2, H_2S, and HCl (15.3, 15.4, 0.145, and 2.55 mmol/mol, respectively), and low CH_4, H_2, and N_2 (2.67×10^{-6}, 3.42×10^{-3}, and 1.50 mmol/mol, respectively). The relatively low Ar (0.0189) mmol/mol) and O_2 (0.0331 mmol/mol) concentrations suggest that air contamination did not significantly affect this sample.

3.3.3 Passive SO_2 Flux

A total of 881 separate SO_2 flux measurements were collected over the three field campaigns, with the significant majority being collected in 2009 (n = 850) when the addition of an automatic scanner for the FLYSPEC enabled scans to be collected more efficiently compared to manually scanned measurements. With the exception of one successful helicopter traverse in 2008, all measurements were collected in scanning mode within ~5 km from the dome (Fig. 3.1). The average calculated SO_2 flux and standard deviation from FLYSPEC measurements for the 2007, 2008 and 2009 field campaigns were 280 ± 130 t/d (n = 10), 140 ± 90 t/d (n = 21), and 220 ± 200 t/d (n = 850), respectively. While average 2008 SO_2 flux values were lower than observed in 2007 and 2009, they fall within one standard deviation of 2007 and 2009 measurements, indicating no significant difference in SO_2 flux among the three years. The standard deviations of the measurements fall within the estimated error bounds, therefore, we cannot distinguish volcano-related variability in these emissions. Plume opacity and cloud cover likely contribute the largest sources of error in SO_2 flux due to multiple scattering and dilution

(Kern et al., 2010). Kern et al. (2010) find that scattering and dilution effects are minimized (to -10%) for both vertical and diagonal measurements of transparent plumes collected within 1 km from the plume. Therefore, we consider a small sample of measurements collected from the crater rim (~1 km from the plume) on 25 July 2009 to be our most accurate measurements of the study period, with an average SO_2 flux of 200 t/d. Good agreement between this value and the average SO_2 flux measured in the 2009 field season of 220 t/d, as well as the similar average SO_2 flux measured among the three years, suggests that the average SO_2 flux values measured during individual field campaigns are fair representations of typical SO_2 emissions.

3.3.4 Explosive SO_2 Mass

SO_2 emissions associated with the October 2007 and May 2010 explosive eruptions of Bezymianny Volcano were detected by the OMI satellite sensor and explosive SO_2 masses were calculated (Fig. 3.4). Contemporaneous SO_2 emissions from Okmok Volcano, Alaska, prevented detection of Bezymianny explosive SO_2 mass for the August 2008 eruption, and poor signal/noise due to low high-latitude winter UV radiation prevented OMI detection of explosive SO_2 mass from Bezymianny Volcano for the December 2009 eruption.

The first explosive eruption at Bezymianny Volcano evaluated in this study occurred on 14 October 2007 (Fig. 3.4). According to KVERT, multiple phases of explosive activity occurred between 14:27 on 14 October and 14:00 on 15 October 2007, with maximum plume altitudes ranging from 7 to 10 km (Girina, in press). An OMI overpass at 01:26 on 15 October detected elevated SO_2 and an SO_2 mass of 1.1 kt was calculated for this image according to the OMSO2 7.5 km CMA data product (Fig. 3.5a). A second OMI image acquired at 16 October 02:09 captured emissions from the second part of the eruption and was used to calculate an SO_2 mass of 4.8 kt (Fig. 3.5b). Good agreement between OMI detected plume location for the image acquisition times and HYSPLIT plume trajectory models for the altitude range estimated for the eruption clouds suggests

that OMI detected unique parcels of eruptive SO_2 on both days and that "double-counting" (i.e. counting residual plume parcels from previous images rather than "new" SO_2) was not a concern for this dataset. Considering that the OMI images were acquired between 11 and 13 hours after the explosive events, it is possible that some SO_2 was lost due to chemical reactions within the plume (Pfeffer et al., 2006; Bluth and Carn, 2008; Rodriguez et al., 2008) resulting in an underestimate of the explosive SO_2 mass. We attempt to correct for this using the following equation from Oppenheimer et al. (1998):

(2) $$M_i = M_f \exp^{k_1(t_f - t_i)}$$

Where M_i is the initial SO_2 mass, M_f is the OMI measured SO_2 mass, K_1 is the SO_2 loss rate constant, t_f is the time of the OMI overpass, and t_i is the time of the eruption. We assume an SO_2 loss rate of 2.8×10^{-6} s^{-1}, which was calculated by Hobbs et al. (1991) for Redoubt Volcano, Alaska, a volcano of similar latitude and climate to Bezymianny Volcano. We find a corrected SO_2 mass emitted during the two day period of explosive activity at Bezymianny Volcano of ~6.6 kt (1.2 + 5.4 kt).

The final explosive eruption of Bezymianny Volcano evaluated in this study occurred approximately six months following the December 2009 eruption on 31 May 2010 (Fig. 3.4) at 12:34 with a second pulse at 17:00 (Girina, in press). OMI detected SO_2 emissions from Bezymianny Volcano approximately 12 hours after the eruption onset at 01:20 on 1 June 2010. We expect that SO_2 from both eruptive pulses was captured in this image. An SO_2 mass was estimated from this image to be ~4.6 kt (Fig. 3.6) according to the 7.5 km CMA OMSO2 data product. Following the methods described above, and assuming an average plume age for the two eruptive pulses of 10.5 hours, we calculate a corrected SO_2 mass for the two eruptive pulses of 5.1 kt. Additionally, OMI detected elevated SO_2 emissions from central Kamchatka in the months preceding and following this eruption. It is possible that these elevated SO_2 emissions could be associated with pre- or post-explosive effusive activity at Bezymianny Volcano, however we cannot be certain of this

as nearby Kliuchevskoi Volcano (Figs. 3.1, 3.2) was also active at this time, producing Strombolian eruptions and ash and gas plumes (Girina, 2012). Therefore we estimate the total SO_2 mass associated with the 31 May 2010 explosive eruption to be ~5.1 kt, but caution that elevated SO_2 emissions from Bezymianny Volcano may not be fully captured in our 2010 analysis due to simultaneous activity at Kliuchevskoi Volcano.

3.4 Discussion

3.4.1 Comparison of Eruptive and Passive Degassing

Assuming that the SO_2 flux values measured during field campaigns are representative of typical passive degassing for the remainder of the year, we calculate a total annual SO_2 mass emitted from Bezymianny Volcano and determine proportions of passive and eruptive emissions. We consider the time period from July 2007 through July 2008, during which only one minor to moderate-sized explosive eruption occurred and we have both passive and explosive SO_2 measurements. SO_2 was detected by OMI on two days following explosive activity with a total explosive SO_2 mass of 6.6 kt. We assume passive degassing emissions of the average value measured during the 2007 field campaign of 280 t/d SO_2 persisted throughout the year producing an annual passive SO_2 mass of ~102 kt and calculate a total annual volatile mass (passive and explosive) of ~109 kt (Table 3.3). According to these assumptions we estimate that only ~6% of total SO_2 emissions from Bezymianny Volcano are emitted during explosive eruptions for years with minor to moderate sized eruptions. Acknowledging the limitations in our measurements, we can further refine this estimation. A recent comparison between OMI and airborne SO_2 flux at Redoubt Volcano, Alaska, found that OMI underestimated SO_2 flux relative to airborne measurements by 28–40% (Lopez et al., 2012). Assuming that OMI underestimates eruptive mass in a similar manner, we calculate a range of corrected explosive SO_2 masses for the October 2007 eruption of 8400 to 9200 t. These corrected values increase the percent explosive degassing to 7–8%. If we further acknowledge that the average passive SO_2 flux may not be representative of the entire sample period, and calculate annual passive emissions using one standard deviation above and below the

average (400 and 150 t/d SO_2, respectively) along with the minimum and maximum explosive SO_2 mass estimates, we find a range of explosive SO_2 of 5% to 13%. We conclude that passive degassing is the primary degassing mechanism at Bezymianny Volcano comprising between 87 and 95% of total emissions in years with minor to moderate explosive eruptions. These findings are in fairly good agreement with studies conducted at other arc volcanoes with similar eruptive styles such as Soufriere Hills Volcano, Montserrat, and Redoubt Volcano, Alaska, that find between 91-94% (Edmonds et al., 2001) and ~67% (Werner et al., 2012), respectively, of emissions to be released passively.

3.4.2 Total Volatile Flux

Flux for individual major volatile species and total volatiles (both $F_{volatiles}$ in the equation below) were calculated for 2007 and 2009 using the average measured SO_2 flux (F_{SO2}) and fumarole composition according to the following equation:

$$F_{volatiles} = F_{SO_2}\left(\frac{M_{volatiles} \times X_{volatiles}}{M_{SO_2} \times X_{SO_2}}\right) \quad (3)$$

where M_{SO2} is the molecular weight of SO_2 (64 g/Mol), X_{SO2} is the average mole percent of SO_2 in the fumarole samples, $M_{volatiles}$ is the total molecular weight of the measured individual volatile species, or the weighted average molecular weight calculated for major species for the total volatile calculation, and $X_{volatiles}$ is the average mole percent for either the major volatile species or total volatiles (100%). This equation assumes that all measured gases are magmatic in origin and that measurements collected during the field campaigns are representative of typical emissions. The results of these calculations find a high total volatile flux in 2007 of ~49,000 t/d and a low total volatile flux of ~3,000 t/d in 2009 (Table 3.3). 2007 was the only year in which gas composition, passive SO_2 flux, and eruptive SO_2 mass were all measured, enabling the most complete total volatile flux to be calculated. The total volatile flux from 2009 was based only on passive emissions

and is therefore considered an underestimate. As described in detail in Section 3.4.3.4, we expect that the large variation in total volatile flux between these years could be due to differences in the depth of gas exsolution and degassing from magma at the time of sample collection. In this case, we assume that the observed 2007 and 2009 total volatile fluxes approximate annual maximum and minimum values and calculate a range in total annual volatile mass of 1.1 x 10^6 to 18 x 10^6 t/year for Bezymianny Volcano (Table 3). This range of values encompasses values estimated for other persistently degassing volcanoes such as Mount Etna Volcano, Italy (~7.67 x 10^6 t/year) (Aiuppa et al., 2008), and Masaya Volcano, Nicaragua (~5.11 x 10^6 t/year) (Martin et al., 2010).

3.4.3 Subsurface Processes Affecting Gas Composition and Flux

The surface composition of volcanic gases can be affected by several deep and shallow processes that may complicate interpretation of geochemical signatures. Deep processes that control volcanic gas composition include the exsolution of volatiles; which is a function of temperature, pressure, magma composition, and redox conditions at depth; and the separation of volatiles from the melt. Shallow processes include cooling and reequilibration of the exsolved gases, interaction with hydrothermal and/or shallow water systems, reactions with wall-rock minerals, and contamination by air and/or air saturated water (Giggenbach, 1996). In the following sections we will aim to constrain the various processes influencing the Bezymianny gas samples and, when possible, to use the geochemical signatures of the volcanic gas emissions to reveal subsurface conditions and magma processes.

3.4.3.1 Chemical Signatures of Air Contamination

Bezymianny fumarole samples for 2007, 2009, and 2010 exhibit geochemical trends consistent with air contamination. Specifically, samples contain average N_2/Ar of 94.4, 84.5, and 79.4, respectively, values similar to that of air (84.5). These ratios are lower than expected for arc volcanoes that typically have high N_2/Ar ratios due to contributions of nitrogen originating from subducted slab sediments (Giggenbach, 1996). These low N_2/Ar ratios combined with relatively high concentrations of O_2, an atmospheric

component that is rapidly consumed during underground fluid circulation and thus should not be present in volcanic gases, confirm that the Bezymianny fumarole samples are affected by significant air contamination, particularly in 2007 and 2009. The highly porous character of many volcanic domes facilitates interactions between volcanic gases and ambient air, such that air contamination of dome fumarole samples is expected. Atmospheric O_2 can react with reduced volcanic gases to modify their absolute concentrations measured at the surface (Giggenbach, 1987); therefore interpretations of redox conditions should be done with care. Considering total S, instead of SO_2 and/or H_2S, can allow trends in gas composition involving S species to be interpreted without concern for air contamination.

3.4.3.2 Chemical Signatures of Dilution or Scrubbing by Subsurface Water

Interaction between magmatic gases and subsurface waters, including shallow meteoric water and/or a well-developed hydrothermal system, can modify the original magmatic gas composition. Specifically, boiling of meteoric water can provide an additional source of water vapor and bias the surface emissions to higher water content (Chiodini and Marini, 1998). Additionally, upon interaction with subsurface water, the highly water-soluble magmatic gas species such as SO_2 and HCl (for pH > 1) can be removed from the gas phase in a process known as scrubbing (Symonds et al., 2001). The impact of these factors will strongly depend on the volume of water in the subsurface relative to the volume of magmatic gases (e.g. Vaselli et al., 2003; Capaccioni et al., 2007; Werner et al., 2008), and the temperature and pH of the system at depth (Symonds et al., 2001). The proportions of magmatic versus meteoric water can be distinguished within volcanic gas samples through isotopic analysis of gas condensates (Giggenbach, 1992); unfortunately these samples were not collected in our study and we therefore cannot accurately constrain the influence of meteoric and/or hydrothermal waters on our samples. The high level of magmatic activity that occurs at Bezymianny, likely prevents significant hydrothermal systems from developing. Moderate SO_2 fluxes and moderate fumarole concentrations of SO_2 and HCl were observed during all field campaigns suggesting that

scrubbing of water soluble species is not occurring. Furthermore, observation of SO_2/total S ratios were consistently between ~97 and 100% for all three years sampled, which would not be expected if hydrothermal scrubbing were occurring due to the lower water solubility of H_2S relative to SO_2. These lines of evidence suggest that a well-developed hydrothermal system is not present at depth beneath Bezymianny Volcano.

3.4.3.3 Additional Secondary Processes Affecting Surface Emissions

Following exsolution and separation from the melt, volcanic volatiles that are quickly transported to the surface will retain their composition at depth, while volatiles that are transported slowly will re-equilibrate with their surroundings (including melt, wall-rock, hydrothermal fluids) and will reflect a modified composition. The equilibrium relationships among volatile species within the SO_2-H_2S and CO_2-CO-CH_4 systems can be used to constrain equilibrium temperature and redox conditions at depth, in the absence of secondary shallow processes and/or sampling artifacts. In addition to the previously mentioned air contamination (Section 3.4.1.1), condensation of elemental sulfur (Eq. 4) is favored at low temperature, depletes H_2S twice as efficiently as SO_2, and could have modified the SO_2/total S ratio from depth (Giggenbach, 1987):

(4) $SO_2 + 2H_2S = 3S + 2H_2O$

Evaluation of CO-CO_2 equilibria is hindered by incomplete analysis of CO, as this species dissolves in the strongly alkaline sampling solution to form formate and formic acids (Giggenbach and Matsuo, 1991). Considering the above, we focus our evaluation and interpretations on the relative volcanic gas composition and fluxes, and consider total dry-gas concentrations (e.g. total S) when appropriate, to minimize secondary effects and allow changes in this system over the course of the study period to be evaluated.

3.4.3.4 Volatile Exsolution, Separation from the Melt, and Degassing

Solubility trends of magmatic volatiles within an ascending magma show that CO_2 and to a lesser extent SO_2 will exsolve at greater depth than more soluble species, such as HCl, HF, and H_2O (e.g. Gerlach, 1986; Delmelle and Stix, 2000; Aiuppa et al., 2007; Burton et al., 2007). If the volcano exhibits open-system degassing behavior, where exsolved gases are able to separate from the melt and then ascend through the magma to degas at the surface, it may be possible to use the ratios of relatively insoluble to soluble gas species from surface measurements to determine the relative depths of gas exsolution and separation from the melt, in the absence of secondary affects (e.g. Burton et al., 2007; Edmonds and Gerlach, 2007; Aiuppa et al., 2009). According to the relatively high CO_2 emissions observed in both 2007 and 2009, and the ubiquitous gas plume observed (Fig. 3.2) it is likely that Bezymianny Volcano is dominated by open-system degassing behavior. Considering the solubility trends described above for an open-system degassing volcano and assuming that secondary effects are minimal, we would expect the ratios of CO_2/H_2O, CO_2/S, S/HCl, and CO_2/HCl to increase with recharge by a relatively deep, volatile-rich magma and then to decrease as the magma becomes increasingly more shallow and degassed. We evaluate the gas composition and total volatile fluxes from Bezymianny Volcano in the context of these solubility trends and possible secondary affects, to elucidate magma degassing processes.

The composition of 2007 Bezymianny fumaroles is characterized by relatively high H_2O/CO_2, and low CO_2/H_2O, S/HCl, and CO_2/HCl ratios, suggesting that those fumaroles were fed by a relatively shallow and degassed magma source (Table 3.2). The moderate CO_2/S value of ~5.5 is higher than exhibited at many Alaskan and Kamchatkan volcanoes experiencing background activity levels (~1-2) (Werner et al., 2011; Aiuppa et al., 2012), suggesting that in addition to degassing of relatively shallow magma in the upper conduit, there may also have been an additional minor quantity of deeper magma degassing at the time of sample collection. Because Bezymianny Volcano exhibits open-system degassing behavior and attained a CO_2/S of ~1 less than two months following eruption in 2010, we

expect that Bezymianny emissions quickly return to background levels in the absence of new degassing magma. In 2009, fumaroles show relatively low H_2O/CO_2, high CO_2/HCl and S/HCl ratios, and moderate total S and CO_2/S (Table 3.2). These compositional changes support the ascent of hot volatile-rich magma from depth. In 2010 the H_2O/CO_2 ratio is similar to that of 2007 and the CO_2/S ratio is the lowest observed, suggestive of a shallow degassing magma source. The S/HCl and CO_2/HCl ratios are intermediate with respect to those measured in 2007 and 2009, suggesting that the 2010 magma was: (1) shallower than observed in 2009, and/or (2) less degassed than was observed in 2007 (Table 3.2). This appears reasonable, as the 2010 fumarole sample was collected only one and a half months following the previous eruption (compared to three months in 2007) and it is expected that these ratios will decrease over time with further degassing.

Similar average SO_2 and CO_2 flux values along with greater than an order of magnitude decreases in H_2O, HCl and total volatile flux were observed from 2007 to 2009 (Table 3.3). The decrease in total volatile flux is due primarily to a significant decrease in fumarole H_2O concentration in 2009 compared to 2007 (Table 3.1), while SO_2 and CO_2 fluxes remained largely unchanged. We have assumed in our calculations that the fumarolic H_2O is magmatic in origin. If in fact a significant portion of the measured H_2O was non-magmatic in origin (e.g. meteoric), the calculated total H_2O flux and resultant total volatile flux will be overestimated. In their multi-year study at Soufriere Hills Volcano, Montserrat, a volcano of similar composition and eruptive behavior to Bezymianny, Edmonds et al., (2001) find that HCl is a reliable indicator of shallow magma, such that HCl fluxes <100 t/d indicate the absence of shallow magma, while HCl fluxes >100-200 t/d indicate the presence of shallow magma. Assuming that this indicator can be applied at Bezymianny Volcano, then the observed HCl flux of ~440 t/d in 2007 supports degassing of shallow magma, while the HCl flux of ~7 t/d in 2009 supports the absence of shallow magma. While we cannot rule out the possibility that boiling of meteoric water is contributing to high total volatile emissions in 2007, we think that

much of the variations in H_2O flux between 2007 and 2009 can be attributed to variations in the depth of volatile exsolution and separation from the melt.

3.4.4 Comparison with Mutnovsky Volcano's Volatile Emissions

The variations in fumarole composition for the major volatiles sampled from Bezymianny Volcano in 2007, 2009, and 2010 are presented in Figure 3.7, in comparison with fumaroles sampled from Mutnovsky Volcano. Mutnovsky is an active volcano in southern Kamchatka with a range in eruptive products from basalt to rhyodacite, with its most recent magmatic eruption in 1848 having basaltic eruptive products (Zelenski and Taran, 2011). Fumarole samples from Mutnovsky Volcano have been evaluated based on sample location, with three groups specified including: Active Funnel (AF), Upper Field (UF), and Bottom Field (BF), which have been interpreted to be sourced from convecting magma, hydrothermal fluids, and shallow degassed magma, respectively (Taran et al., 1992; Zelenski and Taran, 2011). We compare the average composition of fumarole gases from Bezymianny and Mutnovsky Volcanoes and use the similarities and differences observed to help further constrain our interpretations at Bezymianny Volcano (Fig. 3.7).

We have interpreted the Bezymianny 2007 fumarole samples to be sourced from a shallow degassed magma, and therefore would expect similar compositional trends between these fumaroles and the Mutnovsky BF fumaroles. We find that the compositional trends exhibited by Bezymianny 2007 and Mutnovsky BF fumaroles plot quite similar on CO_2-S_t-HCl and CO_2-H_2O-S_t ternary diagrams (Figs. 3.7a, b) supporting a shallow degassed magma source in both cases.

The Bezymianny 2009 fumarole samples have much lower H_2O/CO_2 and much higher CO_2/S and dry-gas CO_2 than the Mutnovsky AF fumaroles interpreted to be sourced from convecting magma (Fig. 3.7b); (Zelenski and Taran, 2011). This suggests that the magma source for the Bezymianny 2009 fumaroles may have been deeper than that of the magma

supplying gases to the Mutnovsky AF fumaroles (assuming other conditions are similar). The Bezymianny 2009 fumaroles plot similarly to the hydrothermally-sourced Mutnovsky UF fumaroles in Figure 3.7a though a hydrothermal source for the Bezymianny 2009 fumaroles was disputed above. This apparent discrepancy is due to the fact that fumaroles sourced from both deep magma and hydrothermal systems can exhibit high CO_2 concentrations relative to SO_2 and HCl (e.g. Giggenbach et al., 1990; Burton et al., 2007). These similar trends can be explained by: (1) the lower magma solubility of CO_2 relative to SO_2 and HCl, allowing CO_2-rich gases to preferentially exsolve from deep magma; and (2) depletion of SO_2 and HCl relative to CO_2 in hydrothermal environments due the high water solubilities of these species. A significant difference in gas composition between Bezymianny 2009 and Mutnovsky UF fumaroles can be seen in the CO_2-H_2O-S_t ternary diagram (Fig. 3.7b) and highlights the importance of considering multiple gas species in order to accurately interpret the source and secondary effects influencing gas composition. The Bezymianny 2010 sample has a highly similar composition as Mutnovsky AF fumaroles (Figs. 3.7a, b) supporting a shallow and volatile-rich magma source for the 2010 Bezymianny samples.

3.4.5 Model Constraints on Magma Degassing

In the following sections we use a combination of the composition and flux of surface gas emissions, dissolved volatiles within melt inclusions, and the VolatileCalc solubility model to: (1) estimate melt entrapment depths, (2) identify degassing of excess volatiles, (3) estimate the depth of gas separation from the melt, and (4) propose a model to explain magma degassing at Bezymianny Volcano.

3.4.5.1 Constraints on Magma Storage Depths

Melt entrapment depths, estimated from volatile concentrations within melt inclusions, can be used to estimate magma storage depths if we assume that the melt is both trapped during storage and volatile saturated at the time of entrapment. We further assume that magma storage conditions at Bezymianny Volcano have remained fairly constant in recent years such that the median rhyolitic melt composition (71.1 wt% SiO_2) from 2006

may be taken as representative (Table 3.4). We use the melt inclusion volatile concentrations corresponding with the maximum and median CO_2 concentrations of 910 ppm and 432 ppm CO_2, respectively (Izbekov, Unpublished results). We use the VolatileCalc solubility model (Newman and Lowenstern, 2002) to calculate melt entrapment pressures of 1660-2380 bars, which we convert to 6.5-9.4 km depth using a 2600 kg/m^3 crustal density. This estimated magma storage depth corresponds well with the model by Thelen et al. (2010) which puts the top of a magma storage region at approximately 6 km depth according to seismic data, and with the model by Balesta et al. (1976) which proposes a storage region center of mass at ~10 km.

3.4.5.2 Constraints on Excess Volatiles

Volcanic emissions that exceed the quantity of volatiles than can be explained by degassing of dissolved volatiles within erupted magma are referred to as "excess volatiles" and are commonly observed at arc volcanoes (e.g. Gerlach et al., 1994; Wallace and Gerlach, 1994; Wallace, 2001; Shinohara, 2008). The source of these excess volatiles can be explained by an exsolved volatile phase that is sourced from the eruptive melt and/or unerupted melt at depth. To identify the presence of excess volatiles we calculate the mass of surface emissions that can be explained by degassing of the dissolved volatiles within the erupted magma and compare that value to the observed emissions masses for 2007 and 2009. We focus our calculations on CO_2 emissions for which we have fairly good constraints on melt inclusion concentrations and because surface CO_2 emissions were quite similar between field observations in 2007 and 2009, which allows us to assume that average measured CO_2 emissions are representative of typical degassing at Bezymianny Volcano. Using the following equation from Gerlach et al. (1994) we calculate the annual mass of surface CO_2 emissions (E_{CO2}) that can be produced from the CO_2 dissolved within the eruptive magma (C_{CO2}):

$$E_{CO_2} = C_{CO_2} V_m \rho_m \varphi_m (10^{-9}) \quad (5.1)$$

where V_m is the volume of erupted magma (km^3), φ_m is the melt fraction, and ρ_m is the melt density. We calculate melt density of ~2600 kg/m^3 based on the average melt composition of 2006 eruptive products from P. Izbekov (Unpublished results) using the method of Lange and Carmichael (1990), with FeO/Fe_2O_3 partitioning calculated after Kilinc et al. (1983). An eruptive mass of 66 x 10^6 t from the October 2007 eruption deposits is obtained from Zharinov and Demyanchuk (2011), which we convert to dense rock equivalent (DRE) volume of 0.0254 km^3. We calculate a December 2009 eruptive volume using: (1) an estimated ash mass (0.5 x 10^6 t) from Zharinov and Demyanchuk (2011); (2) an extruded lava volume of 3.9 x 10^6 m^3 from V. Dvigalo (Unpublished results); and (3) the areal extent of the pyroclastic flow deposit (~2.0 x 10^6 m^3) as estimated from Advanced Land Imager satellite imagery along with an estimated deposit thickness of 2 m (Merkulova et al., 2010). Densities of 1770 kg/m^3 and 2200 kg/m^3 for pyroclastic flow and lava flow deposit material (Zharinov and Demyanchuk, 2011) are used to convert observed volumes into masses. Masses are then converted to DRE volume using a density of 2600 kg/m^3. A total volume of eruptive material from the 16 December 2009 eruption is estimated to be 0.00545 km^3. To determine the melt fraction, φ_{melt}, of Bezymianny magmas at entrapment depths, we use average phenocryst volume fraction calculated for 1974, 1979, and 1985 Bezymianny eruptive products by Tolstykh et al. (1999) of 0.25–0.30 and find a melt fraction range of 0.70–0.75 (by volume), with an average value of 0.725. Using these input parameters we solve equation 5.1 for the mass of CO_2 that could be produced from dissolved CO_2 within the eruptive magma (Table 3.4). We find that eight and 40 times more CO_2 was emitted from Bezymianny Volcano than can be explained by degassing of dissolved volatiles within the eruptive magma in 2007 and 2009, respectively (Table 3.4). Using estimates of average eruptive magma volume, dissolved volatile concentrations, and assuming that the average measured CO_2 emission rates are typical emissions for a given year we rearrange equation 5.1 to solve for two end-member scenarios in which excess volatiles are: (1) sourced entirely from the (average) eruptive magma as both dissolved and exsolved

volatiles (Eq. 5.2), and (2) sourced entirely from unerupted magma of similar melt composition to the erupted magma (Eq. 5.3):

$$C_{CO_2} = \frac{E_{CO_2}(10^9)}{V_m \rho_m \varphi_m} \quad (5.2)$$

$$V_m = \frac{E_{CO_2}(10^9)}{C_{CO_2} \rho_m \varphi_m} \quad (5.3)$$

We solve these equations assuming three possible melt fractions = 0.5, 0.725, and 1 for the degassed magma. The results of this exercise show that high initial CO_2 concentrations ranging from 12,600 to 25,200 ppm are required to explain surface emissions by degassing of the eruptive magma volume with the measured dissolved CO_2 concentration; while to explain surface emissions by degassing of unerupted magma requires between 13 and 27 times more degassed magma than erupted on average (Table 3.4). While we cannot determine the source of excess volatiles at Bezymianny Volcano, we speculate that a combination of degassing by unerupted magma and an exsolved volatile phase may best describe excess volatiles at Bezymianny Volcano. Using the average melt fraction of 0.0725 we calculate several combinations of degassed magma and CO_2 mass fractions that could explain the observed surface emissions (Fig. 3.8). A volatile budget conducted by Taran (2009) found that approximately seven times more magma intrudes than erupts in the Kamchatka-Kurile Arc, suggesting that ratio of degassed to eruptive magma of seven would be expected at Bezymianny Volcano. Concentrations of up to 1.7 wt% CO_2 have been found within plagioclase melt inclusions and calculated using analogous methods as described here for Mount St. Helens (Washington) and Redoubt (Alaska) Volcanoes, respectively (Blundy et al., 2010; Werner et al., 2012), which suggests that a CO_2 volatile mass fraction up to 1.7 wt% (17,000 ppm) could be a reasonable upper limit for Bezymianny Volcano, as these volcanoes exhibit similar dome-building eruptive activity as Bezymianny Volcano.

Considering the factors above we propose that surface emissions at Bezymianny Volcano could be reasonably explained by degassing of a magma volume approximately seven times greater than the eruptive volume containing a (dissolved and exsolved) volatile fraction of ~2400 ppm CO_2 (Fig. 3.8).

3.4.5.3 Constraints on Magma Degassing Depth

We previously proposed that the differences in surface composition of Bezymianny gases between 2007 and 2009 can be explained by variations in the depth of the degassing magma. Using the VolatileCalc model (Newman and Lowenstern, 2002) we provide quantitative estimates of the upper-limit degassing depths for the gas compositions observed in 2007 and 2009. VolatileCalc calculates the composition of an exsolved fluid phase that would be present in equilibrium with melt of specified composition, temperature, and corresponding pressure (Newman and Lowenstern, 2002), where the fluid is assumed to be composed solely of H_2O and CO_2. By comparing the observed (normalized to only include CO_2 and H_2O) and modeled exsolved gas compositions, we can estimate the upper limit equilibrium degassing pressure. Using the median 2006 CO_2 and H_2O melt inclusions concentration representing the proposed top of the magma storage region, a rhyolitic melt composition, and an estimated magma storage temperature of ~915°C (Shcherbakov et al., 2011), we run the VolatileCalc degassing path model for three different scenarios in which decompression during ascent induces degassing: (1) open-system degassing, (2) closed-system degassing with no initial exsolved volatile phase present, and (3) closed-system degassing with an exsolved volatile phase of 1 wt.%. We caution that because scenarios 1 and 2 do not contain an initial exsolved volatile phase, they cannot sustain the observed surface emissions for more than approximately three days, such that these model results can be used to help estimate the depth of volatile separation from the melt but should not be used to constrain the most likely degassing path. The modeled results can be seen in Figure 3.9 along with the calculated isobars corresponding with melt volatile composition, and calculated isopleths for 98% and 80% H_2O/total fluids representing the exsolved gas composition

observed in 2007 and 2009, respectively. If we evaluate the intersection of the degassing paths with the exsolved gas composition for 2009 we find equilibrium conditions for the open-system degassing path corresponding with a pressure of ~1170 bars (~4.6 km), and for the closed-system (1% exsolved) path corresponding with a pressure of ~800 bars (~3.2 km). Repeating these calculations using the maximum CO_2 melt inclusion concentration, representing the middle of the magma storage region as the initial model conditions, results in a similar trends though lower corresponding pressure of ~1070 bars for the open-system path and ~500 bars for the closed-system (1% exsolved) path). The high H_2O/total fluids observed for 2007 emissions, is higher than can be modeled by VolatileCalc. If we extrapolate the degassing curves to where they would likely intersect the 98% H_2O/total fluids isopleth curve, we estimate a degassing pressure of ~900 bars or ~3.5 km for the open-system curve and ~200 bars or ~0.8 km for the closed system (1% exsolved) curve. We caution however, that if boiling of meteoric water is contributing to surface emissions in 2007, then this depth estimate may be biasing the exsolved gas composition to shallower-degassing conditions. We find that during 2007 and 2009 field campaigns, magma had already begun ascent from the mid-crustal storage region and estimate magma degassing depths of <3.7 km in August 2007, approximately two months prior to eruption, and </=4.6 km in July 2009, approximately five months prior to eruption.

3.4.6 Proposed Model

Based on our observations and model results we propose the following model to describe magma degassing at Bezymianny Volcano (Fig. 3.10). First, we speculate that exsolved fluids from magma within the mid-crustal storage region are able to separate from their source magma, and due to their lower densities, ascend through the stored magma and accumulate at the top of the mid-crustal storage region. We envision that prior to eruptions at Bezymianny Volcano a batch of this volatile-saturated magma begins ascent from the mid-crustal storage region to the surface (e.g. Scandone et al., 2007). The exsolved volatiles within this magma represent a combination of decompression induced

gas exsolution from the host magma and an additional component of previously exsolved volatiles sourced from deeper unerupted magma (e.g. Roberge et al., 2009; Blundy et al., 2010; Edmonds et al., 2010). The presence of un-erupted magma at depth beneath Bezymianny Volcano is consistent with the geochemical model proposed by Turner et al. (this issue) and the volatile budget proposed by Taran (2009). The accumulation of the lower density exsolved volatiles within the ascending magma enables the exsolved volatiles to rise to the head of the ascending magma batch and separate from the melt. Upon separation, the exsolved fluids are then able to quickly rise to the surface via permeable flow through bubble and/or fracture networks within the conduit (e.g. Eichelberger et al., 1986; Edmonds et al., 2003b; Tuffen and Dingwell, 2005; Edmonds et al., 2010). This rapid ascent of the exsolved volatiles prevents reequilibration with the surroundings and enables the surface gas composition to reflect the depth of volatile separation from the melt (Shinohara, 2008). This model is consistent with the observed gas composition and the elevated seismicity leading up to eruptions. In particular, Thelen et al. (2010) interpret increases in low frequency tremor observed prior to the October 2007 eruption of Bezymianny to be due to the rapid ascent of gases within the conduit in advance of juvenile magma.

3.5 Conclusions

Variations in measurements of fumarole composition, passive SO_2 flux, and explosive SO_2 mass acquired between July 2007 and July 2010 were used along with melt inclusion data to estimate total volatile flux and constrain magma degassing processes at Bezymianny Volcano. Total volatile fluxes from Bezymianny Volcano during 2007 and 2009 field campaigns are estimated to be 49,000 t/d and 3,000 t/d, respectively, with an estimated range in annual volatile mass for the study period of 1.1×10^6 and 18×10^6 t. Based on 2007 passive and explosive SO_2 emissions we find that passive degassing is the primary degassing mechanism at Bezymianny Volcano with passive emissions comprising 87-95% of total emissions for years with minor to moderated-sized eruptions. We find that ~8-40 times more CO_2 was emitted in 2007 and 2009 than can be explained

by degassing of dissolved volatiles within eruptive magma and propose that an exsolved volatile phase sourced from either the eruptive magma or unerupted magma at depth is contributing to surface emissions. Trends in observed gas composition and volatile flux, when considered in the context of volatile solubilities, suggests that (1) Bezymianny is a predominantly open-system degassing volcano, and (2) much of the variation in gas emissions over time can be explained by the relative depth of gas exsolution and separation from the degassing magma. The most complete gas datasets of this study were acquired pre- and syn-eruption for the October 2007 and December 2009 eruptions, and these measurements were used to elucidate subsurface conditions prior to eruption. 2007 gas compositional data and high H_2O and HCl fluxes collected approximately two months prior to the October eruption and three months following the May 2007 eruption, suggest degassing of predominantly shallow degassed magma, plus a minor component of degassing by deeper magma. 2009 gas compositional data and low H_2O and HCl fluxes observed ~11 months following the August 2008 eruption and approximately five months prior to the December 2009 eruption, suggest degassing of a deeper, volatile-rich magma source. We speculate that the exsolved volatiles within the ascending magma are able to separate from the melt and then rise rapidly to the surface via permeable flow through either bubble or fracture networks within the conduit, such that they retain their melt-equilibrium composition from depth. The compositions of H_2O and CO_2 observed within 2007 and 2009 fumarole samples are compared with the modeled exsolved fluid composition for an ascending magma to estimate the depth of gas exsolution and separation from the melt at the time of sample collection. We find that at the time of sample collection in both 2007 and 2009 magma had already begun ascent from the mid-crustal storage region with estimated depths of volatile separation and degassing from the melt of less than ~3.5 and ~4.6 km, respectively. These findings suggest that the exsolved gas composition could be a significant monitoring tool to detect magma ascent prior to eruption at Bezymianny Volcano.

3.6 Acknowledgements

We would like to thank Jake Lowenstern, Michelle Coombs and an anonymous reviewer whose constructive comments significantly improved this manuscript. This work benefited from significant help with sample collection, technical, and logistical support from many members of the PIRE science team. In particular, we acknowledge Timothy Clark, Geoffroy Avard, Theresa Kayzar, Helena Buurman, Ronni Grapenthin, and Ashley Shuler for help with sample collection; Sergey Serovetnikov and Slava Pilipenko for technical support; and Oxana Edokimova and Dmitry Muravyov for logistical support. We acknowledge Slava Shapar, who passed away this year, for his analysis of fumarole samples. Your hard work at IVS has been greatly appreciated and we will remember you fondly. TL would like to thank Pavel Izbekov, John Eichelberger, Evgeny Gordeev, Sergey Ushakov, Mike West and Jeff Freymueller for their vision and execution of the PIRE project and for incorporating gas-geochemistry into the project goals. TL would like to thank members of the CCVG, especially Franco Tassi, Yuri Taran, Tobias Fischer, Dario Tedesco and Bruce Christiensen for constructive feedback on earlier presentations of this work regarding interpretation of fumaroles samples. TL would like to thank Sergey Senyukov, Alexei Ozerov, Mike West, Vasily Shcherbakov, Steve Turner, Theresa Kayzar, Ronni Grapenthin, and David Fee for insightful scientific discussions regarding Bezymianny Volcano and the interpretations presented here. TL would like to acknowledge: David Fee for help with figure creation and constructive edits of early drafts of this document and Ronni Grapenthin for providing the DEM for Figure 1. This project was funded by NSF PIRE grant (OISE- 0530278), the UAF Geophysical Institute, and the Alaska Volcano Observatory.

Figures:

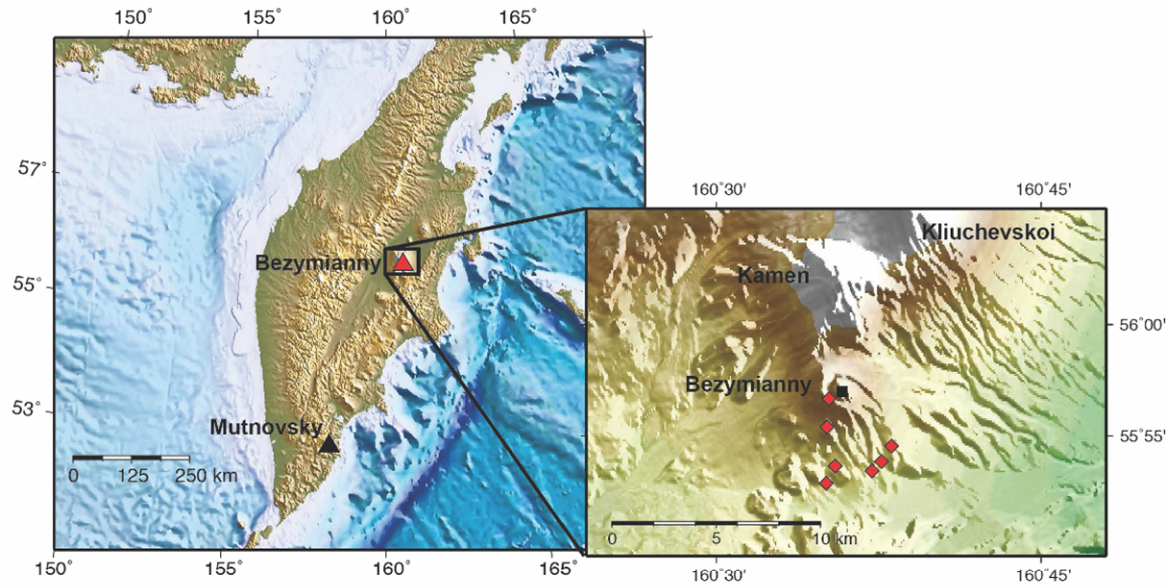

Figure 3.1: Location map. **Left:** Kamchatkan Peninsula, Russia, with Bezymianny and Mutnovsky Volcanoes labeled. **Insert:** Shuttle Radar Topography Mission (SRTM) digital elevation model (DEM) of Bezymianny Volcano and surroundings, with Bezymianny, Kamen and Kliuchevskoi Volcanoes labeled. Fumarole sample location is depicted by the black square while FLYSPEC sample locations are marked by red diamonds.

Figure 3.2: Photo of Bezymianny, Kamen, and Kliuchevskoi Volcanoes. Bezymianny Volcano (right) and Kliuchevskoi Volcano (left) both have visible gas plumes. Photo taken 3 December 2008 by Sergey Serovetnikov, Kamchatka Branch Geophysical Surveys.

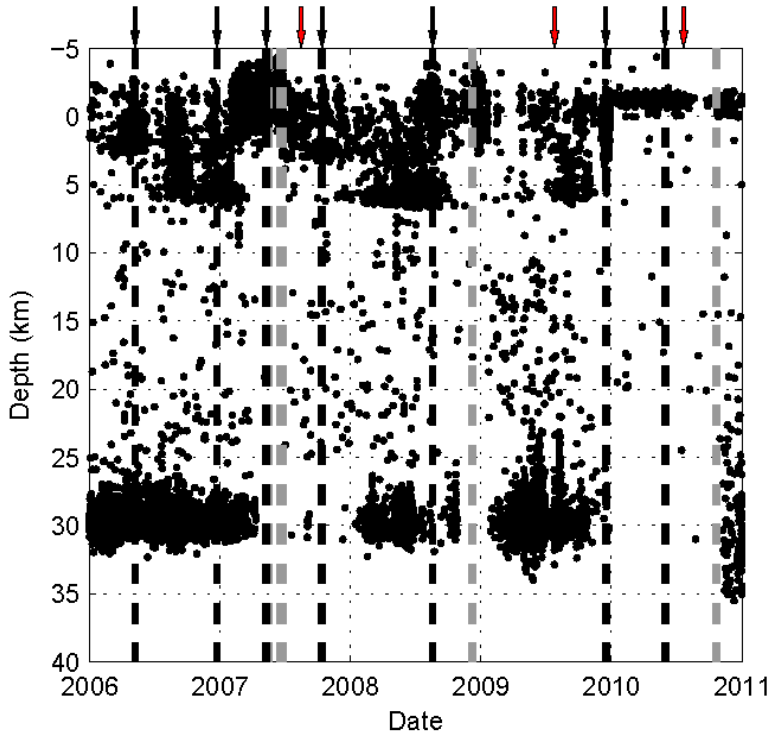

Figure 3.3: Seismicity below Bezymianny and Kliuchevskoi Volcanoes from 2006-2011. Eruptions of Bezymianny Volcano are labeled by black arrows and dashed lines, while eruptions of Kliuchevskoi Volcano are labeled by gray dashed lines. Red arrows mark the date of fumarole sample collection. Pulses of deep seismicity (25 – 35 km depth) have been interpreted to be the result of melt segregation and ascent (George, 2010). Seismic data from the Kamchatka Branch Geophysical Survey's catalog, courtesy of Sergey Senyukov.

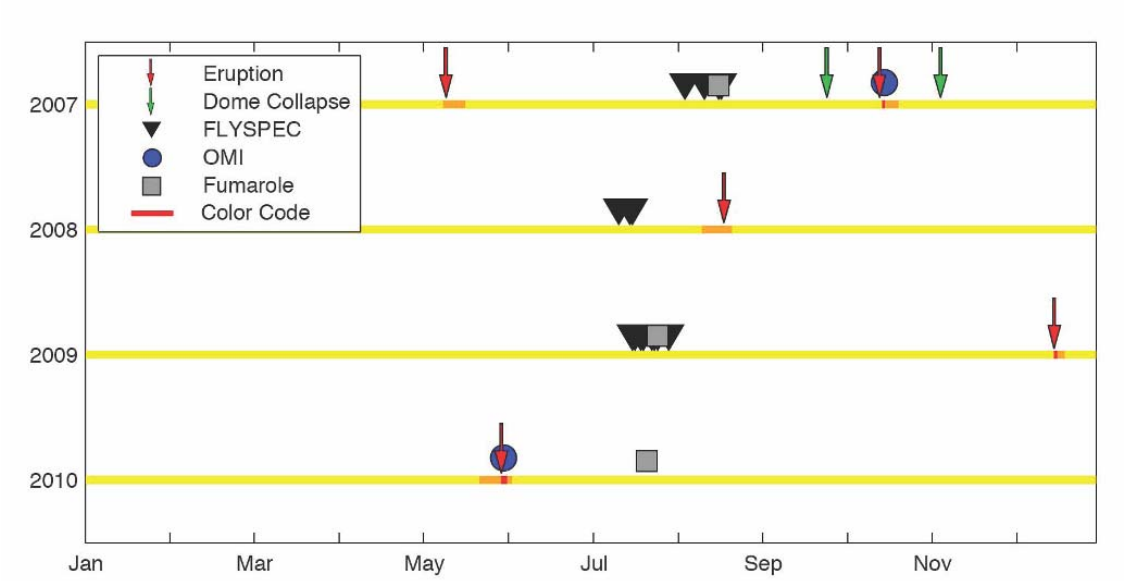

Figure 3.4: Timeline of volcanic activity and sample collection at Bezymianny Volcano. Red and green arrows represent explosive eruptions and dome collapse events, respectively. Black triangles, blue circles, and gray squares mark times of FLYSPEC, OMI and fumarole sample collection, respectively. Aviation color codes corresponding with volcanic activity are shown on the horizontal time lines, where *Red* indicates eruption is imminent, *Orange* represents heightened or escalating volcanic activity, *Yellow* indicates above background activity, and *Green* (not shown) represents background activity (Girina, 2012).

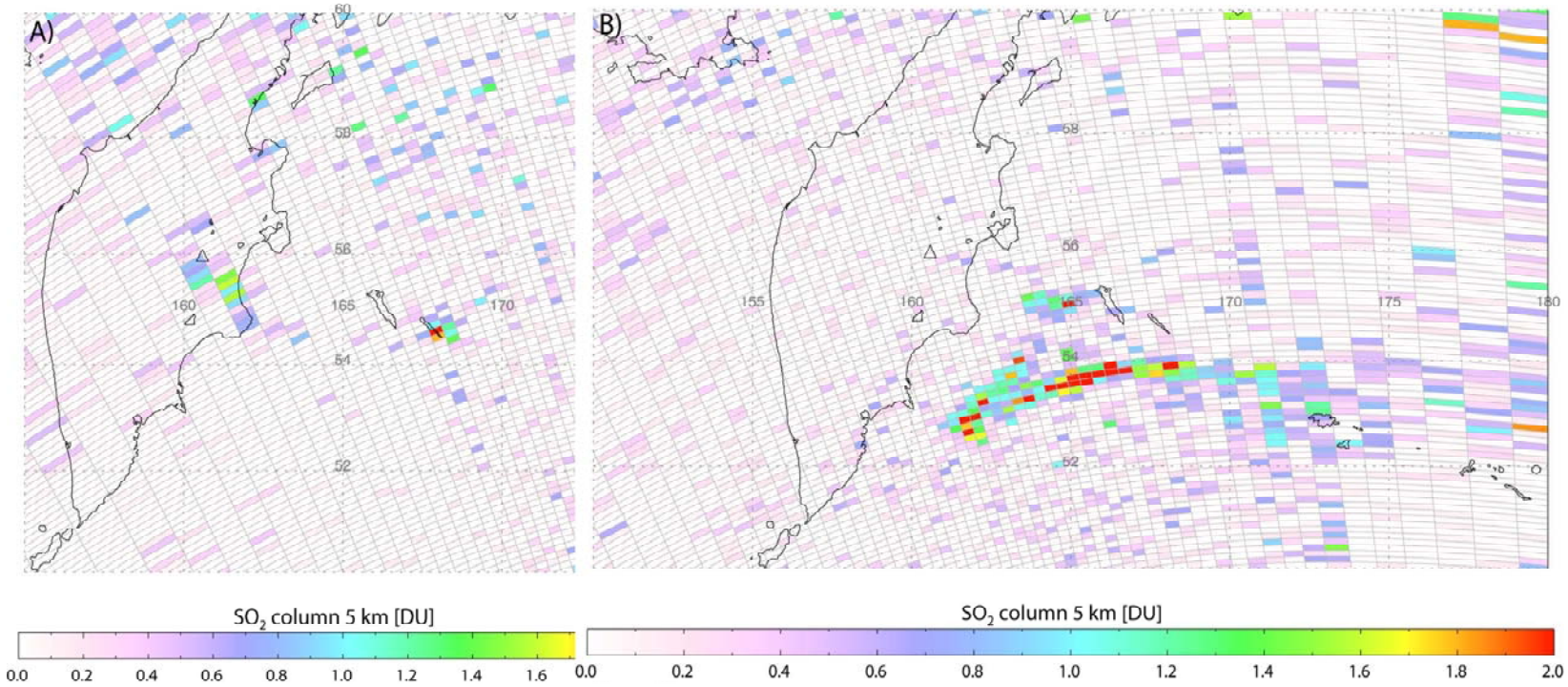

Figure 3.5: October 2007 OMI images of explosive SO_2 from Bezymianny Volcano. SO_2 emissions were produced from eruptive pulses on 14 (A) and 15 (B) October 2007. Images were acquired on the days following explosive events. Estimated SO_2 masses from 7.5 km plume center of mass altitude OMSO2 data products corrected for SO_2 loss are 1.2 and 5.4 kt for A and B, respectively.

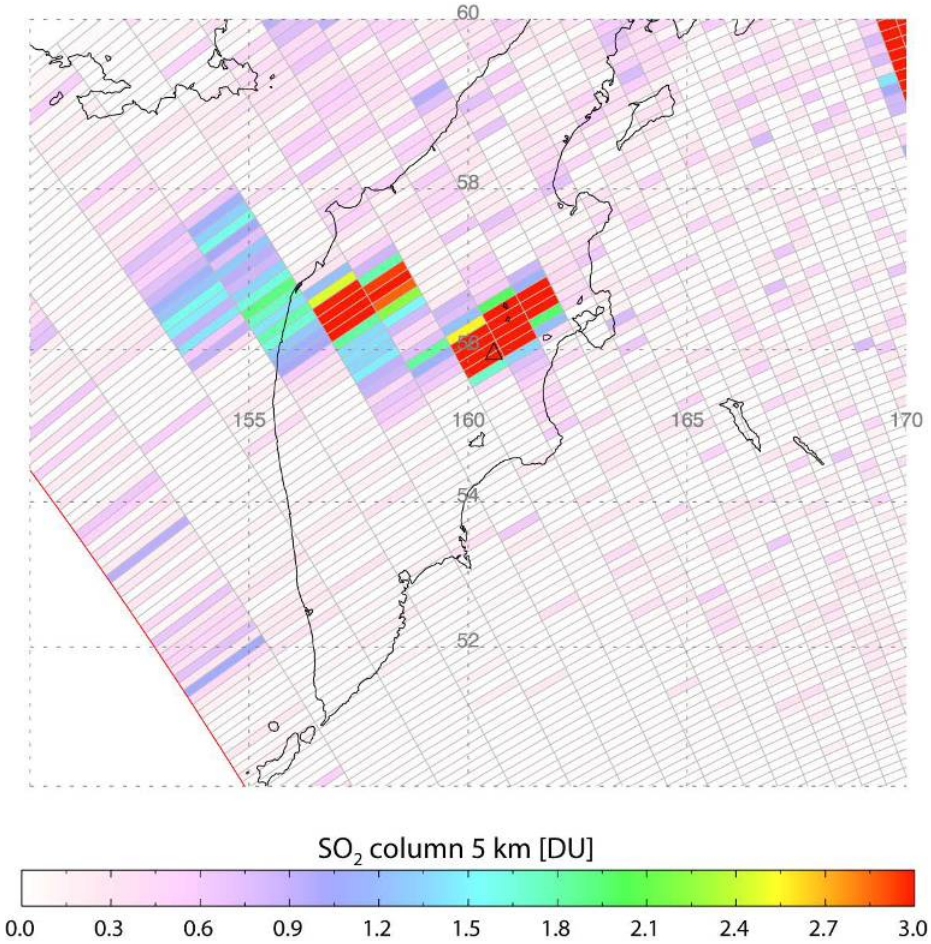

Figure 3.6: May 2010 OMI image of explosive SO_2 from Bezymianny Volcano. Eruption occurred on 31 May 2010 (image from 1 June 2010). Estimated SO_2 mass from 7.5 km plume center of mass altitude OMSO2 data product corrected for SO_2 loss is 5.1 kt.

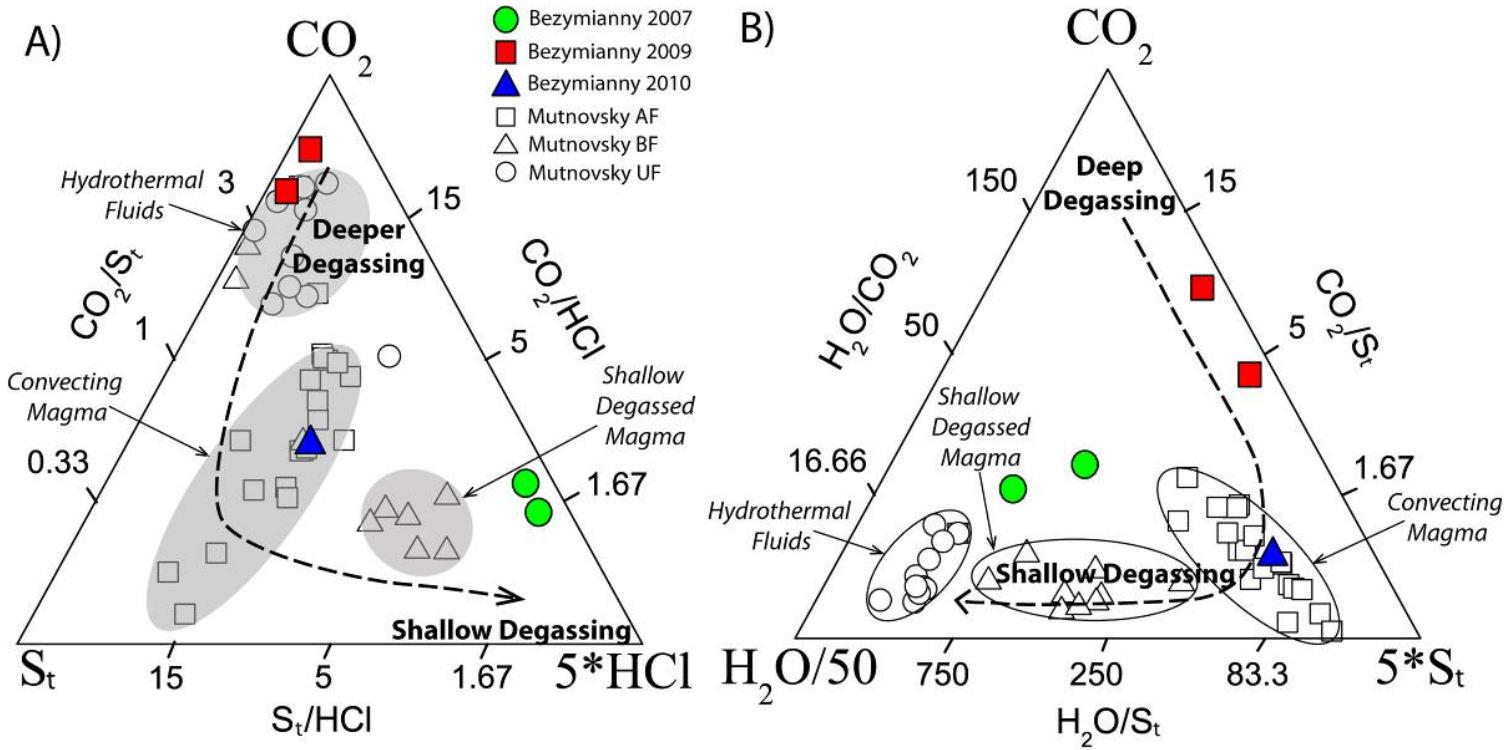

Figure 3.7: Ternary diagrams showing Bezymianny fumarole sample composition for 2007, 2009 and 2010. A) CO_2-S_t-5HCl; B) CO_2-H_2O/50-5S_t (mmol/mol) ternary diagrams, where S_t (total S) = SO_2+H_2S. Mutnovsky Volcanic and hydrothermal gases from Zelenski and Taran (2011) are plotted for comparison. A) high CO_2 relative to S_t and HCl in 2009 Bezymianny fumarole samples indicate degassing of a deeper magma, while moderate to high HCl measured in 2007 and 2010 fumarole samples indicate degassing of shallower magma. High relative CO_2 is also seen for Mutnovsky UF fumaroles reflecting hydrothermal degassing, where the high CO_2 relative to S_t and HCl suggests scrubbing of these water soluble species. B) High CO_2 and S_t observed for 2009 Bezymianny fumarole samples relative to other years supports degassing of a deeper magma source. Similarities between Bezymianny 2010 and Mutnovsky AF fumarole compositions support interpretations of degassing of shallow volatile-rich magma sources; while similarities between Bezymianny 2007 and Mutnovsky BF fumaroles supports degassing of shallow, degassed magma. See text for details.

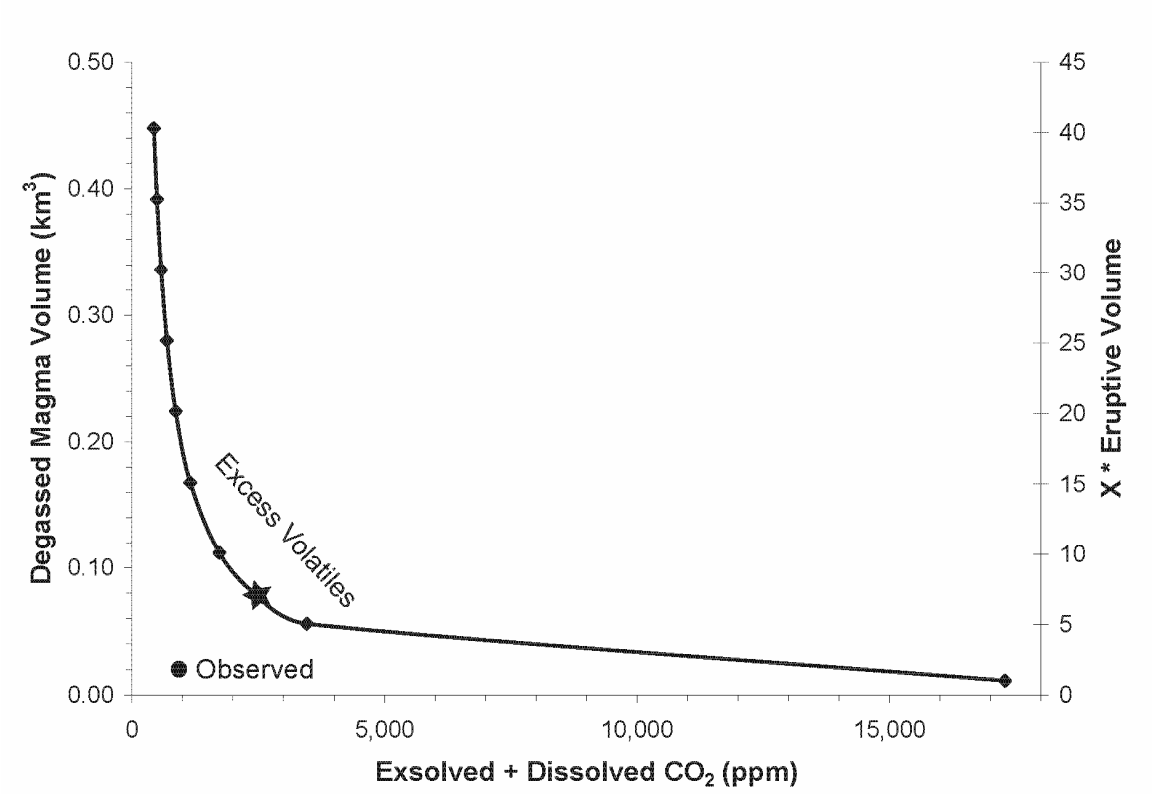

Figure 3.8: Possible sources of excess volatiles at Bezymianny Volcano. Figure depicting the range in degassed magma volume and/or dissolved and exsolved melt CO_2 that can explain degassing of excess volatiles. Calculations were done assuming a melt fraction of 0.725. The maximum dissolved CO_2 concentration (910 ppm) observed in 2006 melt inclusions (Izbekov, Unpublished results) along with the average annual eruptive volume (0.0112 km^3) for Bezymianny Volcano determined by Zharinov and Demyanchuk (2011) is marked by a black circle. We propose a degassed magma volume approximately seven times that of the average eruptive volume containing a total volatile fraction of ~2500 ppm to reasonably explain the observed CO_2 emissions, and mark this value with a black star.

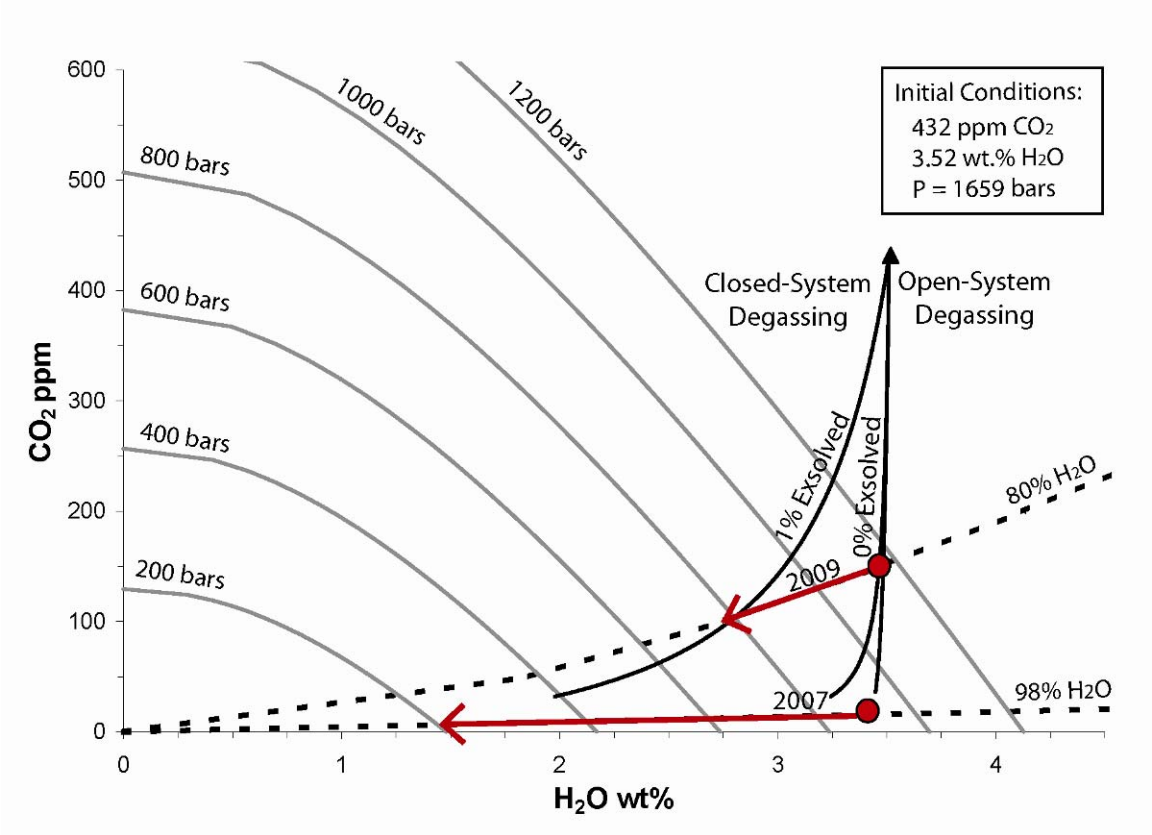

Figure 3.9: Equilibrium degassing behavior as a function of dissolved CO_2 (ppm) and H_2O (wt.%) melt concentration. Isobars (gray lines), degassing paths (black lines) and vapor isopleths (dashed black lines) corresponding with the observed gas composition in 2007 (98% H_2O/total fluids) and 2009 (80% H_2O/total fluids) are modeled using VolatileCalc (Newman and Lowenstern, 2002). Three degassing scenarios, computed using the median 2006 melt inclusion volatile concentration as a starting point to represent the top of the magma storage region, are shown: (1) open-system, (2) closed-system with 0% exsolved volatiles, and (3) closed-system with 1% exsolved volatiles. The intersection between the vapor isopleths and the degassing curves provides a range of possible magma degassing pressures, with the open-system curve representing upper-limit magma degassing depths. See text for details.

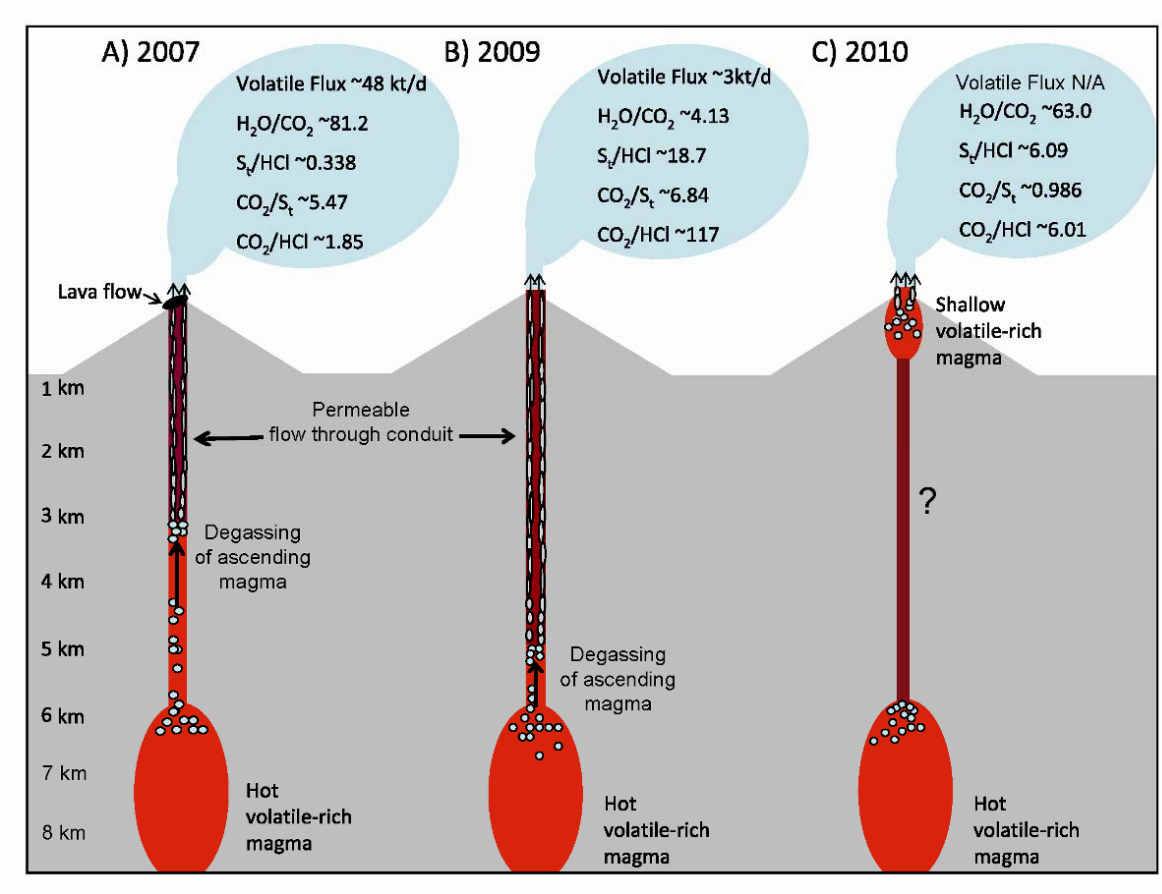

Figure 3.10: Proposed degassing model. Interpretations of subsurface conditions at the time of sample collection for 2007 (A), 2009 (B), and 2010 (C) according to the gas composition and flux measurements, and model results. Ratios of H_2O/CO_2, S/HCl, CO_2/S, and CO_2/HCl and total volatile flux are shown when available. Depths of magma storage from 6 to >9 km are estimated from seismic data (Thelen et al., 2010) and are supported by estimated melt inclusion entrapment depths (Izbekov, Unpublished results). Estimated depths of volatile exsolution and separation from the melt are calculated from the measured H_2O and CO_2 concentrations and the VolatileCalc model (Newman and Lowenstern, 2002). We propose that exsolved volatiles are able to ascend rapidly to the surface from ascending magma via permeable flow through interconnected bubbles and/or fractures within the conduit.

Tables:

Table 3.1: Fumarole concentrations from Bezymianny Volcano.

mmol/mol	T (°C)	H_2O	CO_2	SO_2	H_2S	HCl	CO	CH_4	H_2	N_2	O_2	Ar
2007	301	959	15.0	3.08	0.0220	9.23	4.14E-04	4.17E-04	0.215	13.4	0.215	0.141
2007	301	973	9.89	1.62	3.95E-03	4.76	3.12E-04	3.14E-04	0.0507	10.2	0.170	0.108
2009	250	739	208	22.3	0.774	1.72	9.88E-03	2.34E-04	0.405	28.0	0.345	0.328
2009	220	775	165	34.3	0.769	1.46	7.14E-03	1.92E-04	0.315	22.9	0.368	0.273
2010	313	965	15.3	15.4	0.145	2.55	-	2.67E-06	3.42E-03	1.50	0.0331	0.0189
Average												
2007	301	966	12.4	2.35	0.0130	7.00	3.63E-04	3.65E-04	0.133	11.8	0.193	0.125
2009	235	757	186	28.3	0.771	1.59	8.51E-03	2.13E-04	0.360	25.4	0.357	0.300
2010	313	965	15.3	15.4	0.145	2.55	-	2.67E-06	3.42E-03	1.50	0.0331	0.0189

Table 3.2: Ratios and total dry-gas concentrations of relevant gas species for Bezymianny fumarole samples.

	T (°C)	H_2O/CO_2	H_2/H_2O	CO_2*	SO_2*	Total S*†	HCl*	SO_2/Total S*	CO_2/S*†	S/HCl*	CO_2/HCl*
2007	301	64.0	2.24E-04	36.3	7.46	7.51	22.4	0.993	4.83	0.336	1.62
2007	301	98.4	5.21E-05	36.9	6.04	6.05	17.8	1.00	6.10	0.341	2.08
2009	250	3.56	5.49E-04	79.4	8.54	8.83	0.657	0.966	8.99	13.4	121
2009	220	4.71	4.07E-04	73.2	15.3	15.6	0.649	0.978	4.69	24.1	113
2010	313	63.0	3.54E-06	43.8	44.0	44.4	7.30	0.991	0.986	6.09	6.01
Average											
2007	301	81.2	1.38E-04	36.6	6.75	6.8	20.1	1.00	5.47	0.338	1.85
2009	235	4.13	4.78E-04	76.3	11.9	12.2	0.653	0.972	6.84	18.7	117
2010	313	63.0	3.54E-06	43.8	44.0	44.4	7.30	0.991	0.986	6.09	6.01

*From normalized dry-gas concentrations.
†Total S = SO_2 + H_2S.

Table 3.3: Bezymianny total volatile fluxes, explosive volatile masses, and total annual volatile masses in 2007 and 2009.

	H_2O	**CO_2**	**SO_2**	**H_2S**	**HCl**	**CO**	**CH_4**	**H_2**	**N_2**	**O_2**	**Ar**	
Molecular Weight (g/mol)	18	44	64	34	36.5	28	16	2	28	32	40	
2007												**Total**
Average Composition (mol%)	**97.6**	**0.862**	**0.168**	**8.88E-4**	**0.469**	**2.42E-5**	**2.46E-5**	**8.90E-3**	**0.833**	**0.0244**	**8.86E-3**	100
Passive Mass Flux (t/d)	45,000	980	**280**	0.780	440	0.018	0.010	0.5	600	20	9.2	47,000
Annual Passive Gas Mass (t)	16E6	3.6E5	1.02E5	290	1.6E5	6.6	3.7	170	2.2E5	7,400	3,300	17E6
Annual Explosive Gas Mass (t)*	1E6	23,000	6,600	19	1.1E5	0.42	0.24	11	14,000	480	220	1.1E6
Total Annual Passive and Explosive Mass (t)	17E6	3.8E5	1.09E5	310	1.7E5	7.0	3.9	180	2.30E5	7,900	3,500	18.0E6
Total Annual Flux (t/d)†	47,000	1,000	290	0.85	470	0.019	0.011	0.49	630	22	10	49,000
2009												
Average Composition (mol%)	**75.7**	**18.6**	**2.83**	**0.0771**	**0.159**	**8.51E-4**	**2.13E-5**	**0.0360**	**2.54**	**0.0357**	**0.0300**	100
Passive Mass Flux (t/d)†	1,700	1,000	**220**	3.2	7.2	0.029	4.20E-4	0.089	88	1.4	1.5	3,000
Annual Passive Gas Mass (t)	6.2E5	3.7E5	80,000	1,200	2,600	11	0.15	32.5	32,000	510	540	1.1E6
No Data for Explosive Gas Mass (t)	NA	NA	NA	NA	NA	NA	NA	NA	NA	NA	NA	NA
Total Annual Passive Mass (t)	6.2E5	3.7E5	80,000	1,200	2,600	11	0.15	32.5	32,000	510	540.00	1.1E6

Values in bold are measured, while remaining values are calculated.
*Assumes gas composition ratios are maintained during explosive eruption which is an oversimplification.
†Total Annual Flux in 2007 includes passive and explosive emissions; because no explosive emissions were measured in 2009 total annual flux is approximated by the passive max flux.

Table 3.4: Mass balance constraints on magma degassing at Bezymianny Volcano.

***Melt composition (wt%) from 2006 Bezymianny eruptive products*[a]**

Sample	SiO_2	TiO_2	Al_2O_3	FeO	MnO	MgO	CaO	Na_2O	K_2O	H_2O	CO_2	S[b]	P_s (Bars)	D_s (km)
Maximum	71.5	0.453	15.3	2.19	0	0.819	2.10	5.07	2.57	3.36	0.0910	0.0600	2380	9.4
Median	71.1	0.324	15.0	2.71	0	0.838	2.37	4.78	2.84	3.52	0.0432	0.0600	1660	6.5

Mass of surface emissions explained by dissolved volatiles at entrapment depths

2007	C_i (ppm)	ρ_m (kg/km^3)	φ_m	*2007* $V_{m,e}$[c] (km^3)	$E_{i,d}$ (t)	2009	C_i (ppm)	ρ_m (kg/km^3)	φ_m	*2009* $V_{m,e}$[c] (km^3)	$E_{i,d}$ (t)
H_2O	33,600	2.60E+12	0.725	0.0254	1.61E+06	H_2O	33,600	2.6E+12	0.725	0.00545	3.45E+05
CO_2	910	2.60E+12	0.725	0.0254	4.36E+04	CO_2	910	2.6E+12	0.725	0.00545	9.36E+03

Mass of excess volatiles

2007	$E_{i,t}$ (t)	$E_{i,d}$ (t)	$E_{i,e}$ (t)	$E_{i,t/Ei,d}$ (t)	2009	$E_{i,t}$ (t)	$E_{i,d}$ (t)	$E_{i,e}$ (t)	$E_{i,t}/E_{i,d}$ (t)
CO_2	3.60E+05	4.36E+04	3.16E+05	8.3	CO_2	3.70E+05	9.36E+03	3.61E+05	39.5

Combinations of magma CO_2 concentration (dissolved and exsolved) and volume that can produce average surface CO_2 emissions

Average	C_i (ppm)[†]	ρ_m (kg/km^3)	φ_m	$E_{i,t}$ (t)	$Vm_{,d}$ (km^3)[‡]	$V_{m,d}/V_{m,e}$
CO_2	910	2.65E+12	1	3.60E+05	0.1493	13
CO_2	910	2.65E+12	0.725	3.60E+05	0.2059	18
CO_2	910	2.65E+12	0.5	3.60E+05	0.2986	27
CO_2	12,180	2.65E+12	1	3.60E+05	0.0112	1
CO_2	16,799	2.65E+12	0.725	3.60E+05	0.0112	1
CO_2	24,359	2.65E+12	0.5	3.60E+05	0.0112	1

Table 3.4: Continued

[a]From P. Izbekov, unpublished data.
[b]From Tolstykh et al. (1999).
[c]From Zharinov and Demyanchuk (2010).
[d]Calculated using VolatileCalc model from Newman and Lowenstern (2002). See text for details.
[γ]As S in melt inclusion analysis.
D_s is the saturation depth calculated from P_s assuming a 2600 kg/m^3 crustal density.
C_i is the maximum observed melt inclusion concentration from Bezymianny eruptive products, for volatile species *i*.
φ_m represents the melt fraction within magma. A value of 0.725 is assumed for entrapment depths from Tolstykh et al. (1999) and a value of 1 is assumed for primary magma supply depths.
$V_{m,e}$ represents the estimated volume of erupted magma from Bezymianny Volcano.
$V_{m,d}$ represents the calculated volume of degassed magma from Bezymianny Volcano.
$E_{i,d}$ represents the surface emissions of volatile *i* that can be produced by the dissolved volatile concentration at entrapment depths based on melt inclusion data.
$E_{i,e}$ represents the mass of volatile *i* exsolved at entrapment depths required to explain the observed surface emissions.
$E_{i,t}$ represents the total observed surface emissions of volatile *i*.
[†]910 ppm is the maximum CO_2 concentration observed in melt inclusions from P. Izbekov (unpublished data); the remaining values were calculated. See text for details.
[‡]0.0112 km^3 is the average observed eruptive magma volume since 1956 from Zharinov and Demyanchuk (2010); the remaining values were calculated. See text for details.

References Cited:

Aiuppa, A., Moretti, R., Federico, C., Guidice, G., Gurrieri, S., Liuzzo, M., Papale, P., Shinohara, H. and Valenza, M., 2007. Forecasting Etna eruptions by real-time observations of volcanic gas composition. Geology, 35(12): 1115-1118.

Aiuppa, A., Guidice, G., Gurrieri, S., Liuzzo, M., Burton, M., Caltabiano, T., McGonigle, A., Salerno, G., Shinohara, H. and Valenza, M., 2008. Total volatile flux from Mount Etna. Geophysical Research Letters, 35: L24302. 10.1029/2008GL035871.

Aiuppa, A., Federico, C., Giudice, G., Giuffrida, G., Guida, R., Gurrieri, S., Liuzzo, M., Moretti, R. and Papale, P., 2009. The 2007 eruption of Stromboli volcano: Insights from real-time measurement of the volcanic gas plume CO_2/SO_2 ratio. Journal of Volcanology and Geothermal Research, 182(3-4): 221-230.

Aiuppa, A., Guidice, G., Liuzzo, M., Tamburello, G., Allard, P., Calabrese, S., Chaplygin, I., McGonigle, A. and Taran, Y., 2012. First volatile inventory for Gorely volcano, Kamchatka. Geophysical Research Letters, 39: L06307. 10.1029/2012GL051177.

Balesta, S.T., Farberov, A.I., Smirnov, V.S., Rarakanovsky, A.A. and Zubin, M.I., 1976. Deep crustal structure of the Kamchatkan volcanic regions. Bulletin of Volcanology, 40(4): 260.

Blundy, J., Cashman, K., Rust, A. and Witham, F., 2010. A case for CO_2-rich arc magmas. Earth and Planetary Science Letters, 290: 289-301. 10.1016/j.epsl.2009.12.013.

Bluth, G. and Carn, S., 2008. Exceptional sulfur degassing from Nyamuragira volcano, 1979-2005. International Journal of Remote Sensing, 29(22): 6667-6685. doi:10.1080/01431160802168434.

Bogoyavlenskaya, G., Braitseva, O., Melekestsev, I., Maksimov, A. and Ivanov, B., 1991. Bezymyannyi Volcano. In: S. Fedotov and Y. Masurenkov (Editors), Active Volcanoes of Kamchatka. Nauka, Moscow, pp. 195-197.

Braitseva, O., 1991. Bezymyannyi volcano: Eruptive history and dynamics. Journal of Volcanology and Seismology, 12(2): 165-194.

Burton, M., Allard, P., Mure, F. and La Spina, A., 2007. Magmatic gas composition reveals the source depth of slug-driven strombolian explosive activity. Science, 317: 227-230.

Capaccioni, B., Tassi, F., Vaselli, O., Tedesco, D. and Poreda, R., 2007. Submarine gas burst at Panarea Island (southern Italy) on 3 November 2002: A magmatic versus hydrothermal episode. Journal of Geophysical Research-Solid Earth, 112: B05201.

Carn, S., 2011. OMIplot Software. http://vhub.org/resources/682. http://vhub.org/resources/682.

Chiodini, G. and Marini, L., 1998. Hydrothermal gas equilibria: The H_2O-H_2-CO_2-CO-CH_4 system. Geochimica et Cosmochimica Acta, 62: 2673-2687.

Davaille, A. and Lees, J.M., 2004. Thermal modeling of subducted plates: tear and hotspot at the Kamchatka corner. Earth and Planetary Science Letters, 226(3-4): 293-304.

Delmelle, P. and Stix, J., 2000. Volcanic Gases. In: H. Sigurdsson (Editor), Encyclopedia of Volcanoes. Academic Press, London, pp. 803 - 815.

Doukas, M., 2002. A new method for GPS-based wind speed determineations during airborne volcanic plume measurements, U.S. Geological Survey, Open-File Report 02-395.

Dvigalo, V.N., Unpublished results.

Edmonds, M. and Gerlach, T., 2007. Vapor segregation and loss in basaltic melts. Geology, 35(8): 751-754. 10.1130/G23464A.1.

Edmonds, M., Pyle, D. and Oppenheimer, C., 2001. A model for degassing at the Soufriere Hills Volcano, Montserrat, West Indies, based on geochemical data. Earth and Planetary Science Letters, 186: 159-173. doi:10.1016/S0012-821X(01)00242-4.

Edmonds, M., Herd, R., Galle, B. and Oppenheimer, C., 2003a. Automated, high time-resolution measurements of SO_2 flux at Soufriere Hills Volcano, Montserrat. Bulletin of Volcanology, 65: 578-586.

Edmonds, M., Oppenheimer, C., Pyle, D., Herd, R. and Thompson, G., 2003b. SO_2 emissions from Soufriere Hills Volcano and their relationship to conduit permeability, hydrothermal interaction and degassing regime. Journal of Volcanology and Geothermal Research, 124: 23-43. doi:10.1016/S0377-0273(03)00041-6.

Edmonds, M., Aiuppa, A., Humphreys, M., Moretti, R., Giudice, G., Martin, R.S., Herd, R.A. and Christopher, T., 2010. Excess volatiles supplied by mingling of mafic magma at an andesite arc volcano. Geochemistry Geophysics Geosystems, 11(4): 1-16. doi:10.1029/2009GC002781.

Eichelberger, J.C., Carrigan, C.R., Westrich, H.R. and Price, R.H., 1986. Non-explosive silicic volcanism. Nature, 323: 598-602.

Fedetov, S.A., Zharinov, N.A. and Gontovaya, L.I., 2010. The magmatic system of the Klyuchevskaya Group of Volcanoes infrerred from data on its eruptions, earthquakes, deformation, and deep structure. Journal of Volcanology and Seismology, 4(1): 3-35. 10.1134/S074204631001001X.

Fedotov, S. and Masurenkov, Y. (Editors), 1991. Active Volcanoes of Kamchatka. Nauka, Moscow.

Fedotov, S.A., Zharinov, N.A. and Gontovaya, L.I., 2010. The magmatic system of the Klyuchevskaya Group of Volcanoes infrerred from data on its eruptions, earthquakes, deformation, and deep structure. Journal of Volcanology and Seismology, 4(1): 3-35. 10.1134/S074204631001001X.

Galle, B., Oppenheimer, C., Geyer, A., McGonigle, A., Edmonds, M. and Horrocks, L., 2002. A miniaturised ultraviolet spectrometer for remote sensing of SO_2 fluxes: a new tool for volcano surveillance. Journal of Volcanology and Geothermal Research, 119: 241-254.

George, O., 2010. Relating Deep Magmatic Processes to Eruptive Behavior at Arc Volcanoes Through Analysis of Deep Seismicity. M.S. Thesis, University of Alaska Fairbanks: 92.

Gerlach, T., 1986. Exsolution of H_2O, CO_2, and S during eruptive episodes at Kilauea Volcano, Hawaii. Journal of Geophysical Research, 91(B12): 12,177-112,185.

Gerlach, T., Westrich, H., Casadevall, T. and Finnegan, D., 1994. Vapor saturation and accumulation in magmas of the 1989-1990 eruption of Redoubt Volcano, Alaska. Journal of Volcanology and Geothermal Research, 62: 317-337.

Giggenbach, W., 1975. A simple method for the collection and analysis of volcanic gas samples. Bulletin of Volcanology, 39: 132-145.

Giggenbach, W., 1987. Redox processes governing the chemistry of fumarolic gas discharges from White Island, New Zealand. Applied Geochemistry, 2: 143-161.

Giggenbach, W., 1992. Isotopic shifts in waters from geothermal and volcanic systems along convergent plate boundaries and their origin. Earth and Planetary Science Letters, 113: 495-510.

Giggenbach, W., 1996. Chemical composition of volcanic gases. In: R. Scarpa and R. Tilling (Editors), Monitoring and Mitigation of Volcano Hazards. Springer, Berlin, pp. 221-256.

Giggenbach, W. and Matsuo, 1991. Evaluation of results from Second and Third IAVCEI Field Workshops on Volcanic Gases, Mt Usu, Japan, and White Island, New Zealand. Applied Geochemistry, 6: 125-141. 10.1016/0883-2927(91)90024-J.

Giggenbach, W., Garcia, N., Londono, A., Rodriguez, L., Rojas, N. and Calvache, M., 1990. The chemistry of fumarolic vapor and thermal-spring discharges from the Nevado del Ruiz volcanic-magmataic-hydrothermal system, Colombia. Journal of Volcanology and Geothermal Research, 42: 13-39.

Girina, O., 2012. KVERT Archived Information Releases. http://www.kscnet.ru/ivs/kvert/updates/. http://www.kscnet.ru/ivs/kvert/updates/.

Girina, O., in press. Chronology of the Bezymianny volcano activity in 1956-2010. Journal of Volcanology and Geothermal Research.

Gorshkov, G., 1959. Gigantic eruption of Bezymianny volcano. Bulletin of Volcanology, 34: 261-288.

Hobbs, P., Radke, L., Lyons, J., Ferek, R., Coffman, D. and Casadevall, T., 1991. Airborne measurements of particle and gas emissions from the 1990 volcanic eruption of Mount Redoubt. Journal of Geophysical Research, 96(D10): 18,735-718,752.

Horton, K., Williams-Jones, G., Garbeil, H., Elias, T., Sutton, A.J., Mouginis-Mark, P., Porter, J. and Clegg, S., 2006. Real-time measurement of volcanic SO_2 emissions: validation of a new UV correlation spectrometer (FLYSPEC) Bulletin of Volcanology, 68(4): 323-327.

Izbekov, P., Unpublished results.

Kern, C., Deutschmann, T., Vogel, L., Wohrbach, M., Wagner, T. and Platt, U., 2010. Radiative transfer corrections for accurate spectroscopic measurements of volcanic gas emissions. Bulletin of Volcanology, 72: 233-247. doi:10.1007/s00445-009-0313-7.

Kilinc, A., Carmichael, I., Rivers, M. and Sack, R., 1983. The ferric-ferrous ratio of natural silicate liquids equilibrated in air. Contributions to Mineralogy and Petrology, 83(1-2): 135-140.

Krotkov, N., 2011. OMSO2 Air Mass Factor Corrections. http://so2.gsfc.nasa.gov/Documentation/OMSO2AMFcorrections.pdf.

Lange, R. and Carmichael, I., 1990. Thermodynamic properties of silicate liquids with emphasis on density, thermal expansion and compressibility. Reviews in Mineralogy and Geochemistry, 24(1): 25-64.

Levelt, P., Van den Oord, G.H.J., Dobber, M., Malkki, A., Visser, H., de Vries, J., Stammes, P., Lundell, J. and Saari, H., 2006. The Ozone Monitoring Instrument. IEEE Transactions on geoscience and remote sensing, 44(5).

Levin, V., Shapiro, N., Park, J. and Ritzwoller, M., 2002. Seismic evidence for catastrophic slab loss beneath Kamchatka. Nature, 418: 763-767.

Lopez, T., Carn, S., Werner, C., Fee, D., Kelly, P., Doukas, M., Pfeffer, M., Webley, P., Cahill, C. and Schneider, D., 2012. Evaluation of Redoubt Volcano's sulfur dioxide emissions by the Ozone Monitoring Instrument. Journal of Volcanology and Geothermal Research, Special Issue on the 2009 Redoubt Eruption. doi:10.1016/j.volgeores.2012.03.002.

Martin, R., Sawyer, G., Sampinato, L., Salerno, G., Ramirez, C., Ilyinskaya, E., Witt, M., Mather, T., Watson, I., Phillips, J. and Oppenheimer, C., 2010. A total volatile inventory for Masaya Volcano, Nicaragua. Journal of Geophysical Research, 115. 10.1029/2010JB007480.

Merkulova, M.V., Neill, O.K., Izbekov, P.E. and Dektyarev, A.V., 2010. Physical Characteristics of the 17 December 2009 and 1 June 2010 explosive eruptions of Bezymianny volcano, Kamchatka, Russia, AGU Fall Meeting, San Francisco, California.

Millan, M., 1980. Remote sensing of air pollutants: a study of some atmospheric scattering effects. Atmospheric Environment, 14: 1241-1253. doi:10.1016/0004-6981(80)90226-7.

Mori, T., Mori, T., Kazahaya, K., Ohwada, M., Hirabayashi, J.i. and Yoshikawa, S., 2006. Effects of UV scattering on SO_2 emission rate measurements. Geophysical Research Letters, 33: L17315.

Newman, S. and Lowenstern, J.B., 2002. VolatileCalc: a silicate melt-H_2O-CO_2 solution model written in Visual Basic for excel. Computers & Geosciences, 28(5): 597-604.

Oppenheimer, C., Francis, P. and Stix, J., 1998. Depletion rates of sulfur dioxide in tropospheric volcanic plumes. Geophysical Research Letters, 25(14): 2671 - 2674. doi:10.1029/98GL01988.

Ozerov, A.Y., Ariskin, A.A., Kyle, P., Bogoyavlenskaya, G.E. and Karpenko, S.F., 1997. Petrological-Geochemical Model for Genetic Relationships between Basaltic and Andesitic Magmatism of Klyuchevskoi and Bezymyannyi Volcanoes, Kamchatka. Petrology, 5(6): 550-569.

Pfeffer, M., Langmann, B. and Graf, H.-F., 2006. Atmospheric transport and deposition of Indonesian volcanic emissions. Atmospheric Chemistry and Physics, 6: 2525-2537.

Platt, U. and Stutz, J., 2008. Differential Optical Absorption Spectroscopy Principles and Applications. Springer-Verlag, Berlin - Heidelberg.

Roberge, J., Delgado-Granados, H. and Wallace, P., 2009. Mafic magma recharge supplies high CO_2 and SO_2 gas fluxes from Popocatepetl volcano, Mexico. Geology, 37(2): 107-110. doi:10.1130/G2524A.1.

Rodriguez, L., Watson, I., Edmonds, M., Ryan, G., Hards, V., Oppenheimer, C. and Bluth, G., 2008. SO_2 loss rates in the plume emitted by Soufriere Hills volcano, Montserrat. Journal of Volcanology and Geothermal Research, 173: 135-147. doi:10.1016/j.jvolgeores.2008.01.003.

Scandone, R., Cashman, K.V. and Malone, S.D., 2007. Magma supply, magma ascent and the style of volcanic eruptions. Earth and Planetary Science Letters, 253: 513-529. doi:10.1016/j.epsl.2006.11.016.

Shcherbakov, V.D., Plechov, P.Y., Izbekov, P.E. and Shipman, J.S., 2011. Plagioclase zoning as an indicator of magma processes at Bezymianny Volcano, Kamchatka. Contributions to Mineralogy and Petrology, 162: 83-99. doi:10.1007/s00410-010-0584-1.

Shinohara, H., 2008. Excess degassing from volcanoes and its role on eruptive and intrusive activity. Reviews of Geophysics, 46: RG4005.

Stoiber, R., Malinconico, L. and Williams, S., 1983. The use of correlation spectrometers at volcanoes. In: H. Tazieff and J. Sabroux (Editors), Forecasting Volcanic Events. El Sevier, Amsterdam - New York, pp. 425-444.

Symonds, R.B., Gerlach, T.M. and Reed, M.H., 2001. Magmatic gas scrubbing: implications for volcano monitoring. Journal of Volcanology and Geothermal Research, 108(1-4): 303-341. doi:10.1016/S0377-0273(00)00292-4.

Taran, Y., 2009. Geochemistry of volcanic and hydrothermal fluids and volatile budget of the Kamchatka-Kuril subduction zone. Geochimica et Cosmochimica Acta, 73: 1067-1094.

Taran, Y., Pilipenko, V., Rozhkov, A. and Vakin, E., 1992. A geochemical model for fumaroles of the Mutnovsky volcano, Kamchatka, USSR. Journal of Volcanology and Geothermal Research, 49: 269-283.

Thelen, W., West, M. and Senyukov, S., 2010. Seismic characterization of the fall 2007 eruptive sequence at Bezymianny Volcano, Russia. Journal of Volcanology and Geothermal Research, 194: 201-213.

Tolstykh, M., Naumov, V., Bogoyavlenskaya, G. and Kononkova, N., 1999. The role of Andesite-Dacitic-Rhyolitic melts in the crystallization of phenocrysts in andesite of Bezymyannyi volcano, Kamchatka. Geochemistry International, 37(1): 14-24.

Tuffen, H. and Dingwell, D., 2005. Fault textures in volcanic conduits: evidence for seismic trigger mechanisms during silicic eruptions. Bulletin of Volcanology, 67: 370-387. doi:10.1007/s00445-004-0383-5.

Turner, S.J., Izbekov, P. and Langmuir, C., in press. The magma plumbing system of Bezymianny Volcano: Insights from trace element whole-rock geochemistry and amphibole compositions. Journal of Volcanology and Geothermal Research.

Vaselli, O., Tassi, F., Montegrossi, G., Duarte, E., Fernandez, E. and Bergamashi, F., 2003. Fumarole migration and fluid chemistry at Poás volcano (Costa Rica) from 1998 to 2001. In: C. Oppenheimer, D. Pyle and J. Barclay (Editors), Volcanic Degassing. Geological Society of London, pp. 247 - 262.

Wallace, P.J., 2001. Volcanic SO_2 emissions and the abundance and distribution of exsolved gas in magma bodies. Journal of Volcanology and Geothermal Research, 108(1-4): 85-106.

Wallace, P.J. and Gerlach, T.M., 1994. Magmatic vapor source for the sulfur dioxide released during volcanic eruptions: Evidence from Mount Pinatubo. Science, 265(5171): 497-499.

Werner, C., Hurst, T., Scott, B., Sherburn, S., Christenson, B., Britten, K., Cole-Baker, J. and Mullen, B., 2008. Variability of passive gas emissions, seismicity, and deformation during crater lake growth at White Island Volcano, New Zealand, 2002-2006. Journal of Geophysical Research, 113. 10.1029/2007JB005094.

Werner, C., Doukas, M. and Kelly, P., 2011. Gas emissions from failed and actual eruptions from Cook Inlet Volcanoes, Alaska, 1989-2006. Bulletin of Volcanology, 73: 155-173. doi:10.0117/s00445-011-0453-4.

Werner, C., Kelly, P., Doukas, M., Lopez, T., Pfeffer, M., McGimsey, G. and Neal, C., 2012. Degassing associated with the 2009 eruption of Redout Volcano, Alaska. Journal of Volcanology and Geothermal Research, Special Issue on the 2009 Redoubt Eruption. doi:10.1016/j.jvolgeores.2012.04.012.

Williams-Jones, G., Stix, J. and Nadeau, P., 2008. Using the COSPEC in the Field. In: G. Williams-Jones, J. Stix and C. Hickson (Editors), The COSPEC Cookbook: Making SO_2 Measurements at Active Voclanoes. IAVCEI, pp. 63-119.

Yang, K., Krotkov, N., Krueger, A., Carn, S., Bhartia, P. and Levelt, P., 2007. Retrieval of large volcanic SO_2 columns from the Aura Ozone Monitoring Instrument: Comparison and limitations. Journal of Geophysical Research, 112: D24S43. doi:10.1029/2007JD008825.

Zelenski, M. and Taran, Y., 2011. Geochemistry of volcanic and hydrothermal gases of Mutnovsky volcano, Kamchatka: evidence for mantle, slab, and atmosphere contribution to fluids of a typical arc volcano. Bulletin of Volcanology, 73: 373-394. 10.1007/s00445-011-0449-0.

Zharinov, N. and Demyanchuk, Y., 2011. Assessing the volumes of material discharged from Bezymyannyi Volcano during the1955-2009 period. Journal of Volcanology and Seismology, 5(2): 100-113. 10.1134/S0742046311020072.

CHAPTER 4: Characterization of Volcanic Activity at Karymsky Volcano, Kamchatka, Using Observations of Infrasound, Volcanic Emissions and Thermal Imagery[1]

ABSTRACT

A multiparameter dataset including measurements of infrasound, volcanic emissions and thermal imagery is used to characterize diverse volcanic activity observed during field campaigns in August 2011 and July 2012 at Karymsky Volcano, Kamchatka, Russia. Four end-member activity types are identified visually and quantitatively characterized according to: SO_2 emission rate, ash mass, event duration, peak temperature, thermal energy, infrasound onset and frequency, reduced infrasonic pressure, and acoustic energy. These end-member activity types include: (1) *ash explosions*, consisting of regular, discrete ash explosions which occur approximately every 4 minutes and exhibit relatively high acoustic and thermal energies; (2) *pulsatory degassing*, consisting of pulses of gas emissions producing buoyant plumes with little or no ash; (3) *gas jetting*, consisting of continuous gas emissions, no ash, and associated with a definitive audible roar; and (4) *explosive eruption*, consisting of periods of extended quiescence and apparent vent sealing (~30 minutes to >1 hour) followed by a large explosive eruption producing highly energetic acoustic and thermal signals. Our observations suggest that SO_2 is emitted continuously, though in varying abundance, throughout the field campaigns, while ash is emitted discontinuously and is only associated with certain types of activity. Evidence for a decrease in conduit permeability as a trigger for *ash explosions* and *explosive eruption* activity types is supported by the highly impulsive infrasonic onset and large reduced infrasound pressure (>500 kPa for *explosive eruption*), along with weakened but still detectable SO_2 emission rates prior to eruption. Unique infrasound signals are associated with all four activity types suggesting that these relationships could one day be used to help remotely and continuously detect and characterize volcanic activity at Karymsky and other similar volcanoes using infrasound. We speculate that variations in volcanic activity at Karymsky Volcano are due primarily to changes in magma degassing depth,

[1]López, T., Fee., D., Prata, F., and Dehn, J., Characterization of volcanic activity at Karymsky Volcano, Kamchatka, using observations of infrasound, volcanic emissions, and thermal imagery, prepared for submission in Geochemistry, Geophysics, Geosystems.

which influences conduit permeability through secondary processes such as degassing-induced crystallization and changes in volatile flux.

4.1 Introduction

It has become increasingly evident in the field of volcanology that the best way to advance our understanding of volcanic systems is through the integration of multiple, complementary observational datasets. Numerous studies have successfully integrated observations of seismicity, deformation, infrasound, and/or volcanic emissions to advance understanding of eruptive phenomena at individual volcanoes (Fischer et al., 1994; Lees et al., 2004; e.g. Harris and Ripepe, 2007; Johnson, 2007; Palma et al., 2008; Scharff et al., 2008; Dalton et al., 2010; Fee et al., 2011; Nadeau et al., 2011). Integration of multiple technologies has also been effective for volcano monitoring (e.g. Poland et al., 2008; Werner et al., 2008; Schaefer et al., 2011; Bull and Buurman, 2012; De Angelis et al., 2012). Recent technological advancements in the field of remote sensing allow measurements of volcanic emissions, including SO_2 (and other gases) and ash, at much higher temporal resolutions than was previously possible (Francis et al., 1995; Galle et al., 2002; Edmonds et al., 2003a; Mori and Burton, 2006; Bluth et al., 2007; Prata and Bernardo, 2009). These high temporal resolution emission measurements can then be compared with high temporal resolution geophysical measurements including seismicity, deformation, and infrasound, to (1) remotely characterize volcanic activity, (2) provide a more comprehensive view of volcanic systems, and (3) improve constraints on the physical mechanisms involved in the eruption (e.g. Dalton et al., 2010; Fee et al., 2011; Nadeau et al., 2011). Infrasound is a particularly promising tool to combine with remote sensing techniques. At open volcanic vents, the rapid release and expansion of exsolved volatiles and the eruption of ash and lava accelerate the atmosphere and produce pressure waves. The majority of these pressure waves are low frequency (<20 Hz) and propagate as sound waves termed infrasound (Fee and Matoza, 2013). The source regions for both volcanic emissions and infrasound are typically within the shallow conduit or above the vent, which should permit direct comparisons between volcanic emissions and

infrasound. This is in contrast to seismic and geodetic sources which typically reside at depth and make comparison with volcanic emissions challenging (Fee and Matoza, 2013). Numerous studies have taken advantage of this relationship and found correlations between infrasound and volcanic emissions including ash (Caplan-Auerbach et al., 2010; Fee et al., 2010; Steffke et al., 2010), SO_2 (Fee et al., 2011), and total volatile flux (Dalton et al., 2010). These findings suggest that it may be possible to use infrasound as a tool to detect continuously and characterize volcanic activity, which would significantly advance capabilities for monitoring remote and/or persistently cloudy volcanoes, and could help mitigate eruption hazards.

Here we use high-temporal resolution, coincident measurements of infrasound, SO_2, ash, and thermal radiation collected over two, ten-day field campaigns at Karymsky Volcano to: (1) quantitatively characterize the observed activity, (2) identify unique data signals indicative of certain styles of volcanic activity, (3) refine interpretations of subsurface activity using our multiparameter observations, and (4) evaluate our multiparameter techniques for characterizing diverse and dynamic volcanic activity.

4.2 Karymsky Volcano

Karymsky Volcano (54.0485°N, 159.4425°E, 1536 m), is a predominantly andesitic stratovolcano located within the Eastern Volcanic Front of Russia's Kamchatkan Peninsula (Izbekov et al., 2004) (Fig. 4.1). It is one of the most active and dynamic volcanoes in Kamchatka, experiencing seven multi-year eruptive cycles within the 20th century with activity dominated by regular, small explosive eruptions (frequently described as Vulcanian to Strombolian in appearance), producing ash and gas plumes from several hundred meters up to 5 km above-vent altitudes, and periodic effusion of blocky lava flows (Izbekov et al., 2004). Karymsky Volcano began its current eruptive cycle on 2 January 1996 with an explosive summit eruption of andesitic ash (~62 wt.% SiO_2) and gas, followed ~12 hours later by a phreato-magmatic eruption of basalt to basaltic andesite (~52 wt.% SiO_2) from a new vent within the Akademia Nauk caldera

lake located approximately 5 km south of Karymsky's main edifice (Izbekov et al., 2004). Activity since 1996 has been described as consisting of discrete, explosive eruptions of andesitic ash and gas, along with various styles of degassing frequently accompanied by audible chugging or jetting/roaring (Johnson et al., 1998; Johnson and Lees, 2000; Fischer et al., 2002). These studies largely proposed increased gas pressure combined with vent sealing as the eruption trigger mechanism (Johnson et al., 1998; Fischer et al., 2002; Ozerov et al., 2003). In recent years, weekly to monthly explosive eruptions producing ash clouds to ~6 km above sea level (ASL) have been reported by the Kamchatkan Volcano Eruption Response Team (KVERT, 2012). Additionally, on occasion pilots have observed small lava domes within Karymsky's summit (P. Firstov, pers. comm.); however, it is not clear how frequently these occur and what their relation is with other activity observed. The range of activity exhibited and frequent eruptions make Karymsky Volcano a natural volcano laboratory for investigating the relationships between various styles of volcanic activity, with the potential to constrain subsurface processes.

4.3 Methods

Two field campaigns were conducted in 2011 and 2012 to characterize quantitatively volcanic activity at Karymsky Volcano. During the field campaigns, volcanic activity was recorded using the following methods: (1) infrasound was recorded using 3-4 and 5-6 element arrays of National Center for Physical Acoustics (NCPA) digital microphones (e.g. Fee and Matoza, 2013), in 2011 and 2012, respectively, (2) a NicAIR thermal infrared camera with broadband (7-14 μm), 8.6, 10, and 11 μm filters was used to remotely detect and quantify both SO_2 and ash (Prata and Bernardo, 2009), (3) SO_2 emissions were measured using a scanning FLYSPEC (Horton et al., 2006) ultraviolet spectrometer system (Galle et al., 2002; Edmonds et al., 2003a), and (4) a FLIR thermal infrared camera was used to record high sample frequency thermal observations of the volcanic emissions and hot eruption products (Spampinato et al., 2011) (Figs. 4.1b, 4.2). All remote sensing instruments were deployed at the same approximate location ~3.65

km southeast of Karymsky's summit (54.02445°N, 159.48032°E, 605 m), while the infrasound array was located in a vegetated area nearby (Fig. 4.1b). We note that at these relatively long sample distances, significant molecular scattering of UV and IR radiation will bias measurements to lower than actual values. Several factors contribute to measurement error for the various remote sensing instruments such that throughout this study we focus on the relative differences and/or similarities in the observed parameters over time and with respect to the end-member activity types. The equipment and methods for each technique are described in the following sections.

4.3.1 FLIR Thermal Imaging Camera

All objects with temperatures greater than absolute zero emit radiation as a function of temperature and emissivity, according to the Stefan-Boltzmann Law. An ideal radiation source, referred to as a blackbody, is one that absorbs and re-emits all incident radiation. Planck's Law relates temperature and radiance as a function of wavelength for a blackbody, and serves as the basis of thermal remote sensing. Application of these principles allows thermal camera radiance measurements to be used to remotely estimate pixel integrated brightness temperatures. Such measurements have been used extensively by ground-based instruments to successfully characterize behavior of hot eruptive material (Harris et al., 2007). In particular direct correlations between thermal energy and eruptive mass have been found (Pieri and Baloga, 1986; Ripepe et al., 2005; Scharff et al., 2008). In this study we used a FLIR model A320 thermal imaging camera to acquire ~5 Hz sample frequency thermal imagery over a broadband wavelength region from 7.5–13 microns, in an effort to characterize volcanic activity and estimate thermal energy released (Fig. 4.2). This thermal camera has a 25° x 18.8° field of view and uses a 320 x 240 pixel focal plane array detector and an uncooled microbolometer. For our study, a sample slant distance of ~3780 m and a camera inclination angle of 17° resulted in an image center pixel resolution of 5.2 m x 5.7 m. Data were analyzed using FLIR ThermaCam Researcher Professional software, which uses operator-input distance to the source, emissivity, ambient temperature and ambient relative humidity (both measured

using a hand-held thermometer/hygrometer in the field) along with the LOWTRAN radiative transfer model to convert measured radiance into temperature according to Planck's Law (Spampinato et al., 2011). Emissivity was estimated to be 0.98, assuming a non-transmitting source such that *emissivity = 1 – reflectance* (Spampinato et al., 2011), and the average reflectance of andesite and water from the ASTER Spectral Library for the 8-14 μm wavelength region (Baldridge et al., 2009) to represent a mixed-phase plume composed predominantly of condensed water vapor and silicate ash. We make the simplifying assumptions that a single emissivity can describe a mixed-phase plume, and that emissivity, ambient temperature, and relative humidity remain constant for each measurement period (~1 hour). These assumptions combined with the unconstrained effects of solar reflection (Spampinato et al., 2011), absorption and scattering by gases and aerosols (Sawyer and Burton, 2006), and subpixel temperature variations (Dozier, 1981; Rothery et al., 1988; Harris et al., 1997), lead to uncertainties in the derived temperatures, typically resulting in derived temperatures being lower than at-source kinetic temperature (Spampinato et al., 2011). Acknowledging these limitations all temperatures reported here should be considered estimates, and we focus on evaluating relative changes over time.

Time series measurements of temperature observed in the region immediately above the vent were evaluated to allow comparisons with volcanic emissions and infrasound to be made. Within the sample period each image was analyzed for the maximum pixel temperature within a region directly above the vent ~1 pixel (~5.7 m) in height by 40 pixels (~228 m) wide, approximately equivalent to the width of the summit region. Peaks in maximum temperature corresponding with individual pulses in activity were evaluated over the analysis periods. In addition to temperatures above the vent, the thermal radiation energy released from individual explosions and/or degassing events (E_{TR}, Joules) can be calculated from the thermal imagery data to provide insight into explosion style following the methods of Marchetti et al. (2009). Specifically, eruption onset is associated with high initial ascent speeds due to the momentum-driven release of

pressurized material, referred to as the gas-thrust or jet portion of the plume. As the plume entrains ambient air, the plume decelerates and transitions to buoyancy-controlled ascent (Wilson and Self, 1980). The total thermal energy of an eruption is composed of the energy associated with both the gas thrust and buoyant portions of the plume, and can be used to compare eruptive events for a particular volcano or among different volcanoes to provide insight into the eruption processes (Marchetti et al., 2009). By integrating the Stefan-Boltzmann equation over the duration of the explosion, Marchetti et al. (2009) derive the following equation, which we use to calculate thermal energy from events at Karymsky Volcano:

$$E_{TR} = \int_{t=t_i}^{t=t_f} A\sigma\varepsilon\left(T_a^{\,4} - T_t^{\,4}\right)dt \qquad (1)$$

In Equation 1, t_i and t_f, are the event onset and completion times, respectively, A is the analysis region (m^2), σ is the Stefan-Boltzmann constant (5.6697 x 10^{-8} W m^{-2} K^{-4}), ε is emissivity, T_a is the pixel integrated temperature (K), and T_t is the threshold (i.e. background) temperature (K). Event onset and completion times were selected by manual evaluation of the thermal waveforms (i.e. maximum temperature over time). Event onset times were clearly identified in the data by sharp increases in maximum temperature, while event completion times were chosen when the maximum temperature decreased to background temperature or a new event began. The area of the analysis region (~440-860 m x ~580-1100 m) includes the region directly above the vent to the top of the field of view, and varied depending on atmospheric conditions (i.e. wind direction, wind speed, cloud cover) and plume geometry at the time of observation. This region was selected to include as much of the gas-thrust and plume region as possible, while excluding background clouds. We note that for relatively large eruptions (i.e. *explosive eruption*, Section 4.4.4) in which the plume altitude exceeded above-vent altitudes of ~1100 m and pass out of the instrument field of view, the thermal energy will be underestimated. Clear

sky conditions, which were common during the field campaigns, exhibited temperatures of -20°C (the lower FLIR detection limit). We therefore use a threshold value of -20°C in these calculations and note that in the presence of background clouds thermal energy will be overestimated relative to observations made under clear skies. Cumulative thermal radiation energy released over a specified analysis period can be calculated using a similar technique. In this method thermal data are divided into consecutive 30 second time windows. Thermal radiation energy for each time period is then calculated for the analysis region for each time period, and the values are then summed together to find cumulative thermal radiation energy.

4.3.2 NicAIR IR Camera for Detection of Ash and SO_2

An improved multi-spectral infrared imaging camera (NicAIR) originally described in Prata and Bernardo (2009) is used to calculate ash masses, SO_2 masses, SO_2 emission rates, and plume ascent speeds for the various styles of volcanic activity observed at Karymsky Volcano (Fig. 4.2). The NicAIR uses a commercially available thermal infrared camera core, with a 640 x 512 pixel array detector, a 26° x 20° field of view, and an uncooled microbolometer with good temperature sensitivity in the region of 8-12 μm. Three filters centered at 8.6, 10, and 11 μm with bandwidths from 0.5-1.0 μm, and a broadband filter with a bandwidth from 7-14 μm, are used to detect and quantify fine ash (1-16 μm radii) and SO_2 column densities (g/cm^2). These filters were selected to exploit the characteristic infrared absorption/emission features of SO_2 and silicate ash to allow these emissions to be distinguished from meteorological clouds using radiative transfer calculations. Specifically, SO_2 has a strong absorption/emission peak at 8.6 μm, while silicate ash preferentially absorbs/emits IR radiation at 12 μm relative to 11 μm and 10 μm; this is in contrast to a (mixed phase) meteorological cloud which absorbs IR radiation from 10 to 12 μm in an opposite manner to silicate particles (Prata, 1989). The reader is referred to Prata and Bernardo (2009) and Prata and Bernardo (submitted) for figures depicting the absorption spectra of ash and SO_2, respectively. The temperature differences between the plume and background sky for each of the filter measurements

allows both SO_2 and ash column densities to be retrieved. The filters are mounted on a rotatable "filter wheel" and during operation the camera acquires passive radiation of the image target for ~1 second by cycling through each of the four filters. Following each round of filtered image acquisitions a "field calibration" is conducted in which of the camera views a temperature controlled black-body shutter through each filter to account for the effects of changing environmental conditions. This results in a maximum sample rate of approximately one sample every ~5 seconds, where one sample consists of measurements through each of the four filters and the black-body shutter. The field calibration measurements are used along with pre- and post-experiment laboratory calibrations, and a radiative transfer model, to allow both SO_2 and ash column densities to be quantified. In the radiative transfer model, absorption and emission of SO_2 and silicate ash are considered, while scattering of radiation is ignored (Prata and Bernardo, submitted). Since the camera did not utilize the 12 μm filter (as in Prata and Bernardo, 2009) and instead used filters at 11 μm and 10 μm, the ash retrieval scheme was modified to use optical constants (i.e. extinction coefficient, single-scattering albedo, and phase function) appropriate for these wavelengths as calculated using Mie theory. For the purpose of the radiative transfer calculations ash particles are assumed to be andesitic, spherical and log-normally distributed, and no account is taken of shape, asperities or contaminating minerals, water or ice (unlikely to be present in these plumes). These assumptions suggest that the retrievals of ash column densities and derived masses should only be considered estimates with errors approaching 100% in the worst cases of opaque plumes, due to either the large number of particles or due to the individual particles being large. The ash masses are restricted to particle size ranges of 1-16 μm radii. The reader is referred to Prata and Bernardo (2009) for more details on an earlier version of the camera and the ash column density retrieval, and to Prata and Bernardo (submitted) for more details regarding the SO_2 column density retrieval.

The acquired time series of SO_2 and ash column density image data can be used to calculate plume ascent speeds, SO_2 emission rates, cumulative SO_2 mass, SO_2 event

masses, and ash masses. Plume ascent speeds (m/s) are calculated using a multi-step process. First, individual pixel sizes for the camera geometry and experimental setup are calculated using the known distance to source, camera geometry, and camera detector dimensions. Single channel images are then analyzed to identify the plume-top edge at many locations along the plume. The average plume-top height along with its respective standard deviation is then calculated. The change in height of the plume divided by the temporal duration (time between consecutive images) provides an estimate of the plume ascent speed at the plume top. When these plume heights are plotted against time, clear linear trends can be seen with slopes representing approximately constant plume ascent speed consistent with buoyant convection. In between these trend lines plume height varies erratically with time, due to the plume reaching neutral buoyancy or sometimes because the plume top leaves the field of view of the camera. Second, multiple (up to 20 per image) horizontal cross-sections of plume SO_2 column density integrated over the plume width (referred to throughout as plume SO_2 cross-sections) are made from the base to the top of the plume within each image (Fig. 4.3). Sequential images are then analyzed for spatial trends in SO_2 column density for each cross-section. These values are used along with the appropriate (time-dependent) plume ascent speeds to estimate emission rates for individual explosions and/or continuous degassing activity. SO_2 emission rates are calculated by multiplying plume SO_2 cross-sections by plume-top ascent speeds. SO_2 emission rates are calculated using multiple SO_2 cross-sections per image, and the average emission rate per image is selected as the most representative. In some cases, discrete degassing events allow SO_2 masses to be calculated. These calculations can be done by first selecting images in which as much of the SO_2 emitted from a particular event is contained within the image as possible. Then for each pixel within the image containing SO_2, the SO_2 column density (g/m^2) is multiplied by the pixel size (m^2) and then summed together to get a total event SO_2 mass. Precision in retrieved SO_2 column density is ± 0.2 g/m^2. Absolute error in SO_2 column density and derived emission rates are poorly constrained and estimated to be <50% (Prata and Bernardo, submitted). We note that the NicAIR emission rate analysis has the significant advantage of not requiring an

independent plume speed estimate, which are often cited as contributing up to 40% error in SO_2 emission rate measurements (Stoiber et al., 1983).

The same methods used to calculate SO_2 event mass (above) are used to calculate ash masses, where ash column densities are used in place of SO_2 column densities. For some activity types, abundant ash significantly attenuated IR radiation and prevented SO_2 and ash column densities from being accurately retrieved. In these cases, plume imagery acquired following the initial event, once ash had dissipated to the point that the plume was no longer opaque, could be used to estimate ash and/or SO_2 masses associated with these events. We consider the calculated ash and/or SO_2 masses to be conservative minimum estimates when abundant ash was present.

4.3.3 FLYSPEC UV Spectrometer System

A FLYSPEC scanning ultraviolet (UV) spectrometer system (Fig. 4.2; Horton et al., 2006) was used to measure SO_2 column density within Karymsky's plume in an application of the Lambert-Beer law (e.g. Platt and Stutz, 2008). Measurements of UV absorption by the volcanic plume are fit to a calibration curve generated from field measurements of cells containing known concentrations of SO_2 viewed in front of the background (SO_2-free) sky in the 305-315 nm wavelength region (Horton et al., 2006) to calculate SO_2 column density. The FLYSPEC collects repeated series of SO_2 column density measurements (ppmm, where 1 ppmm $SO_2 \sim 2.663 \times 10^{-6}$ kg/m^2 SO_2; Gerlach, 2003) perpendicular to plume motion which are then integrated over the plume width and multiplied by the plume speed to derive SO_2 emission rates. Accurate emission rate measurements require a plume geometry in which clear (SO_2-free) sky is present on each side of the plume such that complete plume SO_2 cross-sections are acquired. The FLYSPEC was deployed to collect SO_2 column density measurements via horizontal scans immediately above Karymsky's vent to allow minimal time delay between the SO_2 emission rates, infrasound, and thermal energy produced by Karymsky Volcano. Plume width is calculated geometrically using the instruments' scan angles, and known sample

and source locations. The FLYSPEC's 90° scan position was centered immediately above Karymsky's vent such that a typical scan would range from 80-100° at 1° increments. Considering the FLYSPEC's 2° circular field of view, the approximate scan width covers an area ~1330 m wide by ~136 m high (Fig. 4.4). The plume scan range, combined with the time to make an individual column density observation (~0.3 to 3 per second, depending upon UV radiation intensity) results in a total time to record the FLYSPEC's SO_2 emission rate of between ~20 seconds and ~3 minutes. On several days during each field campaign sampling conditions were favorable, with the plume rising vertically from the vent before bending in the downwind direction, such that accurate SO_2 column density measurements were possible. On several days strong winds blew the plume down the flanks of the edifice and directly towards the remote sensing instruments, such that derived emission rates are inaccurate. We used the FLIR imagery to provide a visual record of the emissions activity, to assist in interpretation of FLYSPEC SO_2 column density scan measurements, and to identify measurements collected under poor sample conditions and remove the resulting SO_2 emission rates from our analysis (Fig. 4.4). Plume ascent speeds for time periods with corresponding FLYSPEC SO_2 measurements were calculated using FLIR image data, known distance to source, and plume parcel tracking methods (Williams-Jones et al., 2008). The time period over which it took an individual plume parcel to ascend a fixed distance (~150-200 m) above the vent was manually tracked in the FLIR imagery. For typical activity, multiple ascent speeds were calculated per minute and the average ascent speed calculated for the duration of a single FLYSPEC scan was used in the SO_2 emission rate calculations.

The error in FLYSPEC SO_2 emission rates depends on the combined error in SO_2 column density, plume width, and plume ascent speed measurements (Stoiber et al., 1983; Lopez et al., in press). Of these factors, the error in SO_2 column density due to molecular scattering and dilution is likely the most significant (Mori et al., 2006; Kern et al., 2010). Using a radiative transfer model, Kern et al. (2010) estimate the error associated with SO_2 column density measurements for ash-free plumes considering various sampling conditions including: plume opacity, distance to plume, SO_2 column density, and

wavelength region analyzed. They find that for conditions similar to those described here (slant geometry, ~4 km distance, SO_2 column density <400 ppmm, and a wavelength of 310 nm [the center of our fitting window]) SO_2 column densities will be underestimated by ~30% for transparent plumes and overestimated by ~40% for aerosol-rich plumes (i.e. condensed plumes) (Kern et al., 2010). Considering these factors we estimate error in SO_2 column density for ash-free plumes to be ±40%. We estimate error in plume width of ±25%, and error in plume ascent speeds calculated from plume parcel tracking methods of ±30% (Williams-Jones et al., 2008). The total error in SO_2 emission rates for transparent to translucent, ash-free plumes is estimated from the uncertainties in these individual factors (square root of sum of squares) to be ±56%.

The presence of ash in plumes is known to significantly scatter and attenuate radiation (Millan, 1980; Andres and Schmid, 2001), which can decrease the pathlength of UV radiation that passes through the plume, and result in an underestimation of SO_2 column density (C. Kern, pers. comm.). A laboratory experiment was conducted by Andres and Schmid (2001) to determine the effects of ash on SO_2 column density measurements by a correlation spectrometer (COSPEC), the instrument upon which the FLYSPEC was based (Stoiber et al., 1983; Horton et al., 2006). They found that the presence of ash in a plume less than 50% opaque would cause SO_2 column density to be underestimated by ~10%, while plumes greater than 50% opaque would have significantly greater error. It is likely that in a field setting, such as described here, involving a significantly longer atmospheric path (e.g. ~4 km) and where scattered UV radiation is employed as the radiation source, the error may be much greater (C. Kern., pers. comm.). Because the actual plume opacity cannot be determined from FLYSPEC measurements the amount that the SO_2 column density has been underestimated cannot be constrained, though for visibly opaque (i.e. dark) plumes underestimation by a factor of two or more may be reasonable (C. Kern, pers. comm.). During SO_2 measurement collection at Karymsky Volcano, we noticed that scans corresponding with dark (visibly opaque to nearly opaque) plumes resulted in high noise levels such that clean SO_2 peaks could not be identified, resulting in non-detection by the FLYSPEC. Therefore some measurements of ash-rich plumes are eliminated from

analysis in this manner. We propose that the remaining SO_2 column densities and derived emission rates collected for plumes containing ash (e.g. *ash explosions* and *explosive eruption* activities described in Sections 4.4.1 and 4.4.4) will be significantly underestimated relative to ash-free plumes, with the actual uncertainties unconstrained. In addition, high noise from poor sampling conditions including: ash-rich plumes, condensed plumes, low UV radiation, ponding of SO_2, resuspended ash, etc. can reduce the plume SO_2 signal to noise and complicate data interpretation, further inhibiting accurate SO_2 emission rate calculations. In these cases we identify "noisy scans" (marked as gray columns in Figs. 4.5, 4.12) and exclude these data from analysis.

4.3.4 Infrasound Data and Methods

Infrasound was continuously recorded at a 125 Hz sample rate during the 2011 campaign using a 4-element array of NCPA digital microphones with flat response between 0.02 and 250 Hz. The array was installed approximately 4 km southeast of Karymsky's summit vent in areas with moderate vegetation to reduce wind noise (Fig. 4.1b). Microphones were distributed in a centered-triangle array to permit source azimuth and trace velocity (propagation velocity across the array) identification, allowing volcanic infrasound to be distinguished from noise and infrasound produced by other sources. In 2012, five NCPA digital microphones were deployed in a more sparse network-like configuration between ~2-4 km northwest of the active vent (Fig. 4.2). Each stand-alone digital microphone consists of a piezo-ceramic acoustic sensor, onboard digitizer, and GPS connected to a battery. The microphones were able to record pressure signals between ±125 Pa and ±750 Pa for 2011 and 2012, respectively.

To quantify the eruption energetics at Karymsky Volcano, and for comparison with other volcanoes, we calculate the acoustic energy and reduced infrasonic pressure for individual eruptive events. The acoustic energy of a volcanic source, E_a, can be determined by integrating the acoustic intensity over time and the region through which it propagates. The acoustic intensity, I, is the average rate of flow of energy through a unit

area normal to the direction of propagation, $I=p^2/\rho c$, where p is the excess pressure, ρ the density of the medium, and c is the sound speed. The acoustic energy is then found by:

$$(2) \qquad E_a = \frac{\Omega}{\rho c}\int_0^T \Delta p^2(t)dt$$

In Equation 2, Ω is the area through which sound passes, ρ is the density of the atmosphere, $\Delta p(t)$ is the change in pressure as a function of time, and T is the duration of the signal of interest. This is a common technique in volcano acoustics and the assumptions have been well-documented (Johnson and Ripepe, 2011; Fee and Matoza, 2013). Reduced pressure ($p_{red} = p \times r/r_{ref}$) is the infrasound pressure, p, scaled to a common source distance (r_{ref} = 1 m here), where r is the distance to the source. This equation for reduced pressure allows comparison between different volcanoes and recording locations. Event onsets and endings are selected by manual inspection of the pressure waveform rising above and then falling back to the background pressure. In addition to acoustic energies calculated for individual events, cumulative infrasound energy is calculated for specified time periods. To accomplish this analysis, data are first band-pass filtered between 0.3-10 Hz for low frequency activity, and 15-60 Hz for high frequency activity. Acoustic energies are then calculated for 30 second time windows and progressively summed to get cumulative values. Infrasound array processing was performed using standard methods to determine coherent infrasound signals and trace velocity. Spectrogram estimates are obtained using Welch's modified periodogram method. Filtering of infrasound data is performed using a using a two-pole, zero-phase Butterworth filter.

4.4 Results

Field campaigns were conducted from 13-24 August 2011 and 17-30 July 2012. During these time periods, four end-member volcanic activity types were observed which we define as: (1) *ash explosions*, (2) *pulsatory degassing*, (3) *gas jetting*, and (4) *explosive eruption*. All four activity types were observed during the 2011 field campaign, reflecting an active and dynamic system. Specifically, during the 2011 field campaign multiple hours of *ash explosions, pulsatory degassing* and *gas jetting* were observed, along with seven *explosive eruption* events. All four activity types were clearly detected acoustically and several were observed by the various remote sensing instruments. In contrast, the activity in 2012 was dominated by *gas jetting*, with only a few minor *ash explosions* observed. We select four ~40 minute time periods that: (1) best demonstrate the four end-member activity types, and (2) have the most complete multiparameter observations. Figure 4.5 shows representative visual images, infrasound pressure, maximum temperature, and SO_2 emission rates for each of the selected activity types. In the following sections we characterize the four end-member activity types using quantitative observations of ash mass, SO_2 emission rates, temperature, thermal radiation energy, reduced infrasound pressure, acoustic energy, and plume ascent speeds. We report values for maximum, mean, and one standard deviation above/below the mean, when possible. An infrasound-based timeline depicting the 2011 field campaign, the six infrasonically-observed *explosive eruptions*, and the example end-member activity type time periods can be seen in Figure 4.6. Infrasound spectrograms for each activity type are displayed in Figure 4.7, permitting frequency-based interpretations.

4.4.1 Ash Explosions

Activity referred to as *ash explosions* was visually characterized as consisting of discrete ash explosion occurring every 4 minutes on average, that either jet or roil out of the vent, and produce plumes to 500-1500 m (above-vent) altitudes (Fig. 4.5a). Explosions were often accompanied by an audible “crack” at the onset. The 40-minute example period representing typical *ash explosion* activity spans from 20:10-20:50 (all times as UTC) on

15 August 2011. During this time period ~26 events were observed in the FLIR imagery, with a maximum event duration of 4.3 minutes and a mean duration of 1.9±0.8 minutes. In most cases, events were discrete, with periods of quiescence up to ~100 s between events, though on approximately seven occasions new events began before the prior event had ceased. Maximum and mean peak temperatures of 230°C and 120±60°C, along with maximum and mean thermal energies for individual events of 1.0×10^{10} J and $5.3 \times 10^{9} \pm 2.2 \times 10^{9}$ J, were observed during this time period. Maximum and mean SO_2 emission rates of 1.3 kg/s and 0.7±0.4 kg/s, respectively, were calculated for this time period from FLYSPEC data. Unfortunately, only two out of four potential NicAIR filters were selected at this time (8 μm and broadband), such that ash mass retrievals were not possible. Maximum and mean plume ascent speeds of 9.0 and 7.4±1.0 m/s were calculated using parcel-tracking methods with FLIR data. Infrasound signal onsets were impulsive, with individual events producing maximum and mean reduced infrasonic pressures of 21,500Pa and 6240 Pa, respectively. Infrasound codas consisted of relatively high-amplitude, sustained signal coincident with visible ash jetting. The infrasound onsets were broadband in frequency (~0.1-20 Hz), followed by jetting focused between ~0.1-5 Hz (Fig. 4.7; Table 4.2). Peaks in both temperature and infrasound pressure occurred near coincidentally for most events of this time period, though no correlation in peak amplitude between these datasets was observed. Cumulative sums of acoustic energy and thermal radiation energy this analysis period were 1.8×10^{7} J and 1.6×10^{11} J, respectively.

4.4.2 Pulsatory Degassing

Pulsatory degassing activity is described by individual pulses of volcanic gas emissions with little or no ash, low altitude (100-200 m) plumes, and no associated audible sound. The selected time period representing typical *pulsatory degassing* activity is 16 August 2011 from 21:00-21:40 (Fig. 4.5b, 4.6). During this time period ~17 degassing pulses were identified in the FLIR imagery, with at least three of these truncated by subsequent events. Mean event durations of ~1.5 minutes were shorter than periods of quiescence

between events (~2.9 minutes). Maximum and mean peak temperatures of 160 and 70±40°C, and mean thermal radiation energy of 3.4 x 10^8 J were observed during this time period. Poor plume geometry (blown-over plume) from relatively strong winds prevented SO_2 emission rate calculation from FLYSPEC data using the horizontal scan geometry. However, SO_2 measurements were collected by the NicAIR IR camera and distinct pulses in SO_2 emission rates with a mean value of 1.4±0.8 kg/s were observed. No obvious correlation between SO_2 emission pulses and infrasound pressure and/or maximum temperature were apparent (Fig. 4.5b). Upon inspection of the 40-minute analysis period, the infrasonic signals for *pulsatory degassing* pulses have emergent onsets and cigar-shaped codas that taper at both ends (Fig. 4.5b). Maximum and mean peak reduced infrasound pressures were 500 Pa and 130±130 Pa, and mean acoustic energies were ~6.8 x 10^3 J. Dominant infrasonic frequencies for *pulsatory degassing* were between ~1-20 Hz (Fig. 4.7). Plume ascent speeds (in this case reflecting horizontal motion) were calculated from NicAIR data with maximum and mean values of 8.0 and 6.4±0.7 m/s (Table 4.2). Cumulative acoustic energy and thermal radiation energy for this analysis period were 3.4 x 10^5 J and 8.3 x 10^9 J, respectively.

4.4.3 Gas Jetting

Gas jetting activity consisted of continuous degassing, with pulses of more vigorous degassing overprinting the background emissions, accompanied by strong audible jetting or roaring. Like *pulsatory degassing* little or no ash emissions were associated with this activity type (Fig. 4.5c). While *gas jetting* activity was observed during the 2011 field campaign (most easily recognized by its audible roar), poor sampling conditions including ground-hugging plumes and/or plumes traveling directly towards the instruments prevented accurate temperature and SO_2 retrievals in 2011, therefore we use measurements collected under favorable conditions in 2012 for this analysis. The time period selected was 21 July 2012 from 22:30-23:10. Using FLIR maximum temperature waveforms for this activity we selected event durations based on periods of more vigorous degassing, and find ~16 pulses during the 40-minute analysis period (Fig. 4.5c).

Pulses of more vigorous degassing had an average duration of ~3.5 minutes. Periods of weaker degassing between pulses were relatively short with an average duration of ~20 seconds. Vigorous degassing produced relatively high maximum and average ascent speeds (12.6 and 9.2±1.6 m/s, respectively). Maximum and average peak temperatures associated with *gas jetting* were 80°C and 40±20°C, respectively, and the mean thermal energy produced was 6.6 x 10^7 J. Infrasonic signals were emergent exhibiting distinct cigar-shaped amplitudes, with maximum and mean reduced infrasound pressures of 160 and 110±30 Pa, respectively. Mean acoustic energies were 6.0 x 10^3 J. *Gas jetting* activity exhibited a strong component of high frequency infrasound, in fact the signal was focused above the infrasound band into the audible region between ~15-60 Hz (Fig. 4.7). A general temporal agreement between waxing and waning of infrasonic pressure and maximum temperature was observed (Fig. 4.5c). FLYSPEC SO_2 emission rates for this time period exhibited noticeable temporal variations with periods of higher emissions occasionally corresponding in time with periods of higher maximum temperatures and infrasound pressures. Cumulative acoustic energy and thermal radiation energy for this analysis period were 6.7 x 10^5 J and 2.0 x 10^9 J, respectively.

4.4.4 Explosive Eruption

Explosive eruption activity was characterized by periods of relatively long duration (~30 minutes to >1 hour) quiescence, with no visible emissions, followed by an explosive, eruption producing ash-rich plumes to >2000 m and centimeter to meter (or greater) sized pyroclastic bombs that rolled down the flanks of the edifice (Fig. 4.5d). *Explosive eruptions* viewed at night showed abundant incandescent material that mantled the edifice following eruption, indicative of involvement of juvenile magma (Fig. 4.8). Seven *explosive eruption* events were observed visually during the 2011 field campaign. The time period encompassing the *explosive eruption* event that we selected as representative is 17 August 2011 from 01:38-02:18. This eruption was preceded by ~40 minutes of quiescence. During the quiescent period emissions were not visible in FLIR imagery (no ascent speeds calculated), but clear SO_2 peaks were detected by the FLYSPEC resulting

in average SO_2 emission rates of 0.3±0.3 kg/s (Fig. 4.5d). No infrasound or elevated temperatures were apparent leading up to the eruption. The explosive eruption commenced at 01:55 and had a duration of ~1.7 minutes, at which point the initial eruption was truncated by a secondary eruption according to FLIR thermal waveform, thermal imagery, and infrasound. The initial explosive eruption, as well as two secondary eruption pulses, reached peak temperatures in excess of 350°C, the FLIR temperature saturation range. Average temperatures for this time period are not considered as the actual explosive eruption only comprises a small portion of the 40-minute analysis period. The eruption produced a very high amplitude, impulsive infrasonic pressure signal, which clipped the microphones at ±125 Pa at a distance of ~4 km, and resulted in a reduced infrasound pressure of >500,000 Pa. The estimated acoustic energy for this event was >5.4 x 10^9 J. Abundant ash produced in the first few minutes of the eruption decreased UV signal to noise such that SO_2 peaks were not detected (gray bars in Fig. 4.5d). Following this time period, clear plume SO_2 peaks were detected, allowing SO_2 emission rates to be calculated; however, these values are likely underestimated due to the presence of ash in the plume. The maximum and mean SO_2 emission rates calculated for the entire analysis period were 2.3 kg/s and 0.7±0.6 kg/s, respectively. Unfortunately, only two of four NicAIR IR camera filters were being used during this time period, preventing the potential retrieval of ash masses for this eruption. A maximum plume ascent speed corresponding with the initial explosive eruption of 74.4 m/s was calculated. Cumulative acoustic and thermal radiation energy for this analysis period were 4.9 x 10^9 J and 4.5 x 10^{10} J, respectively. These observations are summarized in Table 4.2.

4.4.5 Hybrid Activity

In addition to the four end-member activity types, there was also activity representing a mix or "hybrid" of *ash explosion, pulsatory degassing,* and *gas jetting* activity (Fig. 4.9). This activity was highly variable but can generally be characterized as continuous to pulsatory emissions of gas and/or ash, and was often observed following *explosive eruptions* and during transitions between the end-member activity types. While not an

end-member, *hybrid* activity was the dominant activity observed (Fig. 4.6). An example of the infrasound and thermal signals observed during a 40-minute period of hybrid activity on 18 August 2011 from 07:15-07:55 can be seen in Figure 4.9 and is summarized in Table 4.2. During this time period approximately eight pulses of ash and/or gas emissions occurred, with event durations lasting ~52 seconds on average and inter-event quiescent periods lasting from <2 seconds to greater than 10 minutes. During this time period a maximum peak temperature of 220°C was observed. The estimated mean thermal energy associated with individual events was 8.7×10^8 J. Both ash and SO_2 masses were calculated from NicAIR data with a mean ash mass for individual pulses of activity of 1000±343 kg and maximum ash mass of 1080 kg (Figs. 4.9, 4.10; Table 4.2). While no high temporal resolution SO_2 emission rate data were acquired for this time period, SO_2 masses were acquired using the NicAIR camera for individual degassing events with maximum and mean masses of 250 and 170±50 kg, respectively. The infrasonic signals for this time period have mixed characteristics. Infrasound onsets ranged from emergent to impulsive, with ash-rich events producing impulsive onsets compared to more emergent gas-rich events. The maximum reduced infrasound pressure associated with these events was 1960 Pa, while the average value was 750 Pa (Table 4.2).

4.5 Discussion

4.5.1 Evaluation of Acoustic and Thermal Radiation Energy

Marchetti et al. (2009) analyze variations in relative thermal and acoustic energies for four volcanoes exhibiting explosive eruptive behavior and deduce that such comparison can be used to distinguish eruption style. In particular ash-rich eruptions of higher viscosity magma at Santiaguito and Fuego Volcanoes (Guatemala) exhibit thermal energies on the order of 10^7-10^{10} J. These relatively high thermal energies are related to a significant buoyant rise portion of the plume that Marchetti et al. (2009) presumed to be due to relatively high fragmentation of the magma resulting in more efficient transfer of thermal energy to the plume. In contrast, explosions of gas and volcanic bombs

interpreted to be due to gas slug bursting within low viscosity magmas at Stromboli (Italy) and Villarica (Chile) Volcanoes produce comparatively lower thermal energies on the order of 10^5-10^7 J. They attribute these lower thermal energies to less efficient transfer of thermal energy to the plume due to larger pyroclasts and weaker fragmentation. We conduct a similar analysis and plot the relative thermal radiation and acoustic energies associated with the four end-member and hybrid activity types observed at Karymsky Volcano in Figure 4.10. The various activity types cluster into distinct groups. *Pulsatory degassing* activity shows the lowest range in acoustic energies (~10^2-10^4 J) of the four types, while *gas jetting* has a moderate range in acoustic energy between ~10^3-10^4 J. Conversely, *pulsatory degassing* has slightly higher thermal energy (~10^7-10^9 J) than *gas jetting* (~10^7-10^8 J), which has the lowest thermal radiation energy observed. *Ash explosions* and *explosive eruption* activity exhibit relatively high and similar thermal radiation energies (10^9-10^{10} J) compared with the degassing-dominated activity types; while *explosive eruption* activity has significantly higher acoustic energies (10^{10} J) than *ash explosions* (10^5-10^7 J). We note that thermal and acoustic energies for *explosive eruption* are underestimated due to saturation of the relative sensors, while the thermal radiation energies for *ash explosions* are overestimated relative to the other types due to the presence of background clouds in the image analysis region. Additionally, *explosive eruption* thermal energies are further underestimated because much of the buoyant plume rose above and out of the camera field of view. This effect is likely significant for these explosive events. If the activity types observed at Karymsky Volcano are compared with acoustic and thermal radiation energies calculated by Marchetti et al. (2009) for Fuego, Santiaguito, Stromboli and Villarica Volcanoes, it can be seen that the *ash explosions* observed at Karymsky Volcano are quite similar, though with slightly more thermal energy (possibly an artifact of the background clouds), than the explosions observed at Fuego Volcano (Fig. 4.11). The Fuego explosions were described as being ash-rich, acoustically impulsive, occurring every 10-60 minutes and producing plumes to ~1500 m (Marchetti et al., 2009), which are similar in description to the *ash explosions* observed here at Karymsky Volcano, suggesting that they erupt in a similar manner. We

also note that *pulsatory degassing* and *gas jetting* activity at Karymsky Volcano exhibit lower thermal and acoustic energies than the *ash explosions* and *explosive eruption*, which Marchetti et al. (2009) attribute to plume dominance by a gas-thrust region, which seems reasonable for Karymsky's *gas jetting* activity in particular. Ripepe et al. (2005) use visual and thermal observations of eruption plumes from Stromboli Volcano to propose that thermal energy can be directly related to mass of eruptive material (i.e. gas and magma). This hypothesis was supported by coincident thermal and Doppler radar observations of eruptive plumes in which a strong correlation between thermal energy and integrated reflected energy (a proxy for eruption mass) is observed (Hort et al., 2003; Scharff et al., 2008). Based on these studies and our observations at Karymsky Volcano, we conclude that higher thermal energies observed for *ash explosions* and *explosive eruption* activity relative to *pulsatory degassing* and *gas jetting*, are due to higher quantities of ash and gas emissions or a higher quantity of more fragmented material.

If we further consider the infrasound pressure observed for individual events, as well as the cumulative acoustic energy calculated for the analysis periods, we can make inferences on the relative overpressure and resultant fragmentation level of the erupted magma. The two to four order of magnitude larger cumulative acoustic energies observed for *ash explosions* and *explosive eruptions*, relative to *pulsatory degassing* and *gas jetting* activity, suggest relatively high overpressure in the conduit and resulting high fragmentation level associated with these activity types. We speculate that these variations can be attributed to low conduit permeability that hinders the release of exsolved volatiles until volatile pressure exceeds the confining pressure and the viscous magma in the conduit is fractured. Following this reasoning, the relatively low infrasound pressures and cumulative acoustic energies associated with *pulsatory degassing* and *gas jetting* activity may indicate a higher conduit permeability during these styles of activity. Conduit processes are discussed in more detail in Section 4.5.4.

4.5.2 Characterization of the Four End Member Activity Types

Distinct differences in the character of the four end-member activity types observed at Karymsky Volcano can be seen among the various parameters evaluated using the remote sensing and infrasonic datasets (Figs. 4.5, 4.7). These differences allow the four activity types to be uniquely characterized, with the potential to identify these activity types from the remote sensing and infrasound datasets. In this section we discuss the distinct characteristics of each activity type and any correlations observed among the datasets.

4.5.2.1 Ash Explosions

Ash explosions exhibited the second highest maximum and mean temperatures, reduced infrasound pressure, acoustic energies and cumulative acoustic energies of the four types (Fig. 4.5a; Table 4.2). This suggests that *ash explosions* represent the second highest explosive energy events, following *explosive eruption* activity. High peak temperatures and thermal energies were observed during *ash explosions* compared with that for *pulsatory degassing* and *gas jetting* activity (Table 4.2). This suggests that in comparison with other volcanoes exhibiting similar behavior, Karymsky's *ash explosions* emit more fragmented material (Fig. 4.11) (Marchetti et al., 2009). While no ash masses were obtained for this activity type we expect that the ash mass for these events will be larger than the ash masses for the *hybrid* events, and smaller than the *explosive eruption* events, according to their relative thermal energies and visual observations (Table 4.2; Fig. 4.11) (Scharff et al., 2008). Infrasonic signal onsets are broadband and impulsive, with the second highest acoustic energy and mean reduced infrasound pressure observed. The high-amplitude infrasound coda is fairly distinct and corresponds with a long-duration gas-thrust phase for each event. Variations in SO_2 emission rate during this time period were observed, however no correlations between SO_2 emission rate and maximum temperature or infrasound pressure were apparent, likely the result of poor temporal resolution SO_2 measurements collected under low UV (early morning) conditions. Both mean SO_2 emission rates and plume ascent speeds are similar to other activity types observed, and thus not useful as distinguishing factors. We note that ash attenuation

during these events could result in an underestimation of SO_2 during this time period. The thermal and infrasonic signals observed for *ash explosions* are sufficiently unique such that it would be possible to identify this type using either one of these datasets, as well as draw conclusions on the style of eruption and associated products.

4.5.2.2 Pulsatory Degassing and Gas Jetting

Pulsatory degassing and *gas jetting* activity show several similarities to each other, and share several differences when compared to the other activity types (Figs. 4.6b, c; Table 4.2). Temperatures, SO_2 emission rates, and reduced infrasound pressures all had similar mean values between *pulsatory degassing* and *gas jetting*, with significantly larger maximum values for *pulsatory degassing* relative to *gas jetting.* Similar order of magnitude cumulative acoustic energies were observed for these types of activity, which were two to four orders of magnitude lower than observed for *ash explosions* and *explosive eruption*. Acoustic onsets were also emergent for both types. These observations suggest that both degassing styles occurred under relatively permeable conduit conditions. On several occasions minor quantities (<5 within the 40-minute analysis period) of hot volcanic bombs were observed visibly and/or in FLIR thermal imagery to be erupted during the *pulsatory degassing* study period that were not observed during the *gas jetting* study period. We speculate that the significantly higher thermal energies observed for *pulsatory degassing* relative to *gas jetting* could be explained by the eruption of minor quantities of volcanic bombs. This is consistent with observations of degassing at Karymsky Volcano in 2008 by Lopez et al. (2011). We caution however, that the emission of minor quantities of volcanic bombs during *gas jetting* activity may also occur, but were not observed in the 40-minute study period we selected. Overall the temperatures and infrasonic pressures associated with the degassing types are significantly lower than observed for the other activity types involving the eruption of abundant pyroclastic material, which is consistent with lower fragmentation levels associated with these styles of activity. We note that the primary difference between *pulsatory degassing* and *gas jetting* activity as observed from our datasets is in the

acoustic frequency content. In particular little to no infrasound (<20 Hz) was detected during *gas jetting*, rather it was associated with an audible roar and exhibited abundant high frequency acoustic energy (>20 Hz; Fig. 4.7; Table 4.2) that was not as evident for *pulsatory degassing*. Noise from volcanic jets has been observed at a range of frequencies (Woulff and McGetchin, 1976), and jet noise at lower frequencies has been suggested to result from turbulent interactions within the volcanic jet itself, similar to that from man-made jet engines (Matoza et al., 2009). More work is required to determine the physical implications of the high frequency acoustic signals. We propose that *pulsatory degassing* and *gas jetting* activity can be distinguished from *ash explosions* and *explosive eruption* using the infrasound data according to their emergent onsets and significantly lower reduced infrasound pressure and acoustic energies. *Pulsatory degassing* and *gas jetting* can then be distinguished from each other based on their infrasound frequency content.

4.5.2.3 Explosive Eruption

Explosive eruption activity is distinct from other activity types with respect to all parameters evaluated and is clearly identified using infrasound and/or thermal datasets. In particular saturated peak temperatures (>350°C), very high reduced infrasonic pressures (>500 kPa), and ascent speeds up to 74 m/s, were all significantly larger than observed for other activity types. The infrasonic onset was extremely impulsive and high pressure, saturating the sensors with pressures in excess of 125 Pa at a distance of 4 km. These pressures were much greater than those observed in previous infrasound studies at Karymsky Volcano (e.g. Johnson et al., 1998). The acoustic energies for *explosive eruption* activity are significantly higher than observed for *ash explosions*, as well as in comparison to other volcanoes that exhibit small explosive eruptions (Fig. 4.11) (e.g. Ripepe et al., 2005; Marchetti et al., 2009; Johnson and Ripepe, 2011). The maximum temperature observed was over 100°C greater than observed for ash explosions, which may indicate the involvement of hotter material or the involvement of relatively more abundant hot material. Unlike the other data types, clear trends in SO_2 emission rates can be seen with volcanic activity during the *explosive eruption* analysis period. Some of the

highest SO_2 emission rates observed during the field campaigns (~2.3 kg/s) were seen ~75 minutes prior to the type example *explosive eruption* (Fig. 4.12). These values dropped significantly in the 20 minutes prior to eruption down to ~0.14 kg/s. These low but clearly detectable SO_2 emission rates corresponded with apparent vent sealing, during which emissions were not visible by eye or in the thermal imagery and no infrasound was detected from the volcano. This observation supports previous findings by Fischer et al. (2002) that Karymksy's vent does not seal entirely prior to eruptions. Our observations suggest that magma ascent combined later with a decrease in conduit permeability may have occurred prior to explosive eruption. During the initial explosive eruption significant ash attenuation prevented accurate SO_2 measurements; however after ~10 minutes SO_2 could again be detected and exhibited a correlation with peaks in infrasound and thermal energy, corresponding with secondary eruptions (Fig. 4.5d). It appears that the SO_2 emission rates may increase ~1 minute prior to peaks in infrasound and thermal energy associated with the secondary eruption pulses after the initial eruption (Fig. 4.5d; ~02:00-02:15 UTC). This could be expected as the removal of material in the upper conduit during each eruption reduces pressure in the lower conduit and thus induces volatile exsolution (Carroll and Webster, 1994). Improved temporal resolution SO_2 emission rate data is required to better relate trends in volcanic emissions to the dynamic volcanic activity observed at Karymsky Volcano. We note that while ash masses could not be calculated for this *explosive eruption* event, ash mass was estimated for a different *explosive eruption* event at 08:21 on 22 August 2011 using the NicAIR camera (Fig. 4.13). The ash mass estimated for this *explosive eruption* was >69,000 kg. In this analysis the plume remained partially opaque such that we consider this ash mass to be a minimum estimate. If we compare the estimated ash mass for this event, assuming a 1 hour sample period, to *hybrid* activity occurring over a similar duration (~15 events per hour), we can see that *explosive eruption* activity exhibits significantly higher ash eruption rates of 69,000 kg/hour compared with 15,000 kg/hour for *hybrid* events, and ~0 kg/hour for *pulsatory degassing* and *gas jetting* events (note that unfortunately no ash masses were acquire during *ash explosion* activity). However, we note that these

measurements are limited to ash particles in the size fraction of 1-16 μm (i.e. very fine ash), representing only a portion of the pyroclastic material emitted during an explosive eruption. In addition to larger ash particle sizes, abundant volcanic bombs are also erupted during these events. Using detailed isopach maps and maps of erupted pyroclastic material, Rose and Durant (2009) estimate that the eruptive mass produced by a Vulcanian eruption observed at Fuego Volcano (Guatemala) was composed of only 4% by mass of very fine ash. As activity at Fuego Volcano is often described to be similar to activity observed at Karymsky Volcano (Sections 4.5.1; Marchetti et al., 2009; Lyons et al., 2010) we apply these constraints to our study. Assuming that the very fine ash mass estimated by the NicAIR comprises only 4% the total eruptive mass, we find a total eruptive mass for an explosive eruption of 1.73×10^6 kg. Using a magma density for Karymsky andesite of 2470 kg/m^3 (Izbekov et al., 2004) we roughly estimate an eruptive volume of ~700 m^3. If we assume a cylindrical conduit with diameters of 5, 10, 15, and 20 m, the eruptive volume would occupy only the upper 71, 18, 8, and 4 m of the conduit, respectively. Considering that we observed seven of these eruptions in the course of a one week time period during the 2011 field campaign, we estimate an annual eruptive volume of 2.55×10^5 m^3 for that year. This estimated annual volume is similar to the eruptive volume for a single "small" (i.e. VEI 1) eruption according to the classification system by Newhall and Self (1982). This may suggest a low magma production at Karymsky Volcano; however, as this calculation is based on several large assumptions we caution that more accurate eruptive volumes are required to better constrain the magma budget at Karymsky Volcano.

4.5.3 Evaluation of SO_2 Emissions

Several sampling challenges prohibit the direct comparison of SO_2 emission rates among the four activity types. Specifically, the presence of ash in plumes for both *ash explosions* and following *explosive eruption* (Figs. 5a and 5d) can decrease the pathlength of light through the plume and cause an unquantified underestimation of SO_2 column density and derived emission rates (C. Kern, pers. comm). Additionally, 'mean' SO_2 emission rate is

a function of the specific activity observed during the 40-minute time period selected for analysis, such that the time period selected may bias the mean value (e.g. Fig. 4.5d). Furthermore, SO_2 measurements for *pulsatory degassing* activity were made using the NicAIR IR camera, while SO_2 measurements for the other activity types were collected using the FLYSPEC. Without direct comparison of the two instruments we cannot be certain that measurements are comparable. Finally, poor sampling conditions (ground-hugging plume) prevented accurate measurement of SO_2 emission rates for *gas jetting* activity in 2011, such that SO_2 emission rates from gas jetting activity in 2012 are considered here, though we acknowledge that these may not be representative of activity in 2011. Considering the serious uncertainties in the SO_2 measurements and the problems of combining measurements from different instruments and different years, a relative comparison of the SO_2 emission rates among the four activity types is not possible. We can however conclude that: (1) variations in SO_2 emission rates observed within the analysis time periods for the *gas jetting and explosive eruption activity* types exist, and positively correlate with infrasound and temperature (Figs. 4.5c, d); and (2) detectable SO_2 emission rates persist through all activity types observed.

The continuous gas emissions observed at Karymsky Volcano require a mechanism to allow volatiles to continuously exsolve and separate from their host melt, and permeate through the conduit to the surface. Volatile exsolution is a function of the solubility and concentration of volatiles within melt, and the primary mechanisms to induce volatile exsolution are: (1) decompression (i.e. magma ascent) (Giggenbach, 1996), and (2) melt crystallization (Burnham, 1985). These processes are closely related, and a direct feedback between crystallization and degassing can occur (Sparks, 2003). SO_2 is the third most abundant gas emitted at volcanoes after H_2O and CO_2 (Symonds et al., 1994) and is the easiest to detect using remote sensing techniques due to its low background concentration. SO_2 and H_2O are more soluble in magma than CO_2, as can be seen in Table 4.3 by their saturation concentrations in rhyolitic melt at mid to shallow crustal pressures (Moretti et al., 2003). We note that a rhyolitic melt composition is appropriate

for Karymsky Volcano because crystallization of 25-32 vol.% phenocrysts results in the andesitic whole-rock composition having a dacitic to rhyolitic melt composition (Izbekov et al., 2004). These solubility trends suggests that an ascending magma will release CO_2-rich fluids first, followed by SO_2-rich and H_2O-rich fluids (Gerlach, 1986). Once the magmatic volatiles have exsolved, separation from their host melt is required in order to degas at the surface. Several models have been proposed to explain passive degassing at silicic volcanoes involving the permeable flow of volatiles through either a foam, fracture, or interconnected bubble network within the conduit (Eichelberger et al., 1986; Edmonds et al., 2003b; Gonnermann and Manga, 2003), or directly through conduit walls (Jaupart and Allegre, 1991). We propose that permeable flow through a conduit fracture or bubble network (Edmonds et al., 2003b; Gonnermann and Manga, 2003) is the most appropriate mechanism to explain the continuous surface degassing at Karymsky Volcano. This model has been used to explain the transport of gases released from depths greater than 5 km at Soufriere Hills Volcano (Montserrat) (Edmonds et al., 2003b; Shinohara, 2008) and can explain the persistent SO_2 emissions released through a central vent. If we assume that the conduit is permeable to volatile flow, then an increase in surface SO_2, CO_2 and/or H_2O emissions may indicate magma ascent (Aiuppa et al., 2007; Burton et al., 2007). In addition to indicating changes in relative magma depth, changes in surface gas emissions can also be attributed to changes in conduit permeability. For example, decreases in SO_2 emission rates observed prior to explosive eruption at Galeras Volcano (Colombia) and at Karymsky Volcano in 1999 were interpreted to represent a decrease in conduit permeability (Fischer et al., 1996; Fischer et al., 2002). Secondary processes such as hydrothermal scrubbing (Symonds et al., 2001) and in-plume oxidation of H_2S and SO_2, can also affect surface SO_2 emissions, though we consider these processes to be minimal. Specifically, the high frequency of magmatic eruptions observed at Karymsky Volcano during these study periods, with an average rate of one *explosive eruption* per day observed in 2011, would likely prohibit the development of a hydrothermal system within the conduit path such that scrubbing of SO_2 is considered unlikely. Secondly, at Karymsky Volcano the above-vent SO_2 measurements are acquired

only seconds to minutes after release. Previous work by Aiuppa et al. (2005) found that H_2S is chemically inert in volcanic plumes over second-to-minute time scales. Additionally, an SO_2 loss rate in the atmosphere of ~2.8 x 10^{-6} s^{-1} estimated for Redoubt Volcano, Alaska (Hobbs et al., 1991), a volcano with similar latitude as Karymsky Volcano, produces no noticeable loss in SO_2 over the emission-measurement timescale employed. These observations suggest that secondary processes are not likely to be contributing to variations in SO_2 emissions observed at Karymsky Volcano.

Our observations suggest that over day-to-week time scales SO_2 emissions are continuous and persist throughout the various styles of volcanic activity (Fig. 4.5). In addition to observations of continuous emission rates observed at Karymsky Volcano, we also observe significant short-term variations within the 40-minute analysis periods. This is evidenced by the relatively large standard deviations about the mean seen for SO_2 emission rates associated with *pulsatory degassing* and *explosive eruption* that exceed the proposed measurement error (Table 4.2; Fig. 4.5). We note that in the case of *explosive eruption* the presence of ash may be resulting in a post-eruption underestimation of SO_2 emission rates (greater than the proposed error); however, this would serve to minimize artificially, as opposed to increasing, the standard-deviation. Only *gas jetting* activity exhibited a standard deviation that was similar or smaller than the estimated error value. The variations in SO_2 emission rate observed for both *gas jetting* and *explosive eruption* collected at a moderate temporal resolution appear to correlate with both maximum temperature and infrasound pressure (Fig. 4.5b-d). This suggests that short-term processes are influencing surface SO_2 emissions at Karymsky Volcano. Considering these observations, we speculate that the SO_2 emissions produced here are the result of a deeper process such as magma ascent from the shallow storage region, while the short-term variations in surface SO_2 emissions may be due to changes in conduit permeability as has been previously proposed at Karymsky Volcano (Fischer et al., 2002).

4.5.4 Proposed Models

4.5.4.1 Previous Models

Previous studies have used observations of seismicity, infrasound, and volcanic emission data from Karymsky Volcano to infer shallow vent processes (Johnson and Lees, 2000; Fischer et al., 2002; Lees et al., 2004; Johnson, 2007). These studies largely proposed increased gas pressure combined with vent sealing as the eruption trigger mechanism (Johnson et al., 1998; Fischer et al., 2002; Ozerov et al., 2003). We note that activity at Karymsky described in these studies was slightly different than observed during our field campaigns in 2011 and 2012. In particular, observations from field campaigns in 1997 and 1999 were dominated by (1) small, explosive, ash-rich events (similar to our *ash explosions*) that occurred ~6 times per hour with impulsive infrasonic signals (e.g. Johnson et al., 1998), and (2) gas chugging events that were associated with waxing and waning SO_2 emission rates (Fischer et al., 2002), as well as distinct acoustic and seismic waveforms and frequency content (Johnson et al., 1998; Johnson and Lees, 2000; Lees et al., 2004). Fischer et al. (2002) used high temporal resolution SO_2 emission rate measurements (1 per 5 seconds) to identify decreases in SO_2 emission rates prior to ash explosions, followed by increases in SO_2 emission rates following the explosions. Additionally, Johnson et al. (1998) identified highly impulsive infrasonic signals at the time of explosion, both of which support the vent-sealing eruption trigger. Ozerov et al. (2003) propose a model in which the conduit is topped by a relatively short in length, high viscosity magma plug, with the remaining conduit filled by a low-viscosity, compressible magma that is continuously fed from depth. Dense, angular, ash and bombs, along with scratched bomb surfaces interpreted to have formed during extrusion, support a highly viscous and volatile depleted magma in the upper conduit (Johnson et al., 1998; Fischer et al., 2002; Ozerov et al., 2003). In their model, Ozerov et al. (2003) propose that the two types of activity observed from 1996-2000 could be explained by the following: (1) variations in stick and slip of the viscous conduit plug along the conduit margins, due to changes in compression of the lower-viscosity magma beneath the plug that could lead to discrete ash explosions, and (2) the viscoelastic response of the

solidified plug at the top of the conduit could explain gas chugging activity. Similarly, Fischer et al. (2002) propose a mechanism in which second boiling (where microlite crystallization induces degassing) increases gas pressure beneath the sealing conduit plug until the excess pressure induces plug failure. They attribute variations in degassing between the two event types observed to be due to the extent of volatile exsolution from depth such that higher gas fluxes from depth observed during gas chugging prevent complete vent sealing.

4.5.4.2 Proposed Model

Our observations are consistent with earlier interpretations that suggest that much of the activity at Karymsky Volcano is influenced by shallow vent processes; however, like Fischer et al. (2002) we speculate that in addition to shallow vent processes, a deeper processes is required to fully explain Karymsky's variable behavior. Our observations of the four end-member activity types can be used to formulate a schematic model in the following manner. First, we observed continuous SO_2 emission rates, with pulses of stronger and weaker emissions observed for all four activity types (Table 4.2). We note that *gas jetting* exhibited smaller fluctuations as evidenced by the relatively small standard deviation in the measurements (±0.3 kg/s) compared with the other types (Table 4.2; Fig. 4.5c). Ash emissions were discontinuous among the four activity types and varied from absent for *pulsatory degassing* and *gas jetting* activity to abundant for *ash explosions* and *explosive eruption* activity with estimated very fine ash masses ranging from ~1,000 to >69,000 kg per event (Table 4.2; Section 4.5.2.3). This combination of continuous SO_2 emissions and discontinuous ash emissions indicates a decoupling of gas and magma, and supports open-system degassing behavior at depth. High peak temperatures observed in FLIR waveforms for *ash explosions* and *explosive eruption*, as well as incandescent material observed visually at night for *ash explosions*, *pulsatory degassing*, and *explosive eruption*, confirm that at least some erupted material is juvenile and not simply previously erupted material that filled the crater. The significantly hotter temperatures observed for *explosive eruption* may indicate the involvement of hotter

magma for this activity type compared to *ash explosions*. *Ash explosions* and *explosive eruption* activity have significantly higher thermal and acoustic energies than *pulsatory degassing* and *gas jetting*, requiring a more energetic (i.e. higher pressure) emission mechanism. The highly impulsive and energetic infrasonic onsets of *ash explosions* and *explosive eruption* activity, along with the decrease in SO_2 emission rates and absence of emissions seen visibly or in the FLIR imagery during the period of quiescence leading up to the *explosive eruption* event (Fig. 4.12), support a decrease in conduit permeability prior to eruption. The high acoustic pressures observed for *ash explosions* and *explosive eruption* may indicate that the conduit is relatively impermeable prior to these events in contrast to the proposed high conduit permeability for *pulsatory degassing* and *gas jetting* activity. The detectable SO_2 emissions observed prior to the *explosive eruption* here and by Fischer et al. (2002) in 1999, indicate that degassing persists during this period of quiescence. *Ash explosions* and *pulsatory degassing* events are highly repeatable and occasionally new explosions or pulses begin prior to cessation of the previous event. Field observations suggest that hours to days of *gas jetting* and/or *pulsatory degassing* activity, followed by 1-2 hours of hybrid activity and then 40–90 minutes of apparent vent sealing, precede explosive eruption activity (Fig. 4.6). During the 2011 field campaign *ash explosion* activity was only observed on 15 August, two days prior to the first *explosive eruption* event, and thus was temporally well separated from *explosive eruption* activity. This suggests that a simple continuum in conduit permeability cannot explain our observations. We note that after 15 August, *ash explosion* activity was not observed for the remainder of the field campaign, while six explosive eruption events and multiple periods of *gas jetting*, *pulsatory degassing*, and *hybrid* activity occurred; though we acknowledge that *ash explosion* activity could have occurred at night or during times of poor visibility when visual and remotely-sensed observations were not being collected. The combination of: (1) apparent decoupling between gas and magma, and (2) the absence of a distinct temporal pattern and recurrence intervals observed among end-member activity types, leads us to infer that both shallow and deep processes are influencing surface activity at Karymsky Volcano. Similar observations and

interpretations have been made based on seismic and SO_2 datasets at Fuego Volcano (Nadeau et al., 2011), which exhibits eruptive behavior reminiscent of Karymsky Volcano (Marchetti et al., 2009; Lyons et al., 2010).

Considering the above observations, we expand on previous models and speculate that surface activity and shallow vent processes at Karymsky Volcano can be explained by variations in magma degassing depth, which influence the relative proportions of decompression versus crystallization induced degassing, which in turn, influences conduit permeability. This process is illustrated in Figure 4.14. We propose that exsolved volatiles are sourced from magma both ascending from, and stored within, the shallow-crustal storage region estimated to be ~4-6 km beneath the edifice (Izbekov et al., 2004). We speculate that exsolved volatiles are transported to the surface via permeable conduit flow through a bubble or fracture network providing a continuous source of SO_2 emissions (Edmonds et al., 2003b; Gonnermann and Manga, 2003). Prior to the ascent of new magma, the conduit is filled with residual magma from the most recent eruption, which cools, crystallizes, and continues to exsolve volatiles, all of which increase the magma viscosity (Dingwell et al., 1996; Sparks et al., 2000; Sparks, 2003). The relatively high magma viscosity decreases the conduit permeability and inhibits the transport and release of exsolved volatiles. This leads to volatile overpressure which eventually exceeds the confining pressure and explosively fractures magma in the upper conduit. This scenario (Figure 4.14a) can explain *ash explosions*. We propose that the fairly regular time periods of explosions during this activity type could be attributed to the timescales of microlite crystallization which simultaneously increases magma viscosity and induces volatile exsolution, which leads to volatile overpressure. A similar mechanism was proposed for this activity type by Fischer et al. (2002). Additionally, the occurrence of overlapping ash explosions could be explained by only part of the viscous conduit being fractured during each explosion, such that different segments of the viscous magma could fracture separately due to localized forces. This process may repeat until the magma is mostly degassed or new magma enters the system. The loss of mass in the

upper conduit due to ash explosions, or a deeper process such as magma recharge, may trigger magma ascent from the shallow-crustal storage region and transition surface activity from *ash explosions*. Magma ascent within the conduit will lead to volatile saturation and exsolution from the melt. This will be particularly important for S and H_2O dissolved within the melt because: (1) together these species comprise >95 mol% of typical volcanic emissions at arc volcanoes (Gerlach, 2004); and (2) significant quantities of S and H_2O will exsolve from rhyolitic melt during ascent from 100 MPa (~4 km) to the surface (Table 4.3; (Moretti et al., 2003). Therefore, magma ascent will provide an increase in volatile flux to the surface. The relatively large quantity of exsolved volatiles will force paths to the surface, possibly by inducing fractures within the viscous magma and increase the conduit permeability. During the transition period from a relatively impermeable to a permeable conduit pulses of ash and gas will be released at the surface resulting in *hybrid* activity and/or *pulsatory degassing* activity (Figs. 4.14b, c). The increase in volatile flux will lead to improved conduit permeability until eventually a relatively unrestricted path to the surface is available, which can explain *gas jetting* activity (Fig. 4.14c). Once the magma reaches shallow depths, much of the volatiles will have exsolved and degassed, this loss of volatiles will decrease the melt liquidus temperature in a process referred to as under-cooling, which triggers melt crystallization (Sparks et al., 2000). The process of degassing-induced crystallization at Karymsky Volcano is supported by observations of ~30-50 vol.% microlite abundance within ash samples from 16 explosive events at Karymsky Volcano between 1996 and 1998 by Izbekov et al. (2004). The rapid crystallization of microlites will increase the magma viscosity (Dingwell et al., 1996) and likely significantly decrease the conduit permeability. Minor quantities of gas will continue to be released from crystallizing magma in the upper-most portion of the conduit, while volatile exsolution from magma ascent in the lower conduit continues; however, these volatiles are not able to permeate through the conduit and degas at the surface. The volatile pressure from both sources will eventually surpass the confining pressure and trigger explosive eruption. This scenario can explain quiescence followed by *explosive eruption*. The transition between high

conduit permeability during *gas jetting* and relatively low conduit permeability in *explosive eruption* is represented by a short period of *hybrid* activity. In this model, secondary eruption pulses following the initial *explosive eruption* event can be explained by the removal of magma in the upper conduit, which decreases pressure on the lower conduit, which in turn induces volatile exsolution and magma ascent, and leads to subsequent explosions. The larger eruption size associated with *explosive eruption* relative to *ash explosions* can be attributed to the relatively higher volatile flux sourced from the ascending magma for *explosive eruptions*, in comparison to the volatile-depleted magma in the conduit during *ash explosions*.

This speculative model can explain the observed volcanic activity and trends in the evaluated parameters seen during field campaigns at Karymsky Volcano in 2011 and 2012. Additional measurements can be used to help test and refine this proposed model. Specifically, high temporal resolution gas composition measurements (e.g. Multi-Gas (Aiuppa et al., 2007) or open-path FTIR (Francis et al., 1995) could be used to complement SO_2 emission rate measurements to allow changes in gas composition and flux of major species to be detected. The observed trends could then be used along with solubility models to identify magma ascent. Changes in SO_2 and total volatile fluxes over time can then be attributed to changes in magma depth or conduit permeability. Continuous infrasound data and an automated detection algorithm to characterize volcanic activity-type could be used to better constrain temporal trends and characteristics of the various styles of observed volcanic activity. This dataset could then be used to fill in gaps in remote sensing and visual observations due to poor weather and/or sampling conditions. Finally, petrologic analysis of eruptive products could be analyzed for phenocryst and microlite abundance to better constrain processes of degassing-induced crystallization and estimate changes in magma viscosity due to microlite crystallization.

4.5.5 Evaluation of Multiparameter Techniques for Characterizing Activity

Several environmental, instrumental, and volcanological factors made obtaining quality, high temporal resolution remote measurements of Karymsky's volcanic activity challenging. Therefore, the following factors should be considered for subsequent projects in which an objective is to remotely and continuously characterize low-altitude (<6 km) volcanic activity such as observed at Karymsky Volcano. Environmental factors such as wind, clouds and fog, can all prevent accurate remote sensing measurements of volcanic activity. In particular: (1) high winds can blow the plume over such that clear sky cannot be obtained on both sides of the plume and only minimum estimates of ash and/or SO_2 can be obtained; (2) winds blowing the plume directly towards the instrument can result in inflated column densities and can obscure views of vent activity, (3) winds that blow the plume away from the instrument carry the plume out of detection range, (4) strong winds can re-suspend previously deposited ash making distinction between fresh and re-suspended ash impossible, (5) clouds and or fog between the instrument and target inhibits measurement collection by both UV and IR instruments, and (6) in the case of the FLIR clouds behind the plume can produce background radiation that may complicate interpretation of the plume thermal energy. In addition to these environmental factors, several instrument factors also made data collection challenging. The UV and IR remote sensing instruments employed during these field campaigns all needed regular calibration, requiring operator presence and resulting in data gaps. Furthermore, each remote sensing instrument requires power to operate, data storage capacity, and in most cases, labor and/or computationally intensive retrieval and/or data analysis algorithms. Infrasound has the advantages of being able to measure continuously and unattended for extended time periods (~1 year) at a high sample rate (up to 250 Hz here). The infrasound sensors require sufficient power that can be supplied by 12 V batteries and supplemental solar panels; however, deployment by foot over remote volcanic terrain can be difficult and time-intensive, and in our case resulted in a shorter than desired sample period. The main challenge of using infrasound sensors to detect activity at Karymsky Volcano during summer field campaigns is wind noise. By using an array of sensors and installing

each sensor in vegetated areas where winds are low, the effects of wind can be minimized. Finally, several volcanological factors made data collection challenging. Specifically, the highly dynamic activity observed requires sufficiently high sample rates to capture trends in activity. The FLYSPEC in particular did not always allow measurements to be collected at a sample rate commensurate with the dynamic activity observed at Karymsky Volcano. Additionally, abundant ash in Karymsky's plume caused several problems including: (1) attenuation of UV radiation which lowered the FLYSPEC signal to noise and likely resulted in an underestimation of SO_2 column density and derived emission rates, (2) limited visibility of vent activity, (3) high ash concentrations which resulted in opaque plumes that prevented retrieval of accurate ash masses, and (3) deposition on instruments and solar panels, which damaged equipment and reduced recharge capacity, respectively. These challenges experienced by individual techniques highlight the importance of using multiple techniques to fully capture volcanic activity. In particular, our results suggest that infrasound can be used to remotely characterize volcanic activity and can well complement remote sensing data, particularly during conditions of limited visibility. This study also demonstrates the utility of using high sample rate (>100 Hz) acoustic data to detect audible acoustic energy coincident with gas jetting and other processes that do not produce significant acoustic energy at infrasonic frequencies. To robustly capture the dynamic activity at Karymsky Volcanoe, we recommend improved temporal resolution SO_2 emission rate measurements through the use of a UV/IR camera or a fast-scanning DOAS system, of which a prototype is currently being tested by colleagues at Chalmers University (B. Galle, pers. comm.). Finally, to minimize the effects of ash, we recommend: (1) collecting IR camera images for ash retrieval from a slightly greater distance to fully capture the expanded plume within the image field of view, while increasing the likelihood that the plume will be translucent; and (2) supplementing above-vent SO_2 measurements with coincident downwind SO_2 measurements where the plume will be ash depleted and less likely to be underestimated (e.g. NOVAC) (Galle et al., 2010).

4.6 Conclusions

Four end-member volcanic activity types were observed at Karymsky Volcano during field campaigns in 2011 and 2012 based on a quantitative analysis of a multiparmeter dataset including infrasound, volcanic emissions, and thermal imagery. These activity types are defined as: (1) *ash explosions*, (2) *pulsatory degassing*, (3) *gas jetting*, and (4) *explosive eruption*. Each type is associated with unique infrasonic signals, suggesting that it may be possible to remotely and continuously monitor volcanic activity at Karymsky (and potentially other volcanoes) primarily using infrasound data. Our observations of the four activity types suggest that acoustic energies and waveform features associated with *ash explosions* and *explosive eruption* correspond with higher overpressure and decreased conduit permeability, which result in higher fragmentation levels of eruptive products. In contrast the lower acoustic energies and emergent acoustic onsets associated with *pulsatory degassing* and *gas jetting* activity correspond with a permeable conduit and open-system degassing. The relatively higher thermal energies associated with *ash explosions*, *pulsatory degassing* and *explosive eruption* suggest that these plumes are dominated by buoyant rise, in contrast to *gas jetting* activity whose plume is dominated by gas thrust. The four activity types exhibited continuous SO_2 emission rates. Prior to *explosive eruption* an order of magnitude decrease in SO_2 emission rates was observed, during which time period no infrasound was detected and no emissions were visible by eye or in thermal imagery, but were clearly detectable by FLYSPEC. This supports a decrease in conduit permeability prior to eruption. In contrast to the continuous SO_2 emissions observed for the four activity types, ash emissions were discontinuous suggesting a decoupling between the volatile and melt phases, such that exsolved volatiles are able to separate from their host magma in open-system behavior. Based on our observations, we speculate that variations in activity observed at Karymsky Volcano can be explained by changes in relative magma depth within the conduit. In this model, magma degassing depth directly influences the volatile flux and relative proportions of decompression and crystallization-induced degassing, which in turn affects magma viscosity and conduit permeability. This speculative model can explain our

multiparameter observations and expands on previous models proposed for Karymsky Volcano to link changes in shallow conduit processes to the deeper process of degassing magma depth.

4.7 Acknowledgements

We would like to thank Sergey Ushakov, Pavel Firstov, Evgeniy Makhmudov, Sergey Samoilenko, Evgenii Makatov, Olga Khubaeva, and Sergey Serovetnikov for field and logistical support that made this experiment possible. We thank Rick Wessels who graciously providing his FLIR for the experiment; Colin Rowell and Robin Matoza for assistance with data collection and figure generation; and Dima Melnikov for sharing the ALI image used in Figure 1b. This manuscript benefited from scientific discussions with Pavel Izbekov, Robin Matoza, Sergey Samoilenko, Jessica Larsen, Pavel Firstov, Colin Rowell, Bo Galle, Santiago Arellano, as well as constructive reviews by Cindy Werner, Rainer Newberry, Cathy Cahill and Bill Simpson. This project was supported by the UAF Geophysical Institute, the Alaska Space Grant Consortium, and NSF grant EAR-1113294.

Figures:

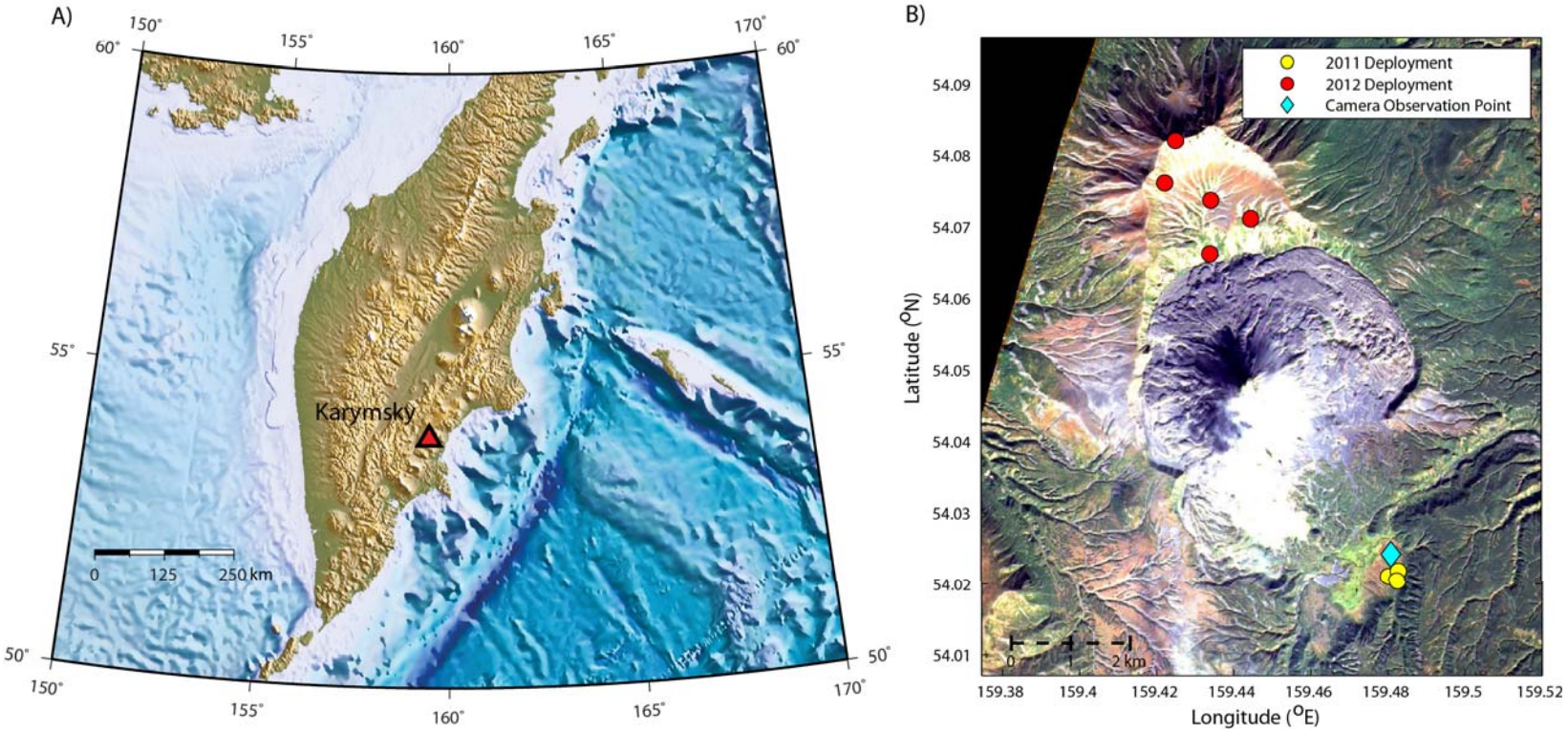

Figure 4.1: Location map. (A) Karymsky Volcano within Russia's Kamchatka Peninsula. (B) ALI satellite image of Karymsky Volcano, with locations of the remote sensing instrument deployment (blue diamond), the 2011 infrasound array (yellow circles) and 2012 infrasound array (red circles). A summit plume obscures the vent and south side of the edifice.

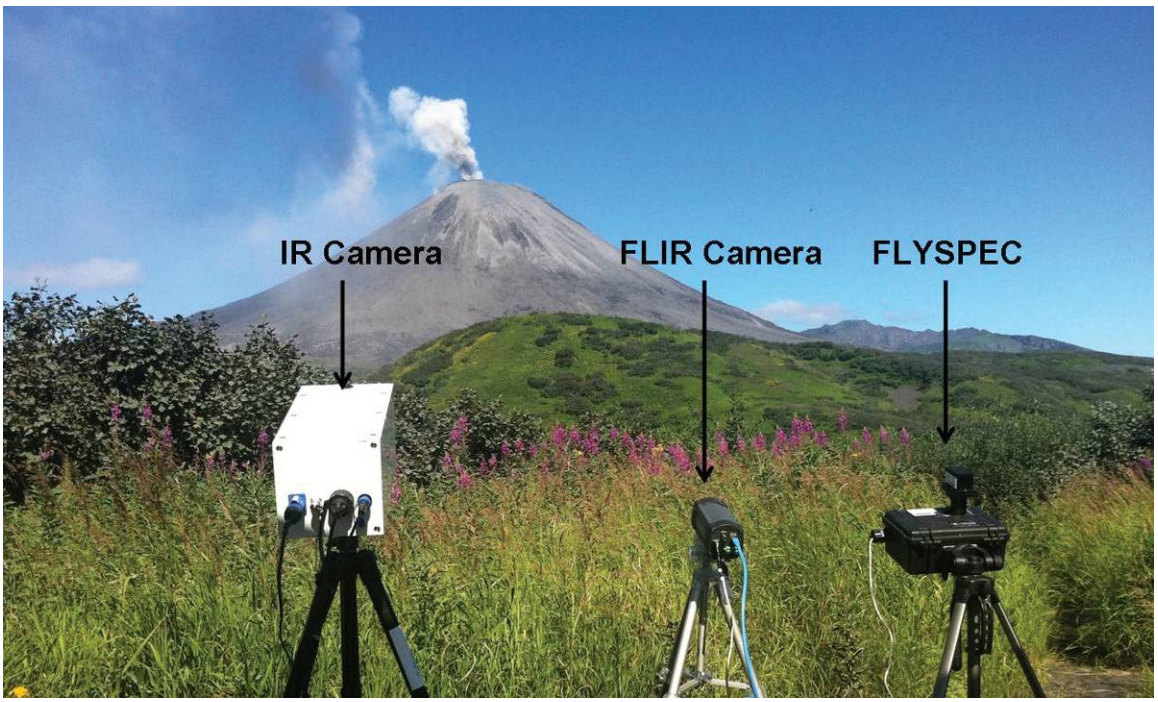

Figure 4.2: Photo of the 2011 experimental setup. Remote sensing instruments including IR camera, FLIR camera and FLYSPEC instruments (labeled) are seen in the foreground, with Karymsky Volcano seen in the background.

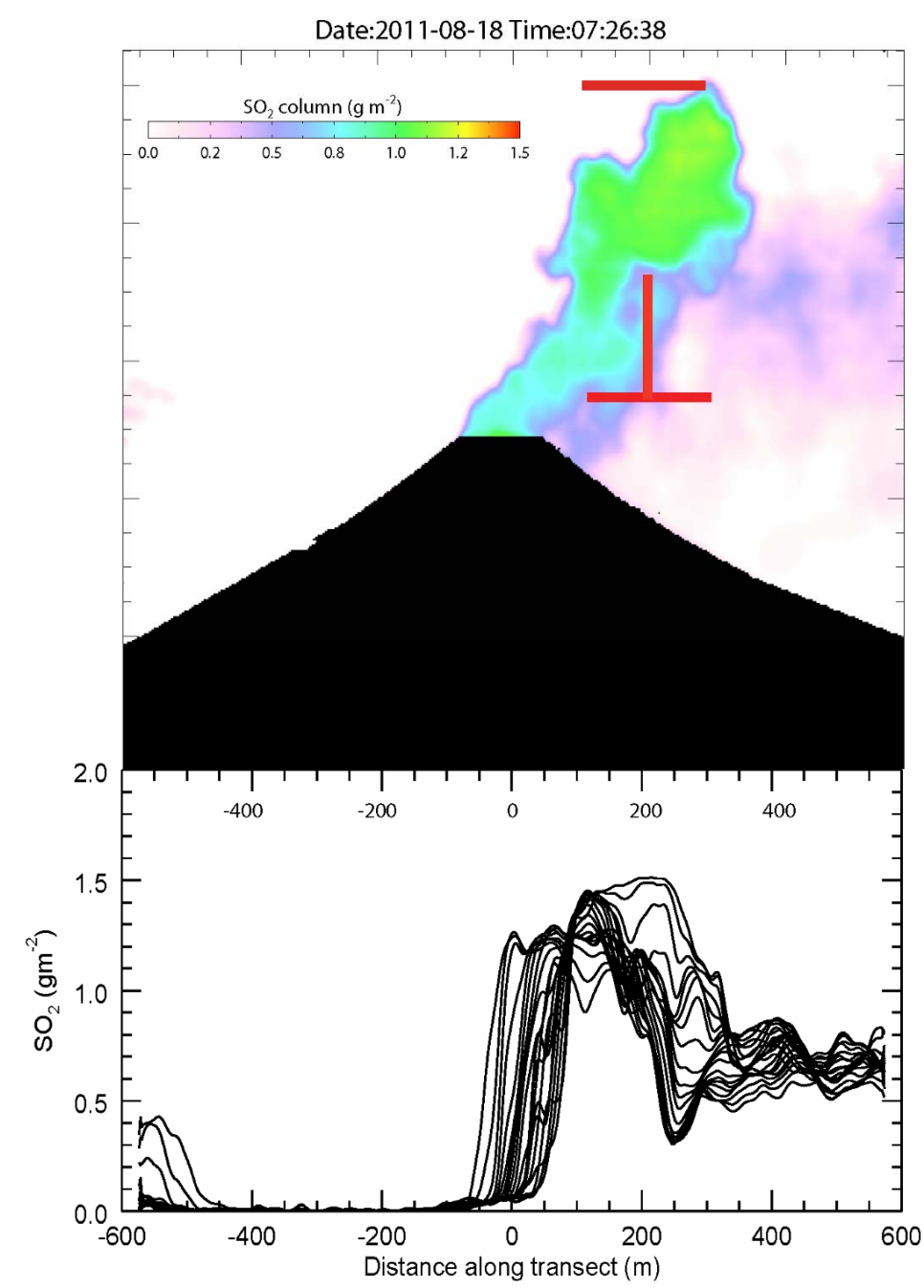

Figure 4.3: IR camera SO_2 retrievals. **Top:** Image showing the retrieved SO_2 column density (g/m^2) during *hybrid* activity. Red lines mark the upper and lower boundaries of transects used to calculate plume SO_2 cross-sections. **Bottom:** Plot of SO_2 column density (y-axis) for each transect resulting in an SO_2 cross-section. Horizontal distance in meters corresponding with the location of each transect in the upper figure is plotted along the x-axis.

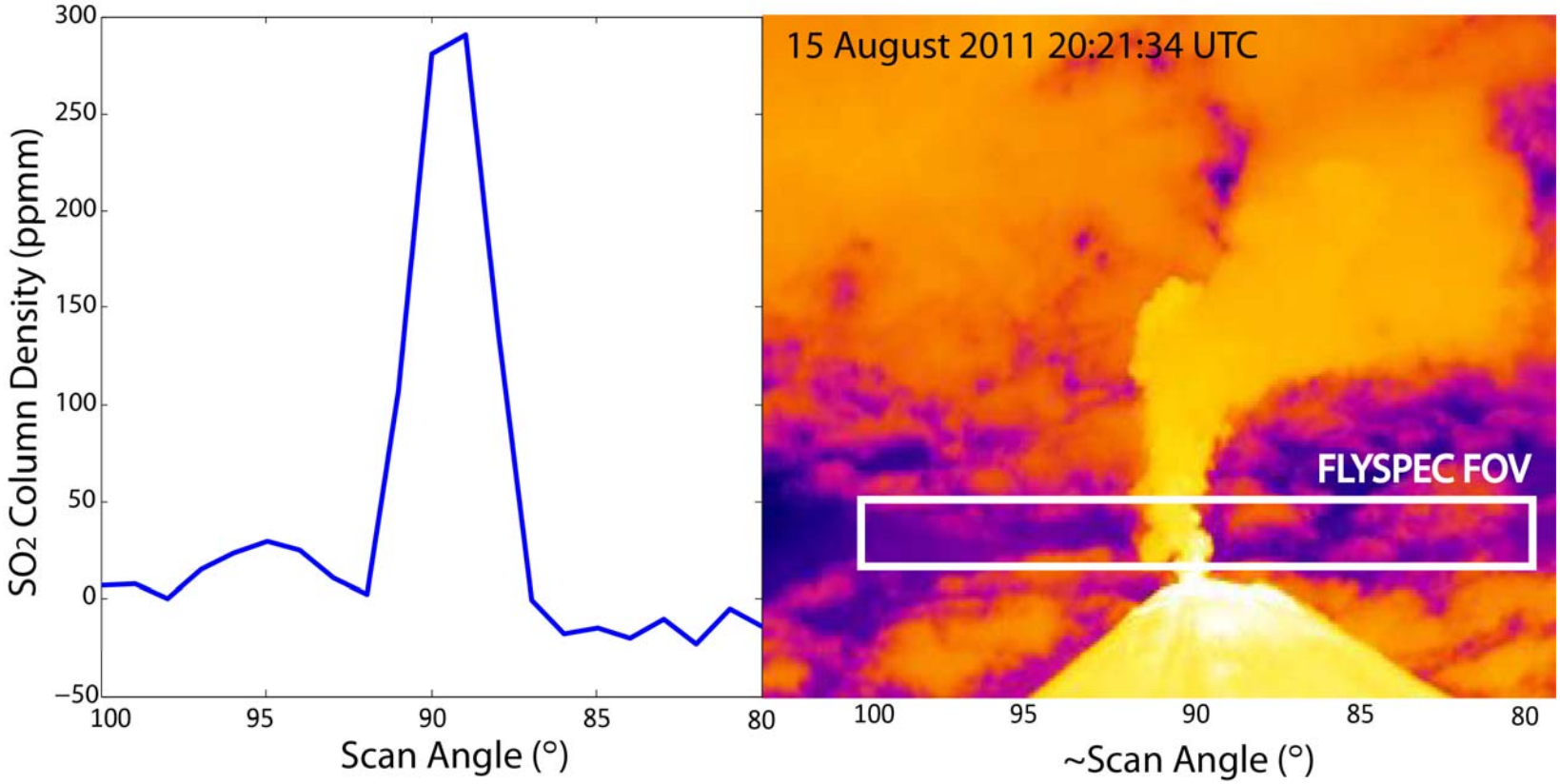

Figure 4.4: FLYSPEC scan region. **Left:** Example FLYSPEC SO_2 scan where the y-axis shows the SO_2 column density in ppmm, and the x-axis shows the FLYSPEC scan angle (90° corresponds with the center of the summit area). **Right:** FLIR image corresponding with the FLYSPEC scan, where FLYSPEC scan area within the FLIR field of view is shown. Measurements are for 16 August 2011 23:58 UTC.

Figure 4.5: Multiparameter observations of the end-member activity types. Subplots show data corresponding with each activity type, including: (A) *ash explosions*; (B) *pulsatory degassing*; (C) *gas jetting*; and (D) *explosive eruption*. Images on the left of the figure depict the visual characteristics of each activity type. Infrasound pressure (Pa; upper), maximum temperature (°C; middle), and SO_2 emission rate (kg/s; lower) subplots show respective datasets observed over each of the 40-minute analysis periods. Width of SO_2 emission rate bars represents the duration of each scan and resulting emission rate. Gray bars represent low signal to noise measurements such that values are not accurate. SO_2 emission rates for (A) and (D) are likely underestimated due to the presence of ash. Additionally, SO_2 emission rates for (B) were collected using the NicAIR IR camera, while remaining measurements were collected with FLYSPEC; and SO_2 emission rates for (C) were obtained in 2012. In (D) photos depicting both the quiescence prior to explosive eruption and the explosive eruption are shown. Note that scales are fixed for each parameter evaluated to facilitate data comparison. Some infrasound pressure and/or maximum temperature values exceed the upper scale limit in (A) and (D).

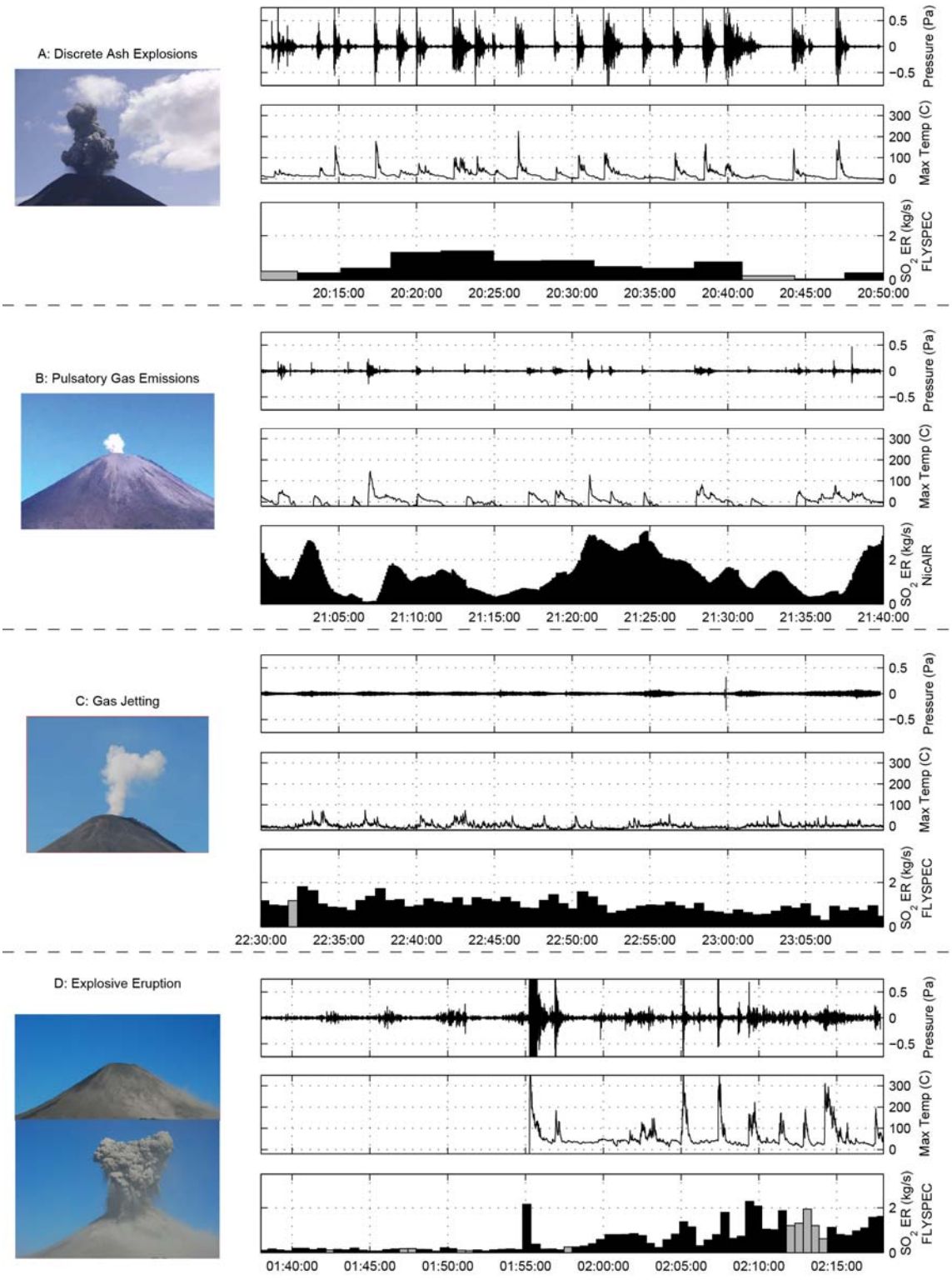
A: Discrete Ash Explosions
B: Pulsatory Gas Emissions
C: Gas Jetting
D: Explosive Eruption
Pressure (Pa)
Max Temp (C)
SO2 ER (kg/s) FLYSPEC
SO2 ER (kg/s) NicAIR
20:15:00 20:20:00 20:25:00 20:30:00 20:35:00 20:40:00 20:45:00 20:50:00
21:05:00 21:10:00 21:15:00 21:20:00 21:25:00 21:30:00 21:35:00 21:40:00
22:30:00 22:35:00 22:40:00 22:45:00 22:50:00 22:55:00 23:00:00 23:05:00
01:40:00 01:45:00 01:50:00 01:55:00 02:00:00 02:05:00 02:10:00 02:15:00

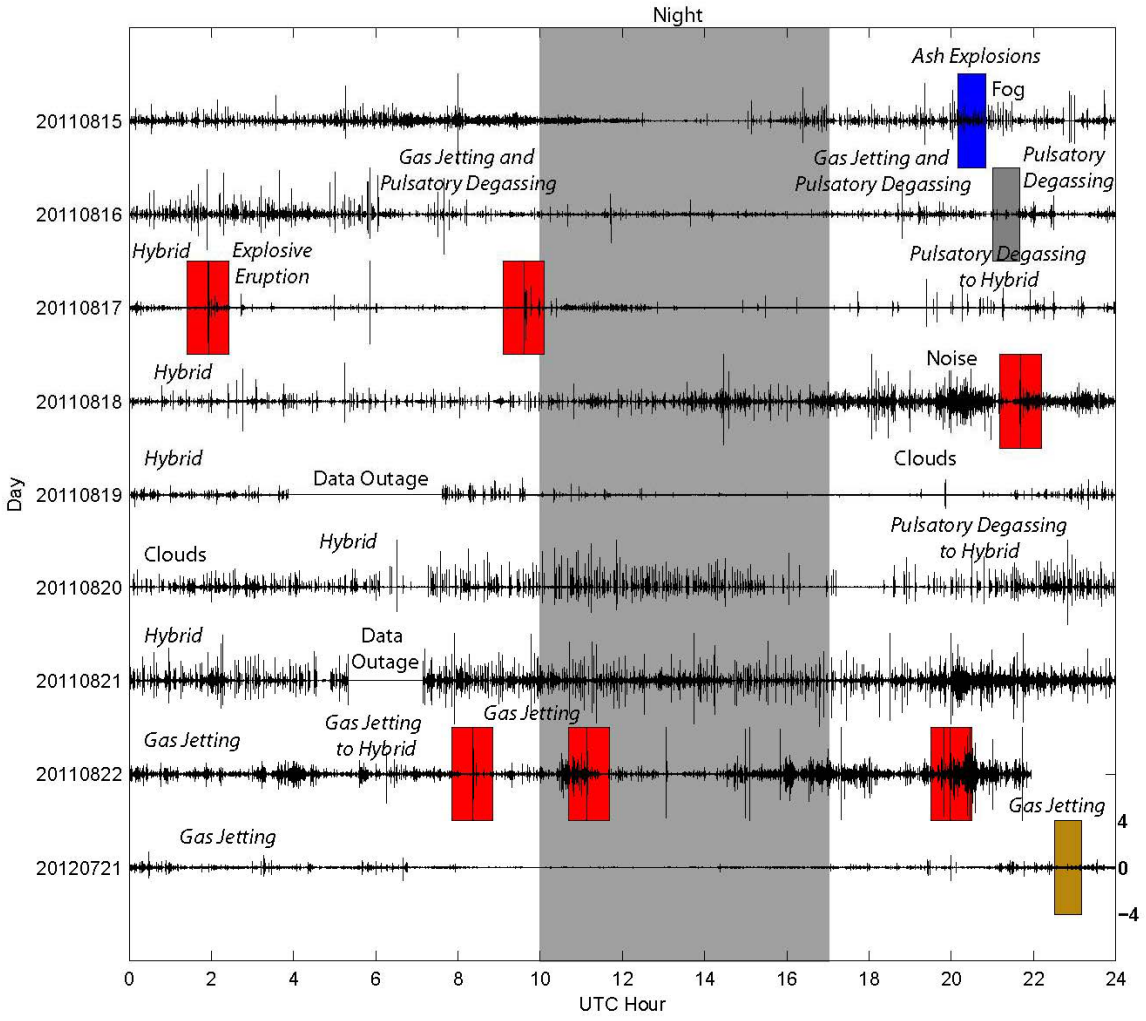

Figure 4.6: Infrasound-based timeline. Top eight traces depict the timeline for the 2011 field campaign, while the bottom trace represents one example day from the 2012 field campaign. Sample date is labeled on the primary y-axis, infrasound pressure up to ±4 Pa is shown on the secondary y-axis, and UTC hour is shown on the x-axis. Periods of interest for this study are marked by colored rectangles; specifically the blue, gray, and yellow rectangles (labeled) represent *ash explosions*, *pulsatory degassing* and *gas jetting* analysis periods, respectively. The red rectangles show the six *explosive eruption* events detected by infrasound in 2011, with the event analyzed labeled. Visual observations of activity type for certain time periods, or other parameter of interest, are labeled above the infrasound trace when available.

Figure 4.7: Infrasound spectrograms for the four activity types. Spectrograms for the following activity types are shown: (A) *ash explosion*, (B) *pulsatory degassing*, (C) *gas jetting*, and (D) *explosive eruption*. The y axis shows the frequency in Hz. The color bar represents signal amplitude in dB. The x-axis shows UTC time. Note the frequency range for A, B, and D are between 0.1-20 Hz (same scale), while C is between 0.1-60 Hz (extended scale). A helicopter signal can be seen in D from 01:38 – 01:40.

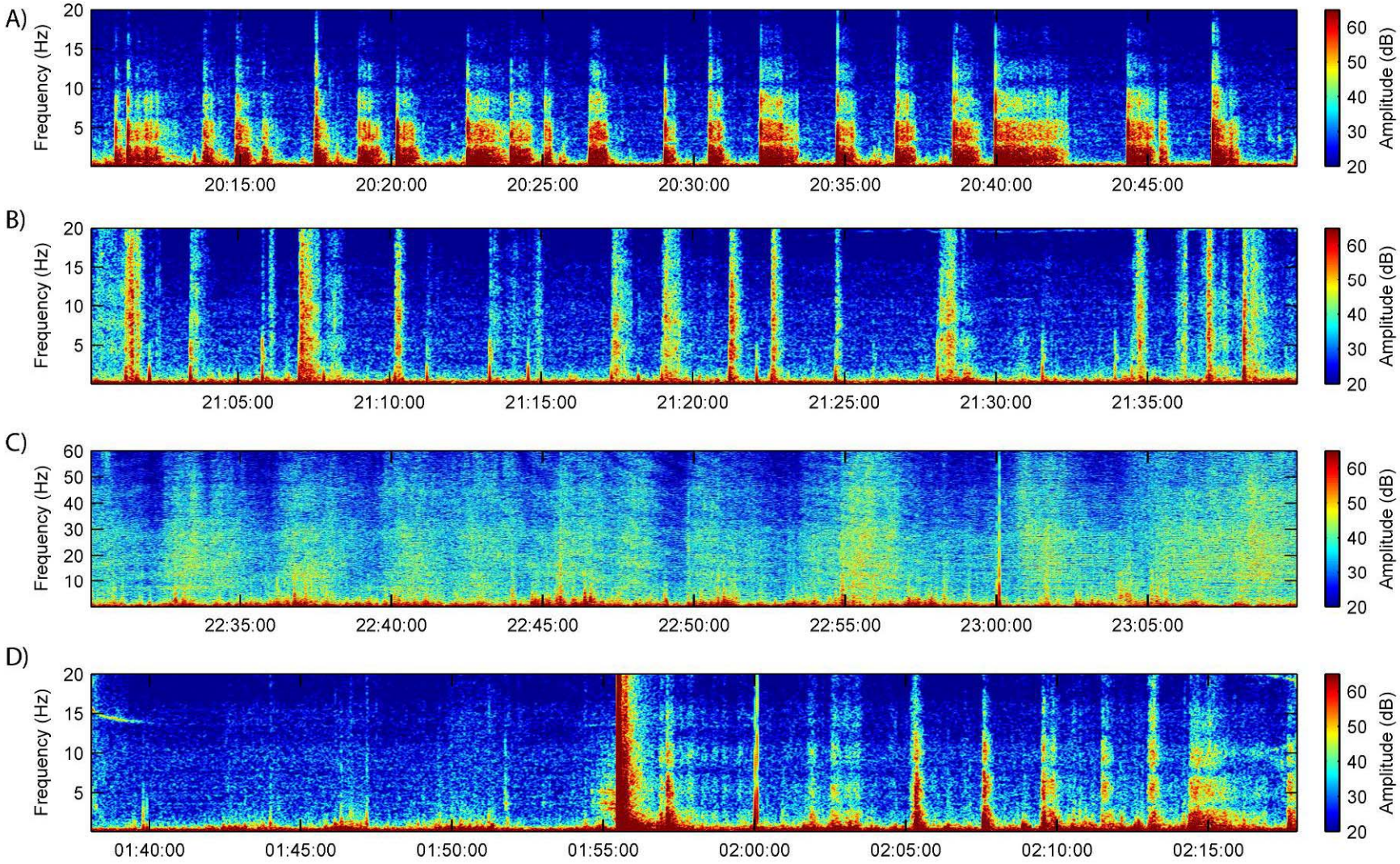
A)
Frequency (Hz)
20
15
10
5
20:15:00
20:20:00
20:25:00
20:30:00
20:35:00
20:40:00
20:45:00
Amplitude (dB)
60
50
40
30
20
B)
Frequency (Hz)
20
15
10
5
21:05:00
21:10:00
21:15:00
21:20:00
21:25:00
21:30:00
21:35:00
Amplitude (dB)
60
50
40
30
20
C)
Frequency (Hz)
60
50
40
30
20
10
22:35:00
22:40:00
22:45:00
22:50:00
22:55:00
23:00:00
23:05:00
Amplitude (dB)
60
50
40
30
20
D)
Frequency (Hz)
20
15
10
5
01:40:00
01:45:00
01:50:00
01:55:00
02:00:00
02:05:00
02:10:00
02:15:00
Amplitude (dB)
60
50
40
30
20

Figure 4.8: Evening photograph of an *explosive eruption* event. Photo taken at 09:35 on 17 August 2011. Abundant incandescent material, ash, and bombs can be seen in the eruption cloud and mantling the edifice.

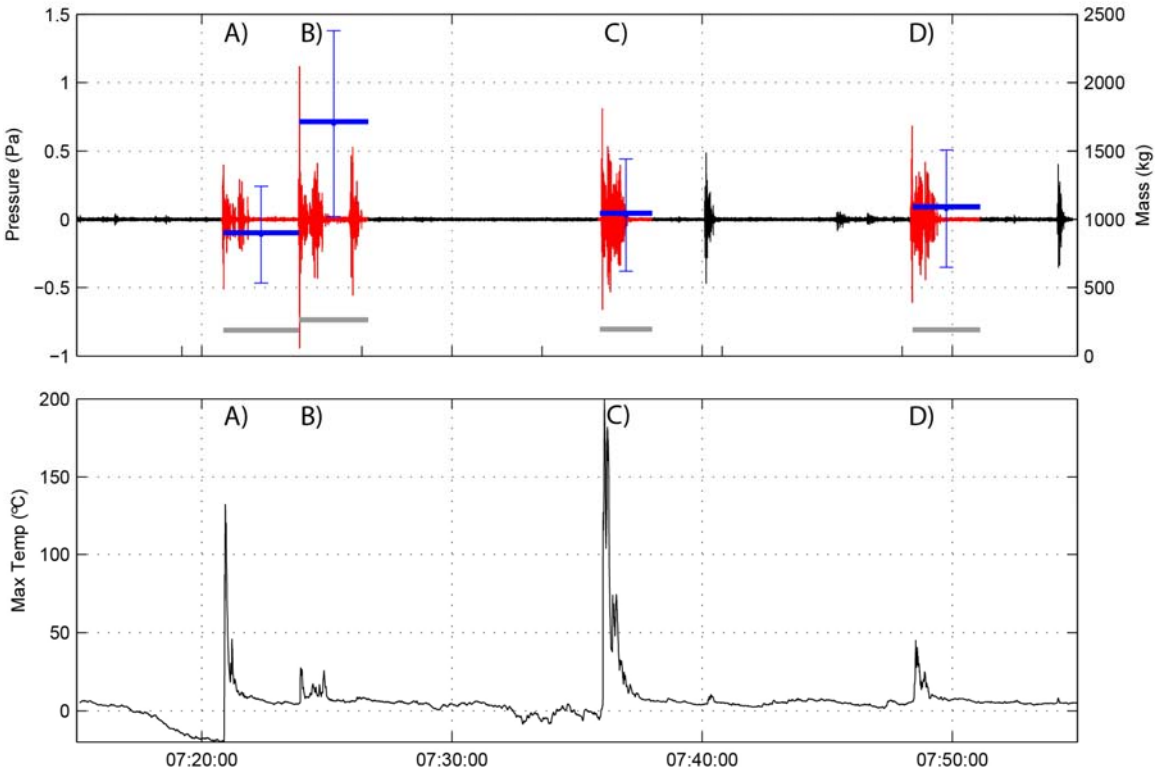

Figure 4.9: Summary of data associated with *hybrid* activity. The lower plot shows the maximum temperature as seen in the FLIR. The upper plot shows the infrasound pressure on the primary y-axis and mass of ash (blue lines) and/or SO_2 (gray lines) on the secondary y-axis, as calculated from the IR camera. Masses of ash and SO_2 were calculated for individual events that were observed in both infrasound and FLIR datasets, when possible. The length of the mass bar represents the time period over which the mass was emitted. The infrasound waveforms for periods associated with the events are colored red.

Figure 4.10: Ash and SO_2 retrievals for four hybrid events. Ash (left) and SO_2 masses (right) correspond with each of the four events shown in Figure 4.9. Color bar scales represent the column density of ash or SO_2 for each pixel. Rectangles of SO_2 depletion shown within the plumes for events C and D are an artifact of the smoothing routine within the analysis algorithm. While SO_2 masses are fairly similar for the four events, the corresponding ash masses show a much higher variability.

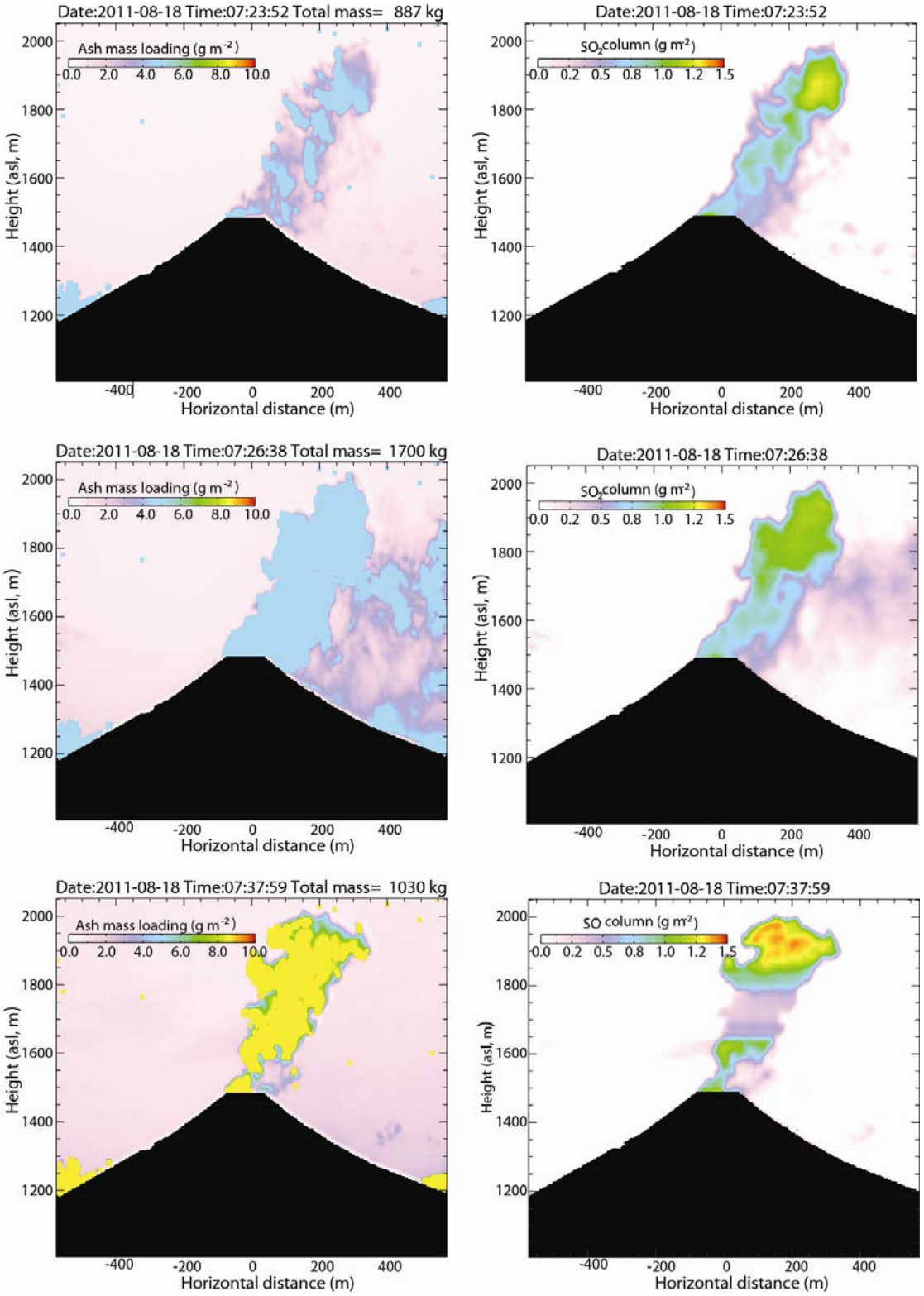
Date:2011-08-18 Time:07:23:52 Total mass= 887 kg
Ash mass loading (g m-2)
0.0 2.0 4.0 6.0 8.0 10.0
Date:2011-08-18 Time:07:23:52
SO2column (g m-2)
0.0 0.2 0.5 0.8 1.0 1.2 1.5
Date:2011-08-18 Time:07:26:38 Total mass= 1700 kg
Ash mass loading (g m-2)
0.0 2.0 4.0 6.0 8.0 10.0
Date:2011-08-18 Time:07:26:38
SO2column (g m-2)
0.0 0.2 0.5 0.8 1.0 1.2 1.5
Date:2011-08-18 Time:07:37:59 Total mass= 1030 kg
Ash mass loading (g m-2)
0.0 2.0 4.0 6.0 8.0 10.0
Date:2011-08-18 Time:07:37:59
SO column (g m-2)
0.0 0.2 0.5 0.8 1.0 1.2 1.5
Height (asl, m)
2000
1800
1600
1400
1200
-400 -200 0 200 400
Horizontal distance (m)

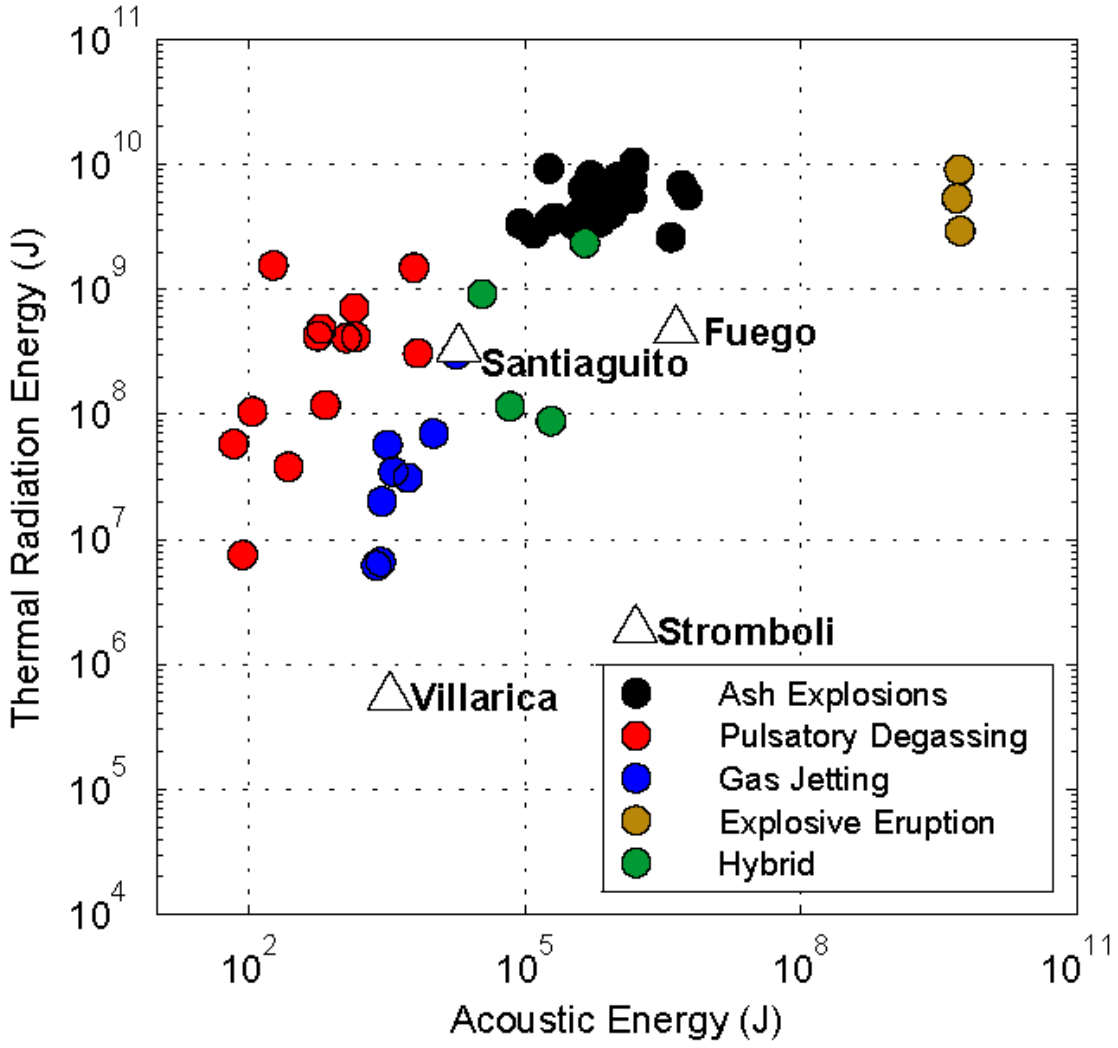

Figure 4.11: Thermal radiation energy (J) and acoustic energy (J) for each activity type. Distinct clusters among the various activity types can be seen. The thermal and acoustic energies calculated by Marchetti et al. (2009) for other volcanoes that exhibit small explosive eruption behavior are also shown. We note that *explosive eruption* thermal radiation and acoustic energies are underestimated relative to other types due to instrument saturation; while thermal energy associated with *ash explosions* is overestimated relative to other types due to the presence of background clouds in the thermal imagery.

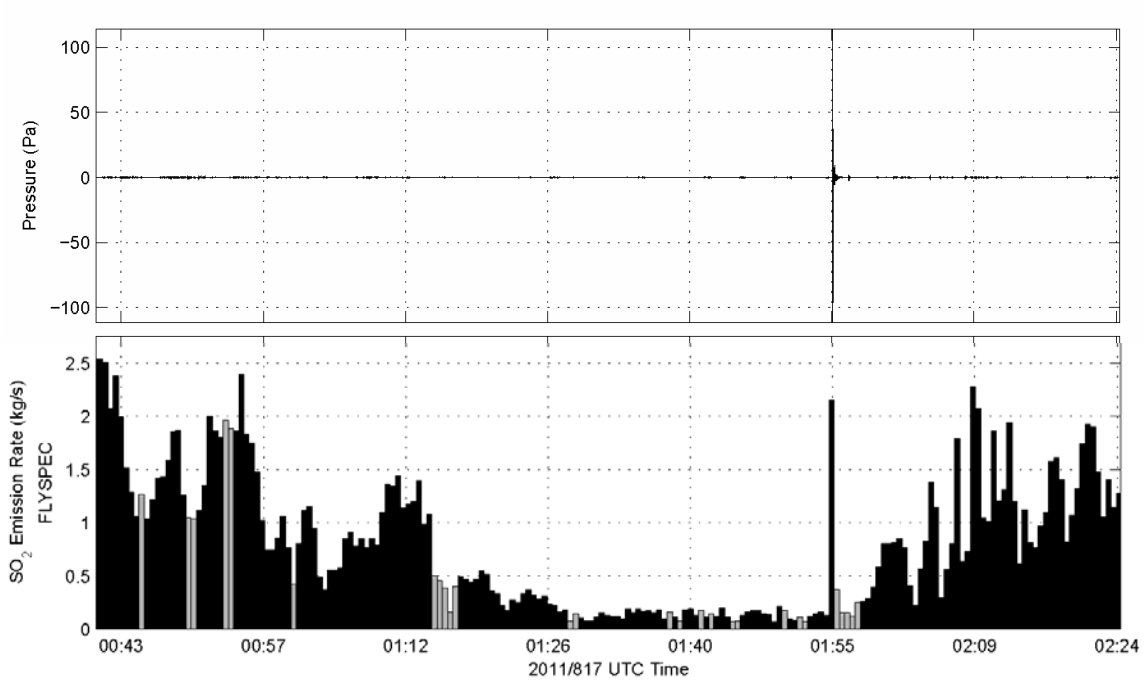

Figure 4.12: Infrasound pressure and SO_2 emission rates surrounding an *explosive eruption*. SO_2 emission rates are elevated (>2 kg/s) and pulsatory approximately one hour before the eruption. In the twenty minutes before the eruption SO_2 emission rates decrease to ~0.14 kg/s, but remain detectable through the eruption onset. A large peak in both infrasound pressure (>125 Pa) and SO_2 emission rate corresponds with the initial eruption onset, however abundant ash in the minutes following prevented accurate SO_2 retrievals. Following the explosive eruption pulses of SO_2 emission rates and infrasound can be seen. Poor signal to noise emission rate data are colored gray.

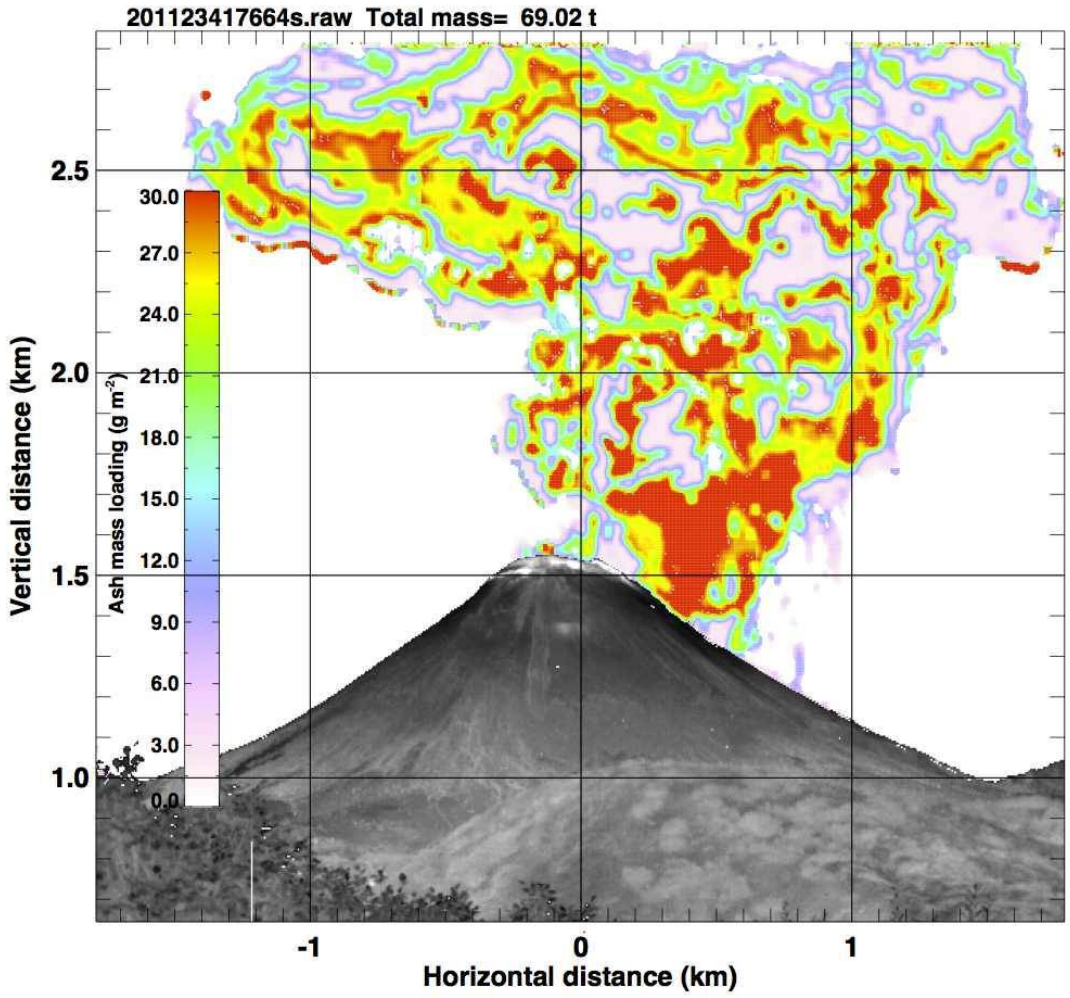

Figure 4.13: Ash mass retrieval for an *explosive eruption*. Data acquired at 08:21 on 22 August 2011. Vertical and horizontal distances are labeled on the y- and x-axes, respectively. The color bar scale shows the ash column density for each pixel. The retrieved ash mass for this image is >69,000 kg. Opaque portions of the plume (seen as low ash column density regions within the plume center) prevent accurate mass retrievals such that this mass should be considered an underestimate.

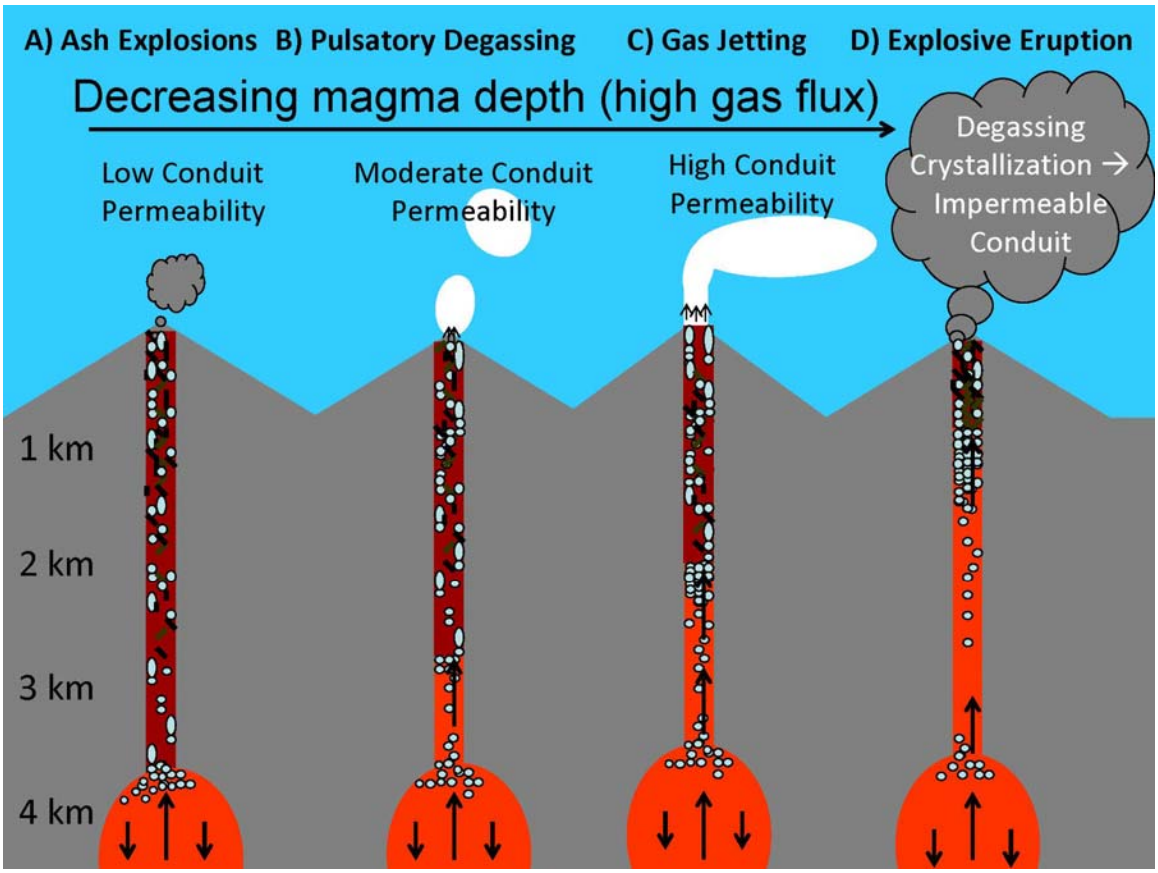

Figure 4.14: Proposed speculative model. End-member activity can be explained by variations in magma degassing depth, which affect the flux and relative proportions of decompression and crystallization-induced degassing, and influence magma viscosity and conduit permeability. Vertical scale is approximate. Scenario (A) describes *ash explosions*, scenario (B) describes *pulsatory degassing*, scenario (C) describes *gas jetting*, and scenario (D) describes *explosive eruption*. See text for details.

Tables:

Table 4.1: Instruments and methods employed in this study.

Instrument	Spectral Region	Sample Frequency	Parameter Detected	Years Deployed	Deployment Mode	References
FLIR A320 IR Camera	7.5-13 μm	5 Hz	Temperature	2011, 2012	Stationary Recording	(Spampinato et al., 2011)
NicAIR IR Camera	7-14 μm	~5 s	SO_2 Emission Rate; SO_2 and Ash Mass	2011	Stationary Recording	(Prata and Bernardo, 2009)
FLYSPEC UV Spectrometer	305-315 nm	20 s to ~3 min	SO_2 Emission Rate	2011, 2012	Horizontal Scans	(Horton et al., 2006)
Microphones	0.02-250 Hz	125 Hz (2011) 250 Hz (2012)	Infrasound (Pressure)	2011, 2012	4-5 Sensor Array	(Fee and Matoza, 2013)

Table 4.2: Multiparameter characteristics of the observed activity.

Description	Ash Explosions	Pulsatory Degassing	Gas Jetting	Explosive Eruption	Hybrid Activity
Date (UTC)	2011-08-15	2011-08-16	2012-07-21	2011-08-17	2011-08-18
Time (UTC)	20:10 - 20:50	21:00 - 21:40	22:30 - 23:10	01:38 - 02:18	07:15 -07:55
Temperature (°C)	Max Peak = 230 Mean Peak = 120±60	Max Peak = 160 Mean Peak = 70±40	Max Peak = 80 Mean Peak = 40±20	Max Peak >350	Max Peak = 220 Mean Peak = 210±80
Thermal Energy (J)	Max =1.0×10^{10} Mean = 5.3± 2.2×10^{9}	Max = 1.6×10^{9} Mean = 3.4± 4.6×10^{8}	Max = 3.0×10^{8} Mean = $6.6\pm0.6\times10^{7}$	Max >5.3×10^{9}	Max = 2. 6×10^{9} Mean = 8.7± 11×10^{8}
Cumulative Thermal Energy (J)	1.6 x 10^{11+}	8.3 x 10^{9}	2.0 x 10^{9}	4.5 x 10^{10}	NA
Ash Mass (kg)	NA	None observed	None observed	>69,000[†]	1,000±344
SO_2 Emission Rate (kg/s)	Max = 1.3 Mean = 0.7±0.4	Max[*] = 3.2 Mean[*] = 1.4±0.8	Max = 1.8 Mean = 1.0±0.3	Max = 2.3 Mean = 0.7±0.6	NA
SO_2 Mass (kg)	NA	Max* = 592 Mean* = 443±105	NA	NA	Max = 249 Mean = 173±46
Ascent Speed (m/s)	Max =9.0 Mean = 7.4±1.0	Max[‡] = 8.0 Mean[‡] = 6.4±0.7	Max = 12.6 Mean = 9.2±1.6	Max = 74.4 Mean = 8.2±8.3	Max[‡] = 10.3 Mean[‡] = 9.1±1.0
Infrasound Onset	Impulsive	Emergent	Emergent	Impulsive	Emergent/ Impulsive
Reduced Infrasound Pressure (Pa)	Max =21,500 Mean = 6240±4900	Max =500 Mean = 130±130	Max =160 Mean = 110±30	Max >500,000	Max =1,960 Mean = 750±500
Acoustic Energy (J)	Max = 5.8×10^{6} Mean = $1.1\pm1.5\times10^{6}$	Max = 6.8×10^{3} Mean = $9.3\pm19\times10^{2}$	Max = 1.8×10^{4} Mean = $6.0\pm5.5\times10^{3}$	Max >5.4×10^{9}	Max = 4.4×10^{5} Mean = $1.8\pm1.9\times10^{5}$
Cumulative Infrasound Energy (J)	1.8 x 10^{7}	3.4 x 10^{5}	6.7 x 10^{5}	4.9 x 10^{9}	NA

One standard deviation above/below the mean values are shown.
[†]This value is from an *explosive eruption* event on 22 August 2011 at 08:21 UTC, and is used as a proxy for the ash mass of the *explosive eruption* presented here.
[*]These measurements were collected using the NicAIR, all other SO_2 emission rates from FLYSPEC.
[‡]Ascent speeds calculated from IR camera. All other ascent speeds from FLIR.
[+]Background clouds are biasing cumulative thermal radiation measurements high for ash explosion activity.

Table 4.3. Volatile saturation in the shallow crust.

Pressure (MPa)	Depth (m)	S* (ppm)	CO_2 (ppm)	H_2O (wt.%)
150	~6000	3300	280	3.7
100	~4000	2800	150	3.2
50	~2000	2000	75	2.2
10	~400	75	25	0.7

Approximate values based on a rhyolitic melt buffered at NNO+1.
*S calculations assume a fixed water concentration of 3 wt.%.
Data from Moretti et al., 2003.

References Cited:

Aiuppa, A., Inguaggiato, S., McGonigle, A., O'Dwyer, M., Oppenheimer, C., Padgett, M., Rouwet, D. and Valenza, M., 2005. H_2S fluxes from Mt. Etna, Stromboli, and Vulcano (Italy) and implications for the sulfur budget at volcanoes. Geochimica et Cosmochimica Acta, 69(7): 1861-1871.

Aiuppa, A., Moretti, R., Federico, C., Guidice, G., Gurrieri, S., Liuzzo, M., Papale, P., Shinohara, H. and Valenza, M., 2007. Forecasting Etna eruptions by real-time observations of volcanic gas composition. Geology, 35(12): 1115-1118.

Andres, R.J. and Schmid, J.W., 2001. The effects of volcanic ash on COSPEC measurements. Journal of Volcanology and Geothermal Research, 108: 237-244.

Baldridge, A.M., Hook, S.J., Grove, C.I. and Rivera, G., 2009. The ASTER Spectral library version 2.0. Remote Sensing of the Environment, 113: 711-715.

Bluth, G.J.S., Shannon, J.M., Watson, I.M., Prata, A.J. and Realmuto, V.J., 2007. Development of an ultra-violet digital camera for volcanic SO_2 imaging. Journal of Volcanology and Geothermal Research, 161: 47-56.

Bull, K.F. and Buurman, H., 2012. An overview of the 2009 eruption of Redoubt Volcano, Alaska. Journal of Volcanology and Geothermal Research, Special Issue on the 2009 Redoubt Eruption. doi:10.1016/j.volgeores.2012.06.024.

Burnham, C.W., 1985. Energy release in subvolcanic environments: Implications for breccia formation. Economic Geology, 80: 1515-1522.

Burton, M., Allard, P., Mure, F. and La Spina, A., 2007. Magmatic gas composition reveals the source depth of slug-driven strombolian explosive activity. Science, 317: 227-230.

Caplan-Auerbach, J., Bellesiles, A. and Fernandes, J.K., 2010. Estimates of eruption velocity and plume height from infrasonic recordings of the 2006 eruption of Augustine Volcano, Alaska. Journal of Volcanology and Geothermal Research, 189(1-2): 12-18. doi:10.1016/j.jvolgeores.2009.10.002.

Carroll, M. and Webster, J., 1994. Solubilities of Sulfur, Noble Gases, Nitrogen, Chlorine and Fluorine in Magmas. In: M. Carroll and J. Holloway (Editors), Volatiles in Magmas. Reviews in Mineralogy. Mineralogical Society of America, Fredericksburg, pp. 231-279.

Dalton, M., Waite, G., Watson, I. and Nadeau, P., 2010. Multiparameter quantification of gas release during weak Strombolian eruptions at Pacaya Volcano, Guatemala. Geophysical Research Letters, 37: L09303. doi:10.0129/2010g1042617.

De Angelis, S., Fee, D., Haney, M. and Schneider, D., 2012. Detecting hidden volcanic explosions from Mt. Cleveland Volcano, Alaska with infrasound and ground-coupled airwaves. Geophysical Research Letters, 39: L21312. doi:10.1029/2012GL053635.

Dingwell, D.B., Romano, R. and Hess, K.U., 1996. The effect of water on the viscosity of a haplogranitic melt under P-T-X conditions relevant to silicic volcanism. Contributions to Mineralogy and Petrology, 124: 19-28.

Dozier, J., 1981. A method for satellite identification of surface temperature fields of subpixel resolution. Remote Sensing of the Environment, 11: 221-229.

Edmonds, M., Herd, R., Galle, B. and Oppenheimer, C., 2003a. Automated, high time-resolution measurements of SO_2 flux at Soufriere Hills Volcano, Montserrat. Bulletin of Volcanology, 65: 578-586.

Edmonds, M., Oppenheimer, C., Pyle, D., Herd, R. and Thompson, G., 2003b. SO_2 emissions from Soufriere Hills Volcano and their relationship to conduit permeability, hydrothermal interaction and degassing regime. Journal of Volcanology and Geothermal Research, 124: 23-43. doi:10.1016/S0377-0273(03)00041-6.

Eichelberger, J.C., Carrigan, C.R., Westrich, H.R. and Price, R.H., 1986. Non-explosive silicic volcanism. Nature, 323: 598-602.

Fee, D. and Matoza, R.S., 2013. An overview of volcano infrasound: From hawaiian to plinian, local to global. Journal of Volcanology and Geothermal Research, 249: 123-139. doi: 10.1016/j.jvolgeores.2012.09.002.

Fee, D., Garces, M. and Steffke, A., 2010. Infrasound from Tungurahua Volcano 2006 - 2008: Strombolian to Plinian eruptive activity. Journal of Volcanology and Geothermal Research, 193: 67-81. 10.1016/j.jvolgeores.2010.03.006.

Fee, D., McNutt, S., Lopez, T., Arnoult, K., Szuberla, C. and Olson, J., 2011. Combining local and remote infrasound recordings from the 2009 Redoubt Volcano eruption. Journal of Volcanology and Geothermal Research, Special Issue on the 2009 Redoubt Eruption doi:10.1016/j.volgeores.2011.09.012.

Fischer, T., Morrissey, M.M., Calvache, M.L., Gomez, D., Torres, R., Stix, J. and Williams, S.N., 1994. Correlations between SO_2 flux and long period seismicity at Galeras volcano. Nature, 368(6467): 135-137.

Fischer, T., Arehart, G., Sturchio, N. and Williams, S., 1996. The relationship between fumarole gas composition and eruptive activity at Galeras Volcano, Colombia. Geology, 24(6): 531 - 534. doi:10.1130/0091-7613(1996)024<0531:TRBFGC>2.3.CO;2.

Fischer, T., Roggensack, K. and Kyle, P., 2002. Open and almost shut case for explosive eruptions: Vent processes determined by SO_2 emission rates at Karymsky volcano, Kamchatka. Geology, 12: 1059-1062.

Francis, P., Maciejewski, C., Oppenheimer, C., Chafflin, C. and Caltabiano, T., 1995. SO_2:HCl ratios in the plumes from Mt. Etna and Vulcano determined by Fourier transform spectroscopy. Geophysical Research Letters, 22: 1717-1720.

Galle, B., Oppenheimer, C., Geyer, A., McGonigle, A., Edmonds, M. and Horrocks, L., 2002. A miniaturised ultraviolet spectrometer for remote sensing of SO_2 fluxes: a new tool for volcano surveillance. Journal of Volcanology and Geothermal Research, 119: 241-254.

Galle, B., Johansson, M., Rivera, C., Zhang, Y., Kihlman, M., Kern, C., Lehmann, T., Platt, U., Arellano, S. and Hidalgo, S., 2010. Network for Observation of Volcanic and Atmospheric Change (NOVAC) - A global network for volcanic gas monitoring: Network layout and instrument description. Journal of Geophysical Research, 115: D05304. doi:10.1029/2009JD011823.

Gerlach, T., 1986. Exsolution of H_2O, CO_2, and S during eruptive episodes at Kilauea Volcano, Hawaii. Journal of Geophysical Research, 91(B12): 12,177-112,185.

Gerlach, T., 2003. Elevation effects in volcano applications of the COSPEC. In: C. Oppenheimer, D. Pyle and J. Barclay (Editors), Volcanic Degassing. The Geological Society of London, London, pp. 169-175.

Gerlach, T., 2004. Volcanic sources of tropospheric ozone-depleting trace gases. Geochemistry, Geophysics, Geosystems, 5: Q09007.

Giggenbach, W., 1996. Chemical composition of volcanic gases. In: R. Scarpa and R. Tilling (Editors), Monitoring and Mitigation of Volcano Hazards. Springer, Berlin, pp. 221-256.

Gonnermann, H.M. and Manga, M., 2003. Explosive volcanism may not be an inevitable consequence of magma fragmentation. Nature, 426(27): 432-435.

Harris, A. and Ripepe, M., 2007. Synergy of multiple geophysical approaches to unravel explosive eruption conduit and source dynamics - A case study from Stromboli. Chemie de Erde, 67: 1-35.

Harris, A., Dehn, J. and Calvari, S., 2007. Lava effusion rate definition and measurement: a review. Bulletin of Volcanology, 70: 1-22. doi:10.1007/s00445-007-0120-y.

Harris, A.J.L., Butterworth, A.L., Carlton, R.W., Downey, I., Miller, P., Navarro, P. and Rothery, D.A., 1997. Low-cost volcano surveillance from space: case studies from Etna, Krafla, Cerro Negro, Fogo, Lascar and Erebus. Bulletin of Volcanology, 59: 49-64.

Hobbs, P., Radke, L., Lyons, J., Ferek, R., Coffman, D. and Casadevall, T., 1991. Airborne measurements of particle and gas emissions from the 1990 volcanic eruption of Mount Redoubt. Journal of Geophysical Research, 96(D10): 18,735-718,752.

Hort, M., Seyfried, R. and Voge, M., 2003. Radar Doppler velocimetry of volcanic eruptions: theoretical considerations and quantitative documentation of changes in eruptive behavior at Stromboli volcano, Italy. Geophysical Journal International, 154: 515-532.

Horton, K., Williams-Jones, G., Garbeil, H., Elias, T., Sutton, A.J., Mouginis-Mark, P., Porter, J. and Clegg, S., 2006. Real-time measurement of volcanic SO_2 emissions: validation of a new UV correlation spectrometer (FLYSPEC) Bulletin of Volcanology, 68(4): 323-327.

Izbekov, P., Eichelberger, J. and Ivanov, B., 2004. The 1996 eruption of Karymsky Volcano, Kamchatka: Historical record of basaltic replenishment of an andesite reservoir. Journal of Petrology, 45(11): 2325-2345. doi:10.1093/petrology/egh059.

Jaupart, C. and Allegre, C., 1991. Gas content, eruption rate and instabilities of eruption regime in silicic volcanoes. Earth and Planetary Science Letters, 102: 413-429.

Johnson, J.B., 2007. On the relation between infrasound, seismicity, and small pyroclastic explosions at Karymsky Volcano. Journal of Geophysical Research, 112: B08203.

Johnson, J. and Lees, J., 2000. Plugs and chugs - seismic and acoustic observations of degassing explosions at Karymsky, Russia and Sangay, Ecuador. Journal of Volcanology and Geothermal Research, 101(101): 67 - 82.

Johnson, J.B. and Ripepe, M., 2011. Volcano infrasound: A review. Journal of Volcanology and Geothermal Research, 206(3-4): 61-69. doi:10.1016/j.jvolgeores.2011.06.006.

Johnson, J., Lees, J. and Gordeev, E., 1998. Degassing Explosions at Karymksy Volcano, Kamchatka. Geophysical Research Letters, 25(21): 3999.

Kern, C., Deutschmann, T., Vogel, L., Wohrbach, M., Wagner, T. and Platt, U., 2010. Radiative transfer corrections for accurate spectroscopic measurements of volcanic gas emissions. Bulletin of Volcanology, 72: 233-247. doi:10.1007/s00445-009-0313-7.

KVERT, 2012. Archived Information Releases. http://www.kscnet.ru/ivs/kvert/van/index.php?type=1.

Lees, J., Gordeev, E. and Ripepe, M., 2004. Explosions and periodic tremor at Karymksy volcano, Kamchatka, Russia. Geophysics Journal International, 158: 1151-1167.

Lopez, T., Dehn, J., Fee, D., Belousov, A., Buurman, H., Grapenthin, R. and Ushakov, S., 2011. Use of high temporal resolution thermal imagery of Karymsky's volcanic plume to constrain volcanic activity and elucidate vent processes. American Geophysical Union Fall Meeting, V33A-2618.

Lopez, T., Ushakov, S., Izbekov, P., Tassi, F., Cahill, C., Neill, O.K. and Werner, C., in press. Constraints on magma processes, subsurface conditions, and total volatile flux at Bezymianny Volcano in 2007-2010 from direct and remote volcanic gas measurements. Journal of Volcanology and Geothermal Research. doi:10.1016/j.volgeores.2012.10.015.

Lyons, J.L., Waite, G.P., Rose, W.I. and Chigna, G., 2010. Patterns in open vent, strombolian behavior at Fuego volcano, Guatemala, 2005-2007. Bulletin of Volcanology, 72: 1-15. doi.10.1007/s00445-009-0305-7.

Marchetti, E., Ripepe, M., Harris, A.J.L. and Delle Donne, D., 2009. Tracing the differences between Vulcanian and Strombolian explosions using infrasonic and thermal radiation energy. Earth and Planetary Science Letters, 279: 273-281.

Matoza, R.S., Fee, D., Garces, M.A., Seiner, J.M., Ramon, P.A. and Hedlin, M.A.H., 2009. Infrasonic jet noise from volcanic eruptions. Geophysical Research Letters, 36: L08303.

Millan, M., 1980. Remote sensing of air pollutants: a study of some atmospheric scattering effects. Atmospheric Environment, 14: 1241-1253. doi:10.1016/0004-6981(80)90226-7.

Moretti, R., Papale, P. and Ottonello, G., 2003. A model for the saturation of C-O-H-S fluids in silicate melts. In: C. Oppenheimer, D. Pyle and J. Barclay (Editors), Volcanic Degassing. The Geological Society of London, London, pp. 81-101.

Mori, T. and Burton, M., 2006. The SO_2 camera: A simple, fast and cheap method for ground-based imaging of SO_2 in volcanic plumes. Geophysical Research Letters, 33: L24804.

Mori, T., Mori, T., Kazahaya, K., Ohwada, M., Hirabayashi, J.i. and Yoshikawa, S., 2006. Effects of UV scattering on SO_2 emission rate measurements. Geophysical Research Letters, 33: L17315.

Nadeau, P.A., Palma, J.L. and Waite, G.P., 2011. Linking volcanic tremor, degassing, and eruption dynamics via SO_2 imaging. Geophysical Research Letters, 38: L01304.

Newhall, C.G. and Self, S., 1982. The volcanic explosivity index (VEI): An estimate of explosive magnitude for historical volcanism. Journal of Geophysical Research, 87(C2): 1231-1238.

Ozerov, A., Ispolatov, I. and Lees, J., 2003. Modeling strombolian eruptions of Karymsky volcano, Kamchatka, Russia. Journal of Volcanology and Geothermal Research, 122: 265-280.

Palma, J.L., Calder, E.S., Basualto, D., Blake, S. and Rothery, D.A., 2008. Correlations between SO_2 flux, seismicity, and outgassing activity at the open vent of Villarica volcano, Chile. Journal of Geophysical Research-Solid Earth, 113: B10201.

Pieri, D. and Baloga, M., 1986. Eruptive rate, area, and length relationships for some Hawaiian lava flows. Journal ov Volcanology and Geothermal Research, 30: 29-45.

Platt, U. and Stutz, J., 2008. Differential Optical Absorption Spectroscopy Principles and Applications. Springer-Verlag, Berlin - Heidelberg.

Poland, M., Miklius, A., Orr, T., Sutton, A.J., Thornber, C. and Wilson, D., 2008. New episodes of volcanism at Kilauea Volcano, Hawaii. Eos Transactions, 89(5). 10.1029/2008EO050001.

Prata, A.J., 1989. Infrared radiative transfer calculations for volcanic ash clouds. Geophysical Research Letters, 16(11): 1293-1296.

Prata, A.J. and Bernardo, C., 2009. Retrieval of volcanic ash partical size, mass and optical depth from a ground-based thermal infrared camera. Journal of Volcanology and Geothermal Research, 186: 91-107. doi:10.1016/j.volgeores.2009.02.007.

Ripepe, M., Harris, A.J.L. and Marchetti, E., 2005. Coupled thermal oscillations in explosive activity at different craters of Stromboli volcano. Geophysical Research Letters, 32: L17302. doi:10.1029/2005GL022711.

Rose, W.I. and Durant, A.J., 2009. Fine ash content of explosive eruptions. Journal of Volcanology and Geothermal Research, 186(1-2): 32-39.

Rothery, D.A., Francis, P.W. and Wood, C.A., 1988. Volcano monitoring using short wavelength infrared data from satellites. Journal of Geophysical Research, 93(B7): 7993-8008.

Sawyer, G.M. and Burton, M.R., 2006. Effects of a volcanic plume on thermal imaging data. Geophysical Research Letters, 33: L14311.

Schaefer, J., Bull, K.F., Cameron, C., Coombs, M., Diefenbach, A.K., Leonard, G., Lopez, T., McNutt, S., Neal, C., Payne, A., Power, J., Schneider, D., Scott, W., Snedigar, S., Thompson, G., Wallace, K., Waythomas, C., Wilson, T., Webley, P. and Werner, C., 2011. The 2009 Eruption of Redoubt Volcano, Alaska. The Alaska Division of Geological and Geophysical Surveys, Report of Investigations: 55.

Scharff, L., Hort, M., Harris, A.J.L., Ripepe, M., Lees, J. and Seyfried, R., 2008. Eruption dynamics of the SW crater of Stromboli volcano, Italy - An interdisciplinary approach. Journal of Volcanology and Geothermal Research, 176: 565-570. doi:10.1016/j.jvolgeores.2008.05.008.

Shinohara, H., 2008. Excess degassing from volcanoes and its role on eruptive and intrusive activity. Reviews of Geophysics, 46: RG4005.

Spampinato, L., Calvari, S., Oppenheimer, C. and Boschi, E., 2011. Volcano surveillance using infrared cameras. Earth-Science Reviews, 106: 63-91. doi:10.1016/j.earscirev.2011.01.003.

Sparks, R.S.J., 2003. Dynamics of magma degassing. In: C. Oppenheimer, D.M. Pyle and J. Barclay (Editors), Volcanic Degassing. Geological Society, London, pp. 5-22.

Sparks, R.S.J., Murphy, M.D., Lejeune, A.M., Watts, R.B., Barclay, J. and Young, S.R., 2000. Control on the emplacement of the andesite lava dome of Soufriere Hills volcano, Montserrat by degassing-induced crystallization. Terra Nova, 12(1): 14-20.

Steffke, A., Fee, D., Garces, M. and Harris, A., 2010. Eruption chronologies, plume heights and eruption styles at Tungurahua Volcano: Integrating remote sensing techniques and infrasound. Journal of Volcanology and Geothermal Research, 193(3-4): 143-160. doi:10.1016/j.jvolgeores.2010.03.004.

Stoiber, R., Malinconico, L. and Williams, S., 1983. The use of correlation spectrometers at volcanoes. In: H. Tazieff and J. Sabroux (Editors), Forecasting Volcanic Events. El Sevier, Amsterdam - New York, pp. 425-444.

Symonds, R., Rose, W., Bluth, G. and Gerlach, T., 1994. Volcanic Gas Studies: Methods, Results, and Applications. In: M. Carroll and J. Holloway (Editors), Volatiles in Magmas. Reviews in Mineralogy. Mineralogical Society of America, Fredericksburg, pp. 1 - 63.

Symonds, R.B., Gerlach, T.M. and Reed, M.H., 2001. Magmatic gas scrubbing: implications for volcano monitoring. Journal of Volcanology and Geothermal Research, 108(1-4): 303-341. doi:10.1016/S0377-0273(00)00292-4.

Werner, C., Hurst, T., Scott, B., Sherburn, S., Christenson, B.W., Britten, K., Cole-Baker, J. and Mullan, B., 2008. Variability of passive gas emissions, seismicity, and deformation during the crater lake growth at White Island Volcano, New Zealand, 2002-2006. Journal of Geophysical Research, 113: B1204. doi:10.1029/2007/JB005094.

Williams-Jones, G., Stix, J. and Nadeau, P., 2008. Using the COSPEC in the Field. In: G. Williams-Jones, J. Stix and C. Hickson (Editors), The COSPEC Cookbook: Making SO_2 Measurements at Active Voclanoes. IAVCEI, pp. 63-119.

Wilson, L. and Self, S., 1980. Volcanic explosion clouds: Density, temperature, and particle content estimates from cloud motion. Journal of Geophysical Research, 85(B5): 2567-2572.

Woulff, G. and McGetchin, T.R., 1976. Acoustic Noise from Volcanoes: Theory and Experiment. Geophys. J. R. Astr. Soc, 45: 601-616.

CHAPTER 5: Conclusions

Measurements of volcanic emissions provide important insight into subsurface and surface processes occurring at active volcanoes that can have significant implications for volcano monitoring, eruption forecasting and hazard mitigation. Throughout this dissertation I aimed to elucidate volcanic behavior through measurements of volcanic emissions at three remote and hazardous arc volcanoes: Redoubt Volcano, Alaska; Bezymianny Volcano, Kamchatka, Russia; and Karymsky Volcano, Kamchatka, Russia. The specific objectives of this project were to: (1) characterize the volcanic activity observed at the target volcanoes using direct and remote volcanic emissions datasets; (2) use temporal trends in volcanic gas composition and flux to infer subsurface conditions including: conduit permeability, magma depth, degassing behavior, and/or the presence of a shallow water system; and (3) evaluate the application of several new technologies for the remote monitoring of volcanic emissions. The key findings of this dissertation are summarized in the following sections and a brief comparison of the target volcanoes is conducted.

5.1 Using Volcanic Emissions Measurements to Characterize Volcanic Activity

At each of the target volcanoes volcanic emissions measurements were used to help characterize eruptive and degassing behavior. In Chapter 2, near-daily measurements of SO_2 mass from Redoubt Volcano by the Ozone Monitoring Instrument (OMI) were compared with volcanic activity. The results showed that significantly higher SO_2 masses were emitted on days with explosive eruption events (~17.3 kt on average) relative to daily SO_2 masses during the effusive phase (~4.7 kt on average). Additionally, positive correlations between OMI daily SO_2 masses and both tephra mass and acoustic energy were observed during the explosive phase of the eruption, which suggests that OMI data may be used to infer relative eruption size and explosivity. The cumulative SO_2 mass calculated for the first three months of the eruption was estimated to range between 542 and 615 kt, with approximately half of this mass (335 kt) being emitted during the

explosive phase. This large portion of SO_2 emitted during the explosive phase suggests that the degassing behavior at Redoubt Volcano is predominantly closed system.

In Chapter 3, direct and remote measurements of volcanic gas composition, SO_2 flux, and eruptive SO_2 masses were acquired from Bezymianny Volcano between July 2007 and July 2010. During this time period Bezymianny had five explosive eruptions. As was seen at Redoubt Volcano, Bezymianny Volcano emitted significantly higher daily SO_2 masses during explosive eruption (~6,600 t in Oct. 2007) in comparison with typical daily passive SO_2 emissions (~280 t/d). Estimates of passive and eruptive SO_2 emissions suggest that passive emissions make up ~87-95% of total SO_2 emissions at Bezymianny Volcano, supporting open-system degassing as the dominant degassing behavior.

In Chapter 4, a multiparameter dataset was used to characterize diverse activity observed at Karymsky Volcano in August 2011 and July 2012. Four end-member activity types were observed and described as: (1) *discrete ash explosions*, (2) *pulsatory degassing*, (3) *gas jetting*, and (4) quiescence followed by *explosive eruption*. Observations of infrasound, volcanic emissions, and temperature were used to quantitatively characterize the four end-member activity types. Unique temperature and infrasound signals were associated with each activity type. Specifically, *ash explosions* and *explosive eruption* events were characterized by high amplitude, impulsive infrasound signals with two and three order of magnitude greater pressures than *pulsatory degassin*g and *gas jetting* activity, respectively. These observations suggest that *ash explosions* and *explosive eruption* events are more explosive and have a higher relative vent overpressure than the degassing activity types. Additionally, maximum temperatures and cumulative thermal energies for the explosive activity were also significantly larger than for the degassing activity types, suggesting the eruption of hotter material or larger quantities of hot material, and a higher level of magma fragmentation. Continuous SO_2 emissions and discontinuous ash emissions were observed throughout the study period and suggest a decoupling between magma and volatiles at depth, consistent with open-system

degassing behavior. Strong temporal correlations between visual observations of explosive activity and peaks in temperature and pressure suggest that for the current eruptive phase, Karymsky's volcanic activity can be characterized using remote measurements of infrasound and thermal energy.

5.2 Using Volcanic Emissions Measurements to Infer Subsurface Conditions

In addition to characterizing surface activity, volcanic emissions measurements can also be used to infer subsurface conditions. Chapter 3 describes observations and interpretations of volcanic gas composition and flux measurements acquired in the months preceding explosive eruptions at Bezymianny Volcano in October 2007 and December 2009. Highly similar passive SO_2 and CO_2 fluxes were observed between the 2007 and 2009 field campaigns, while order of magnitude variations in H_2O, HCl, and total volatile flux were observed over the same time period. The contrasting trends in the various volatile fluxes observed can be explained by trends in volatile solubility within melt, which can be attributed to variations in depth of gas exsolution and separation from the melt under open-system degassing conditions. Specifically, volcanic gas composition and flux collected prior to the 2007 eruption were consistent with degassing of relatively shallow magma, while the composition and flux observed prior to the 2009 eruption were consistent with degassing of relatively deeper magma. Based on our findings we propose that at the times of sample collection in 2007 and 2009 the degassing magma had already begun ascent from the mid-crustal storage region and that exsolved volatiles were able to quickly ascend via permeable conduit flow. These finding suggest that exsolved gas composition can be used at Bezymianny to detect magma ascent prior to eruption.

During the field campaigns at Karymsky Volcano continuous SO_2 emissions were observed for the various styles of eruptive activity exhibited, as described in Chapter 4. When SO_2 emission rates were observed over an extended time period surrounding *explosive eruption,* a significant decrease in SO_2 emission rates from ~220 t/d down to ~10 t/d was observed in the 75 minute prior to the eruption. This decrease in measured

SO_2 emission rates corresponded with a time period when no visible emissions of any kind could be seen by eye. Additionally, as mentioned in Section 5.1, significantly higher infrasound pressures were associated with *ash explosion* and *explosive eruption* activities, implying a higher vent overpressure. We interpret these observations, including decreases in SO_2 emission rates prior to eruption and a high infrasound pressure upon eruption, to indicate that a decrease in conduit permeability leads to more explosive volcanic activity at Karymsky Volcano.

These examples show that: (1) measurements of gas composition, SO_2 emission rate, and total volatile flux can be used to infer changes in relative magma degassing depth at Bezymianny Volcano, and (2) combined measurements of volcanic emissions and infrasound can be used to identify changes in conduit permeability at Karymsky Volcano. Both observations can help scientists better forecast volcanic eruptions.

5.3 Evaluating New Techniques for Remotely Measuring Volcanic Emissions

One of the primary objectives of Chapters 2 and 4 was to evaluate new techniques for measuring volcanic emissions. In Chapter 2, OMI satellite observations of SO_2 emissions from Redoubt Volcano, Alaska, were compared with near-coincident airborne SO_2 measurements conducted by the Alaska Volcano Observatory to: (1) validate OMI SO_2 column density measurements, and (2) develop a method to convert OMI mass into emission rates that would allow these data to be directly integrated into existing volcanic emissions datasets. The results of the comparisons between airborne and OMI SO_2 column densities found that for Redoubt's tropospheric plume OMI overestimated and underestimated SO_2 with respect to airborne measurements for analyses conducted using the PBL and TRL algorithms, respectively. A linear correlation between OMI PBL and airborne SO_2 column densities was found ($R^2 = 0.75$). Several simple methods were developed to convert OMI-measured SO_2 masses into emission rates, which were then evaluated with respect to near-coincident airborne measurements. A strong correlation between airborne and OMI-derived (*Method* 1) emission rates ($R^2 = 0.82$) was found,

with OMI-derived emission rates being underestimated with respect to airborne measurements in most cases. It should be noted that the *Method 1* emission rates were calculated using OMI TRL algorithm-derived SO_2 column densities, which also underestimated SO_2 relative to airborne measurements and can explain the underestimated emission rates. Through comparison of OMI and airborne SO_2 measurements it was possible to constrain OMI's detection limit for high latitude spring-time conditions to be ~2-4 kt. These findings indicate that OMI is a useful volcano monitoring tool that can provide daily SO_2 measurements associated with both explosive and effusive styles of volcanic activity that are linearly correlated with respect to airborne measurements, and can be converted into emission-rates to allow direct comparison with traditional emissions measurements.

In Chapter 4, two new technologies, including a NicAIR IR camera and an infrasound array were employed at Karymsky Volcano to remotely and indirectly measure volcanic emissions, respectively. Additionally, two established techniques, a FLYSPEC UV spectrometer system and FLIR thermal imaging camera were evaluated with respect to their ability to capture the dynamic activity observed at Karymsky Volcano. The NicAIR IR camera allows high temporal resolution measurements of SO_2 and ash column densities and masses, as well as SO_2 emission rates and plume ascent speeds. The instrument is straightforward to operate and easily provides qualitative measurements; however, quantitative analyses requires a computationally and labor-intensive radiative transfer model, which prevents prompt analysis of large quantities of data. Additionally, abundant ash significantly attenuates radiation and can make plumes opaque, such that accurate ash and SO_2 retrievals are not possible. The UV and IR remote sensing instruments were supplemented with infrasound, a well-established tool for detecting volcanic activity, that recent research has shown correlates with volcanic emissions. Infrasound was used at Karymsky Volcano to both detect and characterize volcanic activity, and to identify possible correlations with volcanic emissions measurements. Strong correlations between high temporal resolution FLIR maximum temperatures and

infrasound pressure signals were found that corresponded with vent activity. Additionally, it appeared that correlations between infrasound and SO_2 emission rates exist for some styles of volcanic activity (e.g. *explosive eruptions*); however, the temporal resolution of the SO_2 datasets was often not sufficient to capture the dynamic activity at Karymsky Volcano. The above vent-scanning mode used by the FLYSPEC allowed scans to be conducted within 30 seconds, which would be more than adequate for most volcanoes. I propose that instruments such as the IR camera (described here) or UV camera (Mori and Burton, 2006; Bluth et al., 2007), that provide higher temporal resolution SO_2 emission rate measurements, may better capture short-term variations in SO_2 emission rates that may correlate with infrasound at Karymsky Volcano. Finally, the FLIR thermal imaging camera proved to be highly useful for capturing high temporal resolution thermal measurements and imagery of the volcanic activity, and showed a strong temporal correlation with the infrasound data. The main advantage that infrasound measurements have over the UV and IR remote sensing measurements is the ability to operate continuously, unattended, and under any weather conditions. This is a significant advantage at remote volcanoes around the North Pacific, such as Redoubt, Bezymianny and Karymsky Volcanoes, as these volcanoes are often plagued by persistently cloudy and/or foggy weather conditions, when remote sensing measurements are hindered.

A summary table describing the characteristics of the instruments employed and the advantages and disadvantages of each technique is found in Table 5.1. The characteristics of each measurement technique should be considered when planning a research project at an active volcano as each volcano exhibits different styles of activity and certain instruments will be more appropriate than others with respect to the volcanic activity and the project objectives.

5.4 Comparison of the Target Volcanoes

The target volcanoes of Redoubt, Alaska; Bezymianny, Kamchatka, Russia; and Karymsky, Kamchatka, Russia, are all predominantly andesitic volcanoes that have undergone one or more explosive eruption in the past five years. Several similarities and differences can be found among these volcanoes that were both observed during this study and found within the literature. These similarities and differences are discussed below and summarized in Table 5.2. The three volcanoes have erupted similar composition magmas over the past ~50 years ranging from 56.8 – 62.4 wt.% SiO_2, with Bezymianny's recent eruptive material being the most mafic and Karymsky's being the most silicic (Izbekov et al., 2004; Coombs et al., in press; Turner et al., in press). Redoubt and Karymsky Volcanoes are thought to have magma storage regions located between ~4 and 6 km depth, while Bezymianny's storage region is thought to be located between ~6 and 10 km depth or greater (Braitseva, 1991; Ozerov et al., 2003; Thelen et al., 2010; Bull and Buurman, 2012). The estimated eruptive volume for the 2009 eruption of Redoubt Volcano is similar order of magnitude (10^6 – 10^7 m^3) to that of Bezymianny's eruptions in October 2007 and December 2009 (Zharinov and Demyanchuk, 2011), while Karymsky's eruptive volume, estimated in Chapter 4, is an order of magnitude lower (10^5 m^3). We caution that the Karymsky estimated eruptive volume is based on a particle size distribution from Fuego Volcano and the very fine ash mass estimated for Karymsky Volcano using the NicAIR IR camera, and requires further validation. Additionally, estimated initial melt CO_2 and S concentrations within Redoubt and Bezymianny magmas are highly similar (1.98 wt.% and 1.67 wt.% CO_2; and 5560 ppm and 5070 ppm S) for Redoubt and Bezymianny Volcanoes, respectively (Werner et al., 2012; Chapter 3, this study). These similarities may help constrain typical initial volatile concentration within arc magmas, which could help link gas composition data with magma degassing depth through solubility models. The initial melt S concentration for Karymsky Volcano can be estimated following the methods and equations described in Section 3.4.2 under several assumptions: (1) the average SO_2 emissions observed during the field campaigns (0.82 kg/s) is representative of typical emission throughout the year such that E_{SO2} is

~26,000 t (Chapter 4); (2) melt density (ρ_m) and melt fraction (φ_m) are equal to 2.47 x 10^{12} kg/km^3 and 0.72, respectively (Izbekov et al., 2004); and (3) annual eruptive volume is 2.55 x 10^5 m^3 (Chapter 4). This leads to an estimated initial melt S concentration for Karymsky Volcano of ~57,000 ppm (Table 5.2). This value is two orders of magnitude larger than estimated for Redoubt and Bezymianny Volcanoes. This may suggest a significant source of excess degassing at Karymsky Volcano, such as degassing of unerupted basaltic magma, or may indicate that the eruptive volume is underestimated. More measurements are required to test these hypotheses. Both Bezymianny and Karymsky Volcanoes behave in a manner consistent with open-system degassing, while Redoubt Volcano behaves in a predominantly closed-system degassing fashion (Werner et al., 2012). One of the primary differences seen among the three target volcanoes is with respect to eruption interval. Specifically, Redoubt Volcano erupts on decade-long intervals, Bezymianny Volcano erupts on month to year-long intervals, and Karymsky Volcano erupts on day to week-long intervals. Another significant difference is seen among the passive SO_2 emissions observed throughout the study period at these volcanoes, with mean passive SO_2 emission rates of 4200 t/d, 210 t/d, and 70 t/d observed at Redoubt, Bezymianny and Karymsky Volcanoes, respectively. At all three target volcanoes, degassing of excess volatiles is proposed. The excess volatiles observed at Redoubt and Bezymianny Volcano may be explained by an exsolved volatile phase at depth in addition to passive degassing of unerupted magma (Werner et al., 2012). In Table 5.2, the estimated dissolved volatile concentrations at entrapment depths were subtracted from the calculated initial volatile concentration in the magma to estimate the percent of CO_2 and S that would be exsolved at entrapment depths. In the cases of Bezymianny and Redoubt Volcanoes, 97% and 99% of the initial CO_2, and 37% and 50% of the initial S, respectively, should be exsolved at pressures corresponding with the proposed magma storage regions suggesting that exsolved volatiles can explain a significant portion of the estimated excess volatiles. Improved constraints on the eruptive volume at Karymsky Volcano is required to test the validity of the proposed initial S concentration, and if found to be accurate, degassing of unerupted magma would be

required to explain the relatively high surface SO_2 emissions compared to the relatively small eruptive volume. The variations in eruptive style and degassing behavior at these three volcanoes can best be captured using a monitoring program designed for their specific activity type.

Redoubt Volcano's relatively infrequent eruptions and predominantly closed-system degassing behavior suggests that during periods of quiescence only minimal volcanic emissions measurements are required to maintain records of background emissions. During periods of quiescence, monitoring may be best done by seismic techniques. Once unrest is detected, volcanic emissions measurements will become increasingly important. Increases in SO_2 and/or CO_2 emission rates and a change in the CO_2/SO_2 ratio can be used to detect magma ascent and help forecast when the eruption may occur. One challenge at Redoubt Volcano will be that over the decade long time periods between eruptions, a well-developed hydrothermal system may develop which could result in significant scrubbing of SO_2 emissions (Symonds et al., 2001). In this case, measurements of CO_2 emissions should be collected to facilitate detection of magma ascent. Following eruption, significant SO_2 emissions can be monitored remotely using satellite techniques such as OMI and emission clouds can be tracked to help mitigate hazards. Daily satellite SO_2 measurements can be complemented by weekly to biweekly airborne measurements to monitor changes in gas composition over the course of the eruption.

Eruptions occur at Bezymianny Volcano on time periods of months to years. One challenge for monitoring activity at Bezymianny Volcano is its close proximity to the highly active Kliuchevskoi Volcano (~10 km). This often makes it difficult to remotely detect changes in activity such as seismicity, or elevated SO_2 emissions from satellite data. Scientists from the Kamchatkan Volcano Eruption Response Team have been successful at forecasting eruptions from Bezymianny Volcano using thermal infrared satellite observations and seismicity, when activity at Kliuchevskoi Volcano is quiet

(Senyukov, 2009). We propose that biannual measurements of gas composition (direct sampling) and flux (FLYSPEC) can be used to help forecast eruptions at Bezymianny Volcano by providing constraints on the relative depth of magma degassing at the time of sample collection. These data can help supplement satellite and seismic data, to help forecast eruptions of Bezymianny Volcano even when Kliuchevskoi Volcano is restless. Following eruption, satellite data can be used to track hazardous emissions in the eruption cloud.

Karymsky Volcano erupts on time periods of days to weeks. These eruptions are often relatively small and produce hazards on a predominantly local scale. Our observations show significant decreases in SO_2 emission rates in the minutes preceding explosive eruption. Therefore continuous and automatic high temporal resolution SO_2 measurements acquired by an IR or UV camera would be particularly useful for monitoring emissions at Karymsky Volcano. Additionally, our observations show that infrasound can be successfully used at Karymsky Volcano to remotely characterize volcanic activity and detect explosive eruption in any weather conditions. Therefore a combination of continuous high temporal resolution SO_2 emission rate and infrasound measurements would provide adequate data to monitor volcanic activity at Karymsky Volcano. Additionally, it may be possible to safely acquire gas composition measurements through the use of a remote open-path FTIR spectrometer (Francis et al., 1995), or a Multi-Gas instrument (Shinohara, 2005; Aiuppa et al., 2007) for in situ plume sampling of plume composition when the plume is blown down the side of the volcano. The combined measurements of gas composition and flux would help constrain magma degassing processes at depth and refine proposed models to improve our understanding of this dynamic system.

5.5 Final Conclusions

The results of this dissertation show that direct, remote, and indirect measures of volcanic emissions can provide useful data to characterize volcanic activity and infer subsurface

processes. These results can be used to improve volcano monitoring, eruption forecasting and hazard mitigation. The advantages and disadvantages of each volcanic emissions measurement technique and the high variability in volcanic activity suggest that careful consideration must be made when selecting the instruments to meet a particular science objective. I recommend that: (1) satellite measurements are used to complement ground-based volcanic emissions measurements to capture explosive emissions and track volcanic clouds; and (2) both gas composition and flux measurements be acquired whenever possible to allow both changes in magma degassing depth and conduit permeability to be identified and to assist in eruption forecasting. Furthermore, the results of Chapter 4 find that infrasound provides a highly complementary dataset to volcanic emissions measurements and should be used when possible to monitor and characterize volcanic activity, especially at remote and/or poor visibility volcanoes when direct and remote observations are not available.

Table 5.1: A comparison of instrumental techniques used in this dissertation.

Instrument	Parameter Measured	Derived Products	Wavelength Region	Spatial Resolution	Sample Rate	Error	Required Sample Conditions	Estimated instrument Cost (USD)	Technique Advantages	Technique Disadvantages
FLYSPEC: Scanning UV Spectrometer System[1]	Intensity, absorbance	SO_2 column density, SO_2 emission rate	305 – 325 nm	140 m per degree at 4 km distance	~300 ms – 3 s per measurement; 30 sec – 15 min per scan/traverse depending on plume size	±33% to ±88% for optimal to moderate conditions	Clear sky between instrument and plume, moderate wind speed, perpendicular scan geometry, non-opaque plume, minimal ash	~$15K	Low power consumption, highly portable, easy to acquire measurements, software provided	Requires good sample conditions; data interpretation can be difficult, emission rates require plume speed estimates
COSPEC: UV Correlation Spectrometer[2]	Intensity, absorbance	SO_2 column density, SO_2 emission rate	300 – 315 nm	~50-100 m depending on airspeed	1 s per measurement; 30 sec – 15 min per scan/traverse depending on plume size	±20%	Clear sky between instrument and plume, moderate wind speed, perpendicular scan geometry, non-opaque plume, minimal ash	~$50K	Established technique with lower error than scanning mode	Requires good sample conditions, gas flights are expensive (~$8k for 6 hour flight)
NiCAIR: Thermal Imaging Camera[3]	Radiance, absorbance, emissivity	SO_2 and ash column density, SO_2 mass and emission rate, ash mass and emission rate, plume speed	7 – 14 μm	2.8 x 2.8 m per pixel at 4 km distance	5 s per measurement	±50% SO_2; ±100% Ash	Clear sky, low to moderate winds, perpendicular view, translucent plume	~$30K	Relatively high temporal resolution, detects both SO_2 and ash	Data analysis computationally intensive; Low portability
FLIR A320: IR Thermal Imaging Camera[4]	Radiance	Pixel integrated brightness temperature, plume speed	7.5 – 13 μm	5.2 x 5.2 m per pixel at 4 km distance	up to 30 Hz	NA	Clear sky, low to moderate winds	~$12K	Easy to operate, visually appealing dataset; highly portable	Data analysis computationally intensive; at sample distances (~4km) temperatures are only approximate

Table 5.1: Continued

Instrument	Parameter Measured	Derived Products	Wavelength Region	Spatial Resolution	Sample Rate	Error	Required Sample Conditions	Estimated instrument Cost (USD)	Technique Advantages	Technique Disadvantages
OMI : UV/Visible Satellite Sensor[5]	Intensity, absorbance	SO_2 column density, mass and emission rate	270 – 500 nm	13 x 24 km at nadir	1+ per day	-55% for TRL, +79% for PBL SO_2 column densities	Sufficient UV (low signal/noise for high latitude winters)	Data available online	Free data, daily global coverage	Fairly high detection limit (~2 – 4 kt/day SO_2 for high latitude springtime); Poor spatial resolution; row anomaly
Infrasound: Low Frequency Sound Waves[6]	Pressure	Eruption explosivity, relative magma fragmentation level, potential to discriminate styles of volcanic activity	~17 - 17,000 m (0.02 - 20 Hz), *Note that this is the wavelength of pressure, not radiation*	NA	250 Hz	Sensor noise ~10^{-5} Pa; Error in source location ~1-3°	Low wind, minimum of 4 sensors to constrain event time and source location	~$4K per sensor	Continuous, high temporal resolution, all-weather	Challenging deployment, indirect measure of volcanic emissions only
Fumarole Sampling[7]	Molar concentration of: H_2O, CO_2, SO_2, H_2S, HCl, N_2, Ar, O, HF, HBr, CO, etc.	Gas composition, total volatile flux when combined with SO_2 emission rate	NA	Variable	Variable	±5% Analytical Uncertainty	Scientist must be able to access the fumarole, requires resting volcano and high visibility	~$120 per silica bottle	Many species measured	Unsafe sampling environment, analysis can be time intensive, difficult to transport samples internationally
Melt Inclusion[8]	Weight percent of: H_2O, CO_2 and more	Melt volatile content at entrapment depths, can be used to estimate storage depths	NA	Variable	Variable	±0.4- 0.7 wt.% H_2O, ±20 - 120 ppm CO_2 (Chapter 3 analysis)	Requires constraints on eruption timing (i.e. rocks sampled when warm)	Analysis on Electron Microprobe $45/hr	Provides subsurface constraints on melt volatile content	Labor intensive sample collection, preparation, and analysis

[1]Horton et al., 2006; [2]Stoiber et al., 1983; Millan, 2008; Werner et al., 2012; [3]Prata and Bernardo, 2009; [4]Spampinato et al., 2011; [5]Levelt et al., 2006; [6]Fee and Matoza, 2013; [7]Giggenbach, 1975; [8]Lowenstern, 1995.

Table 5.2: Comparison of the target volcanoes.

Characteristic	Redoubt	Bezymianny	Karymsky
Magma composition	Andesite	Basaltic-andesite	Andesite
Age (years b.p.)	890,000	47,000	74,000
Altitude (m.a.s.l.)	3100	3000	1600
Whole Rock wt.% SiO_2	57.4 – 62.0[a]	56.8 – 60.4[b]	59-62.4[c]
Eruption interval	~20 years	~6 months – 1 year	Minutes - Days
Estimated depth to magma storage	~4-6 km[d]	~6-10 km[e,f]	~4-6 km[g]
Estimated eruptive volume (m^3)	~80-120 x 10^6 (Total 3 months of 2009 eruption)[d]	~2.54 x 10^7 (Oct. 2007) ~5.4 x 10^6 (Dec. 2009)	~2.55 x 10^5
Volcano Explosivity Index (Eruptive volume, Ash cloud height)[h]	2, 4	2, 3	1, 2
Eruptive products	Lava dome, tephra, pyroclastic material	Lava flow, tephra, pyroclastic material	Tephra, pyroclastic material, lava dome
Mean passive SO_2 flux (t/d)	4,200	210	70
Mean explosive SO_2 mass (kt)	30.2	5.9	NA
% Passive/total emissions	45-58%	87-94%	NA
Total volatile flux (kt/d)	NA	3-47	NA
Primary degassing behavior	Closed-system	Open-system	Open-system
Expected conduit permeability	Low	High – Interconnected fracture network model?	High to low – Interconnected fracture network – transitions to vent sealing
Proposed eruption trigger	Dome collapse and/or magma ascent	Dome collapse and/or magma ascent	Decreased conduit permeability, magma ascent
Excess volatiles	Yes	Yes	Yes
Estimated S saturation (ppm) at entrapment depths (rhyolitic melt, NNO+1, 2-4 Wt.% H_2O) [i]	~2800	~3200	~2800
Calculated primary initial SO_2 concentration (ppm)	5,560	5,070	57,600
Exsolved S phase (ppm)	~50%	~37%	~95%
X * eruptive volume	~2	~2	~22
Estimated CO_2 saturation at entrapment/degassing depths in ppm (rhyolitic melt)	~0 – 100 (~4.4 wt.% H_2O[a])	~410 (~3.3 wt% H_2O)	~300 (~1.5 wt% H_2O[j])
Primary calculated initial CO_2 concentration (ppm	~19,800	~16,700	NA
Exsolved CO_2 phase (ppm)	99%	97%	NA
X * eruptive volume	~40	~33	NA

[a]Coombs et al., in press; [b]Turner et al., in press; [c]Izbekov et al., 2004; [d];Bull and Buurman, 2012; [e]Braitseva, 1991; [f]Thelen et al., 2010; [g]Ozerov et al., 2003; [h]Newhall and Self, 1982; [i]Moretti et al., 2003; [j]Newman and Lowenstern, 2002.

References Cited:

Aiuppa, A., Moretti, R., Federico, C., Guidice, G., Gurrieri, S., Liuzzo, M., Papale, P., Shinohara, H. and Valenza, M., 2007. Forecasting Etna eruptions by real-time observations of volcanic gas composition. Geology, 35(12): 1115-1118.

Bluth, G.J.S., Shannon, J.M., Watson, I.M., Prata, A.J. and Realmuto, V.J., 2007. Development of an ultra-violet digital camera for volcanic SO_2 imaging. Journal of Volcanology and Geothermal Research, 161: 47-56.

Braitseva, O., 1991. Bezymyannyi volcano: Eruptive history and dynamics. Journal of Volcanology and Seismology, 12(2): 165-194.

Bull, K.F. and Buurman, H., 2012. An overview of the 2009 eruption of Redoubt Volcano, Alaska. Journal of Volcanology and Geothermal Research, Special Issue on the 2009 Redoubt Eruption. doi:10.1016/j.volgeores.2012.06.024.

Coombs, M., Sisson, T., Bleick, H., Henton, S., Nye, C., Payne, A., Cameron, C., Larsen, J., Wallace, K. and Bull, K.F., in press. Andesites of the 2009 eruption of Redoubt Volcano, Alaska. Journal of Volcanology and Geothermal Research, Special Issue on the 2009 Redoubt Eruption.

Fee, D. and Matoza, R., 2013. An overview of volcano infrasound: From Hawaiian to plinian, local to global. Journal of Volcanology and Geothermal Research, 249: 123-139. doi:10.1016/j.jvolgeores.2012.09.002.

Francis, P., Maciejewski, C., Oppenheimer, C., Chafflin, C. and Caltabiano, T., 1995. SO_2:HCl ratios in the plumes from Mt. Etna and Vulcano determined by Fourier transform spectroscopy. Geophysical Research Letters, 22: 1717-1720.

Giggenbach, W., 1975. A simple method for the collection and analysis of volcanic gas samples. Bulletin of Volcanology, 39: 132-145.

Horton, K., Williams-Jones, G., Garbeil, H., Elias, T., Sutton, A.J., Mouginis-Mark, P., Porter, J. and Clegg, S., 2006. Real-time measurement of volcanic SO_2 emissions: validation of a new UV correlation spectrometer (FLYSPEC) Bulletin of Volcanology, 68(4): 323-327.

Izbekov, P., Eichelberger, J. and Ivanov, B., 2004. The 1996 eruption of Karymsky Volcano, Kamchatka: Historical record of basaltic replenishment of an andesite reservoir. Journal of Petrology, 45(11): 2325-2345. doi:10.1093/petrology/egh059.

Levelt, P., Van den Oord, G.H.J., Dobber, M., Malkki, A., Visser, H., de Vries, J., Stammes, P., Lundell, J. and Saari, H., 2006. The Ozone Monitoring Instrument. IEEE Transactions on geoscience and remote sensing, 44(5).

Lowenstern, J.B., 1995. Applications of silicate-melt inclusions to the study of magmatic volatiles. In: J.F.H. Thompson (Editor), Magmas, Fluids and Ore Deposits. Mineralogical Association of Canada Short Course, pp. 71-99.

Millan, M., 2008. Absorption correlation spectrometry. In: G. Williams-Jones, J. Stix and C. Hickson (Editors), The COSPEC Cookbook: Making SO_2 Measurements at Active Volcanoes. IAVCEI, pp. 1-62.

Moretti, R., Papale, P. and Ottonello, G., 2003. A model for the saturation of C-O-H-S fluids in silicate melts. In: C. Oppenheimer, D. Pyle and J. Barclay (Editors), Volcanic Degassing. The Geological Society of London, London, pp. 81-101.

Mori, T. and Burton, M., 2006. The SO_2 camera: A simple, fast and cheap method for ground-based imaging of SO_2 in volcanic plumes. Geophysical Research Letters, 33: L24804.

Newhall, C.G. and Self, S., 1982. The volcanic explosivity index (VEI): An estimate of explosive magnitude for historical volcanism. Journal of Geophysical Research, 87(C2): 1231-1238.

Newman, S. and Lowenstern, J.B., 2002. VolatileCalc: a silicate melt-H_2O-CO_2 solution model written in Visual Basic for excel. Computers & Geosciences, 28(5): 597-604.

Ozerov, A., Ispolatov, I. and Lees, J., 2003. Modeling strombolian eruptions of Karymsky volcano, Kamchatka, Russia. Journal of Volcanology and Geothermal Research, 122: 265-280.

Prata, A.J. and Bernardo, C., 2009. Retrieval of volcanic ash partical size, mass and optical depth from a ground-based thermal infrared camera. Journal of Volcanology and Geothermal Research, 186: 91-107. doi:10.1016/j.volgeores.2009.02.007.

Senyukov, S., 2009. Experinece of predicting explosive eruptions at Bezymianny Volcano (Russia, Kamchatka). 6th Biennial Workshop on Japan-Kamchatka-Alaska Subduction Processes, June 22 - 26: Fairbanks, Alaska.

Shinohara, H., 2005. A new technique to estimate volcanic gas composition: plume measurements with a portable multi-sensor system. Journal of Volcanology and Geothermal Research, 143: 319-333.

Spampinato, L., Calvari, S., Oppenheimer, C. and Boschi, E., 2011. Volcano surveillance using infrared cameras. Earth-Science Reviews, 106: 63-91. doi:10.1016/j.earscirev.2011.01.003.

Stoiber, R., Malinconico, L. and Williams, S., 1983. The use of correlation spectrometers at volcanoes. In: H. Tazieff and J. Sabroux (Editors), Forecasting Volcanic Events. El Sevier, Amsterdam - New York, pp. 425-444.

Symonds, R.B., Gerlach, T.M. and Reed, M.H., 2001. Magmatic gas scrubbing: implications for volcano monitoring. Journal of Volcanology and Geothermal Research, 108(1-4): 303-341. doi:10.1016/S0377-0273(00)00292-4.

Thelen, W., West, M. and Senyukov, S., 2010. Seismic characterization of the fall 2007 eruptive sequence at Bezymianny Volcano, Russia. Journal of Volcanology and Geothermal Research, 194: 201-213.

Turner, S.J., Izbekov, P. and Langmuir, C., in press. The magma plumbing system of Bezymianny Volcano: Insights from trace element whole-rock geochemistry and amphibole compositions. Journal of Volcanology and Geothermal Research.

Werner, C., Kelly, P., Doukas, M., Lopez, T., Pfeffer, M., McGimsey, G. and Neal, C., 2012. Degassing associated with the 2009 eruption of Redout Volcano, Alaska. Journal of Volcanology and Geothermal Research, Special Issue on the 2009 Redoubt Eruption. doi:10.1016/j.jvolgeores.2012.04.012.

Zharinov, N. and Demyanchuk, Y., 2011. Assessing the volumes of material discharged from Bezymyannyi Volcano during the1955-2009 period. Journal of Volcanology and Seismology, 5(2): 100-113. doi:10.1134/S0742046311020072.